

Universität Stuttgart

Measurement-Induced Entanglement Transitions in Quantum Systems

Von der Fakultät Mathematik und Physik der Universität Stuttgart
zur Erlangung der Würde eines Doktors der Naturwissenschaften
(Dr. rer. nat.) genehmigte Abhandlung

vorgelegt von

Felix Roser

aus Hannover

Hauptbericht:	Prof. Dr. Hans Peter Büchler
Mitbericht:	Prof. Dr. Eric Lutz
Prüfungsvorsitz:	Prof. Dr. Tilman Pfau

Tag der mündlichen Prüfung: 14. Januar 2026

Institut für Theoretische Physik III
Universität Stuttgart
2025

Meinem Großvater

Abstract

Entanglement is an essential concept in quantum mechanics and governs many modern areas of research in physics. The emergence of entanglement is typically associated with the application of unitaries coupling multiple particles. This scrambling (also referred to as *thermalization* in the sense of the eigenstate thermalization hypothesis) is counteracted by the inherent instability of entanglement under monitoring, as local measurements tend to disentangle systems. In this thesis, we study locally connected random quantum circuits in one dimension, which have proven to be a useful platform for the investigation of entanglement phenomena out of equilibrium. In hybrid quantum circuits — which feature local unitaries *and* measurements — the competition of the two can give rise to non-equilibrium phase transitions between volume-law entangled phases (if unitaries dominate) and area-law phases (if measurements dominate). Such transitions demonstrate the robustness of certain entanglement structures against finite monitoring rates. Note that entanglement transitions come in several varieties. Some models feature two distinct area-law phases, or a transition which is driven by the competition of two types of measurements in quantum circuits without unitaries. The *projective transverse field Ising model* is one such measurement-only model which exhibits an entanglement transition. It will play a key role throughout this work and is introduced in Chapter 1, together with some concepts on the characterization of entanglement phases and notes on efficiently simulable quantum circuits. In the remainder of this thesis, we use these foundations to demonstrate that the projective transverse field Ising model can be interpreted as a quantum error correcting code. The techniques developed in this context can be adapted for noise-resilient measurement protocols that make upper and lower bounds on the entanglement transition of the model experimentally accessible. We further investigate circuits that add unitary gates to the projective transverse field Ising model to realize extended critical entanglement phases.

- On the path towards scalable, universal quantum computation, decoherence presents a major obstacle. Residual interactions between a quantum system and its environment can lead to errors on qubits, possibly invalidating the results of a calculation. Here, *quantum error correction* provides a solution. The idea is to encode quantum information (logical qubits) non-locally across multiple physical qubits, thus protecting it from being accessed or changed by local errors. This delocalization of information requires

entanglement between the qubits. Hence, the field of quantum error correction is naturally connected to entanglement transitions.

In Chapter 2, we study the projective transverse field Ising model, where only two types of measurements drive a transition between an entangling and a disentangling area-law phase. Remarkably, circuit realizations in the entangling phase protect quantum information encoded in the initial state. We investigate the capabilities of the projective transverse field Ising model as a quantum error correcting code. A *decoder* is a classical algorithm which uses the recorded measurement history of a circuit in order to retrieve the initially encoded quantum information in a system. For the projective transverse field Ising model, we study three approaches: First, we discuss a naive approach based on *majority voting*, which is derived from the standard decoding scheme for classical repetition codes. This method is instructive, but ultimately fails and subsequently informs our following approaches. Next, we introduce a decoder based on *minimum weight perfect matching*, similar to decoding approaches used for topological surface codes. We verify the existence of an error threshold, below which the system can be reliably decoded. Lastly, we describe an efficient implementation of a *maximum likelihood decoder* for the projective transverse field Ising model, which slightly improves the previous error threshold. Remarkably, the decoding threshold does *not* coincide with the entanglement transition of the model, i.e., there exists a parameter regime in which quantum information is protected but cannot be retrieved.

- One can expand the projective transverse field Ising model by including unitaries in the circuits. This model, first introduced by Merritt and Fidkowski (“MF model”), maps to fermionic Gaussian trajectories via a Jordan–Wigner transformation. It is known that volume-law phases in circuits of this class are unstable under *any* finite monitoring rate. However, recently it was found that some models of this kind do exhibit extended regimes at low monitoring rates in which entanglement measures obey critical scaling laws. The MF model is a great testing ground to investigate this extended criticality, since it maps to a loop model which can be simulated very efficiently.

In a first part of Chapter 3, we verify and expand on the results by Merritt and Fidkowski. In particular, we find evidence that the boundaries of the critical phase can be described by a conformal field theory. This is well-known for second-order phase transitions and stands in contrast to the critical phase itself, which does *not* follow conformal scaling laws. For the MF model to reach criticality, four distinct operations (two types of unitaries and measurements) are needed. If one type of measurement is dropped, the associated loop model becomes *orientable*, which forbids any extended critical behavior. We show that a simple rescaling of the MF model breaks this orientability and allows for the realization of a critical phase with only one type of measurement (instead of two). Lastly, we demonstrate how the loop model underlying the MF model can be realized by a hybrid *Clifford* circuit model,

which does not admit an interpretation in terms of Gaussian fermions but exhibits the same critical phase as the MF model by construction. This model demonstrates that extended critical behavior is not restricted to fermionic models.

In a second part, we introduce and study generalized versions of the MF model called *macro models*. They enable us to generate a multitude of phase diagrams with and without critical phases. In particular, some macro models allow for the realization of an extended critical phase with only one type of unitary and measurement. This simplification stands in contrast to other known circuits which usually require at least three competing operations to reach a critical regime, and is potentially useful in future experimental realizations. We link the qualitative features of all phase diagrams to the properties of the associated loop models; again, their orientability plays a major role. Our numerics suggest that the boundaries of the critical phases are described by some (unknown) conformal field theory.

- It is notoriously difficult to observe measurement-induced entanglement transitions experimentally: Due to the non-linearity of the entanglement entropy, many copies of a state are needed to measure the entanglement of a system (via full state tomography). However, the inherent randomness of projective measurements makes the repeated preparation of states produced by hybrid quantum circuits exponentially unlikely. This *postselection problem* renders direct measurements of entanglement entropies inaccessible *in principle* — even in a noise-free experiment.

In Chapter 4 we propose explicit, platform-agnostic protocols for measuring upper and lower bounds on the entanglement transition of the projective transverse field Ising model. Crucially, these procedures not only avoid the postselection problem but are also robust in the presence of noise. To this end, we first show how decoding quantum information (motivated by the approach described in Chapter 2) can be used to measure a lower bound on the entanglement transition. We then contrive a protocol that combines classical shadow tomography with quantum error correction to also measure an upper bound. The sharpness of both bounds serves as an indicator for the noise rate in the system. Finally, we study another accessible lower bound based on shadow tomography. Our numerics suggest that the two lower bounds — constructed via the decoding of quantum information and error corrected shadow tomography — coincide.

Zusammenfassung

Verschränkung ist eines der grundlegenden Phänomene der Quantenmechanik und liegt vielen modernen Forschungsgebieten der Physik zugrunde. Typischerweise treten Verschränkungen auf, wenn mehrere Teilchen durch unitäre Evolutionen miteinander gekoppelt werden. So kommt es zu einer Durchmischung (oder *Thermalisierung* im Sinne der Eigenzustands-Thermalisierungshypothese), der die Instabilität von Verschränkungen unter Beobachtung entgegenwirkt, da lokale Messungen dazu neigen Verschränkungen in Systemen wieder zu zerstören. In dieser Dissertation betrachten wir zufällig generierte Quantenschaltungen (eher bekannt als *random quantum circuits*) mit lokaler Konnektivität in einer Dimension, die sich als nützliche Plattform zum Untersuchen von Verschrängungsphänomenen etabliert haben. In hybriden Quantenschaltungen führt die Konkurrenz von unitären Gattern und projektiven Messungen zu einem Nichtgleichgewichts-Phasenübergang zwischen verschränkten *Volume-Law-Phasen* (wenn unitäre Gatter dominieren) und *Area-Law-Phasen* (wenn Messungen dominieren). Solche Übergänge zeigen, dass manche Verschränkungsstrukturen gegen endliche Messraten robust sind. Verschränkungsübergänge treten in verschiedenen Variationen auf. Beispielsweise besitzen manche Modelle mehrere Area-Law-Phasen und manche Übergänge entstehen durch die Konkurrenz zweier verschiedener Typen von Messungen (in einer Quantenschaltung ohne unitäre Gatter). Das *projektive Ising-Modell mit transversalem Feld* ist ein solches Modell, das ausschließlich auf Messungen basiert und einen Übergang zwischen zwei Verschränkungsphasen aufweist. Es spielt in dieser Arbeit eine Schlüsselrolle und wird in Kapitel 1 eingeführt, zusammen mit einigen Konzepten zur Charakterisierung von Verschränkungsphasen und zur effizienten Simulation großer Quantenschaltungen. Im weiteren Verlauf dieser Dissertation verwenden wir diese Grundlagen, um zu demonstrieren, dass das projektive Ising-Modell mit transversalem Feld als Quantenfehlerkorrekturcode interpretiert werden kann. Basierend auf den dafür entwickelten Methoden führen wir außerdem fehlerresistente Messprotokolle ein, die es ermöglichen, den Verschränkungsübergang des Modells experimentell einzugrenzen. Im Weiteren untersuchen wir Quantenschaltungen, die das projektive Ising-Modell mit transversalem Feld um unitäre Gatter erweitern, um ausgedehnte kritische Verschränkungsphasen zu realisieren.

- Bei der Entwicklung von skalierbaren, universellen Plattformen für Quantencomputer stellt Dekohärenz ein großes Hindernis dar. Wechselwirkungen zwischen einem Quantensystem und seiner Umgebung führen zu Fehlern auf Qubits und machen das Ergebnis einer Rechnung möglicherweise ungültig. Die *Quantenfehlerkorrektur* bietet hier eine Lösung. Die Grundidee besteht darin, Quanteninformation (logische Qubits) nicht-lokal auf mehreren physikalischen Qubits zu codieren, sodass sie nicht durch lokale Fehler ausgelesen oder verändert wird. Für diese Delokalisierung von Information müssen die Qubits verschränkt sein. Somit ist das Gebiet der Quantenfehlerkorrektur mit dem der Verschränkungsübergänge verknüpft.

In Kapitel 2 betrachten wir das projektive Ising-Modell mit transversalem Feld, in dem nur zwei Arten von Messungen einen Übergang zwischen einer verschränkenden und einer entschränkenden Area-Law-Phase ermöglichen. Bemerkenswerterweise schützen Quantenschaltungen in der verschränkenden Phase die Quanteninformation, welche in den Anfangszustand codiert wurde. Wir untersuchen deshalb, wie gut das projektive Ising-Modell mit transversalem Feld als Quantenfehlerkorrekturcode fungieren kann. Ein *Decoder* ist ein klassischer Algorithmus, der die aufgezeichnete Messhistorie einer Schaltung nutzt, um die zuvor auf einem System codierte Quanteninformation wiederherzustellen. Wir betrachten drei verschiedene Decodier-Ansätze für das projektive Ising-Modell mit transversalem Feld: Zuerst diskutieren wir eine naive Herangehensweise, die auf *Mehrheitsentscheidungen* basiert; ähnlich wie das Decodierungsschema, welches üblicherweise für den klassischen Wiederholungscode verwendet wird. Diese Methode ist zwar lehrreich, kann aber letztendlich die codierte Quanteninformation nicht zuverlässig zurückgewinnen. Davon inspiriert betrachten wir als Nächstes einen Decoder, der auf *minimum weight perfect matching* basiert, ähnlich wie Decodieransätze, die im Zusammenhang mit topologischen surface codes angewendet werden. Wir bestätigen, dass eine charakteristische Fehlerrate existiert, unterhalb derer das System zuverlässig decodiert werden kann. Zuletzt beschreiben wir die effiziente Implementierung eines *Maximum-Likelihood-Decoders* für das projektive Ising-Modell mit transversalem Feld, welcher die zuvor beschriebene charakteristische Fehlerrate geringfügig verbessert. Dabei ist beachtenswert, dass diese Fehlerrate nicht mit dem Verschränkungsübergang des Modells übereinstimmt; somit existiert ein Regime im Parameterraum, in dem Quanteninformation zwar geschützt ist, aber nicht wiederhergestellt werden kann.

- Das projektive Ising-Modell mit transversalem Feld kann um unitäre Gatter erweitert werden. Dieses Modell wurde zuerst von Merritt und Fidkowski eingeführt („MF-Modell“) und lässt sich mithilfe einer Jordan-Wigner-Transformation auf Trajektorien von gaußschen Fermionen abbilden. Es ist bekannt, dass Volume-Law-Phasen in Schaltungen dieser Klasse bei beliebig kleinen Messraten instabil sind. Manche Modelle dieser Art besitzen jedoch ausgedehnte Regimes bei kleinen Messraten, in denen Verschränkungsgrößen ein kritisches Skalierungsverhalten aufzeigen. Das MF-Modell eignet sich hervorragend, um solche ausgedehnten Kritikalitäten zu untersuchen, da

es sich auf ein Loop-Modell abbilden lässt, welches sehr effizient simuliert werden kann.

Im ersten Teil von Kapitel 3 reproduzieren und erweitern wir die Ergebnisse von Merritt und Fidkowski. Insbesondere finden wir Hinweise darauf, dass die Grenzen der kritischen Phase durch eine konforme Feldtheorie beschrieben werden können. Solche konformen Feldtheorien gehen bekannterweise mit Phasenübergängen zweiter Ordnung einher; das steht im Kontrast zur kritischen Phase, die *keinem* konformen Skalierungsgesetz folgt. Um das MF-Modell in die kritische Phase zu bringen, werden vier verschiedene Operationen (je zwei Arten von unitären Gattern und Messungen) benötigt. Wenn eine Art von Messungen wegfällt, wird das zugehörige Loop-Modell *orientierbar*, was ein ausgedehntes kritisches Verhalten verbietet. Wir zeigen, dass eine einfache Reskalierung des MF-Modells genügt, um diese Orientierbarkeit aufzuheben und eine kritische Phase mit nur einer Art von Messungen zu erreichen (anstelle von zwei Messungen). Zuletzt demonstrieren wir, wie das Loop-Modell, welches dem MF-Modell zugrunde liegt, auch von einer hybriden *Clifford-Quantenschaltung* realisiert werden kann. Dieses Modell kann nicht als System von gaußschen Fermionen verstanden werden, besitzt aber per Konstruktion dasselbe Phasendiagramm wie das MF-Modell. Damit wird klar, dass ausgedehntes kritisches Verhalten nicht nur in fermionischen Modellen auftritt.

Im zweiten Teil führen wir verallgemeinerte Versionen des MF-Modells ein, die wir *Makro-Modelle* nennen. Sie ermöglichen uns, eine Vielzahl von verschiedenen Phasendiagrammen mit und ohne kritische Phasen zu realisieren. Insbesondere erreichen manche Makro-Modelle eine ausgedehnte kritische Phase mit jeweils nur einer Art von unitären Gattern und Messungen. Diese Vereinfachung steht anderen bekannten Quantenschaltungen gegenüber, die ein kritisches Regime üblicherweise nur mit mindestens drei konkurrierenden Operationen erreichen können, und könnte für zukünftige experimentelle Realisierungen nützlich werden. Wir verknüpfen die qualitativen Merkmale aller Phasendiagramme mit den Eigenschaften der zugehörigen Loop-Modelle; auch hier spielt deren Orientierbarkeit eine wichtige Rolle. Unsere Numerik weist darauf hin, dass die Grenzen der kritischen Phasen von einer (unbekannten) konformen Feldtheorie beschrieben werden.

- Es ist allgemein schwierig, durch Messungen induzierte Verschränkungsübergänge experimentell zu beobachten: Aufgrund der Nichtlinearität der Verschränkungsentropie werden viele Kopien eines Zustands benötigt, um die Verschränkung eines Systems (mithilfe einer vollständigen Zustandstomographie) zu messen. Die inhärente Zufälligkeit projektiver Messungen macht es jedoch exponentiell unwahrscheinlich, in einer hybriden Quantenschaltung denselben Zustand wiederholt zu erzeugen. Dieses *Postselektionsproblem* macht direkte Messungen von Verschränkungsentropien *prinzipiell* unzugänglich – sogar in idealen, störungsfreien Experimenten.

In Kapitel 4 stellen wir explizite, plattformunabhängige Protokolle zum Messen von oberen und unteren Schranken für den Verschränkungsübergang des projektive Ising-

Modell mit transversalem Feld vor. Entscheidend ist, dass diese Prozeduren nicht nur dem Postselektionsproblem entgehen, sondern auch robust gegenüber Störungen sind. Wir zeigen zunächst, wie das Decodieren von Quanteninformation (motiviert von unserem Ansatz in Kapitel 2) genutzt werden kann um eine untere Schranke für den Verschränkungsübergang zu messen. Anschließend entwerfen wir ein Protokoll, das *classical shadow tomography* mit Quantenfehlerkorrektur kombiniert um auch eine obere Schranke zu messen. Die Breite des Intervalls, welches durch beide Schranken definiert ist, dient als Indikator für die Fehlerrate im System. Zuletzt untersuchen wir eine weitere experimentell zugängliche untere Schranke, welche ebenfalls auf shadow tomography basiert. Unsere numerischen Ergebnisse legen nahe, dass die beiden unteren Schranken – die durch das Decodieren von Quanteninformation und durch fehlerkorrigierte shadow tomography gemessen werden – denselben Wert annehmen.

List of Publications

This thesis is based on the following publications:

- *Decoding the projective transverse field Ising model*
Felix Roser, Hans Peter Büchler, and Nicolai Lang
Phys. Rev. B **107**, 214201 (2023)
doi: [10.1103/PhysRevB.107.214201](https://doi.org/10.1103/PhysRevB.107.214201), arXiv: [2303.03081v2](https://arxiv.org/abs/2303.03081v2)
- *Scaling of entanglement measures in loop models with extended criticality*
Felix Roser, Hans Peter Büchler, and Nicolai Lang
In preparation
- *Robust detection of an entanglement transition in the projective transverse field Ising model*
Felix Roser, Etienne Springer, Hans Peter Büchler, and Nicolai Lang
Preprint (2025)
arXiv: [2511.17370](https://arxiv.org/abs/2511.17370)

Previous publications:

- *Purity oscillations in coupled Bose–Einstein condensates*
Jonathan Stysch, **Felix Roser**, Dennis Dast, Holger Cartarius, and Günter Wunner
Phys. Rev. A **100**, 063605 (2019)
doi: [10.1103/PhysRevA.100.063605](https://doi.org/10.1103/PhysRevA.100.063605), arXiv: [1905.11671v2](https://arxiv.org/abs/1905.11671v2)
- *Experimentalphysik: Mechanik: Grundlagen und Aufgaben zu Massenpunkten, Newton, Fluiden & Co.*
Helga Kumrić and **Felix Roser**
Springer Berlin Heidelberg (2020)
doi: [10.1007/978-3-662-61855-4](https://doi.org/10.1007/978-3-662-61855-4)

Contents

Abstract	v
Zusammenfassung	ix
List of Publications	xiii
Contents	xv
1 Foundations	1
1.1 Random Quantum Circuits	1
1.1.1 Entanglement Measures	2
1.1.2 Measurement-Induced Entanglement Transitions	4
1.2 Efficient Simulation of Quantum Circuits	5
1.2.1 Stabilizer Formalism	5
1.2.2 Matchgate Quantum Circuits	8
1.3 The Projective Transverse Field Ising Model	12
1.3.1 The Colored Cluster Model	13
1.3.2 Entanglement Transition in the Projective Transverse Field Ising Model	15
2 Decoding the Projective Transverse Field Ising Model	19
2.1 Related Works	19
2.2 Repetition Code	22
2.3 Quantum Error Correction on the Projective Transverse Field Ising Model	26
2.3.1 The Model	27
2.3.2 Decoding	30
2.3.3 Efficient Numerical Simulations	32
2.4 Decoding with Majority Voting	39
2.4.1 Algorithm	39
2.4.2 Results	40

CONTENTS

2.5	Decoding with Minimum Weight Perfect Matching	44
2.5.1	Algorithm	44
2.5.2	Interpretation of the MWPM Decoder	48
2.5.3	Results	49
2.6	Maximum Likelihood Decoding	52
2.6.1	Algorithm	53
2.6.2	Results	57
2.7	Conclusion	58
	<i>Appendices</i>	60
2.A	Equivalence of Classical Samplings	60
2.B	Thermodynamic Limit of the MVD for $q = 0$	61
2.C	Graph Construction for the MWPM Decoder	63
2.C.1	Breadth-First Search	64
2.C.2	Crossing Nodes	65
2.D	Explicit Algorithm for the Maximum Likelihood Decoder on the PTIM	66
2.E	Extended Proof for the Equivalence of Maximum Likelihood Decoders	69
2.E.1	Useful Concepts	69
2.E.2	Proof	73
3	Scaling of Entanglement Measures in Loop Models with Extended Criticality	81
3.1	Introduction	81
3.2	Critical Scaling in Random Matchgate Circuits	83
3.3	Loop Models	85
3.3.1	Unitaries that are Cliffords and Matchgates	86
3.3.2	Encoding Initial States	87
3.3.3	Projective Measurements	88
3.3.4	Entanglement Measures	89
3.3.5	Loop Models with Ancilla Systems	91
3.3.6	The PTIM as a Loop Model	91
3.4	The Merritt–Fidkowski Model	92
3.4.1	The Model	92
3.4.2	Phase Diagram	95
3.4.3	Goldstone Phase	97
3.4.4	Conformal Scaling of Entanglement Measures	100
3.4.5	Transitions at $q \in \{0, 1\}$	104
3.4.6	Re-Interpretation of the MF Model	105
3.5	Generalized Loop Models	109
3.5.1	Initial Considerations	111
3.5.2	Volume Law at $p = 1$	112
3.5.3	Phase Diagrams	114
3.5.4	Extended Critical Phase	118
3.5.5	Conformal Scaling of Entanglement Measures	119

3.6	Conclusion	125
	<i>Miscellaneous Projects</i>	126
3.7	On Popcorn and Stars over Babylon	126
3.7.1	A Very Simple Quantum Circuit Model	126
3.7.2	Relation to the Popcorn Function	127
3.8	Majorana Flavors	130
3.9	Braiding Entanglement Dynamics and Simple Exclusion Processes	134
3.9.1	Unitary Bell Model	134
3.9.2	Introducing Local Measurements	135
	<i>Appendices</i>	139
3.A	Efficient Implementation of Matchgate Quantum Circuits	139
3.B	Periodic Boundaries in Fermionic Circuits	141
3.B.1	Without Ancilla Qubits	141
3.B.2	With Ancilla Qubits	143
3.C	On MF Model Aspect Ratios	146
3.D	Symmetry of the 2314 Phase Diagram	147
3.E	On Loop Models and their Phase Diagrams	150
3.E.1	Orientability in the Model 4231	150
3.E.2	Non-Orientable Loop Models	151
3.E.3	Phase Diagram Boundaries of the Models 4312 and 4321	153
3.E.4	Trivial Phase diagrams	153
4	Robust Detection of an Entanglement Transition	157
4.1	Related Works	157
4.2	Setting	159
4.3	Lower Bound via Decoding	160
4.4	Entanglement Bounds via Shadow Tomography	163
4.4.1	Detection of the Entanglement Transition on a Single Qubit	166
4.4.2	Upper Bound	169
4.4.3	Lower Bound	170
4.5	Summary	170
	<i>Appendices</i>	172
4.A	Extended Colored Cluster Model	172
4.B	Shadow Tomography Without Error Correction	173
4.C	Error Correction Algorithms for the PTIM	174
4.C.1	Error Correction Algorithm \mathcal{E}_E	175
4.C.2	Error Correction Algorithm \mathcal{E}_S	179
4.D	Classical State Prediction via Error Correction	182

CONTENTS

Ausführliche Zusammenfassung in deutscher Sprache	185
List of Figures	195
Bibliography	197
Acknowledgments	217

CHAPTER 1

Foundations

This thesis examines the entanglement dynamics of one-dimensional quantum circuits and some related phenomena. Chapters 2 to 4 are concerned with different aspects of this field. However some general introductions will be useful for the entirety of this thesis. This chapter establishes the most important concepts and models that will reappear later on. References to more extensive literature will be provided for interested readers.

1.1 Random Quantum Circuits

To set the stage, we start with a high-level description of the systems we investigate in this thesis. Consider a chain of L spin-1/2 degrees of freedom (*qubits*) in some initial state $|\Psi_0\rangle$. Qubits are indexed by their sites $i \in \{1, \dots, L\}$.¹ We are interested in *quantum circuits* that act on the qubits over T discrete time steps t_1, \dots, t_T . In every time step, local operations are randomly applied to the state. These operations may be unitary gates or projective measurements. The probabilities p, q, \dots , with which different kinds of operations are applied, span the (possibly high-dimensional) parameter space for a certain circuit model. If a circuit contains unitaries *and* measurements, we call it a *hybrid quantum circuit*. We show a model of this kind in Figure 1.1. A trajectory $\mathcal{T} = \{|\Psi(t)\rangle\}$ is fully determined by the initial state and the full record of operations including the results of all projective measurements. Note that the evolution of the state contains two kinds of randomness: Gates and measurements are applied randomly according to a *classical* process with the probabilities p, q, \dots . This stands in contrast to the inherent *quantum* randomness of the measurement outcomes [1].

¹In the case of periodic boundaries we assume $i \mapsto (i \bmod L)$ if $i > L$.

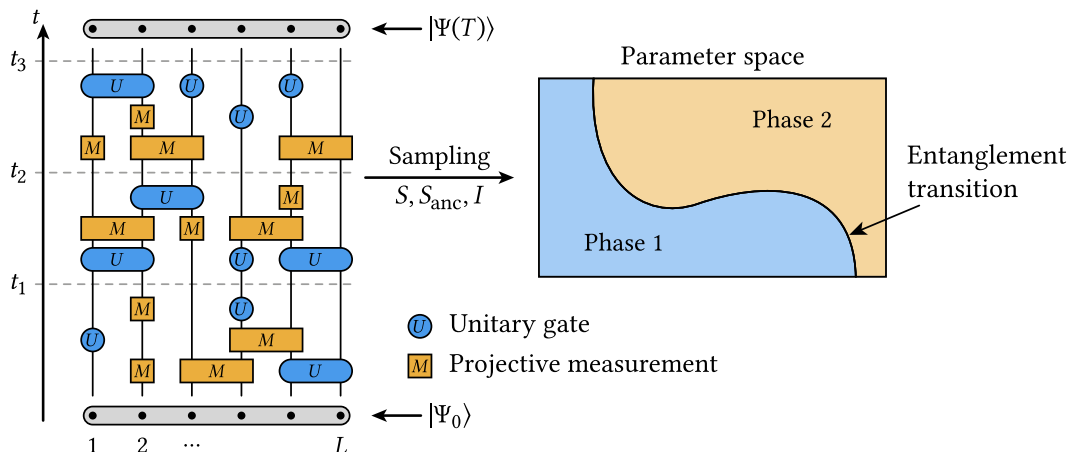


Figure 1.1 • General setting of a one-dimensional hybrid quantum circuit. Trajectory of a random quantum circuit on L qubits. Unitary gates and projective measurements are applied locally. Here we show on-site and nearest-neighbor operations; the particular gates and measurements depend on the model in question. A single trajectory (sample) is initialized in a state $|\Psi_0\rangle$. In discrete time steps, unitary gates and projective measurements are randomly applied. The parameter space for a model is constructed from the probabilities p, q, \dots for different types of operations to occur. To probe entanglement transitions in such circuits, entanglement entropies S, S_{anc} (with ancilla systems) and mutual informations I are measured and averaged over many trajectories. From this a phase diagram is constructed.

1.1.1 Entanglement Measures

In this thesis we are mostly interested in the entanglement dynamics of quantum circuits, i.e., how a state gets entangled or disentangled by the operations applied in the circuit. To quantify entanglement we use the *von Neumann entanglement entropy* [2].

Let $A \subseteq \{1, \dots, L\}$ be a subset of the system and \bar{A} its complement. $\rho = |\Psi\rangle\langle\Psi|$ is the density operator describing the (pure) state of the qubits. The reduced density matrix on A is defined as $\rho_A = \text{Tr}_{\bar{A}}[\rho]$. The von Neumann entanglement entropy of A is defined as

$$\mathcal{S}(A) = -\text{Tr}[\rho_A \log_2 \rho_A] = \mathcal{S}(\bar{A}) \quad (1.1)$$

and quantifies how strongly the qubits in A are entangled with the qubits in \bar{A} (and vice versa). Here we choose to use the logarithm in base 2 such that a pair of entangled qubits can contribute at most 1 to the entanglement entropy (instead of $\ln 2$). We can understand the entanglement entropy as a measure of the purity of a state ρ_A .² If a subsystem A is not entangled with its complement (which poses as an “environment” to A), ρ_A is pure and $\mathcal{S}(A) = 0$. If on the other hand the subsystems are entangled, ρ_A can never be pure and we

²In fact in a special class of circuits called stabilizer circuits, the von Neumann entropy is proportional to the logarithm of the purity.

find $\mathcal{S}(A) > 0$. In most cases we will be considering contiguous subsystems $A = \{1, 2, \dots, l\}$ of length $l = |A| \leq L$. In a slight abuse of notation, we denote the entanglement entropy by $\mathcal{S}(l)$.

To analyze the behavior of the entanglement entropy of a collection of circuit trajectories, we define the ensemble average $S(A) = \langle\langle \mathcal{S}(A) \rangle\rangle$ with

$$\langle\langle f \rangle\rangle = \sum_{\mathcal{T} \in \{\mathcal{T}\}} P_{p,q,\dots}(\mathcal{T}) \cdot f(\mathcal{T}). \quad (1.2)$$

For the ensemble average we take the sum over all possible trajectories $\{\mathcal{T}\}$ in a circuit (usually for a fixed initial state) and weigh every term with the probability $P_{p,q,\dots}(\mathcal{T})$ of a trajectory \mathcal{T} occurring given the circuit parameters p, q, \dots . As Equation (1.2) generally contains an exponential amount of terms, we are usually unable to determine ensemble averages exactly. Instead, we make use of the law of large numbers [3, 4] and perform simulations of *some* of the possible trajectories while making sure to sample them correctly according to the probabilities p, q, \dots . This is the sample average.³

To gain further insights into the entanglement *structure* of a state, we use the *mutual information*

$$\mathcal{I}(A, B) = \mathcal{S}(A) + \mathcal{S}(B) - \mathcal{S}(A \cup B) \quad (1.3)$$

which quantifies the entanglement between two disjoint subsystems A and B . In particular, we will consider the entanglement between two single qubits i and j

$$\mathcal{I}(i, j) = \mathcal{S}(\{i\}) + \mathcal{S}(\{j\}) - \mathcal{S}(\{i, j\}). \quad (1.4)$$

Again, the sample average is $I = \langle\langle \mathcal{I} \rangle\rangle$. On circuits with periodic boundaries, a translational invariance emerges. Shifting all qubits by a multiple of the size of a unit cell leaves all sample averages invariant.⁴ If the unit cells in a circuit contain only a single qubit, the average entanglement of two qubits can only depend on their distance and we write $I(i, j) = I(|i - j|)$. This will allow us to measure how quickly entanglement decays with increasing separation in a collection of states.

Lastly we introduce a modified version of the von Neumann entropy. Consider the chain of L *system qubits* and another chain of L *ancilla qubits*. We initialize the state such that the system qubits are fully entangled with the ancilla qubits; i.e., the state ρ of only the system qubits is fully mixed. When the circuit is applied to the system qubits, the ancilla qubits stay isolated and are not part of any operations. After some time T , we define the averaged entropy $S_{\text{anc}}(L, T)$ which measures the von Neumann entropy between the system and the ancilla qubits. With $S_{\text{anc}}(L, T = 0) = L$, in any unitary-only circuit it is also $S_{\text{anc}}(L, T > 0) = L$. Measurements do however purify the state and gradually disentangle

³In this thesis, we often use the terms “sample average” and “ensemble average” interchangeably.

⁴Operations in circuits are applied randomly, but there may be a predefined repeating pattern leading to the emergence of unit cells.

the two subsystems. Under any finite measurement rate it is therefore $S_{\text{anc}}(L, T \rightarrow \infty) \rightarrow C$ with some constant C . Nonetheless, S_{anc} allows us to measure how quickly a circuit is able to purify the system. This purification behavior turns out to be a very powerful tool to examine the entanglement dynamics of a circuit.⁵

1.1.2 Measurement-Induced Entanglement Transitions

Hybrid quantum circuits show particularly interesting entanglement dynamics [5–14]: Multi-qubit unitaries generally create entanglement and the repeated application of many unitaries allows entanglement structures to grow in the system. Local measurements on the other hand disentangle the qubits they act upon from the rest of the system. The competition between unitary gates and projective measurements typically drives an *entanglement transition*, which is characterized by a sudden change in the scaling of entanglement entropies between subsystems, averaged over many sample trajectories [5, 6]. In parameter regimes where unitaries dominate, we observe a volume law, i.e., entanglement measures like $S(L/2) \propto L$ scale with the number of qubits in the steady state. This is often referred to as a *thermalization* in the sense of the eigenstate thermalization hypothesis [15, 16]. If measurements dominate a circuit, the steady state is typically (mostly) disentangled and obeys an area law.⁶ In our one-dimensional case we find entanglement measures like $S(L/2)$ to be approximately constant in L . We also speak of a *purification* of the state. Some entanglement transitions of this kind have recently been realized experimentally [18–20].

While hybrid quantum circuits usually exhibit a transition between a volume-law and an area-law entangling phase, other dynamics are also possible. In this thesis we will for example investigate hybrid circuits with unitaries derived from the Hamiltonians of free fermions (see Subsection 1.2.2). Such circuits can only support a volume law if no measurements are performed at all. At any finite monitoring rate, the volume law breaks down [21–23]. In Chapter 3 we will demonstrate that circuits of this kind still exhibit very interesting entanglement dynamics. We will also consider circuits with no unitaries but instead competing types of projective measurements (see Section 1.3). Such measurement-only circuits may still exhibit entanglement transitions [21, 24–27]; in some special cases, they were even found to generate volume-law phases [28, 29].⁷

⁵In most cases, S_{anc} contains similar information as $S(l)$ but the entangling properties of a circuit can be evaluated without running simulations into a steady state $T \gg L$. Instead, S_{anc} will prove to be very revealing when considering constant aspect ratios $L \propto T$.

⁶This area law can be understood as a “quantum Zeno regime” where sufficiently frequent measurements suppress the growth of entanglement [5, 17].

⁷We note that entanglement transitions were also studied in time-continuous settings (see Refs. [22, 30–38]) as well as setups with Hamiltonian evolutions and repeated instantaneous measurements (see Refs. [39–41]). Further investigations indicate that entanglement transitions can also be controlled by varying the range of interactions in circuits [42–44] (instead of the monitoring rate).

Note that we are using the term “entanglement phase” very loosely. Technically, it is not possible to determine which phase a single state $|\Psi\rangle$ belongs to for two reasons:

1. Entanglement phases are defined by the average scaling behavior of entanglement measures. Determining the phase requires a whole collection of states of different system sizes L .
2. Actually measuring the entanglement in a single state experimentally turns out to be impossible. We expand on this in Chapter 4.

Nonetheless, we investigate entanglement transitions using tools and descriptions known from thermodynamics and therefore will use the word “phase” for convenience. In this thesis we will (among other things) employ the entanglement measures introduced in Subsection 1.1.1 to construct phase diagrams of different quantum circuits as indicated schematically in Figure 1.1.

1.2 Efficient Simulation of Quantum Circuits

To investigate the scaling behavior of entanglement measures (as for example the sample-averaged entanglement entropy S) numerically, we must simulate quantum circuits at relatively large system sizes L on a classical computer. For generic universal quantum circuits, this requires exponential resources.⁸ Therefore we will consider special classes of circuits which allow us to use exact numerical techniques with polynomial runtime in L , by imposing restrictions on unitaries and measurements. We refer to such circuits as *efficiently simulable*. In this section, we introduce two classes of efficiently simulable quantum circuits.

1.2.1 Stabilizer Formalism

The most widely used formalism for the efficient simulation of quantum circuits is the *stabilizer formalism*. In the context of this thesis, it is not only used as a numerical technique, but it will also serve as a framework to help us understand the physics underlying the models we investigate. Here we give a short introduction to this approach, following Ref. [45].

Consider a system of L qubits with the Hilbert space $\mathcal{H} = \bigotimes_{i=1}^L \mathbb{C}_i^2$. Let $X_i \equiv \sigma_i^x$, $Y_i \equiv \sigma_i^y$ and $Z_i \equiv \sigma_i^z$ be the Pauli matrices on the qubit i . The set of all Pauli matrices on all L qubits generates the *Pauli group*

$$\mathcal{P}_L = \{\chi \pi_1 \cdots \pi_L \mid \pi_i \in \{\mathbb{1}_i, X_i, Y_i, Z_i\}, \chi \in \{\pm 1, \pm i\}\}. \quad (1.5)$$

We call a state $|\Psi\rangle \in \mathcal{H}$ a *stabilizer state* if and only if there exists a subgroup $\mathfrak{S} \subset \mathcal{P}_L$ such that

$$\mathfrak{S} = \{p \in \mathcal{P}_L \mid p|\Psi\rangle = |\Psi\rangle\}. \quad (1.6)$$

⁸This is commonly assumed, but no proof is known.

In this case we call \mathfrak{S} the *stabilizer* of $|\Psi\rangle$.⁹ Herein lies the power of the stabilizer formalism: Conventionally storing a state $|\Psi\rangle$ would require the storage of the complex-valued coefficients for all 2^L basis vectors. Stabilizer states can however be defined by the generators of their stabilizer group. The stabilizer group of a pure stabilizer state is generally generated by L Pauli elements

$$\mathfrak{S} = \langle g_1, g_2, \dots, g_L \rangle \quad (1.7)$$

where the choice of generators $g_i \in \mathcal{P}_L$ is not unique. For example, the state $|00\rangle$ is stabilized by $\mathfrak{S} = \langle Z_1, Z_2 \rangle = \langle Z_1, Z_1 Z_2 \rangle$. Stabilizer states can thus be stored very efficiently. Intuitively, we can expand on Equation (1.7): Every generator g_i represents a constraint on the state $|\Psi\rangle$. If the generating set of \mathfrak{S} contains $n < L$ entries, it does not fully define a state $|\Psi\rangle$. This allows for the representation of specific mixed states.¹⁰ Consider for example $\mathfrak{S} = \langle Z_1 Z_2 \rangle$ which stabilizes both $|00\rangle$ and $|11\rangle$. The purity of a stabilizer state increases with the cardinality of the minimal generating set of its stabilizer group and is maximal at L . Importantly, the stabilizer formalism restricts itself to the subset of the Hilbert space \mathcal{H} which contains only stabilizer states. As a consequence, any unitary and projective actions (gates and measurements) in the stabilizer formalism must leave a state contained in this subset.

The *Clifford group* \mathcal{C}_L is the set of all $2^L \times 2^L$ unitaries that map the Pauli group \mathcal{P}_L onto itself

$$\mathcal{C}_L = \{V \in U(2^L) \mid V \mathcal{P}_L V^\dagger = \mathcal{P}_L\}. \quad (1.8)$$

It is generated by the Hadamard gate H , the phase gate S and the controlled-NOT gate $CNOT$. We call a quantum circuit a *stabilizer circuit*, if it consists only of unitary Clifford gates and projective Pauli measurements. The Gottesman-Knill theorem states that such stabilizer circuits can be simulated efficiently on a classical computer [46–48]. In the following, we describe on a basic level how stabilizer circuits can be implemented. Improvements to these techniques can be made [49], but are not important in this context.

We note that the restriction to Clifford gates is what makes the stabilizer circuits simulable – here they lose their universality. A universal set of quantum gates can be generated from the Clifford group and the T gate ($T = \sqrt{S}$).

Application of Clifford Gates

Let $V \in \mathcal{C}_L$ be a Clifford gate and $|\Psi\rangle$ a state that is stabilized by some generators g_i . When the unitary is applied to the state, we find

$$V|\Psi\rangle = V g_i |\Psi\rangle = V g_i V^\dagger V |\Psi\rangle. \quad (1.9)$$

The new state $V|\Psi\rangle$ is thus stabilized by $V g_i V^\dagger$ which is again a Pauli element [see Equation (1.8)]. From this, we understand how the stabilizer group \mathfrak{S} transforms under the

⁹It is easy to show that \mathfrak{S} is abelian.

¹⁰The density operator is $\rho \propto \prod_{i=1}^n (\mathbb{1} + g_i)$.

application of Clifford gates:

$$\mathfrak{S} \xrightarrow{V} V\mathfrak{S}V^\dagger = \{VgV^\dagger \mid g \in \mathfrak{S}\}. \quad (1.10)$$

As the classical simulation stores only the generators of \mathfrak{S} , any Clifford gate can be applied by only mapping those generators $g \rightarrow VgV^\dagger$, which can be done in $\mathcal{O}(L^2)$ time using a tableau algorithm [49].

Application of Projective Pauli Measurements

The stabilizer formalism also allows for the application of projective Pauli measurements. Consider an observable $O \in \mathcal{P}_L$ and a stabilizer group $\mathfrak{S} = \langle g_1, \dots, g_n \rangle$. To measure O on states stabilized by \mathfrak{S} we must distinguish three cases:¹¹

1. If the state is already an eigenstate of O , then the observable must be a stabilizer $\pm O \in \mathfrak{S}$. In this case, the result of the measurement is deterministic (± 1) and the state itself remains unchanged.
2. If $\pm O \notin \mathfrak{S}$ but $[O, g] = 0 \forall g \in \mathfrak{S}$, the stabilizer group represents a mixed state that does not contain any information about O . In this case, the measurement of O purifies the state and the new stabilizer group is $\langle O, g_1, \dots, g_n \rangle$. The measurement result is fully random ± 1 .
3. If there is at least one $g \in \mathfrak{S}$ such that $\{O, g\} = 0$ anticommute, the state stabilized by \mathfrak{S} is in an equal superposition of the eigenstates of O . In this case we first reorder the generating set such that g_1 anticommutes with O . If any other g_i for $i \neq 1$ anticommutes with O , we replace it by $g_1 g_i$. Thus there is always a generating set $\langle g_1, \dots, g_L \rangle$ such that $\{O, g_1\} = 0$ and $[O, g_{i \neq 1}] = 0$. The measurement is performed by replacing g_1 with $\pm O$. The measurement result is fully random ± 1 . This method ensures that the correct generator is replaced and the new stabilizer group is again abelian.

All of these cases can be calculated in $\mathcal{O}(L^2)$ time or faster, using a tableau algorithm that sacrifices memory in order to avoid performing Gaussian eliminations [49]. For the simulation of a stabilizer circuit with L qubits and T time steps, we expect the number of operations (unitaries and measurements) to scale with $\mathcal{O}(LT)$, amounting to a total runtime $\mathcal{O}(L^3T)$.

Entanglement Measures in the Stabilizer Formalism

Consider a system in the state ρ (stabilized by \mathfrak{S}) with L qubits and a subsystem A and its complement \bar{A} with the corresponding reduced density matrices ρ_A and $\rho_{\bar{A}}$. The stabilizer formalism does allow for the efficient calculation of the entanglement entropy

¹¹The simplicity of the stabilizer formalism relies on the fact that Pauli matrices can only commute or anticommute.

$\mathcal{S}_A = -\text{Tr}[\rho_A \log_2 \rho_A]$ in time $\mathcal{O}(L^3)$. This was outlined by Fattal et al. in Ref. [50].¹² Here we shortly review this procedure.

The key insight is that for a product state $|\Psi\rangle = |\Psi\rangle_A \otimes |\Psi\rangle_{\bar{A}}$ of two stabilizer states it is possible to generate the stabilizer group from two subsets \mathfrak{S}_A and $\mathfrak{S}_{\bar{A}}$ which only contain Pauli generators acting on their respective subsystem. This is not possible if the subsystems are entangled; here any set of stabilizer generators must include elements that act nontrivially on both subsystems (they generate a third subgroup $\mathfrak{S}_{A\bar{A}}$). The generating set for any stabilizer group \mathfrak{S} can be brought into a *canonical form* $\mathfrak{S} = \langle f_i \otimes \mathbb{1}_{\bar{A}}, \mathbb{1}_A \otimes g_j, h_k, \bar{h}_k \rangle$ where the first two subsets of generators $\{f_i \otimes \mathbb{1}_{\bar{A}}\}$ and $\{\mathbb{1}_A \otimes g_j\}$ generate \mathfrak{S}_A and $\mathfrak{S}_{\bar{A}}$ and represent constraints on only one subsystem. The generators (h_k, \bar{h}_k) form pairs and generate the group $\mathfrak{S}_{A\bar{A}}$. They have the form $h_k = h_k^A \otimes h_k^{\bar{A}} \in \mathfrak{S}_{A\bar{A}}$ and $\bar{h}_k = \bar{h}_k^A \otimes \bar{h}_k^{\bar{A}} \in \mathfrak{S}_{A\bar{A}}$. The pairs (h_k, \bar{h}_k) are chosen such that $h_k^A \otimes \mathbb{1}_{\bar{A}}$ commutes with all canonical generators of \mathfrak{S} except \bar{h}_k and $\bar{h}_k^A \otimes \mathbb{1}_{\bar{A}}$ commutes with all canonical generators of \mathfrak{S} except h_k . This canonical form can be found in $\mathcal{O}(L^3)$ steps. The entanglement entropy $\mathcal{S}_A = \mathcal{S}_{\bar{A}}$ is equal to the number of pairs (h_k, \bar{h}_k) in the canonical generating set of \mathfrak{S} .

1.2.2 Matchgate Quantum Circuits

Here we introduce a second class of quantum circuits that can also be simulated efficiently on a classical computer. A *matchgate* is a parity-preserving 2-qubit gate of the form [51, 52]

$$G(A, B) = \begin{pmatrix} a_{1,1} & 0 & 0 & a_{1,2} \\ 0 & b_{1,1} & b_{1,2} & 0 \\ 0 & b_{2,1} & b_{2,2} & 0 \\ a_{2,1} & 0 & 0 & a_{2,2} \end{pmatrix} \quad (1.11)$$

with the two unitary 2×2 matrices A and B which share the same determinant $\det(A) = \det(B)$.¹³ Ignoring global phases, we generally choose $A, B \in SU(2)$. Particular interest must be given to matchgates acting on nearest-neighbor pairs of qubits $G_{i,i+1}(A, B)$ in one-dimensional systems. Circuits consisting only of these gates can be simulated efficiently [51, 52] — here we call them *matchgate quantum circuits*. Universality is lost at the nearest-neighbor constraint for the gates. Under the addition of either next-nearest-neighbor matchgates or nearest-neighbor SWAP gates, matchgate quantum circuits would become universal.

Relation to Quadratic Fermions

The key feature of nearest-neighbor matchgates $G_{i,i+1}$ lies in their fermionic representation. To show this, we first need to introduce a fermionic framework. Consider the fermionic

¹²In stabilizer circuits, all Rényi entropies $\mathcal{S}_A^\alpha = \log_2 [\text{Tr}(\rho_A^\alpha)] / (1 - \alpha)$ are identical. This includes the von Neumann entropy as the limit $\mathcal{S}_A = \lim_{\alpha \rightarrow 1} \mathcal{S}_A^\alpha$.

¹³This definition is commonly used in the context of quantum information; a more general definition exists.

ladder operators a_k and a_k^\dagger with $k \in \{1, \dots, L\}$ fulfilling the fermionic anticommutation relations

$$\{a_i, a_j^\dagger\} = \delta_{ij} \quad (1.12a)$$

$$\{a_i^\dagger, a_j^\dagger\} = \{a_i, a_j\} = 0. \quad (1.12b)$$

The corresponding Majorana operators are $\gamma_{2k-1} = a_k + a_k^\dagger$ and $\gamma_{2k} = (a_k - a_k^\dagger)/i$. These also obey fermionic commutation relations and are self-adjoint

$$\{\gamma_\mu, \gamma_\nu\} = 2\delta_{\mu\nu} \quad (1.13a)$$

$$\gamma_\mu = \gamma_\mu^\dagger \quad (1.13b)$$

$$\gamma_\mu^2 = \mathbb{1}. \quad (1.13c)$$

For clarity, in this thesis, indices from the Latin alphabet will generally be used to describe physical sites in the system (such as qubits or fermionic modes) and Greek indices correspond to Majorana modes – two neighboring Majorana modes make up one physical site. We further define the Jordan–Wigner transformation [53] mapping qubits to fermions as

$$\gamma_{2k-1} = \left[\prod_{i=1}^{k-1} Z_i \right] X_k \quad (1.14a)$$

$$\gamma_{2k} = \left[\prod_{i=1}^{k-1} Z_i \right] Y_k. \quad (1.14b)$$

A *quadratic Hamiltonian* has the form

$$H = i \sum_{\mu, \nu} h_{\mu\nu} \gamma_\mu \gamma_\nu \quad (1.15)$$

with the $2L \times 2L$ matrix h . As the diagonal elements of h contribute just a constant added to H (remember $\gamma_\mu^2 = 1$), we can omit them. Furthermore, the fermionic algebra requires $\gamma_\mu \gamma_\nu = -\gamma_\nu \gamma_\mu$ and thus multiple choices of h correspond to the same H . Without loss of generality we can choose h to be a real antisymmetric matrix.¹⁴ Lastly we construct unitaries of the form $U = e^{iH}$ and denote them as *Gaussian* operations.

When rewriting terms of the form $i\gamma_\mu \gamma_\nu$ in fermionic ladder operators a and a^\dagger , we find hopping and superconducting contributions. This leads us to the observation that H (and by extension U) preserves the parity of a state. This similarity with matchgates is not misleading: Nearest-neighbor matchgates can be mapped to Gaussian operations via a Jordan–Wigner transformation and any bosonic matchgate quantum circuit has a corresponding fermionic Gaussian circuit. In the following we will detail this mapping.

¹⁴This choice also fulfills $H = H^\dagger$.

Gaussian operations U act as rotations on Majorana modes

$$U\gamma_\mu U^\dagger = \sum_{\nu=1}^{2L} R_{\mu\nu}\gamma_\nu \quad (1.16)$$

with the matrix $R = e^{4h} \in SO(2L)$. The proof of Equation (1.16) is straightforward. We write γ_μ as $\gamma_\mu(0)$ and introduce the time evolution in the Heisenberg picture as $\gamma_\mu(t) = U(t)\gamma_\mu(0)U^\dagger(t)$ with $U^\dagger(t) = e^{iHt}$. The dynamics is described by Heisenberg's equation of motion

$$\frac{d\gamma_\mu(t)}{dt} = i[H, \gamma_\mu(t)]. \quad (1.17)$$

After inserting Equation (1.15), the commutator can be calculated, and we find

$$\frac{d\gamma_\mu(t)}{dt} = \sum_{\nu=1}^{2L} 4h_{\mu\nu}\gamma_\nu(t). \quad (1.18)$$

This differential equation has the formal solution

$$\gamma_\mu(t) = \sum_{\nu=1}^{2L} R_{\mu\nu}\gamma_\nu(0) \quad (1.19)$$

with $R = e^{4ht}$. Setting $t = 1$ gives Equation (1.16). \square

Consider two qubits and a matchgate $G(A, B)$. With $A, B \in SU(2)$, G is a representation of an element of the group $SU(2) \times SU(2)$. On the other hand, a Gaussian unitary U on two fermions is defined by the matrix $R \in SO(4)$. The correspondence of matchgates and Gaussian operations is thus defined by a covering map $SU(2) \times SU(2) \rightarrow SO(4)$. The exact map is fixed by the Jordan–Wigner transformation and defined by

$$R = [Q^\dagger(A \otimes B)Q]^\top \quad (1.20)$$

with the matrix

$$Q = \frac{1}{\sqrt{2}} \begin{pmatrix} 1 & -i & 0 & 0 \\ 0 & 0 & -1 & i \\ 0 & 0 & -1 & -i \\ -1 & -i & 0 & 0 \end{pmatrix}. \quad (1.21)$$

This explicit relation between matchgates and Gaussian operators allows for the simulation of matchgate circuits in the picture of their Gaussian counterpart. In the following we describe an efficient algorithm for this.

Efficient Simulation of Gaussian Fermions

Here we give an introduction to the efficient simulation of Gaussian circuits, including projective single-site measurements $a_i^\dagger a_i$. We will follow the algorithm described in Refs. [54–56]. This is a didactic choice. Actual simulations of matchgate quantum circuits shown in this thesis were performed using a more advanced algorithm by Bravyi in Ref. [57]. We expand on this in Section 3.A.

Equation (1.16) can be transformed to find the action of Gaussian unitaries on the fermionic ladder operators

$$U^\dagger a_i U = \sum_v T_{iv} \gamma_v \quad (1.22a)$$

$$U^\dagger a_i^\dagger U = \sum_v T_{iv}^* \gamma_v \quad (1.22b)$$

with the $L \times 2L$ matrix $T_{iv} = (R_{2i-1,v}^\top + iR_{2i,v}^\top) / 2$ and its complex conjugate T_{iv}^* . We assume the initial state of the L -qubit system to be a product state in the z -basis. A circuit now consists of Gaussian unitary evolutions U_t (which may consist of many two-fermion unitaries) and single-site particle number measurements which may be represented as projectors $P_t \in \{a_i a_i^\dagger, a_i^\dagger a_i\}$. The state is thus given by the concatenation

$$P_t U_t \dots P_2 U_2 P_1 U_1 |\Psi_0\rangle. \quad (1.23)$$

Here we neglect any normalization factors. To propagate the circuit to the next time step, the unitary U_{t+1} is performed. The result of the next measurement on the site j is determined by calculating the expectation value $\langle a_j a_j^\dagger \rangle$ – according to which the projector P_{t+1} will be randomly chosen. Here we show the simplest case for $t = 0$:

$$\langle a_j a_j^\dagger \rangle = \langle \Psi_0 | U_1^\dagger a_j a_j^\dagger U_1 | \Psi_0 \rangle = \langle \Psi_0 | U_1^\dagger a_j U_1 U_1^\dagger a_j^\dagger U_1 | \Psi_0 \rangle \quad (1.24a)$$

$$= \sum_{\mu, \nu} T_{1,j\mu} T_{1,j\nu}^* \langle \Psi_0 | \gamma_\mu \gamma_\nu | \Psi_0 \rangle \quad (1.24b)$$

It is straightforward to expand this to more time steps: Instead of $U_1 |\Psi_0\rangle$, we insert the full previous state evolution [as in Equation (1.23)] in Equation (1.24a). Every previous projector will contribute 4 sums and add 4 Majorana operators in the bracket in Equation (1.24b) and every additional unitary will provide its T_t matrix to the corresponding sum. This reduces the calculation of expectation values to a sum of known matrix elements and expectation values of the form $\langle \Psi_0 | \gamma_\mu \gamma_\nu \gamma_\xi \gamma_\eta \dots | \Psi_0 \rangle$ which can be calculated efficiently using Wick's theorem [58]. While the string of Majorana operators becomes longer with the number of projective measurements in a circuit, it can still be calculated in polynomial time. This allows for the efficient simulation of fermionic Gaussian circuits including single-site occupation number measurements, and by Jordan–Wigner transformation [see Equation (1.20)] the simulation of matchgate quantum circuits with single-site Z_i measurements. For more details on the

algorithm to calculate expectation values of the form in Equation (1.24) we refer the reader to Refs. [54–56]. As stated before, there exists a more efficient (but less intuitive) algorithm for the simulation of Gaussian circuits [57]. Importantly, this also allows for the calculation of entanglement entropies.

1.3 The Projective Transverse Field Ising Model

One example of a quantum circuit that can be simulated within the stabilizer formalism while also exhibiting an entanglement transition is the *projective transverse field Ising model* (PTIM). As the one-dimensional version of this model will also play a major role in this thesis, we will give it a rather detailed introduction here. The following results have been found by Lang and Büchler in Ref. [24] and we will follow their approach in this section. Similar work was also done by Nahum and Skinner in Ref. [21].

Take a one-dimensional chain of L spin-1/2 degrees of freedom with T discrete time steps. We will consider these spins as *physical qubits* and indicate them individually as sites (or nodes) i . The state of a single qubit may be expressed via the basis states $|0\rangle$ and $|1\rangle$, with $Z|0\rangle = +|0\rangle$ and $Z|1\rangle = -|1\rangle$. The qubits are prepared in an initial state $|\Psi(t=0)\rangle \equiv |\Psi_0\rangle$ and the Hilbert space of the system is $\mathcal{H} = \bigotimes_{i=1}^L \mathbb{C}_i^2$. A time step in the model is divided into two substeps:

1. First, on every qubit i projective measurements of the $E_i := X_i$ operator are performed with the probability $p \in [0, 1]$.
2. Next, parity measurements of the operator $S_e := Z_i Z_{i+1}$ are performed with the probability $1 - q$ (with $q \in [0, 1]$) on every pair of neighboring qubits i and $i + 1$. We refer to a pair of neighboring qubits as an *edge* $e = (i, i + 1)$.

This two-step process is repeated T times and generates the trajectory $\mathcal{T} = \{|\Psi(t)\rangle\}$ of the PTIM; an illustration of a typical circuit is shown in Figure 1.2. Given a fixed initial state, the trajectory is fully determined by the projective measurements and their outcomes. We will denote the space-time patterns of the measurements with $E^{\mathbb{P}}$ ($S^{\mathbb{P}}$) and the corresponding measurement results with $E^{\mathbb{R}}$ ($S^{\mathbb{R}}$). With a slight abuse of notation we will refer to a trajectory as $\mathcal{T} = M^{\mathbb{P},\mathbb{R}} := (E^{\mathbb{P},\mathbb{R}}, S^{\mathbb{P},\mathbb{R}})$ where $E^{\mathbb{P},\mathbb{R}} := (E^{\mathbb{P}}, E^{\mathbb{R}})$ and $S^{\mathbb{P},\mathbb{R}} := (S^{\mathbb{P}}, S^{\mathbb{R}})$. We interpret $M^{\mathbb{P},\mathbb{R}}$ as a measurement history that may be recorded by an observer. This allows us to write the final state as $|\Psi(T)\rangle = |\Psi_{\mathbb{F}}(\mathcal{T})\rangle = |\Psi_{\mathbb{F}}(M^{\mathbb{P},\mathbb{R}})\rangle$.

It is important to emphasize that this model contains two kinds of randomness: The classical randomness of the quantum circuit as the measurements E_i and S_e are only performed stochastically with the probabilities p and $1 - q$ on every site or edge in every time step; and the quantum randomness as the measurement outcomes are generally random. Furthermore, as the PTIM only contains measurements of Pauli operators, it can be simulated efficiently within the stabilizer formalism (see Subsection 1.2.1). Note that all measurements E_i and S_e commute with the total parity $X_1 X_2 \cdots X_L$ (in the x -direction) which is therefore a conserved quantity in the PTIM.

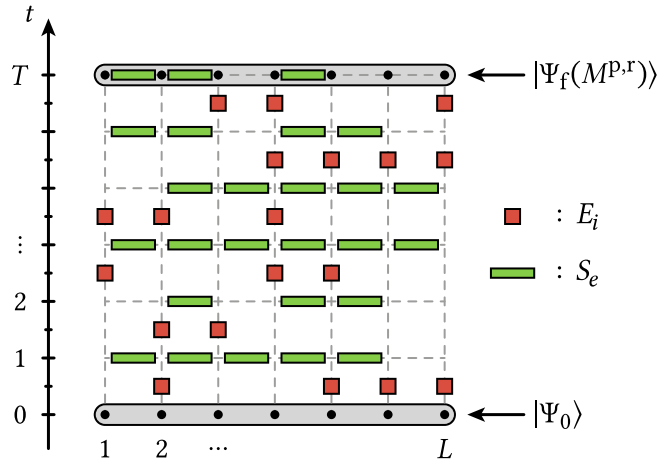


Figure 1.2 • Example trajectory of the PTIM. Each time step of the PTIM is a stochastic process where first E_i measurements are performed with probability p on every site i . Afterwards, S_e measurements are performed on the edges e with probability $1 - q$. This is repeated for T time steps. In this depiction, the qubits live on the vertical dashed lines. The final state $|\Psi_f(M^{P,r})\rangle$ is a function of the initial state $|\Psi_0\rangle$ and the measurement history $M^{P,r}$. Here we only show the measurement pattern M^P and not the corresponding results M^r .

The PTIM is related to the more commonly known transverse field Ising model on a chain of spin-1/2 degrees of freedom with the Hamiltonian

$$H_{\text{TIM}} = -J \sum_e S_e - H \sum_i E_i. \quad (1.25)$$

Here the prefactors J and H correspond to the coupling of the spins to their nearest neighbors and to an external magnetic field. The terms of H_{TIM} are exactly the observables which are measured projectively in the PTIM, which explains the name of our model.

1.3.1 The Colored Cluster Model

As a stabilizer circuit, the PTIM can be simulated efficiently on a classical computer. However in this thesis we will often only consider the entanglement structures of a system. This does not actually require knowledge of the full trajectory. The *colored cluster model* (CCM) was introduced by Lang and Büchler in Ref. [24] and illustrates this nicely by only tracking Bell clusters instead of the actual state. This model does not only reduce the runtime of simulations, but will also give an intuitive understanding of how the E_i and S_e measurements act on a state in the PTIM.

Consider a minimal example of two qubits in a product state, both polarized in the positive x -direction $|++\rangle = (|0\rangle + |1\rangle) \otimes (|0\rangle + |1\rangle)$.¹⁵ Performing an S_e measurement will transform

¹⁵For simplicity we will generally ignore normalization factors in these types of calculations.

the product state into a fully entangled Bell pair:

$$|++\rangle = |00\rangle + |11\rangle + |01\rangle + |10\rangle \xrightarrow{\text{meas. } Z_1 Z_2} \begin{cases} |00\rangle + |11\rangle, & \text{meas. result } +1, \\ |01\rangle + |10\rangle, & \text{meas. result } -1 \end{cases} \quad (1.26)$$

The measurement result does affect the actual state of the qubits, but it has no effect on their entanglement — in both cases, the two qubits are fully entangled after the measurement is performed. This principle extends to more qubits. Consider some bit configuration \mathbf{m} with $m_i \in \{0, 1\}$ on some qubits $\{i\} \subset \{1, \dots, L\}$ (note that the sites $\{i\}$ are not necessarily concurrent). Assume that these qubits are entangled in a *Bell cluster* of the form $|\mathbf{m}\rangle \pm |\bar{\mathbf{m}}\rangle$ with the complement $\bar{m}_i = [(m_i + 1) \bmod 2]$. Measuring $S_e = Z_i Z_j$ on two neighboring clusters entangles them in a new combined Bell cluster:

$$(|\mathbf{m}\rangle + |\bar{\mathbf{m}}\rangle) \otimes (|\mathbf{n}\rangle + |\bar{\mathbf{n}}\rangle) \xrightarrow{\text{meas. } Z_i Z_j} \begin{cases} |\mathbf{mn}\rangle + |\bar{\mathbf{m}\bar{n}}\rangle, & \text{meas. result } (-1)^{m_i n_j}, \\ |\mathbf{m}\bar{\mathbf{n}}\rangle + |\bar{\mathbf{m}}\mathbf{n}\rangle, & \text{meas. result } (-1)^{m_i \bar{n}_j} \end{cases} \quad (1.27)$$

Here we chose i (j) to be a site on the first (second) cluster. S_e measurements combine Bell clusters and thus create entanglement between qubits which were previously not entangled.¹⁶ The single-site measurements E_i have the opposite effect, as they project a qubit onto the x -basis. This removes all entanglement of the qubit with the rest of the system:

$$\begin{aligned} |\mathbf{m}\rangle \pm |\bar{\mathbf{m}}\rangle &= |\dots m_i m_j m_k \dots\rangle \pm |\dots \bar{m}_i \bar{m}_j \bar{m}_k \dots\rangle \\ &\xrightarrow{\text{meas. } X_j} \begin{cases} (|\dots m_i m_k \dots\rangle \pm |\dots \bar{m}_i \bar{m}_k \dots\rangle) \otimes |+\rangle_j, & \text{meas. result } +1, \\ (|\dots m_i m_k \dots\rangle \mp |\dots \bar{m}_i \bar{m}_k \dots\rangle) \otimes |-\rangle_j, & \text{meas. result } -1 \end{cases} \end{aligned} \quad (1.28)$$

The PTIM can now be simulated by tracking Bell clusters of the form $|\mathbf{m}\rangle \pm |\bar{\mathbf{m}}\rangle$, their configurations \mathbf{m} and the sign \pm (which amounts to their parity in the x -basis). Any two qubits which belong to the same cluster are entangled; if they belong to two different clusters, they are not entangled. Thus to simulate entanglement structures we can neglect configurations and signs and only track the clusters. This is what the CCM does, by giving every cluster its own color. We show a sample time step in the CCM in Figure 1.3. The entanglement structure of the state is encoded via colors representing a cluster configuration. In the first substep of the time step, E_i measurements are performed on some qubits. They are thus projected onto the state $|\pm\rangle$ depending on the measurement result (which we do not track here), as in Equation (1.28). Note that if the qubit i was previously already in the state $|\pm\rangle$ the measurement result is deterministic. We interpret this state as a single-site Bell cluster and give it a new color. In the second time step, S_e measurements are performed on pairs of neighboring qubits. If these qubits previously belonged to the same cluster (share the same color), nothing needs to be done. If they belonged to different clusters (have different colors), those clusters are fused together by the measurement as in Equation (1.27). One of the two colors is chosen to be dominant and one as recessive. All qubits with the recessive color are assigned the dominant color.

¹⁶In this context we can think of the state $|\pm\rangle$ as a “single-qubit Bell cluster”.

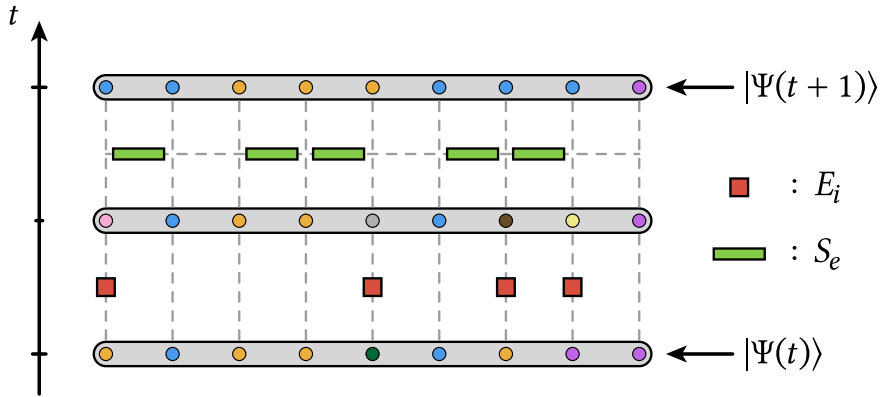


Figure 1.3 • Time step in the colored cluster model. The entanglement structure of the state is simulated by tracking Bell clusters with colors. E_i measurements project a single qubit onto the x -basis and create a new single-qubit Bell cluster which is indicated by a new color. S_e measurements fuse clusters by combining them in one color. Note that S_e measurements act locally but clusters can be large. Thus a single measurement can entangle qubits over long distances.

By using a hash table to track positions of colors, the CCM is able to simulate the PTIM in $\mathcal{O}(L^2T)$ time which is a significant improvement over the stabilizer formalism.¹⁷ The entanglement entropy $S(A)$ of a subsystem A with its environment is equal to the number of colors which are found inside *and* outside A . Moreover, the CCM also allows for an intuitive understanding of how the PTIM really works, which we will make use of in this thesis.

1.3.2 Entanglement Transition in the Projective Transverse Field Ising Model

One of the features of the PTIM – which makes it particularly relevant for this thesis – is its entanglement transition. Here we will very shortly discuss this transition and its relation to a bond percolation model. Again these notes closely follow the remarks by Lang and Büchler in Ref. [24].

To probe the entanglement structure of the PTIM, we consider the sample-averaged entanglement entropy $S(L/2)$ between the left and right halves of the system in its steady state $T \gg L$.¹⁸ For simplicity, here we choose the probabilities $p = q$. We show the simulation data in Figure 1.4, given the initial state $|+\dots+\rangle$ (with $|+\rangle = |0\rangle + |1\rangle$). Clearly there exists an entanglement transition at $p_c \approx 0.5$ which separates two area-law phases. At $p \gg 0.5$, E_i measurements dominate and limit the size of the Bell clusters. Thus the entanglement entropy does not grow when increasing the system size which makes this

¹⁷For a single S_e measurement, at most $\mathcal{O}(L)$ qubit colors need to be changed. If the system is in a disentangled phase, this reduces to $\mathcal{O}(1)$ and the PTIM is simulated in $\mathcal{O}(LT)$ time.

¹⁸For simulations of a steady state, we generally use $T \geq 10L$ in this thesis.

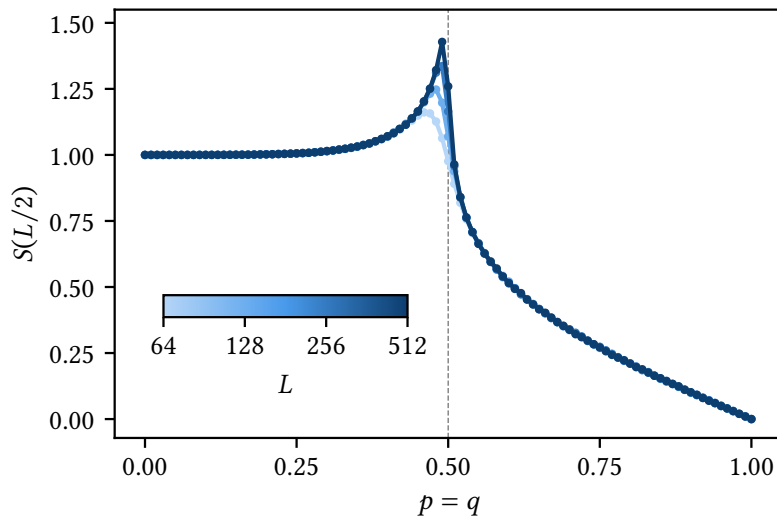


Figure 1.4 • Entanglement transition in the PTIM. The entanglement entropy $S(L/2)$ between the left and right halves of the PTIM in the steady state $T \gg L$ shows a clear entanglement transition between two area-law phases, given the initial state $|+\dots+\rangle$. Here the model was simulated with open boundaries which slightly shifts the transition away from the critical point $p_c = 0.5$ at finite sizes L . The probabilities were chosen to be equal $p = q$. Simulations were averaged over 10^5 samples. Error bars are smaller than the data points.

an area-law phase. At $p \ll 0.5$, S_e measurements dominate which allows for the clusters to condense into one single global cluster. E_i measurements do create small new clusters which appear as holes in the global cluster. However these holes cannot grow without merging to the global cluster. In Figure 1.4 we see $S(L/2) \geq 1$ for $p \ll 0.5$ because there are always qubits on the left and right sides of the system which are entangled in the global cluster. At the critical probability p_c the entanglement entropy grows logarithmically with the system size L . This slow divergence is a typical feature of continuous phase transitions in one-dimensional systems and usually described by a conformal field theory [59, 60]. It was shown [24] that the PTIM closely matches a conformal description at its critical point.¹⁹ We will expand on this in Chapter 3 of this thesis.

To better understand the entanglement transition of the PTIM, we relate the model to a bond percolation model on a square lattice in two dimensions. This connection has an intuitive interpretation in the CCM (Figure 1.3): Clusters are propagated by S_e measurements in space and propagate forward through time, if no E_i measurements are performed. We show this correspondence in Figure 1.5. Nodes on the percolation lattice represent qubits at specific time steps. Here we draw missing bonds as dashed lines. This picture expands our previous notion of a Bell cluster to a space-time *percolation cluster* in $1 + 1$ dimensions,

¹⁹An emerging conformal invariance was for example also found at a critical point between a volume-law phase and an area-law phase [61].

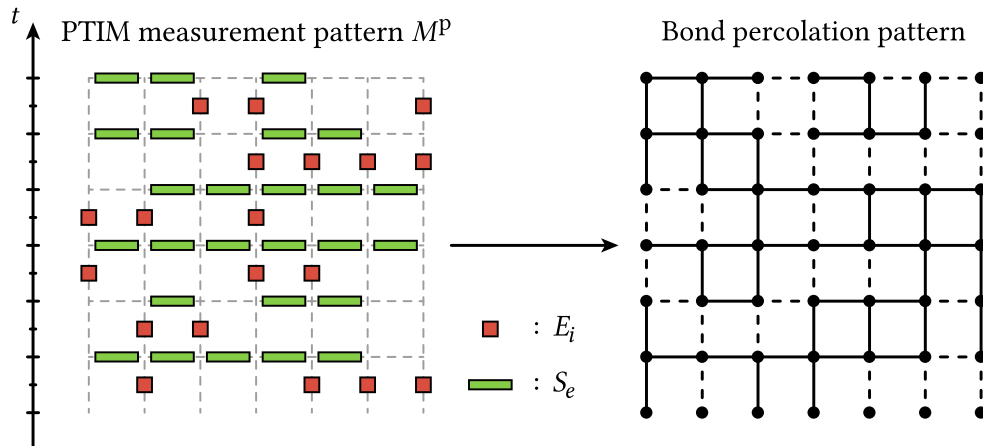


Figure 1.5 • Relation of the PTIM to bond percolation. PTIM measurement patterns M^P can be converted to two-dimensional bond percolation patterns on a square lattice. Nodes on this lattice belong to the same percolation cluster if they are connected via bonds (solid lines).

where a cluster is a collection of nodes which are connected via bonds.²⁰ Importantly, the bond percolation model on a two-dimensional square lattice exhibits a percolation threshold at exactly $p_c = 0.5$ [62]. This value follows from a duality argument [63] and allows us to pinpoint the entanglement transition of the PTIM at exactly $p_c = 0.5$. Note that Figure 1.4 shows the transition slightly shifted to the left. This is a finite-size effect and could be largely minimized by considering the PTIM with periodic boundaries [24].

In this subsection we considered the entanglement transition of a slightly simplified PTIM with $p = q$. In a more generic setting, the transition occurs at $p + q = 1$. We will consider this case in Chapter 2.

²⁰This includes nodes, which would have different colors in the CCM because the percolation model is able to track clusters backward in time.

CHAPTER 2

Decoding the Projective Transverse Field Ising Model

The projective transverse field Ising model (PTIM) is a fully projective quantum circuit that features an entanglement transition between two area-law phases. As we discussed in Section 1.3, these two entanglement phases and their transition are manifested in the behavior of sample-averaged entanglement entropies. While the entanglement structures of the PTIM were already explored by Lang and Büchler in Ref. [24], here we want to consider the PTIM from a quantum information point of view. To this end, we will show how a logical qubit can be encoded in the PTIM and how it can be recovered using different decoding schemes. This will be a more in-depth discussion of the work published in Ref. [64].

2.1 Related Works

On the path towards scalable, universal quantum computation, decoherence remains a major obstacle. Couplings between a system and its environment may change the state of physical qubits during storage or during the application of a gate. Such *errors* may then propagate through an algorithm and render its result incorrect. *Quantum error correction* aims to overcome this challenge and therefore represents a crucial step in the creation of any quantum computer [65, 66]. The discovery of *quantum error correcting codes* (QECCs) – first described by Peter Shor in Ref. [67] – is a cornerstone in the promises of quantum computation [68, 69]. The threshold theorem gives us some clarity here [45]: For a quantum computer with a finite physical error rate below a certain threshold, by applying an error

correcting scheme, the logical error rate can (in principle) be suppressed.¹ QECCs work by protecting quantum information in entangled states across multiple physical qubits [70]. This draws a connection between quantum error correction and the field of measurement-induced entanglement transitions in monitored quantum circuits [5, 6, 71–73]. We have already described this concept in Subsection 1.1.2: Random unitary gates typically create a volume-law entanglement. Monitoring circuits via local projective measurements tends to reduce their entanglement to an area law. Importantly, in some circuits, long-range entanglement structures are resilient to small monitoring rates [5–8] and entanglement transitions only occur at a finite monitoring threshold. With random quantum circuits serving as model systems for investigating entanglement structures, it is natural to also examine their capabilities in the context of quantum error correction. In this chapter we study the projective transverse field Ising model (as introduced in Section 1.3) as a quantum error correcting code and develop decoding schemes for it. These provide a concrete implementation of a fault-tolerant quantum memory and allow us to better understand the relation between quantum error correction and entanglement in this measurement-only setting.

The approach is the following [45]: The quantum information (*logical qubits*) which is to be protected, is encoded in a subspace of a quantum circuit known as the *code space*. Random projective measurements on the system leak information about its state to the environment. In this process the environment may either gain access to the encoded quantum information (and it is lost irretrievably), or it does not and the information is still preserved in the state. Even if the logical qubits survive the interactions with the environment, the state gains entropy in the process. The goal of quantum error correction is to reconstruct the logical qubits from this scrambled state. To do so, an observer performs measurements in order to obtain partial information about the quantum state without reading out the encoded qubits.² The recorded information is called the *syndrome*.³ It is used in the next step to steer the state back into the code space while restoring the encoded quantum information — we refer to this as *decoding*. Classical algorithms that take the syndrome as input and provide instructions to the observer on how to reconstruct the initial state of the system are called *decoders*. The success of a quantum error correcting scheme depends on the rate at which the environment gains access to the logical qubits, the amount of information contained in the syndrome and — crucially — on the decoding algorithm. The maximum monitoring rate tolerated by a decoder is the *decoding threshold*. Early examples of fixed-size QECCs are Shor’s nine-qubit code [68] and the seven-qubit Steane code [69]. Scalable codes have been derived from topologically ordered quantum systems, as for example surface codes [84–87]. For these quantum error correcting codes, efficient classical decoding algorithms are known and their decoding thresholds have been analyzed [75, 88–94]. The relatively high decoding

¹The threshold theorem does not come without any caveats, for example concerning the actual value of the threshold or the number of qubits involved in a correcting scheme. The real task lies in the design of error correcting schemes that are suited to the specific physical platform at hand.

²A common approach is to measure the stabilizers of the code space.

³Measurement-free quantum error correction also exists [74–83] but will not be of concern in this thesis.

thresholds of surface codes make them a particularly interesting candidate for the realization of fault-tolerant quantum memory [95, 96].

Consider a random quantum circuit with projective measurements and interpret it as a quantum error correcting code. A logical qubit is encoded in an entangled initial state by storing its amplitudes non-locally on all sites (physical qubits).⁴ Any quantum error correcting scheme can only ever succeed if these amplitudes survive the evolution of the circuit; if the environment gains access to the encoded information it can never be restored. Thus, before considering any decoding algorithms, we must determine how long a logical qubit survives for certain system parameters – and in particular how its average lifetime scales with the system size. This turns out to be tightly connected to entanglement transitions in such circuits (see Subsection 1.1.2) [24, 71, 97–103]: In the entangling phase (below the critical monitoring rate) the lifetime typically grows exponentially with the system size, i.e., the logical qubit survives indefinitely in large systems. In the disentangled phase (above the critical monitoring rate) any global entanglement is destroyed quickly and the average lifetime of the encoded qubit typically scales logarithmically with the number of sites. Thus the survival of the logical amplitudes is governed by the entanglement transition of the circuit. A decoder can only ever be successful in the entangling phase and therefore the critical monitoring rate is an upper bound to the decoding threshold.⁵ The obvious question is: If a logical qubit survives a circuit evolution, under what circumstances can it be retrieved? The answer to this question highly depends on the system of choice, its coupling to the environment (i.e., the noise model) and the recorded syndrome.

In this chapter we answer these questions for the projective transverse field Ising model (see Section 1.3). We interpret the two competing kinds of measurements of the PTIM as noise (E_i) applied by the environment and syndrome measurements (S_e) performed by the observer. This particular quantum circuit is interesting for multiple reasons: Firstly, the PTIM is a measurement-only quantum circuit. Its entangling phase only features an area-law scaling. As we will see, this is still enough to protect a logical qubit [24]. Secondly, our approach models noise in the form of projective measurements which were not recorded by the observer. More common settings generally assume unitary errors (qubit flips X and phase flips Z). We will analyze multiple decoders numerically and provide an in-depth review of the similarities and differences between our projective noise model and a different (classical) system with unitary errors. In particular we will demonstrate that it is possible to implement an optimal decoder for the PTIM (maximum likelihood decoder). This will provide us with some insights about the decoding threshold in relation to the critical monitoring rate.

⁴In principle one might also store multiple qubits. Here we focus on the simplest case.

⁵In Chapter 4 we turn this concept around and use an approach rooted in quantum error correction to detect a bound for an entanglement transition.

2.2 Repetition Code

Before we dive straight into the quantum error correction of the projective transverse field Ising model, we clarify the terminology and quantities that we use later on. For this purpose, as a simplest example that is already well understood, we introduce the *repetition code* [45, 68] of L physical qubits in a scenario where noise manifests as single-qubit flips by the action of the Pauli operator X_i on any site $i \in \{1, \dots, L\}$. A single qubit flip may be considered as an *error* and we call p the *error rate*, i.e., the probability of an error to occur on a physical qubit. We store a single logical qubit in an entangled state

$$|\Psi(t=0)\rangle = \alpha|00\dots 0\rangle + \beta|11\dots 1\rangle \quad (2.1)$$

across all L qubits.⁶ The amplitudes α and β again encode the quantum information and are generally not known to the observer. Any logical qubit is encoded in the space spanned by the basis vectors $\{|0\rangle \equiv |00\dots 0\rangle, |1\rangle \equiv |11\dots 1\rangle\}$ which we call the *code space*. The qubits are allowed to evolve for T time steps $|\Psi(0)\rangle \rightarrow |\Psi(T)\rangle$. In this time, some errors might occur. With n_i being the number of errors on the site i , it is

$$|\Psi(T)\rangle = \left[\prod_{i=1}^L X_i^{n_i} \right] |\Psi(0)\rangle = \alpha|\mathbf{m}\rangle + \beta|\bar{\mathbf{m}}\rangle. \quad (2.2)$$

Here, $|\mathbf{m}\rangle$ and its complement $|\bar{\mathbf{m}}\rangle = X_1 X_2 \dots X_L |\mathbf{m}\rangle$ are qubit configurations ($m_i \in \{0, 1\}$) which depend on the errors that occurred and are therefore unknown to the observer. To be able to correct the errors, we take measurements of all nearest-neighbor parity operators $Z_i Z_{i+1}$ and record the corresponding outcomes.⁷ These parities are stabilizers of the code space and can be measured without leaking information about the logical qubit to the environment, i.e., without changing the amplitudes α and β . We call the record of the measurements the *syndrome* S . The full evolution of the state, including the errors and syndrome measurements, is the trajectory \mathcal{T} . The task at hand is to use the syndrome to reconstruct the original qubit $|\Psi(0)\rangle$.

A *decoder* $\mathcal{D}(S)$ is a function that takes a syndrome S as input and returns a unitary *correction operator* C . The goal is to find a function \mathcal{D} that allows us to reconstruct the original logical qubit $\mathcal{D}(S)|\Psi(T)\rangle = C|\Psi(T)\rangle = |\Psi(0)\rangle$, thus correcting the errors that happened during the time T .⁸ To quantify how well a decoder performs at this task, we define the *evaluation function* $f(\mathcal{T}; C)$, which depends on the trajectory \mathcal{T} of a system and a unitary C . Generally, f should be defined according to the scenario at hand. For our repetition code, we choose

$$f(\mathcal{T}; C) := \begin{cases} 1, & \text{if } C|\Psi(T)\rangle = |\Psi(0)\rangle, \\ 0, & \text{else} \end{cases} \quad (2.3)$$

⁶Here lies the origin of the name of this code: Information is *repeated* over multiple sites.

⁷These are only $L - 1$ measurements and therefore the information we gain about the state is always incomplete.

⁸As the syndrome generally only contains partial information about a trajectory, the task of a decoder is nontrivial.

and define the *decoding probability* as

$$P_{\mathcal{D}}(p) := \langle\langle f(\mathcal{T}; \mathcal{D}(S)) \rangle\rangle = \sum_{\mathcal{T} \in \{\mathcal{T}\}} P(\mathcal{T}) f(\mathcal{T}; \mathcal{D}(S)). \quad (2.4)$$

The ensemble average $\langle\langle \cdot \rangle\rangle$ is the sum over all possible trajectories $\{\mathcal{T}\}$ weighted by the probability $P(\mathcal{T})$ for a single trajectory to occur (which depends on the error rate p).⁹ A decoding probability close to one corresponds to the decoder being able to perfectly decode almost every state. At high error rates, we expect the decoding probability to drop to smaller values.

For our repetition code, finding a decoder is a trivial task. The syndrome contains the measurements of all $L - 1$ parities. Therefore it is straightforward to find the two qubit configurations $|\mathbf{m}\rangle$ and $|\bar{\mathbf{m}}\rangle$ that match the measured parities. The decoder must now decide, if the current state is $|\Psi_1\rangle = \alpha|\mathbf{m}\rangle + \beta|\bar{\mathbf{m}}\rangle$ or the opposite $|\Psi_2\rangle = \alpha|\bar{\mathbf{m}}\rangle + \beta|\mathbf{m}\rangle$. Correspondingly it will return the correction operator

$$C = \prod_{i=1}^L X_i^{m_i} \quad (2.5)$$

or the complement $\bar{C} = \left(\prod_j X_j\right) C$. To decide which correction operator to return, our decoder will assume that errors are *unlikely* to occur ($p < 1/2$) and employ a *majority voting* approach: The more likely qubit configuration $|\mathbf{m}\rangle$ or $|\bar{\mathbf{m}}\rangle$ is the one that is closer to the original state $|00 \dots 0\rangle$. In other words, the decoder will return the correction operator, which flips fewer qubits.

Consider the simplest nontrivial case $L = 3$. The state is initialized as $|\Psi(0)\rangle = \alpha|000\rangle + \beta|111\rangle$. After some time, the parities $Z_1 Z_2$ and $Z_2 Z_3$ are measured with the results $S_{1,2} = +1$ and $S_{2,3} = -1$. It is clear that the current state must be either $|\Psi_1\rangle = \alpha|001\rangle + \beta|110\rangle$ or $|\Psi_2\rangle = \alpha|110\rangle + \beta|001\rangle$. Independent of the unknown amplitudes α and β , the state $|\Psi_1\rangle$ can be corrected back to $|\Psi(0)\rangle$ with just a single qubit flip, compared to two flips for $|\Psi_2\rangle$. The majority voting algorithm will therefore assume the first option and the decoder returns the correction operator $C = X_3$. We will apply this operator to the state $C|\Psi(T)\rangle$. Whether or not the new state is identical to the initial state, i.e., we successfully retrieved our initial qubit, depends on the errors that really occurred in the physical system. If it actually was $|\Psi(T)\rangle = |\Psi_1\rangle$, the correction step will have restored the qubit $|\Psi(0)\rangle = C|\Psi(T)\rangle$. As long as the number of errors is $< L/2$, the majority voting algorithm will always yield the correct result (for $|\Psi_2\rangle$ to be the actual state in our example, two errors needed to occur). This observation allows us to calculate the decoding probability analytically by taking the sum over all possible trajectories that include fewer than $L/2$ errors:

$$P_{\mathcal{D}}(p; L) = \langle\langle f(\mathcal{T}; \mathcal{D}(S)) \rangle\rangle = \sum_{j=0}^{\lfloor L/2 \rfloor} \binom{L}{j} (1-p)^{L-j} p^j \begin{cases} 1/2, & \text{if } j = L/2, \\ 1, & \text{else} \end{cases} \quad (2.6)$$

⁹Whenever we are unable to calculate the ensemble average analytically, we will make use of the law of large numbers and only simulate some of the possible trajectories to approximate it via the sample average. In the limit of many samples, both averages are equal – therefore we use both terms interchangeably.

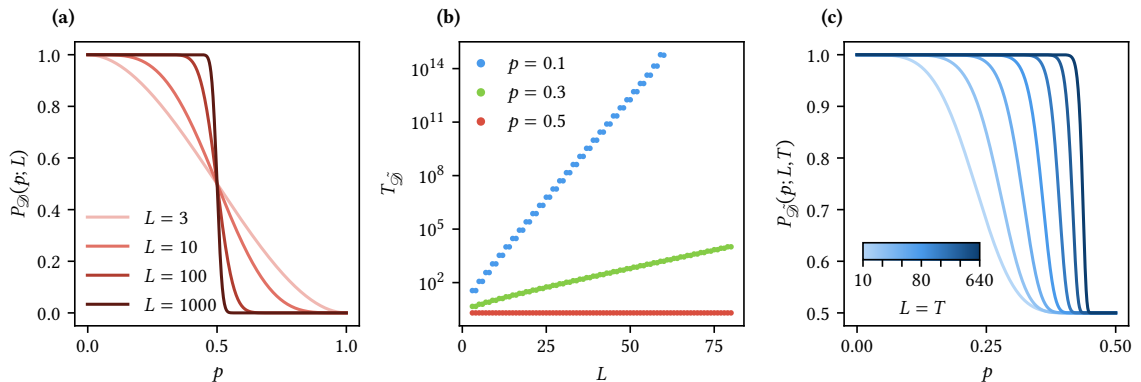


Figure 2.1 • Measures for decoder performances on the repetition code. (a) Decoding probability for the majority voting algorithm \mathcal{D} on the repetition code for different system sizes L according to Equation (2.6). There is a decoding threshold at $p_{\text{thr}} = 1/2$. At $p < p_{\text{thr}}$ we find that the decoding probability approaches $P_{\mathcal{D}} \rightarrow 1$ for large systems $L \rightarrow \infty$. (b) and (c) show the performance of the decoder $\tilde{\mathcal{D}}$ for a repetition code with T time steps. (b) shows the mean time to first failure $T_{\tilde{\mathcal{D}}}$ and (c) the corresponding decoding probability $P_{\tilde{\mathcal{D}}}(p; L, T)$ for the repeated use of our majority voting algorithm in $T = L$ time steps. Again, in the thermodynamic limit $L = T \rightarrow \infty$, the critical error rate approaches $\tilde{p}_{\text{thr}} = 1/2$.

For the case of an even system size L , we included a correcting factor of $1/2$ – if exactly $L/2$ errors occur, the decoder will return the correct operator in half of the cases. We show the decoding probability for our algorithm in Figure 2.1 (a). The plot shows a decoding threshold at $p_{\text{thr}} = 1/2$. At this value, the decoding probability drops to $P_{\mathcal{D}}(p = 1/2; L) = 1/2$, which corresponds to the decoder “flipping a coin”. At values $p < 1/2$ the decoder will more likely than not be able to restore our qubit – in fact, the decoding probability approaches 1 for large system sizes L . We also show the values $p > 1/2$ – here the decoder will mostly be returning the wrong correction operator. We can visualize this case as flipping all qubits once and then flipping every qubit with the probability $1 - p$.

As a last step, we make our example slightly more realistic. An actual logical qubit in a quantum computation may need to be stored for an extended amount of time until it is used again. Thus, it may be required to continuously monitor and decode. On the repetition code, we can consider the syndrome measurements and the decoding step as one time step and repeat the process T times. To do that, it is actually not necessary to apply a correction operator in every time step. Instead it is sufficient to modify the decoding algorithm slightly such that the majority voting algorithm finds the qubit configuration that is closest to the assumed result of the previous time step. Thus this new decoder $\tilde{\mathcal{D}}$ finds the trajectory that matches all parity measurements and assumes the smallest possible amount of errors in every time step. To evaluate the decoder, we can calculate how many time steps can, on

average, be performed until the system is decoded wrongly for the first time. We call this the *mean time to first failure* $T_{\tilde{\mathcal{D}}}$. For our example, where the decoder considers every time step separately, this expectation value is calculated as follows:¹⁰

$$T_{\tilde{\mathcal{D}}} = \sum_{t=1}^{\infty} t \underbrace{[P_{\mathcal{D}}(p; L)]^{t-1} [1 - P_{\mathcal{D}}(p; L)]}_{\text{prob. of a mistake occurring at } t} = \dots = \frac{1}{1 - P_{\mathcal{D}}(p; L)} \quad (2.7)$$

Figure 2.1 (b) shows the mean time to first failure for different error rates depending on the system size. For error rates $p < 1/2$, we find an approximately exponential dependence. The repetition code is slightly inefficient with even system sizes; for example, the $L = 4$ code can only safely decode one error, just like the $L = 3$ code. For that reason, the plot shows an even-odd effect. At $p = 1/2$, the single-step decoding probability is exactly $P_{\mathcal{D}}(p = 1/2; L) = 1/2$ and the mean time to first failure is constant $T_{\tilde{\mathcal{D}}} = 2$.

Again, given specific values for L and T , we can define a decoding probability for our modified problem. The decoder returns the appropriate correction operator, if the algorithm assumed the right qubit configuration in every one of the T time steps. However, the decoder is also be successful if it made a mistake in an even number of time steps (two mistakes cancel each other). Therefore, the decoding probability is actually

$$P_{\tilde{\mathcal{D}}}(p; L, T) = \sum_{\substack{j=0 \\ j \text{ even}}}^T \binom{T}{j} [P_{\mathcal{D}}(p; L)]^{T-j} [1 - P_{\mathcal{D}}(p; L)]^j \quad (2.8)$$

with the result $P_{\mathcal{D}}(p; L)$ for single time steps from Equation (2.6). This decoding probability serves us as an alternative to the mean time to first failure in evaluating the performance of a decoder. If the system size is scaled with the number of time steps (here we arbitrarily choose a “square” spacetime with $L = T$) the validity of a decoding algorithm will show in the thermodynamic limit $L \rightarrow \infty$. The resulting decoding probability is shown in Figure 2.1 (c). Clearly, the decoding transition exhibits a strong finite-size effect. It can be shown that the limit is actually $P_{\tilde{\mathcal{D}}}(p < 1/2; L \rightarrow \infty, T = L) = 1$. Thus for very large system sizes L , we again find the critical error rate $\tilde{p}_{\text{thr}} = 1/2$.¹¹ This means that systems for any error rate $p < 1/2$ can be corrected with the decoder $\tilde{\mathcal{D}}$ using a large enough system with a size proportional to the number of time steps.¹²

Even though we used notations and terminologies known from quantum mechanics, it is important to note that the repetition code is actually fully classical [105], as all parity measurements produce deterministic results. Had we chosen an initial state without a superposition ($\alpha = 0$ or $\beta = 0$), we could have modeled any trajectory by flipping coins instead of qubits. This is not uncommon for quantum error correcting schemes with only

¹⁰The full calculation can be done easily by relating the sum to a derivative of the geometric series.

¹¹For the single time step we found the same critical error rate. This is a feature of this model and not true in general.

¹²A quantum repetition code was realized on up to 21 superconducting qubits in Ref. [104] and proven to be stable over 50 rounds of error correction.

one type of unitary errors. As we will see later, even some truly quantum mechanical error correcting schemes bear a striking resemblance to classical models. In the following we will introduce the projective transverse field Ising model as an error correcting code and formally define the quantities we showed in Figure 2.1 for this system.

2.3 Quantum Error Correction on the Projective Transverse Field Ising Model

We can interpret the projective transverse field Ising model (see Section 1.3) as a topological quantum memory with competing syndrome measurements and errors [24]. This approach was already found to be viable in hybrid quantum circuits [71, 72, 98] – here we apply it to a measurement-only quantum circuit.

We consider the code space \mathcal{C} to be the subspace of the Hilbert space which is stabilized by the operators S_e

$$\mathcal{C} = \{|\Psi\rangle \in \mathcal{H} : S_e |\Psi\rangle = |\Psi\rangle \forall e \in \{(1, 2), (2, 3), \dots, (L-1, L)\}\}. \quad (2.9)$$

\mathcal{C} is spanned by the logical states $|0\rangle = |00 \dots 0\rangle$ and $|1\rangle = |11 \dots 1\rangle$ – this is also the code space of the repetition code [see Equation (2.1)]. Accordingly, a logical qubit is encoded in the initial state as

$$|\Psi_0\rangle = \alpha|0\rangle + \beta|1\rangle \quad (2.10)$$

with the amplitudes $\alpha, \beta \in \mathbb{C}$ and $|\alpha|^2 + |\beta|^2 = 1$. As the stabilizers of the code space, S_e measurements can never gain access to the encoded qubit. We interpret them as syndrome measurements of an error correcting code. They are performed repeatedly by an observer in order to gain insights on the noisy trajectory of the state. The syndrome is the recorded measurement history $S^{\text{p},r}$. E_i measurements are not recorded by the observer and thus represent the errors of the code. They anticommute $\{E_i, S_e\} = 0$ with the syndrome measurements S_e for all $i \in e$ and are not stabilizers of the code space. Via errors, the environment may gain access to the amplitudes and the logical qubit is lost.¹³ For the remainder of this chapter we will refer to S_e and E_i as *syndrome* and *error measurements*.

The colored cluster model (see Subsection 1.3.1) can help us to understand, what happens to the quantum information in the system. The qubits are initialized in one global cluster. This is not a Bell cluster but contains the arbitrary amplitudes α and β .¹⁴ Error measurements destroy the amplitudes on a qubit. Crucially, α and β always survive the fusion of clusters:

$$(\alpha|0\rangle + \beta|1\rangle) \otimes (|0\rangle + |1\rangle) \xrightarrow{\text{meas. } Z_1 Z_2} \begin{cases} \alpha|00\rangle + \beta|11\rangle, & \text{meas. result } +1, \\ \alpha|01\rangle + \beta|10\rangle, & \text{meas. result } -1 \end{cases} \quad (2.11)$$

We can imagine this as the initial cluster having a dominant color in the CCM. Whenever two clusters are joined, this color survives and the quantum information is preserved in the

¹³This is the noise model we choose here; a different one is considered in Chapter 4.

¹⁴A Bell cluster requires the amplitudes to be equal: $|\alpha| = |\beta| = 1/\sqrt{2}$.

state. If the initial cluster is destroyed by an error measurement, the quantum information is lost irretrievably. This represents a major difference between the PTIM and the repetition code: Due to the projective noise model of the PTIM, syndrome measurements are not only used by the observer to gain information about the state, but they are also necessary to protect the quantum information such that it is not lost to the environment via error measurements.

2.3.1 The Model

We consider the following setting: An open chain of L qubits is initialized in a state $|\Psi(0)\rangle = |\Psi_0\rangle = \alpha|0\rangle + \beta|1\rangle$ encoding a single logical qubit. The system is propagated in T discrete time steps in a PTIM circuit (see Section 1.3). We understand the probability p for error measurements as an *error rate* and q for missing syndrome measurements as a *failure rate*. The full trajectory $\mathcal{T} = \{|\Psi(t)\rangle\}$ is determined by the measurement history $M^{\mathcal{P},\mathcal{X}}$ and the initial state $|\Psi_0\rangle = |\Psi(0)\rangle$. In a slight abuse of notation, we write $\mathcal{T} = (M^{\mathcal{P},\mathcal{X}}, |\Psi_0\rangle) = (E^{\mathcal{P},\mathcal{X}}, S^{\mathcal{P},\mathcal{X}}, |\Psi_0\rangle)$.

To comply with the concept of quantum error correction, we measure all syndromes in the last time step, i.e., we set $q = 0$ at $t = T$. This projects the final state $|\Psi_f(\mathcal{T})\rangle = |\Psi(T)\rangle$ into the two-dimensional subspace spanned by $|\mathbf{m}\rangle$ and $|\bar{\mathbf{m}}\rangle = \prod_i X_i |\mathbf{m}\rangle$. The configurations $\mathbf{m} = (m_1, \dots, m_L)$ with $m_i \in \{0, 1\}$ and its complement $\bar{\mathbf{m}}$ correspond to the final syndrome measurements. It was shown in Ref. [24] that the final state must assume one of two possible forms (up to a global phase)

$$|\Psi_f(\mathcal{T})\rangle = |\Psi(T)\rangle = \begin{cases} \alpha|\mathbf{m}\rangle + \beta|\bar{\mathbf{m}}\rangle, \\ (|\mathbf{m}\rangle \pm |\bar{\mathbf{m}}\rangle) / \sqrt{2}, \end{cases} \quad (2.12)$$

where the qubit configuration $\mathbf{m} = \mathbf{m}(\mathcal{T})$ depends on the trajectory \mathcal{T} .

In the first case $|\Psi_f\rangle = \alpha|\mathbf{m}\rangle + \beta|\bar{\mathbf{m}}\rangle$, the environment did not gain access to the encoded quantum information and the amplitudes α and β survived. This final state has the same form as in the repetition code [cf. Equation (2.2)] – although the trajectories are fundamentally different here. We show a trajectory of this kind in Figure 2.2 (a). In accordance with the CCM, the initial cluster which carries the logical qubit is marked through the trajectory. In the bond percolation model (see Figure 1.5) the survival of the quantum information is manifested by the existence of a percolation path spanning the space-time grid vertically. We show one such path as a dashed line.

In the second case, the system assumes a GHZ state $|\Psi_f\rangle = (|\mathbf{m}\rangle \pm |\bar{\mathbf{m}}\rangle) / \sqrt{2}$ as the quantum information was destroyed by an error measurement. This measurement does determine the sign of the superposition; the final state $|\mathbf{m}\rangle + |\bar{\mathbf{m}}\rangle$ occurs with probability $|\alpha + \beta|^2 / 2$ and $|\mathbf{m}\rangle - |\bar{\mathbf{m}}\rangle$ with probability $|\alpha - \beta|^2 / 2$. We show a trajectory of this kind in Figure 2.2 (b). Again the initial cluster is marked but here it is destroyed by errors and does not reach the final time step. Trajectories of this kind are characterized by the existence of a spanning percolation path connecting the system boundaries on the dual grid to the one shown in

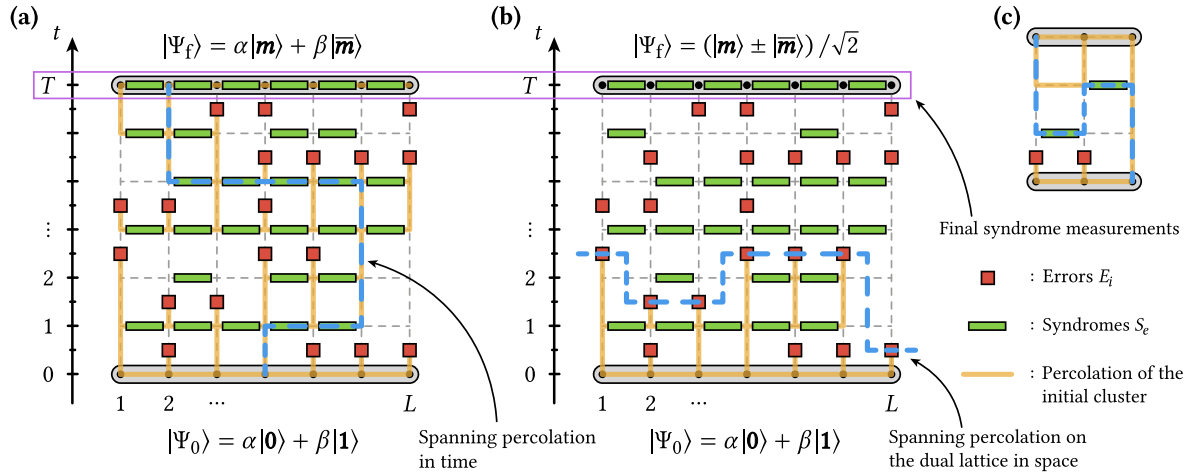


Figure 2.2 • Projective transverse field Ising model as a quantum error correction code. Two possible trajectories for the PTIM as a quantum error correction code. A logical qubit is encoded in the initial state. The model differs from the usual setup of a PTIM (see Figure 1.2) only in the last time step, where all S_e measurements are performed. **(a)** Trajectory in which the initial cluster survives the evolution of the state such that the amplitudes α and β are preserved. We highlight the clusters percolation path in spacetime according to the rules of the CCM. In trajectories of this kind, there exists a spanning percolation which connects the first and final time step. **(b)** Measurement pattern which destroys the initial cluster. In this case there exists a spanning percolation connecting the first and last qubit on the dual lattice. **(c)** Minimal nontrivial example illustrating how the initial cluster percolates in the CCM.

Figure 1.5. We show this path as a dashed line in the figure. Horizontal steps are only allowed to cross through errors, and vertical steps may not cross syndromes. In general, there might be multiple paths of this kind. In Figure 2.2 (b) we indicate the one path that terminates the percolation of the initial cluster through time. From this picture, we can gain an understanding on why the sign of the superposition $|m\rangle \pm |\bar{m}\rangle$ is determined by the last error which destroys the initial cluster: The global parity $X_1 \cdots X_L$ is a symmetry of the PTIM as it commutes with all errors and syndromes. The horizontal percolation shown in Figure 2.2 (b) measures this parity — thus it cannot change afterwards.

It is important to note that the percolation of the initial clusters shown in Figure 2.2 (a) and (b) can invite a slight misinterpretation. In order to track the cluster, it is not sufficient to propagate it along syndrome measurements in space and through time wherever no error occurred. If two larger clusters are joined, *all* involved qubits assume the same color, not only the ones that were part of the syndrome measurement. We show a minimal example for this in Figure 2.2 (c). Here the initial cluster reaches the leftmost qubit without being propagated by a syndrome measurement. This occurs because qubits 1 and 2 are already entangled in a Bell cluster. We can also understand this in the percolation picture. Following

a percolation cluster (which is not the same as a physical Bell cluster; see Figure 1.5) may require some backtracking in the temporal direction. Here we show a spanning percolation which does a step backward in time.

We can consider the PTIM as a generalized repetition code with two key differences. Firstly, due to the failure rate q , not all syndromes are measured in every time step. Secondly, all qubit flips are replaced by measurements which project a qubit onto the x -basis and may destroy the quantum information. We are now able to formulate the goal of this chapter: Find the unitary operator C for a given PTIM trajectory which is most likely to correct the state $C|\Psi_f\rangle = |\Psi_0\rangle$ and thus restores the logical qubit.

Connection to the Entanglement Transition

Before we introduce algorithms that are designed to find correction operators C , we want to draw an important connection. Here we are considering the PTIM from a quantum information perspective. This angle is strongly related to the entanglement dynamics of the PTIM which we introduced in Subsection 1.3.2. A logical qubit is encoded in a cluster on multiple physical qubits and thus the CCM describes how information permeates the trajectory in spacetime as shown in Figure 2.2. For a final state to be correctable, it must inherit the amplitudes α and β , i.e., the initial cluster must have survived the trajectory. Now consider a large system with many time steps $T \gg L \gg 1$. At $p + q < 1$, the PTIM is in the entanglement phase, which is characterized by the existence of one global cluster. Such a global cluster does not exist at $p + q > 1$. This can be probed by tracking the initial cluster in the CCM and recording the time step where it is destroyed. We call this the *cluster lifetime* and its sample average τ . In Ref. [24] numerical simulations were used to verify that in the percolating phase at $p + q < 1$ the lifetime scales exponentially with the system size $\tau \sim \alpha e^{\beta L}$. At $p + q > 1$ the growth of clusters is suppressed by errors and the lifetime of the initial global cluster scales logarithmically $\tau \sim \alpha \log(L) + \beta$. At the critical line $p + q = 1$ an algebraic scaling $\tau \sim L^\beta$ is observed.

Thus we can probe the entanglement dynamics of the PTIM without requiring a simulation to reach a steady state: We initialize the system in a global cluster and scale the number of time steps proportionally with the number of qubits $T \propto L$. Let P_C be the probability for the initial cluster to survive until the final time step. In the thermodynamic limit $L \rightarrow \infty$ we then find $\tau \gg T$ for $p + q < 1$ and $\tau \ll T$ for $p + q > 1$. The cluster survival probability approaches a step function

$$P_C(p, q) \xrightarrow{L \rightarrow \infty} \begin{cases} 1, & p + q < 1, \\ 0, & p + q > 1, \end{cases} \quad (2.13)$$

which pinpoints the location of the entanglement transition. P_C is a measure of the connectivity in the bond percolation model (cf. Figure 1.5); therefore we also refer to the entanglement transition of the PTIM at $p + q = 1$ as the *percolation transition*.

In the context of quantum error correction, the survival of the initial cluster is of great importance. If the cluster is destroyed and the amplitudes α and β are lost, it will be impossible

to restore the quantum information. Any error correction can only succeed in the percolating phase $p + q < 1$. Consequently, the decoding thresholds that we discuss in this chapter are lower bounds on the entanglement transition.¹⁵ For the remainder of this chapter, we will assume $L = T$ if not stated otherwise. One of the questions we aim to answer is the following: Can a logical qubit always be restored if the quantum information is preserved in the system? If so, a correction scheme would directly reproduce the entanglement transition of the PTIM; if not, we would find a true lower bound.

Note that similar relations between quantum information and the entanglement dynamics of different models have been found and used in Refs. [71, 72, 106–108]. Usually in these schemes, quantum information is propagated in a phase dominated by unitary gates and destroyed by projective measurements. This is part of what makes the PTIM interesting: A measurement-only quantum circuit may still protect and propagate quantum information.

2.3.2 Decoding

In this chapter, we describe classical algorithms that take a measurement history as their input and return a correction operator C . As introduced in Section 2.1, we call these algorithms *decoders* $\mathcal{D}(M^{\text{p,r}}) = C$. We aim to find decoders tailored to the PTIM which enable us to restore quantum information such that $C|\Psi_f\rangle = |\Psi_0\rangle$. To evaluate the performance of such algorithms we will reintroduce some of the quantities we defined in Section 2.2 to fit the context of the PTIM.

It is important to realize that part of a decoder's task is trivial. To see this, we first discard the case in which the quantum information does not survive — there is no logical qubit to be restored here. If the information is preserved, our scenario is strikingly similar to the repetition code as only two final states

$$|\Psi_f\rangle = \begin{cases} \alpha|\mathbf{m}\rangle + \beta|\bar{\mathbf{m}}\rangle, \\ \alpha|\bar{\mathbf{m}}\rangle + \beta|\mathbf{m}\rangle \end{cases} \quad (2.14)$$

are possible, where $|\mathbf{m}\rangle$ and $|\bar{\mathbf{m}}\rangle$ match the $L - 1$ measurements of S_e in the final time step. The observer/decoder does not know which of those is the real state of the system. The right choice for the correction operators is [as in Equation (2.5)]

$$C = \prod_{i=1}^L (X_i)^{m_i} \quad (2.15)$$

for the first case and the complement $\bar{C} = \left(\prod_j X_j\right) C$ in the second case. Decoding the PTIM therefore amounts to choosing a correction operator from a set $\{C_{S_T^r}, \bar{C}_{S_T^r}\}$ of only two possible operators that are allowed given the syndrome measurements S_T^r in the final step T . Selecting the wrong one will cause a bit flip error on the logical qubit. We formally define a decoder as a function

$$\mathcal{D} : M^{\text{p,r}} \mapsto \mathcal{D}(M^{\text{p,r}}) \in \{C_{S_T^r}, \bar{C}_{S_T^r}\} \quad (2.16)$$

¹⁵We will make use of this in Chapter 4.

mapping a trajectory \mathcal{T} to one of two possible correction operators.¹⁶

To evaluate a decoder, we compare the corrected final state $\mathcal{D}|\Psi_f\rangle$ to the initial state $|\Psi_0\rangle$. Note that the parity $\prod_i X_i$ is the logical X operator in our setting. An initial state polarized in the logical x -direction $|\mathbf{0}\rangle \pm |\mathbf{1}\rangle$ would not allow us to distinguish the cases in Equation (2.14) and would thus be a bad choice to test a decoder. Instead, we choose an initial state with vanishing x -polarization; here we will always assume $|\Psi_0\rangle = |\mathbf{0}\rangle$ (i.e., $\alpha = 1$, $\beta = 0$). To identify the right correction operator, we calculate the overlap

$$f^{\text{qm}}(\mathcal{T}; C) := |\langle \Psi_0 | C | \Psi_f(\mathcal{T}) \rangle|^2, \quad (2.17)$$

which replaces Equation (2.3) to accommodate the quantum-mechanical nature of the PTIM. Given our choice of $|\Psi_0\rangle$, this expression returns $f^{\text{qm}} = 1$ ($f^{\text{qm}} = 0$) for the correct (incorrect) operator C if the information survived in the system. If the amplitudes were lost, it is $f^{\text{qm}} = 1/2$ independent of the correction operator chosen by the decoder. This allows us to quantify the performance of a decoder \mathcal{D} on a single trajectory \mathcal{T} via the evaluation function

$$f_{\mathcal{D}}^{\text{qm}}(\mathcal{T}) := f^{\text{qm}}(\mathcal{T}; C = \mathcal{D}(M^{\text{p,r}})). \quad (2.18)$$

The ability of a decoder to correct *all* trajectories is then quantified by the *decoding probability*

$$P_{\mathcal{D}}(p, q; L, T) := \langle\langle f_{\mathcal{D}}^{\text{qm}} \rangle\rangle = \sum_{\mathcal{T}} P^{\text{qm}}(\mathcal{T}) f_{\mathcal{D}}^{\text{qm}}(\mathcal{T}). \quad (2.19)$$

This formal definition is similar to Equation (2.4) for the repetition code, but tailored to the PTIM with the correct evaluation function. $P^{\text{qm}}(\mathcal{T})$ is the probability for the trajectory \mathcal{T} to occur. This includes the probability for a measurement pattern $M^{\text{p}} = (E^{\text{p}}, S^{\text{p}})$ to occur (determined by the rates p and q) *and* the probability of the measurement outcomes $M^{\text{r}} = (E^{\text{r}}, S^{\text{r}})$ which are dependent on the history of the trajectory and thus highly nontrivial. The decoding probability will be our most important tool to compare decoders. A value of $P_{\mathcal{D}} = 1$ indicates that the decoder successfully decodes the PTIM. If the decoder fails, we generally find $P_{\mathcal{D}} = 1/2$. This indicates that either the quantum information did not survive or the decoder performs only as good as flipping a coin to choose a correction operator.

As we already showed for the repetition code (see Figure 2.1), we expect a good decoder to perform better on large systems. For a fixed size L though, every additional time step can only decrease $P_{\mathcal{D}}$. This leads us to a second measure for the evaluation of a decoder: the *mean time to first failure* (MTFF) $T_{\mathcal{D}}$ which we already discussed for the repetition code in Equation (2.7). Consider an infinitely long trajectory \mathcal{T} and for $t \in \{0, 1, \dots\}$ define $\mathcal{T}|_t$ as the first t time steps of \mathcal{T} , terminated by a full syndrome measurement. We apply a decoder \mathcal{D} to $\mathcal{T}|_t$ and evaluate it by computing $f_{\mathcal{D}}^{\text{qm}}(\mathcal{T}|_t)$. Let $t_{\mathcal{D}}^{\text{qm}}(\mathcal{T})$ be the first time step t on which the decoder fails ($f_{\mathcal{D}}^{\text{qm}}(\mathcal{T}|_t) < 1$). Then we can define the MTFF as the sample average

$$T_{\mathcal{D}}(p, q; L) := \langle\langle t_{\mathcal{D}}^{\text{qm}} \rangle\rangle, \quad (2.20)$$

¹⁶For now, we are describing a noise-free case, i.e., all measurements are recorded. In general the decoder's input will only be a subset of the measurement history $M^{\text{p,r}}$.

inspired by the average cluster lifetime τ . Given a set of parameters p and q , we will call a decoder *successful* if $T_{\mathcal{D}}(p, q; L)$ grows super-polynomially at large sizes $L \rightarrow \infty$. A decoder *fails* if the MTFE grows sublinearly in the same limit. Typically, we will observe a logarithmic scaling in this case.

Trivial Decoder

As a first example, we describe the trivial case of a noise-free PTIM trajectory, i.e., a decoder \mathcal{D} with perfect knowledge of the measurement history $M^{p,r}$. Here we can profit from the fact that the PTIM can be efficiently simulated on a classical computer: A decoder only needs to run a stabilizer simulation to find the final state and choose a correction string.¹⁷ Note that the decoder does not need to know the initial state for this. If a correction operator reconstructs any one logical qubit, it will correct all possible input states of the form $\alpha|0\rangle + \beta|1\rangle$. In other words, the decoder will return the same correction string for any initial state it assumes.

In Figure 2.3, we show the decoding probability for this trivial setup as a function of the parameters p and q for a system size $L = T = 51$. The decoder works perfectly whenever the quantum information is preserved in the system and thus $P_{\mathcal{D}}(p, q; L = T)$ retraces the percolation transition of the PTIM. At $p + q < 1$ the quantum information survives the trajectory and is decoded. In the disentangling phase at $p + q > 1$ the decoder fails because the environment gains access to the amplitudes of the logical qubit. Note that due to finite-size effects, the transition is smeared out and shifted slightly from the off-diagonal $p + q = 1$, which is predicted by percolation theory.¹⁸

For the remainder of this chapter we will consider a noise model in which the observer (and by extension the decoder) does not know the full measurement history $M^{p,r}$. We interpret the error measurements as noise which leaks information to the environment and is not recorded – neither when and where the measurements occurred (E^p) nor what their results were (E^r). Syndrome measurements are performed randomly by the observer and recorded in the history $S^{p,r}$.¹⁹ Thus we write a decoder as a function $\mathcal{D}(S^{p,r})$ of only the partial measurement history, which does not include any information on the errors.

2.3.3 Efficient Numerical Simulations

To evaluate the performance $P_{\mathcal{D}}$ of a decoder numerically via sampling, every sample requires two steps: First, a trajectory \mathcal{T} is generated. Secondly, based on the syndromes $S^{p,r}$, the decoder is evaluated to compute $f^{\text{qm}}(\mathcal{T}; C = \mathcal{D}(S^{p,r}))$. Here we will provide some comments on the first step.

¹⁷There exists an even more efficient algorithm which performs a modified CCM simulation, tracking clusters and their qubit configurations. This algorithm can operate without knowledge of the outcomes of the error measurements $\mathcal{D}(E^p, S^{p,r})$ without any sacrifices. We expand on this in Section 4.A.

¹⁸The direction of this shift is intuitively clear: At $(p = 0, q = 1)$ the initial cluster always survives and it must be $P_{\mathcal{D}} = 1$. At $(p = 1, q = 0)$ the initial cluster is destroyed in the first time step and it must be $P_{\mathcal{D}} = 1/2$.

¹⁹In Chapter 4 we will expand this to a more general noise model.

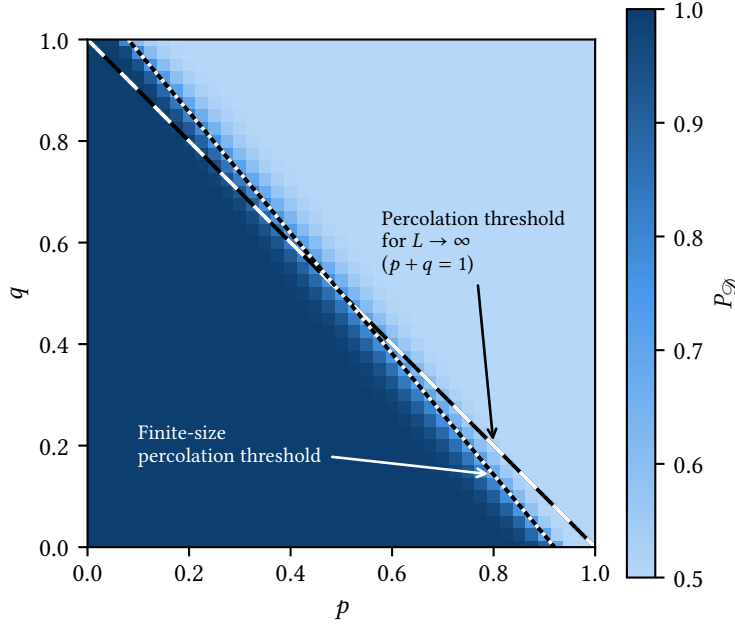


Figure 2.3 • Decoding probability with full knowledge of the trajectory. Probability $P_{\mathcal{D}}(p, q)$ to successfully decode the PTIM with full knowledge of the measurement history $M^{p,r}$, including errors and syndromes for $L = T = 51$. In this trivial noise-free setup, the decoder performs perfectly and reproduces the entanglement transition of the model governed by the percolation threshold. Due to finite-size effects, the percolation threshold is shifted and smeared out. For every data point, we sampled $2 \cdot 10^4$ trajectories.

As the PTIM is a stabilizer circuit and the initial state $|\Psi_0\rangle = |\mathbf{0}\rangle$ is stabilized by the group $\mathfrak{S} = \langle Z_1, \dots, Z_L \rangle$, sample trajectories \mathcal{T} of the PTIM can be simulated exactly and efficiently on a classical computer, as we described in Subsection 1.2.1. However, there exists a more efficient method which samples trajectories of a *classical* stochastic process derived from the PTIM that operates on a chain of L classical *bits* initialized in the configuration $\mathbf{m}_0 = \mathbf{0} = (0 \dots 0)$. Instead of error measurements E_i with probability p , the classical model exhibits bit flips in every time step with probability $p/2$. The bit flip pattern \tilde{E}^p on the space-time lattice determines the final bit configuration \mathbf{m}_T after all T time steps. Syndrome measurements are performed on the classical system just as they would be on the PTIM in the pattern S^p . Here they do not collapse the wave function and all results S^r are determined by the pattern \tilde{E}^p – similar to trajectories in the repetition code (cf. Section 2.2). A syndrome history $S^{p,r}$ sampled in this fashion can be applied to a given decoder \mathcal{D} to compute the correction operator $C = \mathcal{D}(S^{p,r})$. We use the trivial evaluation function

$$f^{\text{bi}}\left(\tilde{E}^p; C = \prod_{i=1}^L X_i^{n_i}\right) := \begin{cases} 1, & \mathbf{n} = \mathbf{m}_T, \\ 0, & \text{otherwise} \end{cases} \quad (2.21)$$

to quantify any decoder on the classical system. Here we write the correction operator as introduced in Equation (2.5) with $n_i \in \{0, 1\}$.²⁰

Crucially, the relation

$$\langle\langle f_{\mathcal{D}}^{\text{qm}} \rangle\rangle_{\text{qm}} = \langle\langle f_{\mathcal{D}}^{\text{bi}} \rangle\rangle_{\text{bi}} \quad (2.22)$$

holds for all decoders \mathcal{D} of the form defined in Equation (2.16). The subscripts $\langle\langle \cdot \rangle\rangle_{\text{qm}}$ and $\langle\langle \cdot \rangle\rangle_{\text{bi}}$ denote the method that is used to sample trajectories. Equation (2.22) allows us to determine decoding probabilities by sampling the classical process described here, instead of performing the full stabilizer simulation of the PTIM. This results in a considerable speedup and will allow us to study larger systems and sample sizes. We verified the validity of Equation (2.22) numerically and will in the following provide an analytical proof for its correctness.

Proof of Equation (2.22)

A PTIM trajectory \mathcal{T}^{qm} is fully determined by the initial state $|\Psi_0\rangle$ and the measurement history $M^{\text{P},r}$. As we only consider $|\Psi_0\rangle = |0\rangle$, we drop this dependence here. Furthermore in our case, the results of the error measurements E^r are not important as they do not affect the syndromes and only impact the final state if the initial cluster is destroyed. Thus we will drop them in the following calculations. A classical trajectory \mathcal{T}^{bi} is technically determined by the bit flip pattern \tilde{E}^{P} , but syndromes $S^{\text{P},r}$ are also sampled. To facilitate our calculations, we introduce the number of measurements/bit flips in a pattern which we denote as $|E^{\text{P}}|$, $|S^{\text{P}}|$ and $|\tilde{E}^{\text{P}}|$. Furthermore not all measurements are created equal. For example, measuring an error twice in a row will give the same outcome both times, as the second measurement result is deterministic. Thus we introduce the concept of reduced measurement patterns $E_{\text{red}}^{\text{P}}$ and $S_{\text{red}}^{\text{P}}$ which are subsets of the original patterns but only include those measurements without a predetermined measurement result.

For any system α , the ensemble average is [cf. Equation (2.19)]

$$\langle\langle f_{\mathcal{D}}^{\alpha} \rangle\rangle_{\alpha} = \sum_{\mathcal{T}^{\alpha} \in \{\mathcal{T}^{\alpha}\}} P^{\alpha}(\mathcal{T}^{\alpha}) \cdot f^{\alpha}(\mathcal{T}^{\alpha}, \mathcal{D}(S^{\text{P},r})) \quad (2.23)$$

with a trajectory \mathcal{T}^{α} in the system α and the set of all possible trajectories $\{\mathcal{T}^{\alpha}\}$. $P^{\alpha}(\mathcal{T}^{\alpha})$ is the probability of \mathcal{T}^{α} to occur in the model α and f^{α} denotes the evaluation function for \mathcal{D} in α . Here we make clear that the decoder $\mathcal{D}(S^{\text{P},r})$ is a function that only depends on the syndromes which are part of the given trajectory – this is all the information available to the observer.

Now we focus on the quantum system. The probability for a single trajectory \mathcal{T}^{qm} to occur is

$$P^{\text{qm}}(\mathcal{T}^{\text{qm}}) := \underbrace{p^{|E^{\text{P}}|} (1-p)^{L T - |E^{\text{P}}|}}_{P^{\text{qm}}(E^{\text{P}})} \cdot \underbrace{q^{(L-1)T - |S^{\text{P}}|} (1-q)^{|S^{\text{P}}|}}_{P^{\text{qm}}(S^{\text{P}})} \cdot \underbrace{\left(\frac{1}{2}\right)^{|S_{\text{red}}^{\text{P}}|}}_{P^{\text{qm}}(S^r|E^{\text{P}}, S^{\text{P}})} \quad (2.24)$$

²⁰We generally use the superscript ^{bi} for “bits” to distinguish this evaluation function from its quantum mechanical counterpart defined in Equation (2.17) which we denote with the superscript ^{qm}.

with the classical probabilities $P^{\text{qm}}(E^{\text{P}})$ and $P^{\text{qm}}(S^{\text{P}})$ for the measurement patterns to occur and the quantum mechanical probability $P^{\text{qm}}(S^{\text{r}} | E^{\text{P}}, S^{\text{P}})$ for the syndromes to return a certain set of measurement results.²¹ We insert this in Equation (2.23):

$$\langle\langle f_{\mathcal{D}}^{\text{qm}} \rangle\rangle_{\text{qm}} = \sum_{\mathcal{T}^{\text{qm}} \in \{\mathcal{T}^{\text{qm}}\}} P^{\text{qm}}(\mathcal{T}^{\text{qm}}) \cdot f^{\text{qm}}(\mathcal{T}^{\text{qm}}; \mathcal{D}(S^{\text{P},\text{r}})) \quad (2.25a)$$

$$= \sum_{E^{\text{P}}} P^{\text{qm}}(E^{\text{P}}) \sum_{S^{\text{P}}} P^{\text{qm}}(S^{\text{P}}) \sum_{S^{\text{r}} | E^{\text{P}}, S^{\text{P}}} P^{\text{qm}}(S^{\text{r}} | E^{\text{P}}, S^{\text{P}}) \cdot f^{\text{qm}}(\mathcal{T}^{\text{qm}}; \mathcal{D}(S^{\text{P},\text{r}})). \quad (2.25b)$$

Here we split the sampling of trajectories into three steps/sums by separately sampling over the measurement patterns (which are independent from each other) and the different possible results of the syndrome measurements (which depend on the patterns). As mentioned before, the results of the error measurements have no effect on any of our observations and are thus ignored here.

We can perform the same calculation for the classical model. The probability for a classical trajectory \mathcal{T}^{bi} to occur is

$$p^{\text{bi}}(\mathcal{T}^{\text{bi}}) := \underbrace{\left(\frac{p}{2}\right)^{|\tilde{E}^{\text{P}}|} \left(1 - \frac{p}{2}\right)^{LT - |\tilde{E}^{\text{P}}|}}_{p^{\text{bi}}(\tilde{E}^{\text{P}})} \cdot \underbrace{q^{(L-1)T - |S^{\text{P}}|} (1 - q)^{|S^{\text{P}}|}}_{p^{\text{bi}}(S^{\text{P}})}. \quad (2.26)$$

There are no undetermined measurement results to consider here. It is possible to sample bit flip patterns \tilde{E}^{P} with the probability $p/2$ on every site in every time step. However it will prove to be useful to use a different approach. Bit flips can also be sampled by first sampling a pattern E^{P} of *potential* bit flips with the probability p and then sampling $\tilde{E}^{\text{P}} \subseteq E^{\text{P}}$ from E^{P} with the probability $1/2$. We formally include the pattern E^{P} in the trajectory \mathcal{T}^{bi} and define the adjusted probability

$$p^{\text{bi}}(\mathcal{T}^{\text{bi}}, E^{\text{P}}) := \underbrace{p^{|E^{\text{P}}|} (1 - p)^{LT - |E^{\text{P}}|}}_{p^{\text{bi}}(E^{\text{P}})} \cdot \underbrace{q^{(L-1)T - |S^{\text{P}}|} (1 - q)^{|S^{\text{P}}|}}_{p^{\text{bi}}(S^{\text{P}})} \cdot \underbrace{\left(\frac{1}{2}\right)^{|E^{\text{P}}|}}_{p^{\text{bi}}(\tilde{E}^{\text{P}} | E^{\text{P}})}. \quad (2.27)$$

The two probabilities in Equations (2.26) and (2.27) are related via

$$p^{\text{bi}}(\mathcal{T}^{\text{bi}}) = \sum_{E^{\text{P}} | \mathcal{T}^{\text{bi}}} p^{\text{bi}}(\mathcal{T}^{\text{bi}}, E^{\text{P}}) \quad (2.28)$$

with the sum over all patterns E^{P} that are consistent with the classical trajectory \mathcal{T}^{bi} . The proof for Equation (2.28) is technical and therefore relegated to Section 2.A. We insert

²¹In stabilizer circuits, any non-deterministic measurement returns the result ± 1 with probability $1/2$.

Equation (2.27) into Equation (2.23) to find the classical sampling average

$$\langle\langle f_{\mathcal{D}}^{\text{bi}} \rangle\rangle_{\text{bi}} = \sum_{\mathcal{T}^{\text{bi}} \in \{\mathcal{T}^{\text{bi}}\}} P^{\text{bi}}(\mathcal{T}^{\text{bi}}) \cdot f^{\text{bi}}(\mathcal{T}^{\text{bi}}, \mathcal{D}(S^{\text{p}}, r)) \quad (2.29a)$$

$$= \sum_{S^{\text{p}}} \sum_{\tilde{E}^{\text{p}}} \sum_{E^{\text{p}} |_{\mathcal{T}^{\text{bi}}}} P^{\text{bi}}(\mathcal{T}^{\text{bi}}, E^{\text{p}}) \cdot f^{\text{bi}}(\mathcal{T}^{\text{bi}}, \mathcal{D}(S^{\text{p}}, r)) \quad (2.29b)$$

$$= \sum_{E^{\text{p}}} P^{\text{bi}}(E^{\text{p}}) \sum_{S^{\text{p}}} P^{\text{bi}}(S^{\text{p}}) \sum_{\tilde{E}^{\text{p}} \subseteq E^{\text{p}}} P^{\text{bi}}(\tilde{E}^{\text{p}} | E^{\text{p}}) \cdot f^{\text{bi}}(\mathcal{T}^{\text{bi}}, \mathcal{D}(S^{\text{p}}, r)). \quad (2.29c)$$

Here we used the fact that $\sum_{\tilde{E}^{\text{p}}} \sum_{E^{\text{p}} |_{\tilde{E}^{\text{p}}}} \dots = \sum_{E^{\text{p}}} \sum_{\tilde{E}^{\text{p}} |_{E^{\text{p}}}} \dots$ and wrote $\sum_{E^{\text{p}} |_{\mathcal{T}^{\text{bi}}}} \dots = \sum_{E^{\text{p}} |_{\tilde{E}^{\text{p}}}} \dots$ and $\sum_{\tilde{E}^{\text{p}} |_{E^{\text{p}}}} \dots = \sum_{\tilde{E}^{\text{p}} \subseteq E^{\text{p}}} \dots$.²²

We now compare the decoding probabilities of the quantum system in Equation (2.25b) and the classical system in Equation (2.29c). Both samplings differ only in the last sum. In the quantum case, the sampling goes over all possible syndrome measurement results and in the classical case we sample all possible bit flips. In the following, we will show that the equation

$$\sum_{S^{\text{r}} |_{E^{\text{p}}, S^{\text{p}}}} P^{\text{qm}}(S^{\text{r}} | E^{\text{p}}, S^{\text{p}}) f^{\text{qm}}(\mathcal{T}^{\text{qm}}, \mathcal{D}(S^{\text{p}}, r)) = \sum_{\tilde{E}^{\text{p}} \subseteq E^{\text{p}}} P^{\text{bi}}(\tilde{E}^{\text{p}} | E^{\text{p}}) f^{\text{bi}}(\mathcal{T}^{\text{bi}}, \mathcal{D}(S^{\text{p}}, r)) \quad (2.30)$$

holds true. We insert the probabilities from Equations (2.24) and (2.27) to find

$$\sum_{S^{\text{r}} |_{E^{\text{p}}, S^{\text{p}}}} \left(\frac{1}{2}\right)^{|S^{\text{red}}|} f^{\text{qm}}(\mathcal{T}^{\text{qm}}, \mathcal{D}(S^{\text{p}}, r)) = \sum_{\tilde{E}^{\text{p}} \subseteq E^{\text{p}}} \left(\frac{1}{2}\right)^{|E^{\text{p}}|} f^{\text{bi}}(\mathcal{T}^{\text{bi}}, \mathcal{D}(S^{\text{p}}, r)). \quad (2.31)$$

On the right-hand side which describes the classical sampling, we can make use of the fact that flipping a bit twice with probability 1/2 yields the same sampling as flipping it once with the same probability. For that reason we can sample \tilde{E}^{p} just on the reduced error pattern $E_{\text{red}}^{\text{p}}$ without changing the result. On the left-hand side describing the quantum mechanical sampling, it is easy to see that sampling over all possible syndrome measurement results which are consistent with the measurement patterns E^{p} and S^{p} amounts to a sampling over the reduced syndrome results $S_{\text{red}}^{\text{r}}$; all other results are deterministic. Thus we find

$$\sum_{S_{\text{red}}^{\text{r}} |_{E^{\text{p}}, S^{\text{p}}}} \left(\frac{1}{2}\right)^{|S_{\text{red}}^{\text{r}}|} f^{\text{qm}}(\mathcal{T}^{\text{qm}}, \mathcal{D}(S^{\text{p}}, r)) = \sum_{\tilde{E}^{\text{p}} \subseteq E_{\text{red}}^{\text{p}}} \left(\frac{1}{2}\right)^{|E^{\text{p}}|} f^{\text{bi}}(\mathcal{T}^{\text{bi}}, \mathcal{D}(S^{\text{p}}, r)). \quad (2.32)$$

Whether or not the initial cluster survives in the quantum system depends solely on the patterns E^{p} and S^{p} . To see that Equation (2.32) holds true, we consider both cases separately.

²²Both sides of the equation $\sum_{\tilde{E}^{\text{p}}} \sum_{E^{\text{p}} |_{\tilde{E}^{\text{p}}}} \dots = \sum_{E^{\text{p}}} \sum_{\tilde{E}^{\text{p}} |_{E^{\text{p}}}} \dots$ sum over the elements of the set $\{(\tilde{E}^{\text{p}}, E^{\text{p}}) \in \{\tilde{E}^{\text{p}}\} \times \{E^{\text{p}}\} \mid \tilde{E}^{\text{p}} \subseteq E^{\text{p}}\}$.

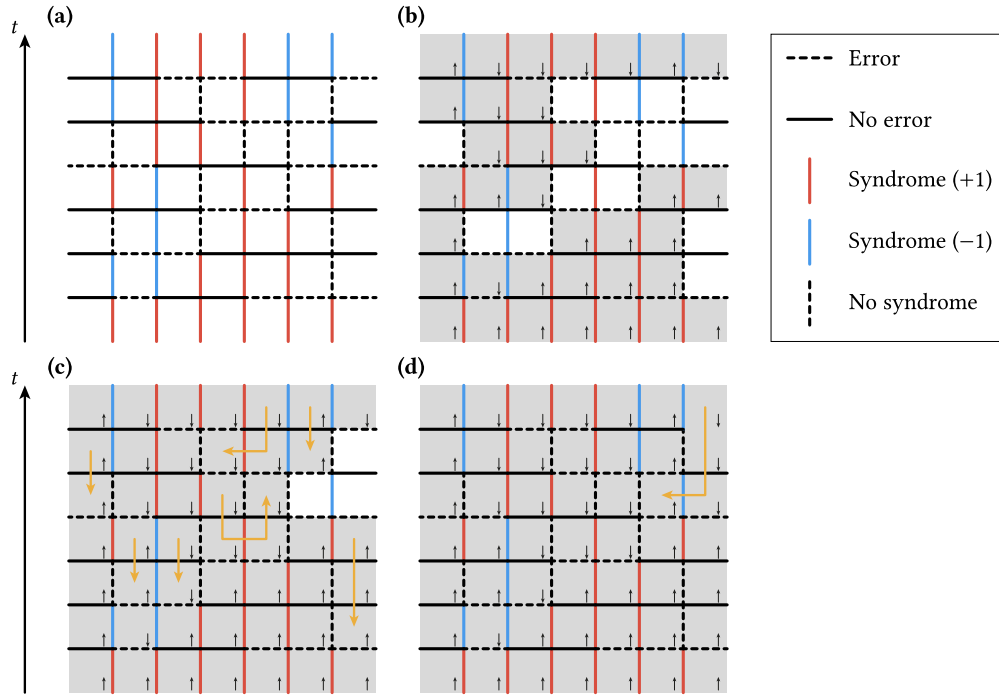


Figure 2.4 • Mapping PTIM trajectories to classical bits. (a) We show a grid \mathcal{L} with the measurements of a PTIM trajectory. The colors indicate syndrome measurement results. (b) The initial product state $|0\rangle$ is marked with gray plaquettes and this cluster is tracked through the lattice. Squares can be associated with a bit orientation according to the syndromes. (c) Some missing plaquettes can be filled by backtracking bit orientations in time. (d) If the initial cluster survives, all remaining plaquettes can be backtracked by removing $E^P \setminus E_{red}^P$. This maps the measurement history $E^P, S^{P,x}$ to a classical trajectory of bits.

1. *Cluster survives.* If the sampling of E^P and S^P is chosen such that the initial cluster in the PTIM survives, it is $|S_{red}^P| = |E_{red}^P|$.²³ The number of terms in both sums is equal. In the following, we will map every PTIM trajectory to a bit trajectory and thus establish a one-to-one correspondence between terms on both sides.

First, we note that if the original cluster survives, the evaluation function f^{qm} only returns the values 1 and 0. A single term on the left side of Equation (2.32) corresponds to a single quantum trajectory \mathcal{T}^{qm} . We show an example for such a trajectory (neglecting the results of error measurements) in Figure 2.4 (a). Here we define a space-time grid \mathcal{L} where qubits live between vertical lines on the plaquettes and measurements occur on the edges of \mathcal{L} .²⁴ Via the CCM, we can mark all plaquettes that are occupied by the initial cluster in gray [see Figure 2.4 (b)]. Assuming that

²³For a syndrome measurement to be non-deterministic, a qubit must have previously been projected onto another basis and vice versa.

²⁴The grid \mathcal{L} is dual to the percolation lattice shown in Figure 1.5.

the state was initialized as $|0\rangle$, every gray plaquette corresponds to a qubit which is polarized in the z -direction. The polarizations can easily be calculated via the syndrome measurement results and are shown in the figure as small arrows. In this step we also determine the final state and thus the value of the evaluation function $f^{\text{qm}}(\mathcal{T}^{\text{qm}}; \mathcal{D}(S^{\text{p},r}))$. The arrows in Figure 2.4 (b) accurately describe the state of the qubits on these points in spacetime. They suggest that on the gray plaquettes, the trajectory \mathcal{T}^{qm} show classical characteristics. White plaquettes do not comply with this picture, but they can be artificially associated with classical states. To illustrate this, we first backtrack the spin orientations on the grey plaquettes in time (without crossing error measurements). We show this step in Figure 2.4 (c).²⁵ White plaquettes can be filled by deleting all predetermined error measurements $E^{\text{p}} \setminus E_{\text{red}}^{\text{p}}$ from \mathcal{L} .²⁶ Then again, we can backtrack the remaining plaquettes and assign every position in \mathcal{L} with a spin orientation [see Figure 2.4 (d)]. Note that this does *not* represent the trajectory of the PTIM. However this spin configuration can be considered as a valid trajectory on classical bits and is represented by one of the terms on the right side of Equation (2.32).

The procedure shown in Figure 2.4 associates terms on both sides of Equation (2.32) in pairs. The evaluation functions in both terms of a pair must be equal

$$f^{\text{qm}}(\mathcal{T}^{\text{qm}}; \mathcal{D}(S^{\text{p},r})) = f^{\text{bi}}(\mathcal{T}^{\text{bi}}; \mathcal{D}(S^{\text{p},r})) \quad (2.33)$$

because the initial cluster behaves classically. Since it is also $|S_{\text{red}}^{\text{p}}| = |E_{\text{red}}^{\text{p}}|$, both terms have the same value overall, and the sums must be equal. Thus, in this case Equation (2.32) holds true.

2. *Cluster does not survive.* If the sampling of the patterns E^{p} and S^{p} does not allow for the initial cluster to survive, the quantum mechanical evaluation will always return $f^{\text{qm}}(\mathcal{T}^{\text{qm}}; \mathcal{D}(S^{\text{p},r})) = 1/2$. Furthermore, it is $|S_{\text{red}}^{\text{p}}| = |E_{\text{red}}^{\text{p}}| - 1$.²⁷ We insert those relations into Equation (2.32) and obtain

$$\sum_{S_{\text{red}}^{\text{r}}|_{E^{\text{p}}, S^{\text{p}}}} \left(\frac{1}{2}\right)^{|S_{\text{red}}^{\text{p}}|} \cdot \frac{1}{2} = \sum_{\tilde{E}^{\text{p}} \subseteq E_{\text{red}}^{\text{p}}} \left(\frac{1}{2}\right)^{|S_{\text{red}}^{\text{p}}|+1} f^{\text{bi}}(\mathcal{T}^{\text{bi}}; \mathcal{D}(S^{\text{p},r})). \quad (2.34)$$

The left sum samples all possible measurement results on the pattern $S_{\text{red}}^{\text{p}}$. This is equivalent to sampling all subsets of a set with cardinality $|S_{\text{red}}^{\text{p}}|$. The right sum samples

²⁵On the percolation grid in Figure 1.5, we now associate every node on the global percolation cluster with a spin orientation. This illustrates the difference between qubit clusters [which can only move forward in time, see Figure 2.4 (b)] and percolation clusters which know no temporal direction.

²⁶This is always possible because every local cluster [represented by missing gray plaquettes in Figure 2.4 (c)] preserves its own parity in the x -direction. The last measurement which destroys a local cluster is always deterministic. If multiple error measurements destroy a single cluster in one time step it is unclear which one of them had a predetermined result. Any choice is valid here.

²⁷There is one additional non-deterministic error measurement compared to the previous case. This is the error that destroys the initial cluster and determines the global parity $X_1 \cdots X_L$ of the system.

all possible bit flip patterns from the pattern $E_{\text{red}}^{\text{p}}$ which is equivalent to sampling all subsets of a set with cardinality $|E_{\text{red}}^{\text{p}}|$. Thus the right sum has twice as many terms.²⁸ For every quantum trajectory, there exist two classical trajectories and half of them are evaluated as $f^{\text{bi}}(\mathcal{T}^{\text{bi}}; \mathcal{D}(S^{\text{p},r})) = 1$. For the other half of the classical trajectories, the evaluation function vanishes. Therefore, Equation (2.32) holds in this case too.

This proves the relation $\langle\langle f_{\mathcal{D}}^{\text{qm}} \rangle\rangle_{\text{qm}} = \langle\langle f_{\mathcal{D}}^{\text{bi}} \rangle\rangle_{\text{bi}}$ independently of the decoder \mathcal{D} . As a consequence, the performance of any decoder \mathcal{D} can be evaluated on either the PTIM or on the classical model of bits. \square

2.4 Decoding with Majority Voting

In this section, we introduce a first attempt \mathcal{D}_{MV} based on majority voting, to decode the PTIM. This decoding algorithm will ultimately fail to restore the encoded quantum information and yield a decoding threshold $p_{\text{th}} = 0$ for all $q > 0$. It does however serve as a good introduction and illustrates very well what approach must be taken to implement successful error correcting schemes on the PTIM. The lessons learned here will motivate the more sophisticated decoders discussed in Sections 2.5 and 2.6.

2.4.1 Algorithm

We aim to implement an algorithm that tracks the state of the system through time by assuming the most likely state in every step. First, we consider the special case $q = 0$, where in every time step *all* syndromes are measured. Errors occur with probability $p \in (0, 1)$. This is the more “common” situation of quantum error correction, where a state may be corrected repeatedly after every time step. To destroy the initial cluster in this scenario, all L error measurements must be performed in a single time step. The probability p^L for this to occur in a single step is exponentially suppressed. Overall, the probability for the initial cluster to be destroyed is $1 - (1 - p^L)^T$, which is also suppressed at $L \propto T$.²⁹ In any other case, a decoder *can* be successful. It is straightforward to see that any projective error measurement results in an effective qubit flip with probability 1/2, after the subsequent syndrome measurements projected the state back into the z -basis. Here the classical picture we introduced in Subsection 2.3.3 actually represents the real trajectory and our problem is reduced to a repetition code with multiple time steps as introduced in Section 2.2 (the flip rate is $p/2$ instead of p ; with $p < 1$, flips are *unlikely* to occur). Given the initial state $|\Psi_0\rangle = |\mathbf{0}\rangle$, every round of syndrome measurements projects the state into a product state polarized in the z -direction of the form $|\Psi(t)\rangle = |\mathbf{m}_t\rangle$. We can now implement the majority voting decoder introduced in Section 2.2: To compute the final correction operator we split

²⁸In this case the procedure in Figure 2.4 fails after the initial cluster is destroyed. The final time step can thus be associated with two possible bit configurations which both obey all syndromes.

²⁹At large L with $p < 1$ it is $p^L \ll 1/L$ and thus $(1 - p^L)^L = \exp[L \cdot \log(1 - p^L)] \approx \exp[-Lp^L] \rightarrow 1$.

$C = \prod_{t=1}^T C_t$ into corrections C_t to (hopefully) correct the qubit flips that occurred in time step t . C_t is computed by comparing the syndromes S_t^r in the corresponding time step with the syndromes S_{t-1}^r from the previous step. The complete syndrome measurements allow for only two possible flip patterns and thus two possible corrections $\{C_{t,1}, C_{t,2} = \bar{C}_{t,1}\}$. The decoder chooses the operator C_t which corresponds to the more likely time step t ; i.e., the correction operator which performs fewer flips (remember $p/2 < 1/2$). This is the premise of the *majority voting decoder* (MVD) $\mathcal{D}_{\text{MV}}(S^{\text{p,r}})$ which we implement here: The algorithm finds the most likely qubit configuration for every single time step. In the following we will generalize the MVD to finite failure rates $q > 0$, where some syndromes are not measured.

With missing syndromes, we still choose the same approach, where a correction C_t is chosen for every time step and $\mathcal{D}_{\text{MV}} = C = \prod_{t=1}^T C_t$. However with every missing syndrome, the number of possible flip patterns in a time step multiplies by two. Thus this lack of knowledge amounts to an enlarged set of consistent corrections $C_t \in \{C_{t,1}, C_{t,2}, C_{t,3}, \dots\}$. To construct this list, we define the qubit configuration assumed by the decoder in the previous time step $\tilde{\mathbf{m}}_{t-1} = \prod_{\tau=1}^{t-1} C_\tau |\mathbf{0}\rangle$. This allows us to find all operators $C_{t,k}$ such that the state $|\tilde{\mathbf{m}}_{t,k}\rangle = C_{t,k} |\tilde{\mathbf{m}}_{t-1}\rangle$ is consistent with the syndromes S_t^r . The MVD then chooses the correction operator $C_{t,k}$ with the fewest flips. This defines the decoding algorithm $\mathcal{D}_{\text{MV}} : S^{\text{p,r}} \mapsto C = \mathcal{D}_{\text{MV}}(S^{\text{p,r}})$. In the following, we will assess the performance of this decoder.

2.4.2 Results

We evaluate the performance of the majority voting decoder by computing the MTFE T_{MV} as a function of the system size L . Figure 2.5 (a) shows the result for the parameters $p = q = 0.2$ and for system sizes up to $L = 501$. To avoid small even-odd effects, only odd sizes L are shown here. The data demonstrates that the MTFE does clearly *not* scale super-polynomially with L . Thus, at these parameters $p = q = 0.2$ the decoder \mathcal{D}_{MV} *fails* to decode the PTIM. This is further illustrated by the decoding probability P_{MV} for a fixed size L as shown in Figure 2.5 (b) (again for $p = q = 0.2$). The decoding probability approaches $P_{\text{MV}} \rightarrow 0.5$ at an approximately exponential rate with increasing T . We made similar observations for all parameters $p > 0$ and $q > 0$: In no parameter regime does the decoder \mathcal{D}_{MV} efficiently decode the PTIM. We note that in the case $q = 0$ the MVD *does* work and its performance can be calculated analytically. We show this in Section 2.B.

To illustrate *why* the MVD fails, we first consider a worst-case scenario shown in Figure 2.6 (a) for a system of size $L = 9$. The trajectory shown here only contains one single error measurement in the first time step (not known to the decoder). As only three syndromes were not measured, it is easy to see that the initial cluster occupies the full system after every time step — thus the system's state is a product state of the form $|\mathbf{m}_t\rangle$ at every step t . Circles indicate the state $|\tilde{\mathbf{m}}_t\rangle$ assumed by the MVD. In the first time step the leftmost syndrome returns the result -1 while the neighboring syndrome was not measured. The decoder must therefore choose between the states $|01\rangle$ and $|10\rangle$ for the first two qubits. Both options require one flip and the decoder incorrectly chooses $|01\rangle$, assuming the flip

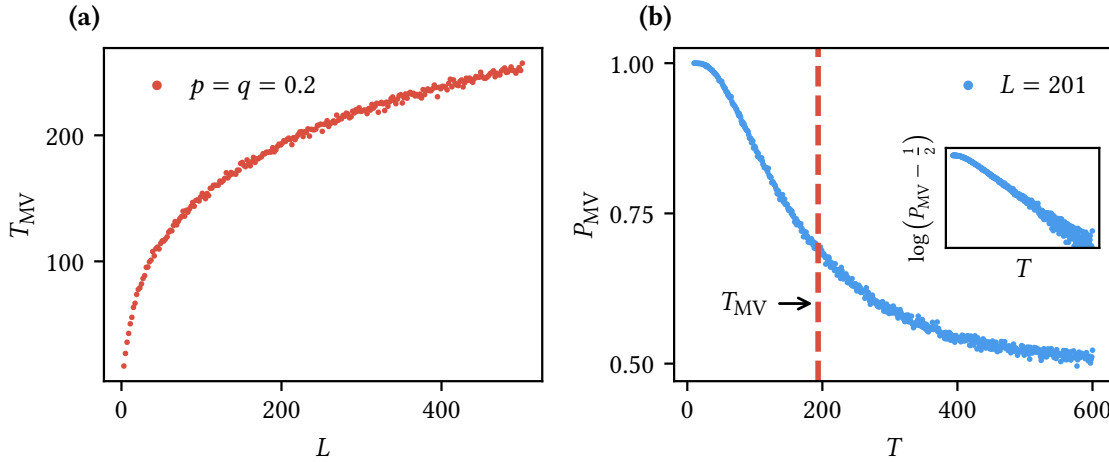


Figure 2.5 • Performance of the majority voting decoder on the PTIM. (a) Mean time to first failure T_{MV} for the MVD \mathcal{D}_{MV} at $p = q = 0.2$. Data points are averaged over $5 \cdot 10^3$ samples each. Only odd system sizes are shown here. (b) Decoding probability $P_{MV}(p, q; L, T)$ for the parameters $p = q = 0.2$ and $L = 201$ as a function of the maximum time T . Data points were averaged over 10^4 samples. The vertical red line indicates the MTF $T_{MV}(p, q; L)$ for the same parameters. The probability decays exponentially towards $P_{MV} \rightarrow 1/2$ (see inset).

to have occurred on the second qubit. On all other qubits, no flips are required. In the next step, the two leftmost syndrome measurements allow for the configurations $|100\rangle$ and $|011\rangle$ (consider only the three leftmost qubits). Compared to the previously predicted state $|010\rangle$, the latter requires fewer flips. This procedure is repeated until the last step, where all syndromes are measured. Crucially, only a single error occurred in the PTIM trajectory, but the decoder assumes that instead $L - 1 = 8$ errors occurred and returns the correction operator $C = X_2 X_3 \cdots X_9$. This points to the real weakness of the MVD: It minimizes the number of errors in every single time step, but not overall. The problem lies in our attempt to construct the correction as $C = \prod_t C_t$.

We do not need to rely on a worst-case scenario to understand this. Consider the syndrome measurements of a single time step S_t^p . The probability for two qubits to be connected via syndrome measurements decreases with their distance and increasing failure rate q . The average number of contiguous syndromes that are performed in a row is a characteristic length $\xi(q) = (1 - q)/q$. This length is finite and generally $\xi(q) \ll L$ for large systems.³⁰

On any time step t we can split the sites into groups such that all sites in a group are connected via syndromes. In a time step, the MVD guesses a configuration for every group of sites — in our picture in Figure 2.6 (a) we color these groups orange (if the decoder assumes an incorrect qubit configuration) or gray (if the decoder assumes the correct state).

³⁰Only in the case $q = 0$ it is $\xi(0) = L$ and the decoder can successfully decode the PTIM.

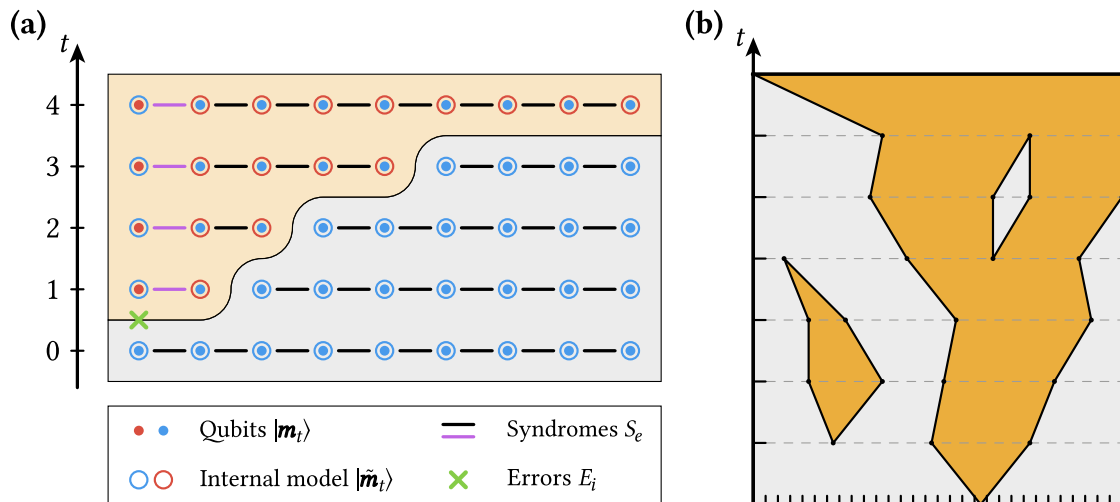


Figure 2.6 • Propagating mistakes in the MVD. (a) Example trajectory to illustrate how the MVD fails. We show the real qubit configuration $|m_t\rangle$ as points and the decoder's assumption $|\tilde{m}_t\rangle$ as circles. Note that in this trajectory, the state is a product state polarized in the z -direction $|m_t\rangle$ at all times t . This is a worst-case scenario, only one single error occurs in the system but the decoder $\mathcal{D}(S^{\text{p},\text{r}})$ proposes the (incorrect) correction operator $C = X_2 X_3 \cdots X_9$. Background colors indicate the region in which the decoder assumes an incorrect state. (b) Sketch of a more general scenario with many qubits. Orange regions indicate qubits on which the MVD guesses an incorrect state. Boundaries between gray and orange regions that are not near other boundaries, perform random walks in the system along edges where no syndromes were measured. Thus large regions may grow or shrink randomly. In the final time step, all syndromes are measured and the regions must combine into a single color.

Boundaries of these regions always coincide with missing syndromes. Now consider an orange region. If this region is small in comparison with $\xi(q)$, it is likely that the region and its surroundings will be connected by syndromes in the next time step and the decoder corrects its mistake. If however the orange region is large in comparison with $\xi(q)$, then the left and right boundary of the region are unlikely to be “correlated” by syndromes in the next step. This allows us to understand the dynamics of region boundaries in the system. Consider the illustration shown in Figure 2.6 (b). Here we only show the regions of correct and incorrect guesses of the decoder in a large system. Whenever the MVD makes a local mistake, an orange region appears. The boundaries between orange and gray regions will now propagate through time in one of two ways:

1. If the distance between two boundaries is small, they may combine. This may close an orange region and amount to the MVD correcting its previous mistake. The same mechanism may also close a gray region and thus have the opposite effect.

2. If a boundary does not combine with a second one [which is impossible if regions are much larger than $\xi(q)$], they must still move along a path of missing syndromes. There is no preferred direction to the trajectory of a boundary; it performs a random walk in one dimension. The boundary is therefore expected to move a distance of order $\sim \sqrt{t_{\text{steps}}}$. In large systems with many time steps, boundaries are thus expected to travel large distances until gray areas are not predominant anymore and the MVD fails.

Note that Figure 2.6 (b) ignores qubits that are not part of the initial cluster; those would be impossible to assign to a gray or orange region. If the initial cluster survives a trajectory, all other Bell clusters are local, and are not expected to affect the “coarse-grained” dynamics. If the initial cluster does not survive, the decoder fails either way. Remembering Equation (2.22), we may also resolve this by assuming a classical trajectory. Then there exists no concept of clusters, and every bit belongs either to a gray or an orange region at all times.

Connection to the Classical Ising Model

When considering the MVD from the perspective shown in Figure 2.6 (b), a deeper connection to the classical one-dimensional Ising model without a transversal field [109] arises. We review this model very shortly to illustrate its relation to our problem. Consider an infinite chain of spins $s_i \in \{\pm 1\}$ with nearest-neighbor interactions and a Hamiltonian

$$H_I = -J \sum_i s_i s_{i+1}. \quad (2.35)$$

In the ferromagnetic case, it is $J > 0$. At temperature $T = 0$, the system will assume one of the two ground states with all spins s_i being aligned in either direction. Now assume a finite temperature $T > 0$. Excitations in the form of single flipped spins will occur in an infinite chain. Crucially – with no external magnetic field – the energy cost of flipping a spin originates not from the spin itself, but from the interactions with the neighboring spins. With left and right neighbors, the cost is $\Delta E = 4J$. Flipping an additional spin next to the first one does not cost any additional energy. Thus we can consider *clusters* of spin orientations. Creating a cluster comes at an energetic cost but it may then grow indefinitely. In a statistical setting at finite temperatures, clusters arise in the Ising chain and their boundaries (“domain walls”) move freely in any direction, i.e., perform random walks. This is exactly the picture we show in Figure 2.6 (b) – and the reason why the one-dimensional Ising model does not exhibit a phase transition at finite temperatures [109, 110]. In other words: At $q > 0$, the MVD models a one-dimensional Ising chain at finite temperature; and it fails for the same reason that the Ising chain exhibits no phase transition at finite temperatures.³¹

Now consider the Ising model on a two-dimensional square lattice, where every spin has 4 neighbors. Again, an excitation at finite temperatures may take the form of a single flipped spin – here now at the energetic cost $\Delta E = 8J$. As before, this energy comes from

³¹Put simply: the MVD fails because there is no spontaneous magnetization in one dimension.

the boundary around a region of flipped spins, but in two (or more) dimensions there is an important difference: Flipping additional neighboring spins does increase the boundary (“surface”) of the cluster. Thus, the boundaries of clusters of flipped spins in two dimensions act as “rubber bands” in order to reduce the system’s energy. As a consequence, there is a phase transition in the two-dimensional Ising model [110–113] at the finite Curie temperature.

These insights point us towards a new approach to create a better decoder for the PTIM. By considering a trajectory in $1 + 1$ dimensions, we can make use of mechanisms reminiscent of the two-dimensional Ising model. In the following, we will describe a decoder for the PTIM which aims to minimize the number of qubit flips over *all* time steps, instead of doing it for every step individually.

2.5 Decoding with Minimum Weight Perfect Matching

In this section, we discuss a decoder that considers the $1+1$ -dimensional space-time trajectory of the PTIM in its entirety and uses the recorded syndrome data $S^{p,r}$ to find the possible error pattern E^p with the minimal number of measurements.³² The error pattern is subsequently used to choose one of the correction operators $\{C, \bar{C}\}$. Our algorithm is inspired by a *minimum weight perfect matching* (MWPM) procedure, which was previously successfully applied to the two-dimensional surface code [85, 92, 114]. The idea is to interpret the $1 + 1$ -dimensional trajectory of the PTIM as a single time step in an anisotropic two-dimensional surface code. Note however that the typical setup of a noisy surface code considers unitary Pauli errors, while in the PTIM, all errors are projective measurements.

An MWPM decoder for the PTIM was first realized by Li and Fisher in Ref. [115]. This work was done in parallel and independently of the work we present here and in Ref. [64]. We are able to qualitatively verify their results; however, our algorithm is able to achieve a higher error threshold. This suggests that our decoder is implemented slightly differently.³³

2.5.1 Algorithm

We show the algorithm for the minimum weight perfect matching decoder $\mathcal{D}_{\text{MWPM}}(S^{p,r})$ in Figure 2.7. This subsection will only describe *how* the decoder works. We will provide an intuition for *why* it works and *what* it really does in Subsection 2.5.2.

Consider a single PTIM trajectory \mathcal{T}^{qm} as shown in Figure 2.7 (a). As a first step, we introduce the lattice \mathcal{L} as a more simplified representation of the trajectory [see Figure 2.7 (b)]. We use colors to represent the results of the syndrome measurements. (We already used the

³²This directly addresses the issue of the MVD illustrated in Figure 2.6 (a).

³³Interestingly, the simulations in Ref. [115] were also performed using the classical circuit we describe in Subsection 2.3.3 – an approach they verified numerically. In this thesis (and in Ref. [64]), we were able to provide a rigorous proof for Equation (2.22).

same representation in Figure 2.4.) The decoder $\mathcal{D}_{\text{MWPM}}$ has only partial information about a trajectory, i.e., it does not know about the initial state and the error measurements. The decoder's input is thus a reduced version of the lattice \mathcal{L} , as shown in Figure 2.7 (c).

The decoding algorithm is split into three steps. First, the PTIM syndromes are mapped to an abstract problem in graph theory. This problem — a minimum weight perfect matching — is then solved. Finally, the solution is mapped back to the PTIM and used to decide which correction operator (C or \bar{C}) should be returned. We will now describe these steps in detail.

1. We identify the endpoints of syndrome measurements with result -1 in the lattice in Figure 2.7 (c) and mark them with *nodes* (blue disks). These will be the nodes of our graph. We now delete all measurement results from the lattice such that the only remaining lines represent missing syndrome measurements. We add horizontal lines spanning the full system, which represent possible locations for error measurements. The resulting picture is shown in Figure 2.7 (d). To allow for our open boundary conditions, we add more boundary nodes which are represented in gray and are located at the ends of the horizontal lines. If the total number of nodes is odd, an additional node is added outside the lattice.

Figure 2.7 (d) is a simplified representation of a weighted graph \mathcal{G} . The nodes we show here are the nodes of \mathcal{G} . Graph edges are constructed by considering all pairs of nodes:

- a) If both nodes are boundary nodes, they are connected in \mathcal{G} by an edge to which we assign the weight 0.
- b) If at least one of the nodes is not a boundary node, an edge between them exists if and only if there is a path between them in Figure 2.7 (d). The weight of this edge is the minimum number of horizontal steps that must be made to walk from one node to the other on lines in Figure 2.7 (d). Vertical steps that need to be taken do not add to the weight.

In Figure 2.7, we never show the full graph \mathcal{G} for our example trajectory as it would be much too large. Instead, we will work with the much simpler representation of \mathcal{G} on the lattice \mathcal{L} as shown in Figure 2.7 (d). For a full abstract graph conversion (using a smaller trajectory), we refer the reader to Section 2.C. Further, we note that using a naive approach, the construction of \mathcal{G} is generally the most costly part of the decoding algorithm. However, significant performance improvements can be made. We expand on this in Subsections 2.C.1 and 2.C.2.

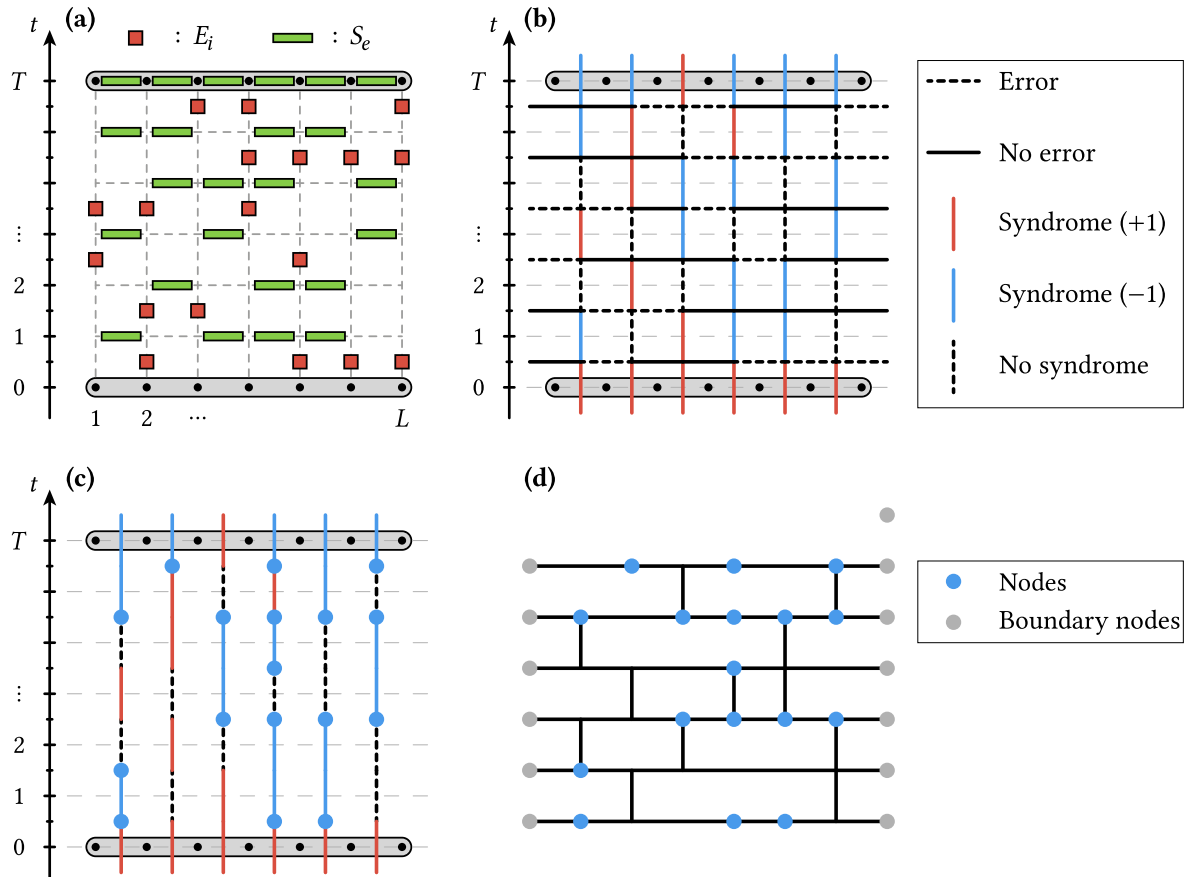
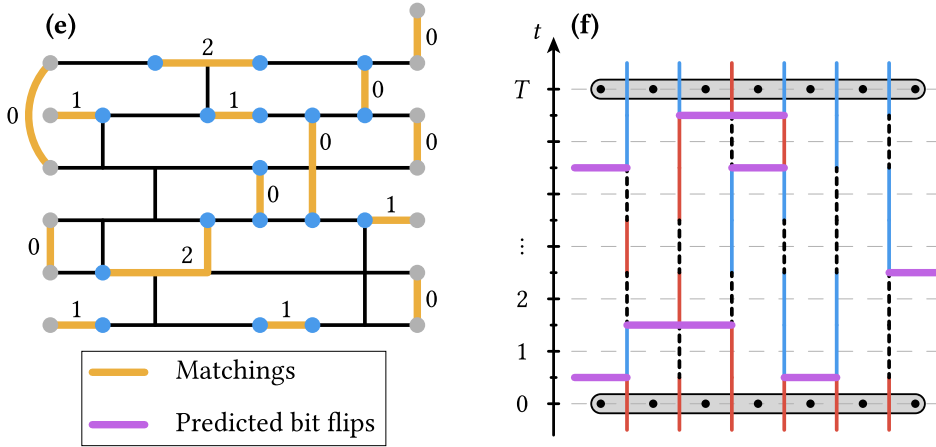


Figure 2.7 • Minimum weight perfect matching on the PTIM. (a) Patterns E^P and S^P of a sample PTIM trajectory. (b) The same trajectory visualized on a lattice \mathcal{L} , including the results of the syndrome measurements S^f . (c) Representation of the information $S^{P,r}$ passed to the decoder \mathcal{D}_{MWPM} . Nodes mark the endpoints of syndromes with result -1 (omitting the upper edge of the lattice). (d) Reduction of the lattice \mathcal{L} to an abstract graph of nodes. Edges are drawn on *all* horizontal lines of \mathcal{L} and *only* along vertical lines on which no syndrome was measured. Boundary nodes are added at the left and right boundaries of the system. An additional boundary node is added outside the system if the total number of nodes is odd. All boundary nodes are connected via edges that are not shown here. \curvearrowright



↪ (e) MWPM on the graph shown in (d). All nodes are matched in pairs along edges of the graph. Every matched edge is assigned a weight, which is the number of horizontal steps in the edge (edges connecting boundary nodes have weight 0). The matching is chosen such that the total weight is minimized. (f) Matched edges are interpreted as “bit flips” on the lattice \mathcal{L} . The correction operator is chosen accordingly – here it is $\mathcal{D}_{\text{MWPM}}(S^{\text{p},r}) = X_2 X_5 X_7$.

2. A *matching* on a graph is a subset of its edges such that some of the graph nodes are paired to exactly one other node. A *perfect matching* is given by pairwise connections of *all* nodes along edges.³⁴ On the graph \mathcal{G} , we perform a *minimum weight perfect matching* – which is the perfect matching minimizing the total weight of all matched edges. We show such an MWPM for our example in Figure 2.7 (e) – numbers represent the weights of the matched edges.

Importantly, minimum weight perfect matchings can be computed efficiently using the *Blossom algorithm* introduced by Edmonds in Ref. [116]. We use an optimized modern implementation of this algorithm by Kolmogorov, known as *Blossom V* [117].

Note that a perfect matching does not necessarily exist for any graph. The construction we described in the previous step is explicitly chosen such that a perfect matching always exists for any physical trajectory \mathcal{T}^{qm} .

3. Finally, the MWPM is transferred to the lattice \mathcal{L} and used to determine the correction operator C returned by the decoder $\mathcal{D}_{\text{MWPM}}$. To do so, we interpret every horizontal step on a matching in Figure 2.7 (e) as a bit flip in a (classical) PTIM trajectory [see Figure 2.7 (f)]. On every qubit i , the number of flips is counted. The correction string is chosen to make the number of flips on every qubit even. In our example, the decoder returns the correction string $\mathcal{D}_{\text{MWPM}}(S^{\text{p},r}) = X_2 X_5 X_7$.

³⁴No node may be matched with more than one other node.

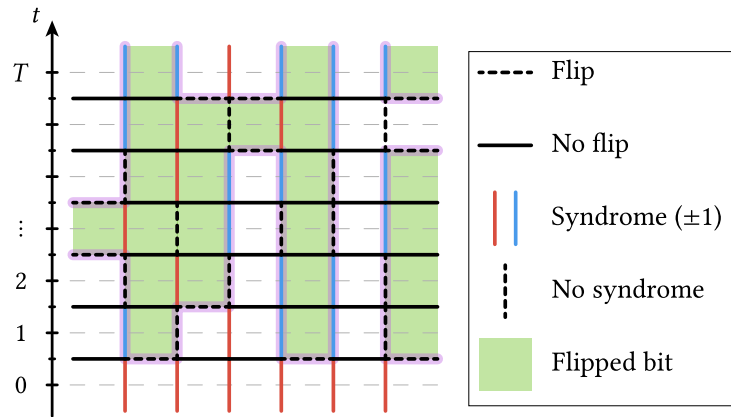


Figure 2.8 • Classical bit-flip trajectory on the lattice \mathcal{L} . Regions of flipped bits are always encircled by blue and dashed lines, i.e., by flips on horizontal edges and negative (or missing) syndromes on vertical edges. Boundaries of flipped regions thus emerge as loops (marked in purple). The MWPM decoder finds such loops and minimizes the total number of bit flips (as bit flips are unlikely $p/2 < 1/2$).

2.5.2 Interpretation of the MWPM Decoder

To understand *how* the MWPM decoder $\mathcal{D}_{\text{MWPM}}$ works, we make use of Equation (2.22) and consider it from the perspective of the classical bit-flip model introduced in Subsection 2.3.3, i.e., we imagine that the decoder’s input shown in Figure 2.7 (c) was generated by a classical trajectory. A scenario of this kind is shown in Figure 2.8. Regions of flipped spins are bound by flips on horizontal edges in the lattice \mathcal{L} and negative syndromes on vertical edges (or missing syndromes that would have yielded the result -1). The perfect matching step in the MWPM decoder connects the endpoints of blue lines either to other endpoints or to the system boundary (via boundary nodes). It thus creates loops (marked in purple in Figure 2.8) in the picture which encircle predicted regions of flipped bits. Any such loop configuration represents a valid classical trajectory where the predicted bit flips produce the recorded syndromes. An MWPM finds the loop configuration with the smallest possible number of bit flips. As bit flips in the classical model are unlikely ($p/2 < 1/2$), the decoder $\mathcal{D}_{\text{MWPM}}$ predicts the *most likely classical trajectory* \mathcal{T}^{bi} which can generate the observed syndromes.

Note that the decoder does not necessarily assume that the most likely trajectory \mathcal{T}^{bi} really occurred in the system (in fact, the probability for a single bit flip pattern $P(\tilde{E}^{\text{P}}|S^{\text{p},r})$ matching the observed syndromes is exponentially small) — instead it assumes that the real (classical or quantum mechanical) trajectory is corrected by the same correction operator C as the most likely classical trajectory.

Since the classical and quantum mechanical models are of course related, we can now also interpret the decoder $\mathcal{D}_{\text{MWPM}}$ from a PTIM perspective. A syndrome can only change its sign if an error measurement was performed on one of the neighboring qubits.³⁵ The

³⁵Here our hand-wavy interpretation of an error measurement as a “possible bit flip” serves us well.

bit flip pattern \tilde{E}^p predicted by the decoder also represents a possible error measurement pattern E^p for a quantum trajectory \mathcal{T}^{qm} that can produce the observed syndromes. Here, the decoder finds the error pattern with the smallest possible amount of errors. If $p < 1/2$, this represents the most likely PTIM trajectory \mathcal{T}^{qm} that could have occurred given the observed syndromes.

As noted before, the approach we take here is very similar to typical decoding approaches for topological quantum memories like the surface code [84, 85, 87]. In these systems, decoders are used to match (fuse) pairs of anyonic excitations with a minimal amount of unitary errors. It has been demonstrated that algorithms based on minimum weight perfect matching successfully decode the surface code [92, 114]. Thus, we can also understand $\mathcal{D}_{\text{MWPM}}$ on the PTIM as an anisotropic version of the surface code with unusual boundary conditions [87].

2.5.3 Results

We first analyze the performance of the decoder $\mathcal{D}_{\text{MWPM}}$ by computing the decoding probability $P_{\text{MWPM}}(p, q; L = T)$ for $L = T = 51$. The result shown in Figure 2.9 demonstrates that there exists a finite region in the parameter space (p, q) where the decoder succeeds.³⁶ Our prediction that decoding in the disentangling phase must fail is verified here, as the region is fully contained within the finite-size percolation threshold (cf. Figure 2.3). Note however that the region where the decoder succeeds is clearly smaller than the entangling phase, i.e., there exists a finite regime where the quantum information survives the PTIM trajectory but cannot be restored by the decoder. The decoding transition separates the region where the decoder succeeds ($P_{\text{MWPM}} \approx 1$) and the region where it fails ($P_{\text{MWPM}} \approx 1/2$). At $L = T = 51$, this transition appears smeared out — this is a finite-size effect. We verified that the transitions sharpens with increasing system size.

In some parameter regimes, we observe a finite-size effect that also shifts the decoding transition. For the trivial case without errors ($p = 0$), we expect the decoder to perform with perfect accuracy (there can never be syndrome measurements with result -1 , and the graph \mathcal{G} in Figure 2.7 (d) only contains boundary nodes). Figure 2.9 verifies this expectation and shows that even at the point $p = 0, q = 1$, the decoder must always succeed. At vanishing failure rates $q = 0$, all stabilizers are always measured. In this case, the graph \mathcal{G} in Figure 2.7 (d) does not contain any vertical edges, and the lines must be matched separately. Here the MWPM decoder and the MVD become identical and the problem at hand reduces to a repetition code with multiple time steps. As shown in Figure 2.1 (c), the decoder should succeed at all $p < 1$ here.³⁷ Instead, Figure 2.9 shows that the decoder $\mathcal{D}_{\text{MWPM}}$ fails at $p \gtrsim 0.7$. In Section 2.B we show that this is a strong finite-size effect and demonstrate that our simulation data matches our analytical predictions. Note that here we observe a decoding transition that not only becomes sharper with increasing system size, but also shifts to larger error rates.

³⁶No such finite region exists for the MVD in Section 2.4.

³⁷Figure 2.1 considers bit flip errors and thus shows a threshold at $p = 1/2$. This corresponds to $p = 1$ in the error model of the PTIM.

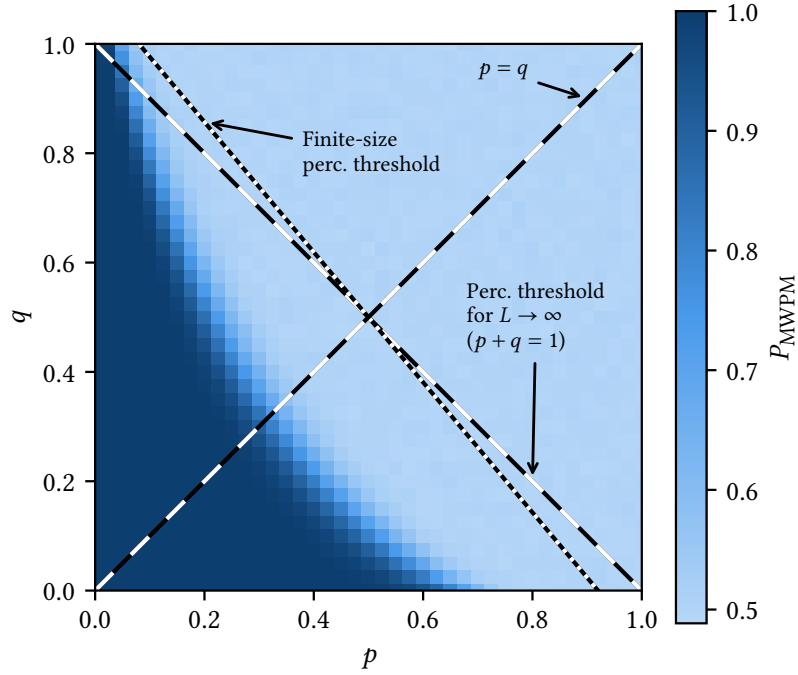


Figure 2.9 • Performance of the MWPM decoder. Decoding probability P_{MWPM} of the MWPM decoder $\mathcal{D}_{\text{MWPM}}$ as a function of the error rate p and the failure rate q . The data shown was computed for system sizes $L = T = 51$ and averaged over $2 \cdot 10^4$ sample trajectories. In the plot, the percolation threshold of the PTIM (for the thermodynamic limit $L = T \rightarrow \infty$ and for the finite size $L = T = 51$) from Figure 2.3 is indicated. This allows for a comparison of the decoding transition and the entanglement transition. The decoding phase is a proper subset of the entangling phase.

At the diagonal $p = q$, we find the finite-size shift of the decoding transition to be minimal. Thus, this case is well-suited for a more detailed scaling analysis. In Figure 2.10 (a), we show the decoding probability P_{MWPM} for different system sizes $L = T$. A clear crossing emerges (unlike the case $q = 0$) and the decoding probability approaches a step function in the limit $L = T \rightarrow \infty$. We use this crossing to estimate the decoding threshold at $p_{\text{thr}}^{\text{MWPM}} = q_{\text{thr}}^{\text{MWPM}} \approx 0.324$. Clearly, the decoding threshold is smaller than the percolation threshold $p_{\text{thr}}^{\text{MWPM}} < p_c = 1/2$. In the regime between these two transitions ($p_{\text{thr}}^{\text{MWPM}} < p = q < p_c$), the amplitudes of the logical qubit survive but cannot be recovered by the algorithm described in this section.³⁸

³⁸Take this statement with two caveats: Firstly, the decoder's performance is bound by the assumption that error measurements are not recorded (in contrast to the trivial case, cf. Figure 2.3). Secondly, it may technically still be possible to decode the PTIM in this region, just with a better decoder. We answer this question in Section 2.6.

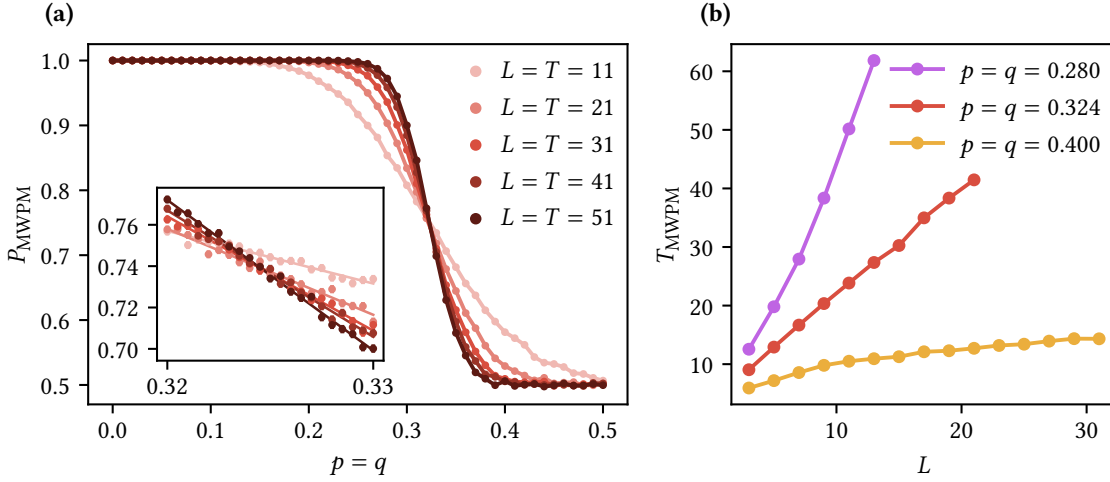


Figure 2.10 • Performance of the MWPM decoder at $p = q$. (a) Decoding probability P_{MWPM} on the diagonal $p = q$ for increasing system sizes $L = T$. Data points show averages over $5 \cdot 10^4$ sample trajectories; error bars are mostly smaller than the points shown. The decoding transition gets sharper with $L = T \rightarrow \infty$ and shows a negligible finite-size shift. The inset shows a finer view of the crossing with linear fits, indicating a decoding threshold at $p_{\text{thr}}^{\text{MWPM}} = q_{\text{thr}}^{\text{MWPM}} \approx 0.324$ (cf. the entanglement transition at $p_c = q_c = 0.5$). (b) Mean time to first failure T_{MWPM} as a function of the system size L at parameters in the decoding phase ($p = q = 0.280$), at the decoding threshold ($p = q = 0.324$), and in the region outside the decoding phase but inside the entangling phase ($p = q = 0.400$). Data points show averages over $5 \cdot 10^3$ sample trajectories. In the decoding phase, the MTFE scales exponentially with L .

To further verify the existence of a decoding transition, we evaluate the mean time to first failure T_{MWPM} in Figure 2.10 (b). Here we show three points on the diagonal $p = q$. Below the decoding threshold ($p = q = 0.280$), we observe a scaling behavior of the MTFE which is consistent with an exponential growth with L .³⁹ On the decoding transition ($p = 0.324$) the MTFE seems to grow algebraically ($T_{\text{MWPM}} \sim L^\alpha$ with $\alpha \approx 1$). Finally, we show a point outside the decoding phase but within the entangling phase of the PTIM ($p = 0.400$). Here the MTFE scales sub-algebraically with the system size [$T_{\text{MWPM}} \sim \log(L)$].

Our findings demonstrate that the PTIM *can* be decoded in some parameter regimes, even though our decoders only have partial knowledge of the system's trajectory (only syndromes are recorded). We note that our decoding threshold $p_{\text{thr}}^{\text{MWPM}} \approx 0.324$ is considerably higher than the threshold reported by Li and Fisher in Ref. [115] ($p_{\text{thr}}^{\text{MWPM}} \approx 0.26$). We are unable

³⁹In this regime, the MTFE grows very quickly and we can only calculate its value for small systems L – this makes it difficult to determine the scaling behavior with high confidence.

to comment on this difference and can only suspect differences in how the algorithms treat the system boundaries. Nonetheless, the existence of a finite decoding threshold is the key takeaway here. In the following, we will take on the last remaining question: Is there a parameter regime in which the amplitudes of the logical qubit survive, but the quantum information *cannot* be recovered reliably? To tackle this problem, we will need to implement the best possible decoder.

2.6 Maximum Likelihood Decoding

The previous considerations have shown that our PTIM error correcting code with errors E_i and syndromes S_e can be decoded with a finite decoding threshold $p_{\text{thr}}^{\mathcal{D}}$. Now we aim to find the upper limit to this threshold. A decoder that reaches this upper bound is called a *maximum likelihood decoder* (MLD). By definition, an MLD returns the correction operator C which is most likely to recover the logical qubit given the recorded syndrome data. The MLD is the best possible decoder and maximizes the decoding probability

$$P_{\text{MLD}}(p, q; L, T) = \sup_{\mathcal{D}} P_{\mathcal{D}}(p, q; L, T). \quad (2.36)$$

The difference to the MWPM decoder is clear: An MLD does not find the most likely trajectory \mathcal{T} , but instead considers *all* possible trajectories (given the syndrome data) and determines the right correction operator for each of them. All trajectories (in which the quantum information survives) can be grouped into two classes, one for each correction operator C and \bar{C} . For each class, we define the probability

$$P_{f^{\text{qm}}}^{\text{qm}}(C|S^{\text{p},r}) := \sum_{\mathcal{T}^{\text{qm}}|_{S^{\text{p},r}}} P^{\text{qm}}(\mathcal{T}^{\text{qm}}) \cdot f^{\text{qm}}(\mathcal{T}^{\text{qm}}; C) \quad (2.37)$$

where the summation is restricted to PTIM trajectories $\mathcal{T}^{\text{qm}}|_{S^{\text{p},r}}$ with the syndrome $S^{\text{p},r}$.⁴⁰ Here, the evaluation function f^{qm} essentially sorts trajectories into classes (if a trajectory cannot be decoded, it contributes to both classes). Note that, as we only sum over a small subset of all possible trajectories, it is usually $P_{f^{\text{qm}}}^{\text{qm}}(C|S^{\text{p},r}) + P_{f^{\text{qm}}}^{\text{qm}}(\bar{C}|S^{\text{p},r}) \ll 1$. An MLD returns the correction operator C , which maximizes Equation (2.37). This reveals one major difference between an MLD and some other decoders like the MWPM decoder we described in Section 2.5: To calculate the probabilities $P_{f^{\text{bi}}}^{\text{bi}}(C|S^{\text{p},r})$, the error rate p must be known. The decoder $\mathcal{D}_{\text{MWPM}}$ does not require this knowledge.

In most quantum error correcting codes, performing the sum in Equation (2.37) is technically straightforward but exponentially expensive as the number of terms diverges. Therefore, it is usually unknown how an MLD can be implemented efficiently. In this section, we demonstrate an algorithm that solves this problem on the PTIM.

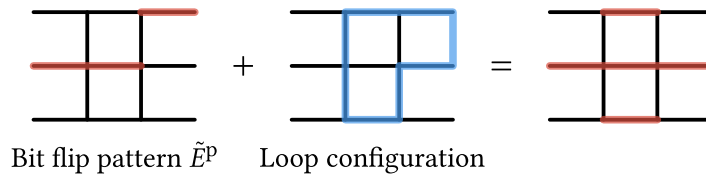
⁴⁰Equations (2.36) and (2.37) are not specific to the PTIM but describe MLDs for any error correcting code. In other codes, the probabilities and evaluation functions are different, and there might be more than two possible correction operators to consider.

2.6.1 Algorithm

Recently, an efficient implementation for a maximum likelihood decoder on the surface code was found by Bravyi et al. [91]. They discovered a relation between the probability in Equation (2.37) and an abstract matchgate quantum circuit, which can then be simulated efficiently (see Subsection 1.2.2).⁴¹

In Section 2.5, we already indicated that the 1 + 1-dimensional PTIM shares some features with the two-dimensional surface code. In fact, the basic principle behind the algorithm described in Ref. [91] might look familiar: A single error pattern on the surface code corresponds to a correction operator C . Now add any closed loop configuration on top of the error pattern — such that wherever two active edges coincide, they cancel out (a “modulo 2 loop addition”). The result is a completely new error pattern which belongs to the same equivalence class as the original one (as it corresponds to the same correction operator). The full equivalence class for C is generated by finding all possible closed loop configurations and adding each one to some error pattern.⁴²

The surface code model considered in Ref. [91] assumes unitary bit flip errors. Thus, the principle of adding loops to find new trajectories in the same equivalence class is also applicable to the classical bit model we describe in Subsection 2.3.3. Bit flips only occur on horizontal edges in our lattice \mathcal{L} . Consider any given bit flip pattern \tilde{E}^p and some loop configuration. A new error pattern on the lattice \mathcal{L} is generated as follows:



Note that not all loop configurations are created equal, i.e., there is a probability for each of them. In particular, some loop configurations generate error patterns that correspond to the same correction operator but are forbidden as they do not comply with the recorded syndrome measurements. This will be taken into account in the algorithm of the MLD.

Implementation

We implement the MLD for the PTIM as follows:

1. We introduce the classical model with random bit flips. An MLD \mathcal{D}_{ML}^{bi} for this model is constructed to choose the correction operator that maximizes the probability $P_{f^{bi}}^{bi}(C|S^{p,f})$ [the classical equivalent of Equation (2.37)]. We then prove that the

⁴¹There is not necessarily a physical interpretation for this matchgate quantum circuit — in fact, the matchgates used here are not even unitary gates.

⁴²This is a very rough simplification of the procedure described in Ref. [91] and relating the loop configurations to matchgates is highly nontrivial. Furthermore, Bravyi et al. implemented a particularly efficient algorithm to simulate matchgates — different from what we describe in Subsection 1.2.2 — and provide some crucial details on how the numerical stability of the algorithm can be improved.

decoder $\mathcal{D}_{\text{ML}}^{\text{bi}}$ performs as well as the MLD $\mathcal{D}_{\text{ML}}^{\text{qm}}$ for the quantum mechanical PTIM [which maximizes a very different probability $P_{f_{\text{qm}}}^{\text{qm}}(C|S^{\text{p},r})$].

2. For both possible correction operators, the probabilities $P_{f_{\text{bi}}}^{\text{bi}}(C|S^{\text{p},r})$ of the classical model are calculated efficiently using a slightly adjusted version of the algorithm by Bravyi et al. [91]. The decoder returns the correction operator with the higher probability.

We shortly review the classical process, which we indicate with the superscript bi here (see also Subsection 2.3.3): A chain of L classical bits in the state 0 is prepared. Every time step includes two substeps. First, every individual bit is flipped with probability $p/2$, then syndromes are measured on neighboring pairs of bits with probability $1 - q$. The bit flip pattern \tilde{E}^{p} records all flips and the syndromes are recorded with their results $S^{\text{p},r}$. A trajectory of this kind is shown in Figure 2.8.

It is straightforward to adapt Bravyi's algorithm to this classical stochastic process. This allows us to calculate the probabilities $P_{f_{\text{bi}}}^{\text{bi}}(C|S^{\text{p},r})$ in an algorithm with a runtime $\mathcal{O}(L^4)$ (assuming $L = T$). The decoder $\mathcal{D}_{\text{ML}}^{\text{bi}}$ returns the correction operator that maximizes this probability. In Section 2.D, we explicitly show how the algorithm for the surface code is adjusted to decode the PTIM.

Now we have an MLD for the classical system. The equivalence between this and the PTIM [remember Equation (2.22)] allows us to rigorously prove that it is

$$P_{f_{\text{qm}}}^{\text{qm}}(C|S^{\text{p},r}) = P_{f_{\text{bi}}}^{\text{bi}}(C|S^{\text{p},r}), \quad (2.38)$$

i.e., an MLD for the PTIM $\mathcal{D}_{\text{ML}}^{\text{qm}}$ would find the exact same probabilities as the classical MLD $\mathcal{D}_{\text{ML}}^{\text{bi}}$ and thus returns the same correction operator. The proof for Equation (2.38) is rather lengthy and technical and we relegate it to Section 2.E. It is however possible to form the slightly weaker statement

$$\left\langle\left\langle f_{\mathcal{D}_{\text{ML}}^{\text{qm}}}^{\text{qm}} \right\rangle\right\rangle_{\text{qm}} = \left\langle\left\langle f_{\mathcal{D}_{\text{ML}}^{\text{bi}}}^{\text{qm}} \right\rangle\right\rangle_{\text{qm}} \quad (2.39)$$

which is sufficient in our context. If Equation (2.39) is true, then the decoder $\mathcal{D}_{\text{ML}}^{\text{bi}}$ performs just as well as $\mathcal{D}_{\text{ML}}^{\text{qm}}$ when being applied to quantum trajectories. Thus, we may as well define $\mathcal{D}_{\text{ML}}^{\text{qm}} := \mathcal{D}_{\text{ML}}^{\text{bi}}$ from now on. In the following, we show a proof for Equation (2.39), which is much easier compared to the proof of Equation (2.38).

Proof for Equation (2.39)

First, we provide some initial thoughts. Consider two discrete variables $A \in \{A\}$ and $B \in \{B\}$, a function $P(B) \geq 0 \forall B$ and a function $f(A; B)$. Then the following relation holds

$$\sup_A \left[\sum_B P(B) f(A; B) \right] \leq \sum_B P(B) \sup_A [f(A; B)] \quad (2.40)$$

with the sum over all $B \in \{B\}$ and the supremum over all $A \in \{A\}$.

Let now $A(B)$ be a function out of the set of all functions that take the values B as input. Then the supremum does reach its upper bound

$$\sup_A \left[\sum_B P(B) f(A(B); B) \right] = \sum_B P(B) \sup_A [f(A(B); B)] \quad (2.41)$$

as we can construct a function $A(B)$, which for every value of B maximizes the function f (independently of the form of f). Equation (2.41) will be useful later.

Now onto the proof of Equation (2.39). Generally, the decoding probability of a decoder \mathcal{D} in a system α is calculated as the ensemble average⁴³

$$P_{\mathcal{D}}^{\alpha}(p, q; L, T) = \langle\langle f_{\mathcal{D}}^{\alpha} \rangle\rangle_{\alpha} \quad (2.42)$$

of the evaluation function f^{α} for many trajectories \mathcal{T}^{α} . Let $P^{\alpha}(\mathcal{T}^{\alpha})$ be the probability for a single trajectory \mathcal{T}^{α} to occur. Then the ensemble average over all possible trajectories $\{\mathcal{T}^{\alpha}\}$ and any function f^{α} is

$$\langle\langle f_{\mathcal{D}}^{\alpha} \rangle\rangle_{\alpha} = \sum_{\mathcal{T}^{\alpha} \in \{\mathcal{T}^{\alpha}\}} P^{\alpha}(\mathcal{T}^{\alpha}) \cdot f^{\alpha}(\mathcal{T}^{\alpha}; \mathcal{D}(S^{\text{p},r})). \quad (2.43)$$

As a first step, we show that a maximum likelihood decoder $\mathcal{D}_{\text{ML}}^{\alpha}$, which returns the most likely correction string, as we defined it in Equation (2.37), maximizes the ensemble average $\langle\langle f_{\mathcal{D}}^{\alpha} \rangle\rangle_{\alpha}$:

$$\sup_{\mathcal{D}} [\langle\langle f_{\mathcal{D}}^{\alpha} \rangle\rangle_{\alpha}] = \sup_{\mathcal{D}} \left[\sum_{\mathcal{T}^{\alpha} \in \{\mathcal{T}^{\alpha}\}} P^{\alpha}(\mathcal{T}^{\alpha}) f^{\alpha}(\mathcal{T}^{\alpha}; \mathcal{D}(S^{\text{p},r})) \right] \quad (2.44a)$$

Here we consider the supremum over *all* possible decoders $\mathcal{D}(S^{\text{p},r})$ that return one of the two possible correction operators. We can group the trajectories \mathcal{T}^{α} into equivalence classes $[\mathcal{T}] = S^{\text{p},r}(\mathcal{T}^{\alpha})$ via their respective syndromes $S^{\text{p},r}$, i.e., all trajectories within an equivalence class share the same syndrome measurements.⁴⁴ This allows us to sum over all trajectories in two steps:

$$= \sup_{\mathcal{D}} \left[\sum_{S^{\text{p},r}} \sum_{\mathcal{T}^{\alpha}|_{S^{\text{p},r}}} P^{\alpha}(\mathcal{T}^{\alpha}) f^{\alpha}(\mathcal{T}^{\alpha}; \mathcal{D}(S^{\text{p},r})) \right] \quad (2.44b)$$

Equation (2.41) now allows us to pull the supremum into the outer sum, since \mathcal{D} is simply *any* function that takes syndromes as an input. Thus it is

$$= \sum_{S^{\text{p},r}} \sup_{\mathcal{D}} \left[\sum_{\mathcal{T}^{\alpha}|_{S^{\text{p},r}}} P^{\alpha}(\mathcal{T}^{\alpha}) f^{\alpha}(\mathcal{T}^{\alpha}; \mathcal{D}(S^{\text{p},r})) \right]. \quad (2.44c)$$

⁴³Remember that the ensemble average is equal to the sample average in the limit of many samples.

⁴⁴As the same syndromes exist for every system, in particular for the PTIM ($\alpha = \text{qm}$) and the classical bit-flip model ($\alpha = \text{bi}$), the equivalence classes $[\mathcal{T}]$ don't need a superscript α here.

The decoders $\mathcal{D}(S^{p,r})$ return one of two possible correction strings C which are also determined by the syndrome. Here we consider the supremum over \mathcal{D} given a fixed syndrome — thus we can now write the supremum as

$$= \sum_{S^{p,r}} \sup_C \left[\sum_{\mathcal{T}^\alpha|_{S^{p,r}}} P^\alpha(\mathcal{T}^\alpha) f^\alpha(\mathcal{T}^\alpha; C) \right]. \quad (2.44d)$$

A maximum likelihood decoder can be defined as follows: *For a given syndrome $S^{p,r}$, choose the correction operator C such that*

$$P_{f^\alpha}^\alpha(C|S^{p,r}) = \sum_{\mathcal{T}^\alpha|_{S^{p,r}}} P^\alpha(\mathcal{T}^\alpha) f^\alpha(\mathcal{T}^\alpha; C) \quad (2.45)$$

is maximized. Thus, we can use the MLD $\mathcal{D}_{\text{ML}}^\alpha(S^{p,r})$ to find

$$\sup_{\mathcal{D}} [\langle\langle f_{\mathcal{D}}^\alpha \rangle\rangle_\alpha] = \sum_{S^{p,r}} \sum_{\mathcal{T}^\alpha|_{S^{p,r}}} P^\alpha(\mathcal{T}^\alpha) f^\alpha(\mathcal{T}^\alpha; \mathcal{D}_{\text{ML}}^\alpha(S^{p,r})) = \langle\langle f_{\mathcal{D}_{\text{ML}}^\alpha}^\alpha \rangle\rangle_\alpha. \quad (2.46)$$

Indeed, the MLD of a given system α with the evaluation function f^α maximizes the decoding probability $\langle\langle f_{\mathcal{D}}^\alpha \rangle\rangle_\alpha$. From Equation (2.22), we know that $\langle\langle f_{\mathcal{D}}^{\text{bi}} \rangle\rangle_{\text{bi}} = \langle\langle f_{\mathcal{D}}^{\text{qm}} \rangle\rangle_{\text{qm}}$. This allows us to determine the connection between the MLD of the classical model $\mathcal{D}_{\text{ML}}^{\text{bi}}$ and the MLD of the quantum mechanical PTIM $\mathcal{D}_{\text{ML}}^{\text{qm}}$. It is

$$\sup_{\mathcal{D}} [\langle\langle f_{\mathcal{D}}^{\text{qm}} \rangle\rangle_{\text{qm}}] = \langle\langle f_{\mathcal{D}_{\text{ML}}^{\text{qm}}}^{\text{qm}} \rangle\rangle_{\text{qm}} \quad (2.47)$$

and

$$\sup_{\mathcal{D}} [\langle\langle f_{\mathcal{D}}^{\text{bi}} \rangle\rangle_{\text{bi}}] = \langle\langle f_{\mathcal{D}_{\text{ML}}^{\text{bi}}}^{\text{bi}} \rangle\rangle_{\text{bi}}. \quad (2.48)$$

Using Equation (2.22) we find

$$\langle\langle f_{\mathcal{D}_{\text{ML}}^{\text{qm}}}^{\text{qm}} \rangle\rangle_{\text{qm}} = \sup_{\mathcal{D}} [\langle\langle f_{\mathcal{D}}^{\text{qm}} \rangle\rangle_{\text{qm}}] \quad (2.49a)$$

$$= \sup_{\mathcal{D}} [\langle\langle f_{\mathcal{D}}^{\text{bi}} \rangle\rangle_{\text{bi}}] \quad (2.49b)$$

$$= \langle\langle f_{\mathcal{D}_{\text{ML}}^{\text{bi}}}^{\text{bi}} \rangle\rangle_{\text{bi}} \quad (2.49c)$$

$$= \langle\langle f_{\mathcal{D}_{\text{ML}}^{\text{bi}}}^{\text{qm}} \rangle\rangle_{\text{qm}}. \quad (2.49d)$$

This is exactly Equation (2.39) and proves that the classical MLD yields the same performance on the PTIM as the quantum mechanical MLD. We can view them as equivalent. \square

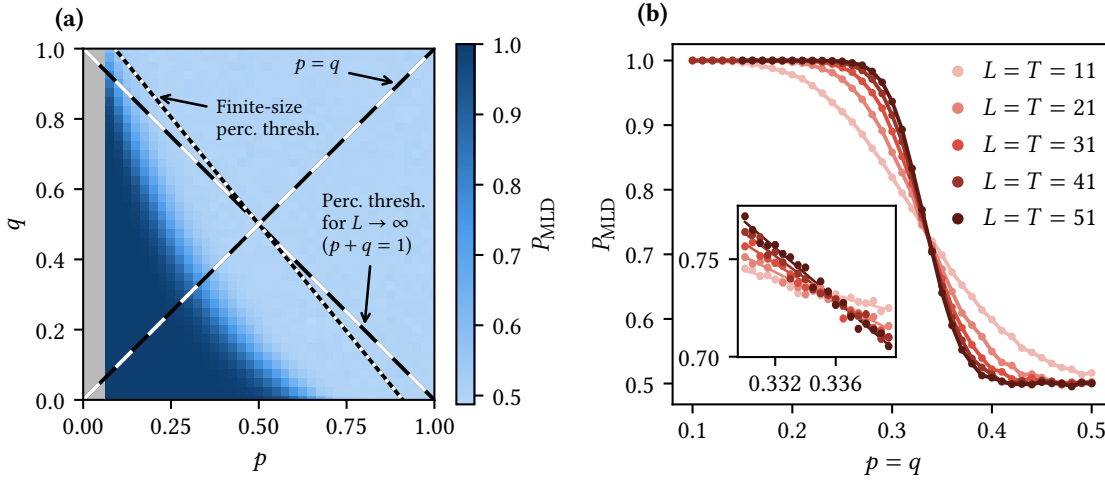


Figure 2.11 • Performance of the maximum likelihood decoder. (a) Decoding probability P_{MLD} of the MLD $\mathcal{D}_{\text{ML}}^{\text{qm}}$ as a function of the error rate p and the failure rate q . The data shown was computed for system sizes $L = T = 41$ and averaged over $2 \cdot 10^4$ sample trajectories. For comparison, we show the percolation threshold at this finite size and in the limit $L \rightarrow \infty$ (cf. Figure 2.3). The decoding phase is a proper subset of the entangling phase. At small values $p \leq 0.05$ the decoder is numerically unstable, and we omit the data. (b) The same decoding probability for different system sizes $L = T$ on the diagonal $p = q$. The emerging crossing features a negligible finite-size shift and gets sharper in the limit $L = T \rightarrow \infty$. A zoomed-in view with linear fits is shown in the inset. We estimate an error threshold $p_{\text{thr}}^{\text{MLD}} = q_{\text{thr}}^{\text{MLD}} \approx 0.336$. Data points in this subfigure show averages over $5 \cdot 10^4$ sample trajectories; the error bars are mostly smaller than the data points.

2.6.2 Results

To analyze the performance of the MLD, we first compute the decoding probability P_{MLD} for a fixed system size $L = T = 41$ across all parameters $p, q \in [0, 1]$. Our simulation data is shown in Figure 2.11 (a). For values $p \leq 0.05$, the probabilities in Equation (2.37) are small enough to cause numerical instabilities – this was already noted in Ref. [91].⁴⁵ The results are very similar to our observations for the MWPM decoder in Figure 2.9. In particular, the decoding phase of the MLD is again a proper subset of the entangling phase of the PTIM.

In order to find a threshold for the decoding transition, we consider the line $p = q$; this case appears to minimize finite-size effects. In Figure 2.11 (b), we show the decoding probability for this case as a function of the system size $L = T$. The clear crossing indicates

⁴⁵We simulate smaller systems compared to Figure 2.9, because compared to the MWPM decoder, the MLD is computationally more expensive and less stable at larger system sizes.

a decoding threshold at $p_{\text{thr}}^{\text{MLD}} = q_{\text{thr}}^{\text{MLD}} \approx 0.336$, which is only a slight improvement over the MWPM decoder ($p_{\text{thr}}^{\text{MWPM}} \approx 0.324$). This allows us to make two key observations. Firstly, the MLD does perform better than the MWPM decoder, which is expected. However, the small difference between the decoding thresholds indicates that $\mathcal{D}_{\text{MWPM}}$ is already a near-optimal decoder. This is in agreement with previous results for similar decoders on the surface code [91, 92]. Secondly, our results demonstrate that there exists a parameter regime in which the logical qubit in the PTIM does survive but cannot be restored by *any* decoder, as clearly $p_{\text{thr}}^{\text{MLD}} < p_c = 1/2$.

2.7 Conclusion

We studied the error correction capabilities of the projective transverse field Ising model, interpreting its competing types of measurements as errors performed by the environment and syndromes recorded by an observer. In its entangling phase, the PTIM is able to protect a single logical qubit and thus act as a quantum memory. We designed decoding algorithms to retrieve this logical qubit after a trajectory of repeated error and syndrome measurements and analyzed their performance.

In a first attempt, we formulated a generalized majority voting decoder inspired by error correcting schemes on the (quantum) repetition code. Our numerical results showed that this approach generally fails on the PTIM, and we are able to provide an intuitive reasoning for this. Our second decoding algorithm — a minimum weight perfect matching decoder — addresses the previous decoder’s weakness by considering the full syndrome of all time steps at once. Our numerical simulations show that this approach succeeds and the MWPM decoder is able to reconstruct a logical qubit up to a finite decoding threshold. The decodable region of the PTIM’s parameter space is however smaller than the entangling phase, suggesting that for some parameters, quantum information is protected in the system but cannot be restored by a decoder. We prove that this suspicion is true by implementing an optimal decoder — the maximum likelihood decoder — which only slightly improves on the decoding threshold of the MWPM decoder. As there cannot be a better decoder, this proves that there is indeed an intermediary parameter regime in which an encoded logical qubit is neither accessed by the environment via error measurements nor can it be retrieved by the observer by syndrome measurements.

Our findings for the different decoders are accompanied by a better understanding of the differences and similarities between this quantum circuit with a projective noise model and more common (“classical”) quantum error correcting codes with unitary noise.⁴⁶ For example, we are able to prove that all decoders perform identically for a classical version of the PTIM. We used this fact to make our simulations more efficient; but this step was technically not necessary, as it is only an improvement over the already efficient stabilizer

⁴⁶The quantum version of the repetition code encodes a logical qubit in an entangled state $\alpha|0\rangle + \beta|1\rangle$, but the remainder of its trajectory consists of unitary qubit flips and measurements with a deterministic result. This is one we might call such circuits “classical”.

simulations we could perform on the real PTIM. This equivalence between a classical and a fully quantum mechanical model in the context of quantum error correction does, however, underline that — at least in some cases — our understanding of classical systems is still hugely beneficial in the quest for fault tolerance in quantum computation, even under projective noise models. We are also able to prove that the PTIM and its classical sibling share the same maximum likelihood decoder, i.e., their separate decoding thresholds are optimized by the same decoding algorithm.

In a real application of a quantum memory using the PTIM, the MWPM decoder might be the best-suited decoding algorithm as it is more efficient than the maximum likelihood decoder and does not require knowledge of the system's error rate. This comes only at a small decrease in the decoding probability and is thus more practical. It is however important to note that the PTIM only allows for the correction of X -noise. Any phase errors would compromise the quantum information. This makes the PTIM only viable in very specific scenarios which suppress Z -noise. More common approaches to make quantum memory fault-tolerant aim to correct for all errors, i.e., for X -noise and Z -noise. Such examples include the Steane code [69] and scalable surface codes [70, 92]. The key takeaway is: A scalable and local quantum error correcting code which is able to correct X - and Z -errors must be at least two-dimensional. In this context, our work on the PTIM is not necessarily aimed towards practical applications in the first place. We will however expand on our findings in Chapter 4 in order to construct error correction schemes that will help us to experimentally access the entanglement transition of the PTIM.

Appendices for Chapter 2

2.A Equivalence of Classical Samplings

Here we give a short proof for the sampling equivalence in Equation (2.28), which relates Equation (2.26) and Equation (2.27). We do this by inserting Equation (2.27) in Equation (2.28) to obtain Equation (2.26).

Consider the term

$$\frac{1}{P^{\text{bi}}(S^{\text{P}})} \sum_{E^{\text{P}}|_{\mathcal{T}^{\text{bi}}}} P^{\text{bi}}(\mathcal{T}^{\text{bi}}, E^{\text{P}}) \quad (2.50a)$$

with the sum over all error patterns E^{P} that contain the bit flip pattern $\tilde{E}^{\text{P}} \subseteq E^{\text{P}}$ which is part of the trajectory \mathcal{T}^{bi} . We insert $P^{\text{bi}}(S^{\text{P}})$ and Equation (2.27) to find

$$= \sum_{E^{\text{P}}|_{\mathcal{T}^{\text{bi}}}} p^{|E^{\text{P}}|} \cdot (1-p)^{LT-|E^{\text{P}}|} \cdot \left(\frac{1}{2}\right)^{|E^{\text{P}}|} \quad (2.50b)$$

$$= \sum_{E^{\text{P}}|_{\mathcal{T}^{\text{bi}}}} \left(\frac{p}{2}\right)^{|E^{\text{P}}|} \cdot (1-p)^{LT-|E^{\text{P}}|} \quad (2.50c)$$

$$= \left(\frac{p}{2}\right)^{|\tilde{E}^{\text{P}}|} (1-p)^{LT-|\tilde{E}^{\text{P}}|} \sum_{E^{\text{P}}|_{\mathcal{T}^{\text{bi}}}} \left(\frac{p}{2(1-p)}\right)^{|E^{\text{P}}-|\tilde{E}^{\text{P}}|}. \quad (2.50d)$$

The summation over all possible patterns E^{P} that are consistent with the trajectory \mathcal{T}^{bi} is equivalent to a summation over all *virtual patterns* $E_{\text{V}}^{\text{P}} := E^{\text{P}} \setminus \tilde{E}^{\text{P}}$. This pattern is constructed such that $0 \leq |E_{\text{V}}^{\text{P}}| = |E^{\text{P}}| - |\tilde{E}^{\text{P}}| \leq LT - |\tilde{E}^{\text{P}}|$. Now we rewrite the sampling as

$$= \left(\frac{p}{2}\right)^{|\tilde{E}^{\text{P}}|} (1-p)^{LT-|\tilde{E}^{\text{P}}|} \sum_{E_{\text{V}}^{\text{P}}} \left(\frac{p}{2(1-p)}\right)^{|E_{\text{V}}^{\text{P}}|}. \quad (2.50e)$$

Sampling over all possible virtual patterns E_V^D is equivalent to choosing all possible subsets of a set with $LT - |\tilde{E}^P|$ elements:

$$= \left(\frac{p}{2}\right)^{|\tilde{E}^P|} (1-p)^{LT-|\tilde{E}^P|} \cdot \sum_{k=0}^{LT-|\tilde{E}^P|} \binom{LT-|\tilde{E}^P|}{k} \left(\frac{p}{2(1-p)}\right)^k \quad (2.50f)$$

$$= \left(\frac{p}{2}\right)^{LT} \cdot \sum_{k=0}^{LT-|\tilde{E}^P|} \binom{LT-|\tilde{E}^P|}{k} 1^k \left(\frac{2(1-p)}{p}\right)^{(LT-|\tilde{E}^P|)k} \quad (2.50g)$$

Here we can use the binomial theorem:

$$= \left(\frac{p}{2}\right)^{LT} \cdot \left(1 + \frac{2(1-p)}{p}\right)^{LT-|\tilde{E}^P|} \quad (2.50h)$$

$$= \left(\frac{p}{2}\right)^{|\tilde{E}^P|} \cdot \left(1 - \frac{p}{2}\right)^{LT-|\tilde{E}^P|} \quad (2.50i)$$

$$= \frac{P^{\text{bi}}(\mathcal{S}^{\text{bi}})}{P^{\text{bi}}(\text{SP})}. \quad (2.50j)$$

This proves the relation in Equation (2.28), and thus the sampling described in Equation (2.27) is correct. \square

2.B Thermodynamic Limit of the MVD for $q = 0$

Here we shortly discuss the performance of the majority voting decoder \mathcal{D}_{MV} for $q = 0$ in the thermodynamic limit. Note that in this case, the MVD (introduced in Section 2.4) is identical to the minimum weight perfect matching decoder (introduced in Section 2.5):

$$P_{\text{MV}}(p, q = 0; L, T) = P_{\text{MWPM}}(p, q = 0; L, T) \quad (2.51)$$

All the following statements are therefore true for both decoders.

With vanishing failure rate $q = 0$, all syndromes are measured at every time step and the state is projected onto a product state in the z -direction of the form $|\mathbf{m}_t\rangle$. Here we can make use of our classical model (see Subsection 2.3.3), as every error measurement results in an effective qubit flip with probability $1/2$. Thus, we consider the PTIM as a repetition code with multiple time steps and flip probability $p/2$. The MVD makes a false assumption whenever more than $L/2$ qubits are flipped in a single time step. The likelihood P_m for such a “mistake” to occur in a single time step is closely related to the decoding probability of the standard repetition code [see Equation (2.6)]:

$$P_m(p; L) = \sum_{b=[L/2]}^L \binom{L}{b} \left(\frac{p}{2}\right)^b \left(1 - \frac{p}{2}\right)^{L-b} \cdot \begin{cases} \frac{1}{2}, & \text{if } b = \frac{L}{2}, \\ 1, & \text{else} \end{cases} \quad (2.52)$$

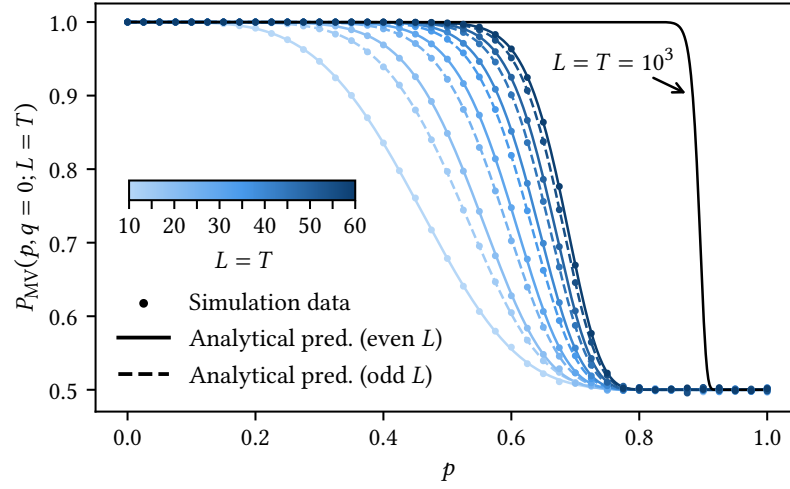


Figure 2.12 • Analytical predictions for the MVD at $q = 0$. Lines in this plot show the analytical predictions for the performance of the MVD at failure rate $q = 0$. Data points were generated by numerical simulations of the MWPM decoder (which is equivalent to the MVD at $q = 0$) and averaged over 10^5 samples each. The plot shows the system sizes $L = 10, 15, 20, \dots, 60$. Dashed (solid) lines represent odd (even) sizes. The analytical prediction for $L = T = 10^3$ demonstrates that the decoding threshold really shifts up to $p = 1.0$ for $L = T \rightarrow \infty$.

We adjusted the probability for the case of exactly $L/2$ flips (here the decoder randomly guesses the correct or incorrect flip pattern). For a trajectory with multiple time steps, the decoder is successful if it fails in an even number of steps. The decoding probability for the MVD on the PTIM at $q = 0$ is thus identical to the well-known result for the repetition code [cf. Equation (2.8)]:

$$P_{\text{MV}}(p, q = 0; L, T) = \sum_{\substack{t=0 \\ t \text{ even}}}^T \binom{T}{t} \cdot [P_m(p; L)]^t \cdot [1 - P_m(p; L)]^{T-t} \quad (2.53)$$

We show this function in Figure 2.12 alongside simulation data for square systems $L = T$. Clearly, the numerical results match our analytical predictions — including the visible even-odd effect.⁴⁷ The decoding probability exhibits a very strong finite-size effect. In the thermodynamic limit $L = T \rightarrow \infty$ it slowly approaches $P_{\text{MV}} \rightarrow 1$ for all $p < 1$.

Careful readers may have noticed that our approach ignores the case of the initial cluster being destroyed, which only occurs if all errors are measured in a single time step. This can be resolved by realizing that here we actually calculate $\langle\langle f_{\mathcal{Q}_{\text{MV}}}^{\text{bi}} \rangle\rangle_{\text{bi}}$, i.e., we sample classical trajectories (which have no clusters) to evaluate the MVD analytically. Equation (2.28) shows that this approach is allowed.

⁴⁷Odd system sizes are generally favored here, as they break the ties occurring when exactly $L/2$ flips occur. See also our discussion of the repetition code in Section 2.2.

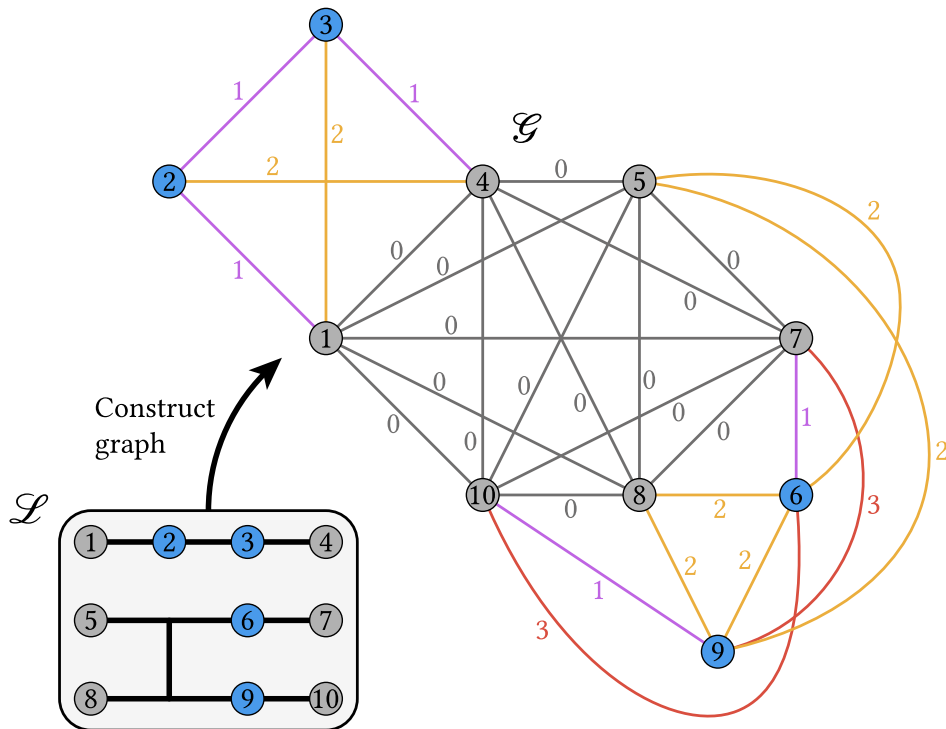


Figure 2.13 • Graph construction for the MWPM decoder. Illustration for the construction of a weighted graph \mathcal{G} from the lattice \mathcal{L} as used in the MWPM decoder $\mathcal{D}_{\text{MWPM}}$. After this step is performed by the decoder, the minimum weight perfect matching is found on \mathcal{G} . For simplicity, we usually show the lattice representation of the graph, as in Figure 2.7 (d).

2.C Graph Construction for the MWPM Decoder

In Figure 2.7 (d), we show a representation of a graph \mathcal{G} embedded on the lattice \mathcal{L} . Here we show explicitly how the graph is extracted from this picture, to be then used in the MWPM algorithm. Following the rules in Subsection 2.5.1 we can construct the weighted graph by hand: From every node on the lattice \mathcal{L} we find the path to any other node along the edges (if such a path exists) with the least amount of horizontal steps. These paths are edges of the graph \mathcal{G} , and their weight is the number of horizontal steps. All boundary nodes are connected via edges of weight 0. We illustrate this construction in Figure 2.13.

The example shown here corresponds to a PTIM circuit with $L = 3$ qubits and $T = 3$ time steps. We use colors to make the graph appear slightly more structured, but clearly, for larger systems a good algorithm is needed to construct \mathcal{G} as efficiently. In the following, we introduce two such algorithms.

2.C.1 Breadth-First Search

In a naive approach, we choose a single node on the lattice \mathcal{L} and find the connection to every other node with the minimum weight in a breadth-first search. The full graph \mathcal{G} is found by performing this search for every node. To explain how this algorithm works in our setting, we make use of a slightly unusual but intuitive zoological picture.

Choose any node that is not a boundary node on the lattice \mathcal{L} and imagine an anthill being placed there. The ants spread out on any vertical link on \mathcal{L} as far as possible without walking on any horizontal links. Any new node reached by the ants in this step is connected to the initial node via an edge of weight 0 in the graph \mathcal{G} . Now the ants will move in discrete time steps. A single step consists of two substeps:

1. First, the ants move a single step horizontally to any place on the lattice that was not reached previously.
2. Secondly, the ants move vertically as far as possible to any point that was not reached previously.

Any new nodes (including boundary nodes) reached in step t are connected to the initial node on the graph \mathcal{G} via an edge of weight t . We repeat the process for all normal nodes and lastly add edges of weight 0 interconnecting all boundary nodes.

When making sure that ants never walk a path twice, this algorithm runs in polynomial time $\mathcal{O}(L^2T^2)$. Some slight improvements can be made to the algorithm by simplifying the graph: If a node on the lattice \mathcal{L} has no outgoing vertical edges, it may act as a stop sign to the ants reaching it. In Figure 2.13, the ants starting at node 6 would reach node 9 and then stop walking – without finding the edge connecting nodes 6 and 10. It is easy to see that an MWPM would never include this edge, because node 9 must be connected somewhere. The resulting graph is slightly reduced without changing the output of the decoder $\mathcal{D}_{\text{MWPM}}$ and can be constructed in less time. However, in practice, the construction of the graph remains the most costly portion of the decoding algorithm (followed by the actual MWPM step).

Cutoff Weights

The breadth-first search can be altered to reach complexity $\mathcal{O}(LT)$ if we are willing to sacrifice some of the performance of our decoder $\mathcal{D}_{\text{MWPM}}$. We can implement a constant cutoff weight and discard any edges in \mathcal{G} that have a higher weight. This reduced graph is easily constructed by only allowing the ants to walk for the corresponding number of steps. This does however come with two caveats: Firstly – especially at small cutoff weights – an MWPM may not exist on the reduced graph. Secondly, we generally observe a performance hit on the decoder, which manifests as a slightly shifted decoding threshold.

For a large enough cutoff weight, a perfect matching typically does exist (i.e., matchings are usually local on the lattice \mathcal{L}). For systems of size $L = T = 31$ we show how the decoding probability shifts with increasing cutoff in Figure 2.14. We will not further examine this cutoff ansatz here and instead focus on a more efficient graph construction algorithm which does not sacrifice any performance of the decoder $\mathcal{D}_{\text{MWPM}}$.

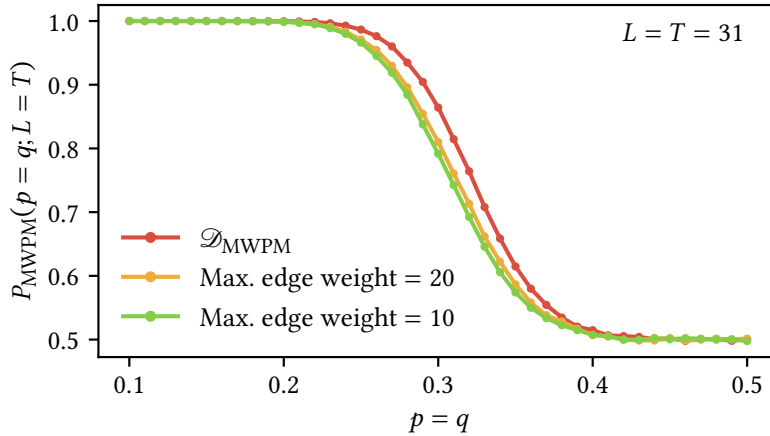


Figure 2.14 • Minimum weight perfect matching with a cutoff weight. If only edges with a weight below a certain cutoff are included in the graph \mathcal{G} , the decoding threshold shifts slightly. This does however come at a significant runtime improvement for the decoder. Data points show averages over 10^5 samples each.

2.C.2 Crossing Nodes

In a more efficient approach to run the MWPM decoder, we create an expanded graph with more nodes. This graph can be constructed much quicker compared to the ansatz described in Subsection 2.C.1. The Blossom algorithm will run slower as it needs to perform the matching on a larger graph, but the implementation by Kolmogorov [117] is very efficient and thus we are still able to reach much shorter runtimes.

Our motivation is the fact that crossings in the lattice representation of the graph only occur around vertical edges. If no node sits on a crossing, any matching paths going in must also go out. We construct a graph enforcing this as follows:

1. In addition to the normal nodes and the boundary nodes, we add crossing nodes wherever a vertical edge crosses a horizontal edge, i.e., two additional nodes at each end of a vertical edge.
2. All crossing nodes located at the same position in \mathcal{L} are connected via edges of weight zero. Further, the crossing nodes are connected to all crossing nodes on the next crossing (up and down) with weight zero.
3. Every node coinciding with crossing nodes is connected to them via edges of weight zero.
4. All normal nodes and boundary nodes are connected only horizontally to the nearest nodes and/or crossing nodes (left and right). These are the only horizontal edges of the graph, and their weight is equal to the distance between the nodes.
5. Finally, all boundary nodes are interconnected with edges of weight zero.

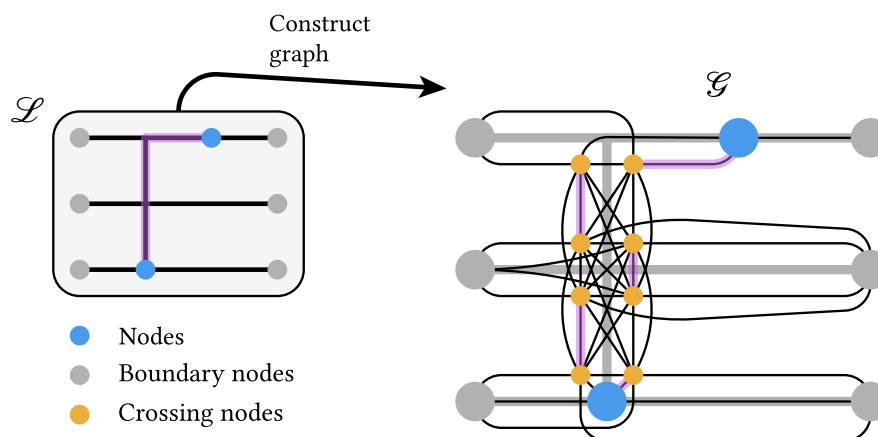


Figure 2.15 • Path construction with crossing nodes. Illustration for the construction of a graph \mathcal{G} from the lattice representation \mathcal{L} using crossing nodes. For orientation purposes, we overlay the lattice representation of the graph on the right side in gray. This figure does not show the edges connecting the boundary nodes. In purple, we highlight the MWPM for this example and show how it translates to the expanded graph.

We show an example of such a construction in Figure 2.15. For simplicity, the edges between boundary nodes are excluded from the image. The figure also marks an MWPM on the lattice and its graph representation. This illustrates how the method works: At every crossing, an even number of nodes can be matched with each other. If a matching path on the lattice \mathcal{L} enters a crossing, i.e., matches one of the crossing nodes, a different crossing node is left and must be connected to another site on the lattice.

While the graph G has more nodes and edges compared to a graph constructed as in Figure 2.13, its construction is very efficient with complexity $\mathcal{O}(LT)$.⁴⁸ This greatly outweighs the increased time for the MWPM of the larger graph. Simulations of the decoder $\mathcal{D}_{\text{MWPM}}$ in this thesis use this method.

2.D Explicit Algorithm for the Maximum Likelihood Decoder on the PTIM

Here we give some concrete instructions to implement an MLD for the PTIM. As our approach is almost completely identical to the algorithm described by Bravyi et al. in Ref. [91] for the surface code, we will not provide the full pseudocode. Instead, we show only the methods that are specific to the MLD on the PTIM.

⁴⁸The number of nodes and crossings scales with LT ; the work to be done to find the edges for every node is $\mathcal{O}(1)$.

As a first step, in order to calculate the probability $P_{f^{\text{bi}}}^{\text{bi}}(C|S^{\text{p},r})$ for a correction operator C , given the syndromes $S^{\text{p},r}$, it is necessary to find a single bit flip pattern \tilde{E}^{p} consistent with C and all syndromes.⁴⁹ Here we can make any choice, without loss of generality we use the following algorithm:

```

1: function POSSIBLEBITFLIPPATTERN( $S^{\text{p},r}$ )
2:   /* Find a possible bit flip pattern for the recorded syndrome */
3:    $\tilde{S}^r \leftarrow S^r$ 
4:   for  $t = 1$  to  $T$  do
5:     for  $x = 1$  to  $L - 1$  do
6:        $e \leftarrow (x, x + 1)$ 
7:       if not  $S_{t,e}^{\text{p}}$  then
8:          $\tilde{S}_{t,e}^r \leftarrow +1$ 
9:       end if
10:    end for
11:  end for
12:  for  $t = 1$  to  $T$  do
13:     $f \leftarrow \text{true}$ 
14:    for  $x = 1$  to  $L$  do
15:       $\tilde{E}_{t,x}^{\text{p}} \leftarrow f$ 
16:       $e \leftarrow (x, x + 1)$ 
17:      if [ $x < L$ ] then
18:        if [ $t > 1$ ] then
19:          if [ $\tilde{S}_{t,e}^r \neq \tilde{S}_{t-1,e}^r$ ] then
20:             $f \leftarrow \text{not } f$ 
21:          end if
22:        else if [ $t = 1$ ] and [ $\tilde{S}_{t,e}^r = -1$ ] then
23:           $f \leftarrow \text{not } f$ 
24:        end if
25:      end if
26:    end for
27:  end for
28:  return  $\tilde{E}^{\text{p}}$ 
29: end function

```

The returned bit flip pattern is consistent with all syndromes and with one of the correction operators C or \bar{C} . To switch between correction operators, we may just invert the pattern \tilde{E}_t^{p} in one of the time steps t , effectively flipping all bits once.

Now consider the lattice shown in Figure 2.8. With our choice of \tilde{E}^{p} , we have just defined one such classical trajectory. Calculating its probability is not difficult. As we explained

⁴⁹From this pattern, all other consistent patterns can be created via the addition of loops, see Subsection 2.6.1.

in Subsection 2.6.1, adding closed loops to the bit flip pattern generates new trajectories that correspond to the same syndromes and correction operator. To find the probability for a newly generated trajectory, Bravyi et al. assign a weight w_{edge} to every edge of the surface code. Here, we adjust this function to the edges of the lattice \mathcal{L} . In a slight abuse of notation, we associate horizontal (vertical) edges \mathbf{e} with entries in the pattern \tilde{E}_e^{p} (S_e^{p}).⁵⁰

```

1: function WEIGHT( $\mathbf{e}$ )
2:   /* Calculate the weight for every edge in the lattice, given a set of possible bit flips
   and recorded syndromes */
3:   if  $\mathbf{e}$  is horizontal in  $\mathcal{L}$  then
4:     if [ $\tilde{E}_e^{\text{p}} = \text{true}$ ] then
5:        $w_{\mathbf{e}} \leftarrow \frac{1-p/2}{p/2}$ 
6:     else
7:        $w_{\mathbf{e}} \leftarrow \frac{p/2}{1-p/2}$ 
8:     end if
9:   else if  $\mathbf{e}$  is vertical in  $\mathcal{L}$  then
10:    if [ $S_e^{\text{p}} = \text{true}$ ] then
11:       $w_{\mathbf{e}} \leftarrow 0$ 
12:    else
13:       $w_{\mathbf{e}} \leftarrow 1$ 
14:    end if
15:  end if
16:  return  $w_{\mathbf{e}}$ 
17: end function

```

Ref. [91] contains all further instructions to calculate $P_{f_{\text{bi}}}^{\text{bi}}(C|S^{\text{p,r}})$ and $P_{f_{\text{bi}}}^{\text{bi}}(\bar{C}|S^{\text{p,r}})$. The decoder $\mathcal{D}_{\text{ML}}^{\text{bi}} = \mathcal{D}_{\text{ML}}^{\text{qm}}$ returns the correction string with the larger probability. Note that the algorithm described assumes a square lattice $L = T$. For our purposes, it was not necessary to lift this constraint. Furthermore, Ref. [91] also provides some crucial instructions for improving the numerical stability of the algorithm. This is very important, as the probabilities of trajectories are exponentially small and quickly reach the precision limits of typical floating-point representations. The overall running time of this algorithm is $\mathcal{O}(L^2 T^2) = \mathcal{O}(L^4)$.

⁵⁰An edge \mathbf{e} on the lattice \mathcal{L} corresponds to a point in space *and* time. Horizontal (vertical) edges correspond to possible bit flips (syndrome measurements). This is not to be confused with edges $e = (i, i + 1)$ between two qubits.

2.E Extended Proof for the Equivalence of Maximum Likelihood Decoders

The two MLDs $\mathcal{D}_{\text{ML}}^{\text{qm}}$ and $\mathcal{D}_{\text{ML}}^{\text{bi}}$ internally calculate the probabilities $P_{f^{\text{qm}}}^{\text{qm}}(C|S^{\text{p},r})$ and $P_{f^{\text{bi}}}^{\text{bi}}(C|S^{\text{p},r})$ [cf. Equation (2.45)]. Here we will prove that

$$P_{f^{\text{qm}}}^{\text{qm}}(C|S^{\text{p},r}) = P_{f^{\text{bi}}}^{\text{bi}}(C|S^{\text{p},r}). \quad (2.54)$$

From Equation (2.54) follows Equation (2.39), i.e., the proof we perform here is slightly stronger than the one we showed in Subsection 2.6.1.

2.E.1 Useful Concepts

First, we introduce some new useful concepts and remind ourselves of some old ones. We have already defined the lattice \mathcal{L} [see Figure 2.7 (b)] as a method to represent trajectories of our one-dimensional models in two dimensions. A trajectory \mathcal{T}^{qm} is fully determined by the initial state $|\Psi_0\rangle$ and the measurements $E^{\text{p},r}$ and $S^{\text{p},r}$. The patterns $M^{\text{p}} = (E^{\text{p}}, S^{\text{p}})$ are associated with the probabilities p and q and we denote the number of performed measurements with the absolute value $|E^{\text{p}}|$ and $|S^{\text{p}}|$. The measurements performed here are part of the stabilizer formalism and thus fall into one of two groups. If the system's state was already projected into the eigenbasis of an observable, the measurement outcome is deterministic and the state projection becomes trivial. Such measurements can be added to a trajectory without ever changing the state evolution $\{|\Psi(t)\rangle\}$. Nontrivial Pauli measurements give the results ± 1 with equal probability and yield true quantum randomness.⁵¹ We define the reduced measurement patterns $E_{\text{red}}^{\text{p}}$ and $S_{\text{red}}^{\text{p}}$ as the patterns that exclude all trivial measurements. Any further reductions of the patterns would affect the state evolution.

Dual Lattice and Islands

We define the lattice \mathcal{L}^* , which is dual to \mathcal{L} . The nodes of \mathcal{L}^* coincide with the plaquettes of \mathcal{L} and vice versa. Edges of both lattices cross each other orthogonally. Assume a measurement pattern M^{p} on the lattice \mathcal{L} . We define the reduced dual lattice $\mathcal{L}_{\text{red}}^*$ by removing all performed error measurements and all syndrome measurements that were *not* performed from \mathcal{L}^* . An illustration of this construction is shown in Figure 2.16 (a). Note that this is exactly the bond percolation model we already showed in Figure 1.5.

Generally, the reduced dual lattice may feature multiple islands which are not connected via any edges (percolation clusters). We indicate them by $\mathcal{I}_i \in \{\mathcal{I}\}$ with indices i and the set of all islands $\{\mathcal{I}\}$. In our decoding scenario, two islands are special: We call the island that

⁵¹Equal probabilities arise under the assumption that the system's state is a stabilizer state. We already made this restriction on the initial state $|\Psi_0\rangle$ in Subsection 2.3.2.

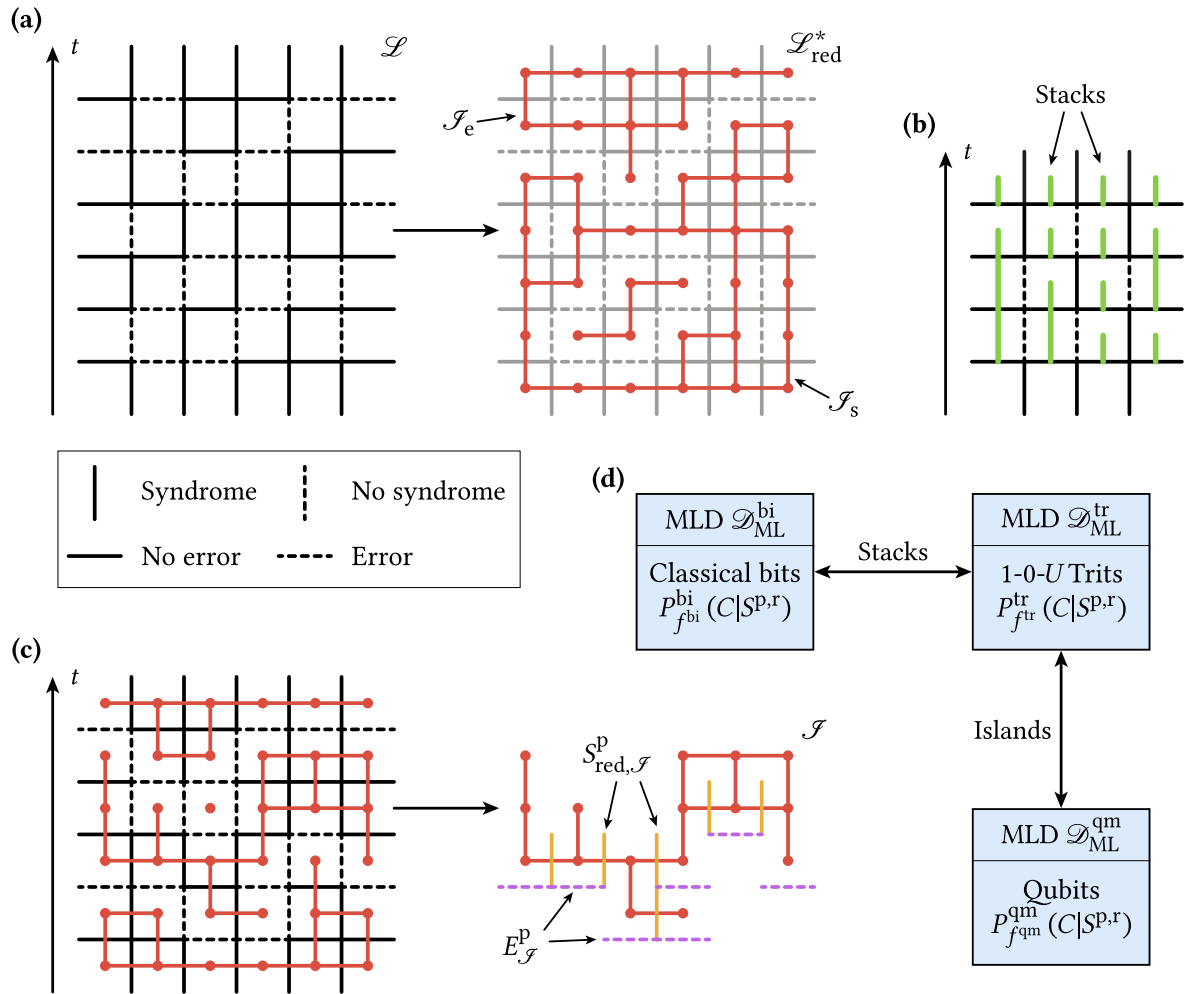


Figure 2.16 • Illustrations for the proof of the equivalence of MLDs. (a) Construction of the reduced dual lattice $\mathcal{L}_{\text{red}}^*$ from the lattice \mathcal{L} and a measurement pattern M^P . We call disconnected regions on $\mathcal{L}_{\text{red}}^*$ islands \mathcal{F} . (b) Construction of stacks on the lattice \mathcal{L} with a given set of syndromes S^P . Stacks start after adjacent syndrome measurements were performed and end with the next syndrome. (c) When extracting a single island \mathcal{F} from the dual lattice $\mathcal{L}_{\text{red}}^*$, we can identify all error measurements $E_{\mathcal{F}}^P$ that create a new (local) cluster on \mathcal{F} (here indicated by purple dashed lines). Correspondingly, a subset of the reduced syndrome pattern $S_{\text{red},\mathcal{F}}^P$ can be selected (here indicated by orange vertical lines) on the island. For any island that does not contain the initial state, it is always $|E_{\mathcal{F}}^P| - 1 = |S_{\text{red},\mathcal{F}}^P|$. (d) Sketch of the structure of the proof shown in Section 2.E.

contains the very first time step \mathcal{J}_s . It fully contains the initial cluster.⁵² Furthermore, we call the island connected to the final time step \mathcal{J}_e . The initial cluster survives in a trajectory (and with it the logical qubit) if and only if $\mathcal{J}_s = \mathcal{J}_e$.

Stacks

Consider a lattice \mathcal{L} with a syndrome pattern S^P . We group the two-dimensional lattice into vertical *stacks*. Every stack groups one or more consecutive time steps of a single qubit together. A stack starts after a syndrome measurement adjacent to the qubit has been performed and it ends on the next adjacent syndrome measurement. We illustrate this construction in Figure 2.16 (b). Within a stack, the single qubit can follow multiple trajectories that are indistinguishable to the syndrome measurement at the end of the stack. We will later use the notion of stacks to group all these trajectories together.

We call the set of all stacks $\{\mathcal{J}\}$ and the number of stacks $|\{\mathcal{J}\}|$. To every stack we assign a thickness $n_{\mathcal{J}} = |\mathcal{J}|$, which indicates the number of time steps within the stack.

Classical Bits

We have already introduced the notion of a classical bit-flip model in Subsection 2.3.3. Instead of qubits, the model consists of a chain of L classical bits (with the state 1 or 0). Syndrome measurements are still well-defined on this model. Error measurements are however replaced by bit flips, which occur with probability $p/2$ on every site in every time step. As trajectories are fully deterministic, the results of the syndrome measurements S^P are a function of the bit flip pattern \tilde{E}^P (unlike the random measurement results of the quantum mechanical PTIM). We call the full pattern of bits on the system lattice for all times Ψ^{bi} .

1-0- U Trits

We will introduce another classical model that aims to emulate the quantum mechanical trajectory $|\Psi(t)\rangle$ classically. Consider two patterns $M^P = (E^P, S^P)$. We define the 1-0- U *trit* as a new particle that occupies the system instead of classical bits or qubits. A trajectory of L trits is fully determined by the measurement patterns and obeys the following rules:

- Each trit assumes the state 1, 0 or U .
- If a trit is in the state 1 or 0 and an error measurement is performed, it switches into the state U (“undecided”). (There is no need to define a result for the error measurement.)
- If a trit is in the state U and an adjacent syndrome measurement is performed, it switches into the state 1 or 0 with equal probabilities.

⁵²As \mathcal{J}_s is a *percolation* cluster and knows no direction in time, it generally contains *more* than just the initial cluster in the CCM picture.

- If a trit is in the state 1 or 0 and an adjacent syndrome is measured, it remains unchanged.
- The results of syndrome measurements are determined by the states of the neighboring trits (after they have both assumed a state 1 or 0).

It is apparent that the system of trits follows similar rules as the quantum mechanical PTIM, and it also utilizes the same patterns E^P and S^P . In contrast, the classical bit-flip model uses a different pattern \tilde{E}^P associated with a different probability $p/2$ and follows different rules. However, the trit model does not feature a concept of entanglement or anything similar to Bell clusters and the CCM. Thus, it also shares some similarities with the bit-flip model. We call a full pattern of trits on the plaquettes of the system lattice Ψ^{tr} .⁵³ $|\Psi^{\text{tr}}|_U$ is the number of times a trit switched from the state U to 1 or 0.

1-0- U Trits on Islands

Consider a quantum mechanical system on the lattice \mathcal{L} with error and syndrome measurements. We will now show that any island \mathcal{I} in the dual lattice $\mathcal{L}_{\text{red}}^*$ can be occupied by trits in a manner consistent with all measurements. To do so, we first need to understand how Bell clusters evolve on islands. In general, every error measurement creates a local single-site Bell cluster. We can group the error measurements by the islands, for which they create clusters. For an island \mathcal{I} , we call the corresponding error measurements $E_{\mathcal{I}}^P$ [see Figure 2.16 (c)]. From the CCM, it is clear that in the case $\mathcal{I} \neq \mathcal{I}_s$, the number of colors within an island is $|E_{\mathcal{I}}^P|$.⁵⁴ All clusters on an island are connected via (reduced) syndrome measurements. Thus, it is easy to see that the total number of reduced syndrome measurements within an island must be

$$|S_{\text{red},\mathcal{I}}^P| = |E_{\mathcal{I}}^P| - 1. \quad (2.55)$$

We will now fill the island with trits such that their rules — as well as the quantum mechanical syndrome measurement results — are fulfilled. To do so, we first consider the clusters on an island separately. The state of the qubits belonging to a cluster generally has the form $\alpha|\mathbf{m}\rangle + \beta|\bar{\mathbf{m}}\rangle$. If the cluster is not the initial cluster, α and β are chosen such that the cluster is polarized in the x -direction ($\alpha, \beta \in \{\pm 1\}$). We can now assign every site on the dual lattice within a cluster (sites with the same color in the CCM) with a number 1 or 0 either according to $|\mathbf{m}\rangle$ or to $|\bar{\mathbf{m}}\rangle$. This can be done in a way consistent with all syndrome measurements, as the quantum mechanical state must also be consistent with the measurements. For each cluster there are two possibilities to assign the numbers 1 and 0, and we find $2^{|E_{\mathcal{I}}^P|}$ possible samplings for the whole island \mathcal{I} . Reduced syndrome measurements $S_{\text{red},\mathcal{I}}^P$ merge clusters and thus impose restrictions on our choices of numbers 1 and 0. If two

⁵³To be precise, the pattern Ψ^{tr} is defined on subplaquettes as the state may change every half time step.

⁵⁴This requires resolving the dual lattice in half time steps. In Figure 2.16 (c) some newly created clusters are immediately joined by syndrome measurements.

clusters are joined, the connecting measurement excludes two samplings on these clusters, halving the total number of possibilities. Thus, there are

$$2^{|E_{\mathcal{I}}^p|} \cdot \left(\frac{1}{2}\right)^{|S_{\text{red},\mathcal{I}}^p|} = 2 \quad (2.56)$$

possible ways to fill an island with ones and zeros such that all stabilizer measurements are obeyed.

We can now consider the two possible configurations and adjust them such that they correspond to valid trajectories of trits. We do this by replacing ones and zeros with U if they follow an error measurement and no adjacent syndrome measurement has been performed yet. This creates two possible trit configurations for every island $\mathcal{I} \neq \mathcal{I}_s$.

For the first island \mathcal{I}_s we find one key difference: One of the clusters in \mathcal{I}_s is the initial cluster, which we chose to be polarized in the z -direction ($|\Psi_0\rangle = |\mathbf{0}\rangle$).⁵⁵ For this cluster, we may only choose one configuration of zeros and ones. Thus there is only one consistent configuration of trits on \mathcal{I}_s .

The protocol we described here allows us to find trajectories of trits to occupy the quantum mechanical lattice consistently (obeying all syndrome measurements and the rules of the trits model). There are $2^{|\{\mathcal{I}\}|-1}$ such trajectories.

2.E.2 Proof

We will structure the actual proof of Equation (2.54) as follows: First, we will focus on the classical model and rewrite the probability $P_{f_{\text{bi}}}^{\text{bi}}(C|S^{\text{p},r})$ in a form that will become useful. We then do the same for the probability $P_{f_{\text{qm}}}^{\text{qm}}(C|S^{\text{p},r})$ calculated by the quantum mechanical MLD for the PTIM. Lastly, we will consider the model of classical trits, which serves as a connecting link between the classical model and the PTIM. Figure 2.16 (d) shows the relations between MLDs of different models as a general orientation for the following proof.

General Maximum Likelihood Decoder

Let us quickly revisit the general approach of an MLD. For any system α , the decoder $\mathcal{D}_{\text{ML}}^\alpha$ calculates the probabilities $P^\alpha(\mathcal{T}^\alpha)$ for all possible trajectories \mathcal{T}^α (consistent with the recorded syndromes) and assigns them weights defined by the evaluation function $f^\alpha(\mathcal{T}^\alpha; C)$ – defining the probability $P_{f^\alpha}^\alpha(C|S^{\text{p},r})$. This is repeated for all correction operators C (in our case, we only need to consider two corrections). The correction that maximizes this probability is then returned. In the following, we will explicitly formulate Equation (2.37) for the classical bit-flip model and for the PTIM.

⁵⁵Here it is $|S_{\text{red},\mathcal{I}_s}^p| = |E_{\mathcal{I}_s}^p|$.

Classical MLD

Consider the decoder $\mathcal{D}_{\text{ML}}^{\text{bi}}$ for the classical bit-flip model. The decoder knows the probability $p/2$ for a flip to occur and the syndrome record $S^{\text{p},r}$. Given this information, the decoder calculates the probability for a possible correction operator C . We can write this as

$$P_{f^{\text{bi}}}^{\text{bi}}(C|S^{\text{p},r}) = \sum_{\tilde{E}^{\text{p}}} \underbrace{P^{\text{bi}}(\tilde{E}^{\text{p}})}_{P^{\text{bi}}(\mathcal{F}^{\text{bi}})} \cdot \delta(\tilde{E}^{\text{p}}; S^{\text{p},r}) \cdot \underbrace{\delta(\tilde{E}^{\text{p}}; C)}_{f^{\text{bi}}(\tilde{E}^{\text{p}}; C)} \quad (2.57a)$$

$$= \sum_{\tilde{E}^{\text{p}}} \left(\frac{p}{2}\right)^{|\tilde{E}^{\text{p}}|} \left(1 - \frac{p}{2}\right)^{LT - |\tilde{E}^{\text{p}}|} \delta(\tilde{E}^{\text{p}}; S^{\text{p},r}) \cdot \delta(\tilde{E}^{\text{p}}; C). \quad (2.57b)$$

Here we perform the sum over all possible bit flip patterns \tilde{E}^{p} and calculate their probability $P^{\text{bi}}(\tilde{E}^{\text{p}})$ (disregarding the syndrome measurements). The function $\delta(\tilde{E}^{\text{p}}; S^{\text{p},r})$ filters all valid bit-trajectories by returning the value 1 if the pattern \tilde{E}^{p} matches the recorded syndromes. Otherwise, it returns the value 0, disregarding trajectories that are incompatible with the syndromes. Similarly, the function $\delta(\tilde{E}^{\text{p}}; C)$ filters the sum for trajectories that actually are corrected by the operator C .

We will now regroup this sum by introducing stacks. It is obvious that multiple patterns \tilde{E}^{p} yield the exact same syndrome results S^r for a given pattern S^{p} . Consider a single stack. Within the stack, the bit may be flipped once or three times — the difference will not be observed by the following syndrome measurement. To be precise, the syndromes can only distinguish between an even or odd number of flips within a stack. We now split the lattice into $|\{\mathcal{J}\}|$ stacks and then only consider whether or not a bit has *effectively* been flipped within a stack.

For a stack with a thickness of n time steps, we call $P_n^{\text{bi}}(\mathbb{1})$ the probability of a bit not being flipped and $P_n^{\text{bi}}(X)$ the probability for it to be flipped. By performing the sum over all stack possibilities, we can rewrite Equation (2.57b) to

$$P_{f^{\text{bi}}}^{\text{bi}}(C|S^{\text{p},r}) = \sum_{\substack{\mathbf{x} \in \left\{ \begin{pmatrix} x_1 \\ \vdots \\ x_{|\{\mathcal{J}\}|} \end{pmatrix} \right\} \\ x_k \in \{\mathbb{1}, X\}}} \left[\prod_{j=1}^{|\{\mathcal{J}\}|} P_{n_j}^{\text{bi}}(x_j) \right] \delta(\mathbf{x}; S^{\text{p},r}) \cdot \delta(\mathbf{x}; C). \quad (2.58)$$

Here we add up all possible stack flip results (“flip” or “no flip”) and multiply their probabilities. The functions $\delta(\mathbf{x}; S^{\text{p},r})$ and $\delta(\mathbf{x}; C)$ again check if the sampling \mathbf{x} complies with all syndromes and the correction operator C .

We will now explicitly calculate the classical stack probabilities $P_n^{\text{bi}}(\mathbb{1})$ and $P_n^{\text{bi}}(X)$. A classical bit will effectively not be flipped within a stack if the stack features any even

number of flips. Thus it is

$$P_n^{\text{bi}}(\mathbb{1}) = \sum_{i=0}^{\lfloor n/2 \rfloor} \left(\frac{p}{2}\right)^{2i} \left(1 - \frac{p}{2}\right)^{n-2i} \binom{n}{2i} \quad (2.59a)$$

$$= \left[\sum_{i=0}^n \left(\frac{p}{2}\right)^i \left(1 - \frac{p}{2}\right)^{n-i} \binom{n}{i} + \sum_{i=0}^n \left(-\frac{p}{2}\right)^i \left(1 - \frac{p}{2}\right)^{n-i} \binom{n}{i} \right] \cdot \frac{1}{2} \quad (2.59b)$$

$$= \frac{1}{2} + \frac{1}{2} \cdot (1-p)^n. \quad (2.59c)$$

Here, we first sum over all combinations of even numbers of bit flips on a stack of n time steps and calculate their probability via the bit flip probability $p/2$. We then split the sum into two sums such that the second sum cancels all odd terms of the first one. This allows us to apply the binomial theorem twice in the final step. The same procedure can also be applied for odd numbers of bit flips, leading to an effective flip in the stack:

$$P_n^{\text{bi}}(X) = \sum_{i=0}^{\lfloor (n-1)/2 \rfloor} \left(\frac{p}{2}\right)^{2i+1} \left(1 - \frac{p}{2}\right)^{n-2i-1} \binom{n}{2i+1} \quad (2.60a)$$

$$= \left[\sum_{i=0}^n \left(\frac{p}{2}\right)^i \left(1 - \frac{p}{2}\right)^{n-i} \binom{n}{i} - \sum_{i=0}^n \left(-\frac{p}{2}\right)^i \left(1 - \frac{p}{2}\right)^{n-i} \binom{n}{i} \right] \cdot \frac{1}{2} \quad (2.60b)$$

$$= \frac{1}{2} - \frac{1}{2} \cdot (1-p)^n \quad (2.60c)$$

Note that as expected $P_n^{\text{bi}}(\mathbb{1}) + P_n^{\text{bi}}(X) = 1$.

Quantum Mechanical MLD

We will now explicitly calculate the probability $P_{f^{\text{qm}}}^{\text{qm}}(C|S^{\text{p},r})$ for the quantum system with a given correction C and syndrome record $S^{\text{p},r}$. It is

$$P_{f^{\text{qm}}}^{\text{qm}}(C|S^{\text{p},r}) = \sum_{EP} \underbrace{P^{\text{qm}}(EP) \cdot P^{\text{qm}}(S^r|EP)}_{P^{\text{qm}}(\mathcal{T}^{\text{qm}}|S^{\text{p}})} \cdot \delta(EP; S^{\text{p},r}) \cdot f^{\text{qm}}(\mathcal{T}^{\text{qm}}|C) \quad (2.61a)$$

$$= \sum_{EP} P^{\text{qm}}(EP) \cdot \left(\frac{1}{2}\right)^{|S_{\text{red}}^{\text{p}}|} \cdot \delta(EP; S^{\text{p},r}) \cdot |\langle \Psi_0 | C | \Psi(T) \rangle|^2 \quad (2.61b)$$

$$= \sum_{EP} P^{\text{qm}}(EP) \cdot \left[\prod_{\mathcal{J} \in \{\mathcal{J}\}} \left(\frac{1}{2}\right)^{|S_{\text{red}, \mathcal{J}}^{\text{p}}|} \right] \cdot \delta(EP; S^{\text{p},r}) \cdot \delta(EP, S^{\text{p},r}; C) \cdot \begin{cases} 1, & \text{cluster survives,} \\ \frac{1}{2}, & \text{else} \end{cases} \quad (2.61c)$$

with the sum over all possible patterns EP and the probability $P^{\text{qm}}(EP) = p^{|EP|} \cdot (1-p)^{LT-|EP|}$ for one of those patterns to occur. Here, $P^{\text{qm}}(\mathcal{T}^{\text{qm}}|S^{\text{p}})$ is the probability for a trajectory to

occur, given a pattern of syndrome measurements.⁵⁶ $P^{\text{qm}}(S^{\text{r}}|E^{\text{p}})$ denotes the probability for a system with given error and syndrome patterns actually to feature a given set of syndrome results S^{r} :

$$P^{\text{qm}}(S^{\text{r}}|E^{\text{p}}) = \left(\frac{1}{2}\right)^{|S_{\text{red}}^{\text{p}}|} \quad (2.62)$$

The function $\delta(E^{\text{p}}; S^{\text{p,r}})$ returns the value 1 if the error pattern is actually consistent with the recorded syndromes and 0 if it cannot even produce the given syndrome results; it filters out all invalid terms from the sum.⁵⁷

In Equation (2.61c), we separate the lattice into islands. $\delta(E^{\text{p}}, S^{\text{p,r}}; C)$ returns 0 if the initial cluster survives in the assumed system *and* the final state $|\Psi(T)\rangle$ is not corrected by the correction operator C . Otherwise, it returns the value 1.

Introducing 1-0- U Trits in the System

To relate the classical probability [Equation (2.58)] and the quantum mechanical probability [Equation (2.61)], we will now consider the system to be filled with trits instead of a real quantum state. A maximum likelihood decoder on this system would internally calculate the probabilities

$$P_{f^{\text{tr}}}^{\text{tr}}(C|S^{\text{p,r}}) = \sum_{E^{\text{p}}} \sum_{\Psi^{\text{tr}}} \underbrace{P^{\text{tr}}(E^{\text{p}}) \cdot \left(\frac{1}{2}\right)^{|\Psi^{\text{tr}}|_U}}_{P^{\text{tr}}(\mathcal{T}^{\text{tr}}|S^{\text{p}})} \cdot \delta(\Psi^{\text{tr}}; E^{\text{p}}) \cdot \delta(\Psi^{\text{tr}}; S^{\text{p,r}}) \cdot \underbrace{\delta(\Psi^{\text{tr}}; C)}_{=: f^{\text{tr}}(\mathcal{T}^{\text{tr}}, C)}. \quad (2.63)$$

Here we sum over all possible patterns E^{p} and all trit patterns Ψ^{p} – filtering out the matching trajectories via the function $\delta(\Psi^{\text{tr}}; E^{\text{p}})$. The probability for an error pattern to arise is the same as for the PTIM $P^{\text{tr}}(E^{\text{p}}) = P^{\text{qm}}(E^{\text{p}})$, and (given the patterns M^{p}) one specific trajectory arises with probability

$$P^{\text{tr}}(\mathcal{T}^{\text{tr}}|M^{\text{p}}) = \left(\frac{1}{2}\right)^{|\Psi^{\text{tr}}|_U}. \quad (2.64)$$

The function $\delta(\Psi^{\text{tr}}; S^{\text{p,r}})$ filters all trajectories that match the recorded syndromes. Finally, the evaluation function for trits f^{tr} filters all trajectories for a given correction C – this function is essentially identical to the classical evaluation function f^{bi} .

We will now regroup Equation (2.63) into islands to relate $\mathcal{D}_{\text{ML}}^{\text{tr}}$ with its quantum mechanical counterpart $\mathcal{D}_{\text{ML}}^{\text{qm}}$ [cf. Figure 2.16 (d)]. Let $P_{\mathcal{I}}^{\text{tr}}(S_{\mathcal{I}}^{\text{r}}|M_{\mathcal{I}}^{\text{p}}, C)$ be the probability for the syndrome results occurring on an island \mathcal{I} , given the measurement patterns M^{p} , and assuming that the correction operator C reconstructs the initial state. On a single island $\mathcal{I} \neq \mathcal{I}_{\text{s}}$ we find that trits are switched from the state U to 1 or 0

$$|\Psi^{\text{tr}}|_U = |S_{\text{red}, \mathcal{I}}^{\text{p}}| + 1 \quad (2.65)$$

⁵⁶For simplicity we exclude the results of the error measurements from the trajectories \mathcal{T}^{qm} as they play no role to a decoder.

⁵⁷ $\delta(E^{\text{p}}; S^{\text{p,r}})$ returns the value 1 if the error pattern allows for a quantum trajectory that complies with all syndrome measurement results.

times.⁵⁸ If the island \mathcal{I} is neither the initial island \mathcal{I}_s nor the final island \mathcal{I}_e , there are two possible trajectories for the trit pattern $\Psi_{\mathcal{I}}^{\text{tr}}$ [cf. Equation (2.56)]; i.e., two ways to create the same syndrome results.⁵⁹ Note that the final island \mathcal{I}_e in the case $\mathcal{I}_e \neq \mathcal{I}_s$ also allows for two trajectories, but only one of them is compatible with the correction operator C . If we instead consider the initial island $\mathcal{I} = \mathcal{I}_s$, the fixed initial state allows for only one possible trajectory $\mathcal{I}_{\mathcal{I}_s}^{\text{tr}}$ and it is

$$|\Psi_{\mathcal{I}_s}^{\text{tr}}|_U = |S_{\text{red}, \mathcal{I}_s}^{\text{p}}|. \quad (2.66)$$

Combining all possible cases, we find the probability

$$P_{\mathcal{I}}^{\text{tr}}(S_{\mathcal{I}}^{\text{r}} | M_{\mathcal{I}}^{\text{p}}, C) = \left(\frac{1}{2}\right)^{|S_{\text{red}, \mathcal{I}}^{\text{p}}|} \cdot \begin{cases} \frac{1}{2} \cdot 2, & \text{if } \mathcal{I} \neq \mathcal{I}_s \wedge \mathcal{I} \neq \mathcal{I}_e, \\ 1, & \text{if } \mathcal{I} = \mathcal{I}_s, \\ \frac{1}{2}, & \text{if } \mathcal{I} = \mathcal{I}_e \neq \mathcal{I}_s \end{cases} \quad (2.67)$$

for a given set of syndrome results to occur on an island \mathcal{I} . We use this result to rewrite Equation (2.63):

$$\begin{aligned} & P_{f^{\text{tr}}}^{\text{tr}}(C | S^{\text{p}, \text{r}}) \\ &= \sum_{EP} P^{\text{tr}}(EP) \cdot \left[\prod_{\mathcal{I} \in \{\mathcal{I}\}} P_{\mathcal{I}}^{\text{tr}}(S_{\mathcal{I}}^{\text{r}} | M_{\mathcal{I}}^{\text{p}}, C) \right] \cdot \delta^{\text{tr}}(EP; S^{\text{p}, \text{r}}) \cdot \delta^{\text{tr}}(EP, S^{\text{p}, \text{r}}; C) \end{aligned} \quad (2.68a)$$

$$\begin{aligned} &= \sum_{EP} P^{\text{tr}}(EP) \cdot \left[\prod_{\mathcal{I} \in \{\mathcal{I}\}} \left(\frac{1}{2}\right)^{|S_{\text{red}, \mathcal{I}}^{\text{p}}|} \cdot \begin{cases} 1, & \text{if } \mathcal{I} \neq \mathcal{I}_e \vee \mathcal{I} = \mathcal{I}_s, \\ \frac{1}{2}, & \text{if } \mathcal{I} = \mathcal{I}_e \neq \mathcal{I}_s \end{cases} \right] \\ &\cdot \delta^{\text{tr}}(EP; S^{\text{p}, \text{r}}) \cdot \delta^{\text{tr}}(EP, S^{\text{p}, \text{r}}; C) \end{aligned} \quad (2.68b)$$

The function $\delta^{\text{tr}}(EP; S^{\text{p}, \text{r}})$ returns the value 1 if the chosen error pattern allows for a trit pattern Ψ^{tr} which is consistent with all syndromes and 0 otherwise. Note that, by construction, the model of trits is created to obey similar rules to the PTIM and it is $\delta^{\text{tr}}(EP; S^{\text{p}, \text{r}}) = \delta(EP; S^{\text{p}, \text{r}})$ [cf. Equation (2.61a)]. The function $\delta^{\text{tr}}(EP, S^{\text{p}, \text{r}}; C)$ returns the value 1 if the assumed measurement patterns and results allow for a trit pattern Ψ^{tr} which is corrected by C . If $\mathcal{I}_s \neq \mathcal{I}_e$, the final island \mathcal{I}_e allows for two different (complementary) trit patterns $\Psi_{\mathcal{I}_e}^{\text{tr}}$ — one of which matches C . In this case, $\delta^{\text{tr}}(EP, S^{\text{p}, \text{r}}; C) = 1$. If however $\mathcal{I}_s = \mathcal{I}_e$, only one trit pattern is allowed which either fits C or \bar{C} . Only in this case $\delta^{\text{tr}}(EP, S^{\text{p}, \text{r}}; C)$ can vanish. In other words: only if the initial cluster survives in the quantum trajectory, there exists a consistent trajectory of trits which complies with all syndromes but not with C . The rules for trajectories of trits are constructed such that they mimic those of the PTIM and it is $\delta^{\text{tr}}(EP, S^{\text{p}, \text{r}}; C) = \delta(EP, S^{\text{p}, \text{r}}; C)$ [cf. Equation (2.61c)]. When comparing Equations (2.61c) and (2.68b) it is now easy to see that

$$P_{f^{\text{tr}}}^{\text{tr}}(C | S^{\text{p}, \text{r}}) = P_{f^{\text{qm}}}^{\text{qm}}(C | S^{\text{p}, \text{r}}). \quad (2.69)$$

⁵⁸This becomes clear from considering an example; see Figure 2.16 (c).

⁵⁹Technically, an island can also only contain a single trit in the state U with $|S_{\text{red}, \mathcal{I}}^{\text{p}}| = 0$. Then it is trivially $P_{\mathcal{I}}^{\text{tr}}(S_{\mathcal{I}}^{\text{r}} | M_{\mathcal{I}}^{\text{p}}, C) = 1$.

This proves that the decoders $\mathcal{D}_{\text{ML}}^{\text{tr}}$ and $\mathcal{D}_{\text{ML}}^{\text{qm}}$ calculate the exact same probabilities for a given record of syndrome measurements and a correction operator C – they are equivalent [cf. Figure 2.16 (d)].

Now we will rewrite Equation (2.63) by regrouping the sum in stacks in order to relate the model of trits to the classical bit-flip model. Consider a single stack in a trajectory of trits. Right before the stack starts, the trit is not in the state U , because every stack starts right after an adjacent syndrome measurement. The stack also ends with a syndrome measurement, which again forbids the trit to be in the state U . In between its endpoints, the stack allows the trit to switch into the state U or not. Thus, we can calculate the effective flip probabilities for a trit with thickness n . We call $P_n^{\text{tr}}(X)$ the probability for the trit switching its state in a stack, and $P_n^{\text{tr}}(\mathbb{1})$ for it to effectively remain in the same state. Then [similarly to Equation (2.58)] we find

$$P_{f^{\text{tr}}}^{\text{tr}}(C|S^{\text{p},r}) = \sum_{\substack{\mathbf{x} \in \left\{ \begin{pmatrix} x_1 \\ \vdots \\ x_{|\mathcal{J}|} \end{pmatrix} \right\} \\ x_k \in \{\mathbb{1}, X\}}} \left[\prod_{j=1}^{|\mathcal{J}|} P_{n_j}^{\text{tr}}(x_j) \right] \delta(\mathbf{x}; S^{\text{p},r}) \cdot \delta(\mathbf{x}; C). \quad (2.70)$$

The only difference between this and the same calculation in the classical bit-flip model [cf. Equation (2.58)] is that the probabilities for the stacks $P_{n_j}^{\text{tr}}(x_j)$ are calculated differently. A trit is effectively flipped if and only if at least one error measurement has been performed *and* the trit is transferred into the flipped state by the final syndrome measurement (which happens with probability 1/2). Thus it is

$$P_n^{\text{tr}}(X) = \frac{1}{2} \sum_{i=1}^n p^i (1-p)^{n-i} \binom{n}{i} \quad (2.71a)$$

$$= \frac{1}{2} - \frac{1}{2} (1-p)^n \quad (2.71b)$$

$$= P_n^{\text{bi}}(X). \quad (2.71c)$$

Here we again used the binomial theorem (note that the sum starts at 1) and compared the result with Equation (2.60c). There are two ways for a trit to effectively remain unchanged in a stack. Either one or more errors are measured and the trit returns into its initial state with the final syndrome measurement, or no error is measured at all. Thus it is

$$P_n^{\text{tr}}(\mathbb{1}) = (1-p)^n + \frac{1}{2} \sum_{i=1}^n p^i (1-p)^{n-i} \binom{n}{i} \quad (2.72a)$$

$$= \frac{1}{2} + \frac{1}{2} (1-p)^n \quad (2.72b)$$

$$= P_n^{\text{bi}}(\mathbb{1}), \quad (2.72c)$$

where we compared the result with Equation (2.59c). A comparison of Equations (2.58) and (2.70) shows that

$$P_{f^{\text{tr}}}^{\text{tr}}(C|S^{\text{p},r}) = P_{f^{\text{bi}}}^{\text{bi}}(C|S^{\text{p},r}), \quad (2.73)$$

which proves that the decoders $\mathcal{D}_{\text{ML}}^{\text{bi}}$ and $\mathcal{D}_{\text{ML}}^{\text{tr}}$ are equivalent [cf. Figure 2.16 (d)].

Now we can finally combine Equations (2.69) and (2.73) to prove that it is indeed

$$P_{f_{\text{qm}}}^{\text{qm}}(C|S^{\text{p},r}) = P_{f_{\text{tr}}}^{\text{tr}}(C|S^{\text{p},r}) = P_{f_{\text{bi}}}^{\text{bi}}(C|S^{\text{p},r}) \quad (2.74)$$

and the classical MLD is actually also the MLD of the PTIM. □

CHAPTER 3

Scaling of Entanglement Measures in Loop Models with Extended Criticality

In Section 1.1, we introduced the notion of random quantum circuits. In particular we focused on the ability of hybrid quantum circuits (which contain unitaries *and* measurements) to exhibit entanglement transitions. These transitions separate parameter regimes in which entanglement measures are governed by distinct scaling laws. Typically, these circuits exhibit a volume-law phase at small monitoring rates and transition into an area-law phase in regimes of stronger monitoring rates. In this chapter, we explore a special class of hybrid quantum circuits that do *not* follow this common behavior: Qubit models that can be mapped to free-fermion circuits generally do not feature a stable volume-law phase under finite monitoring rates [22]. Instead, some circuits of this kind feature extended critical phases which were only recently discovered [30]. Here, we study such critical phases in detail using very efficient simulation models. The contents of this chapter are based on the work published in Ref. [118].

3.1 Introduction

Hybrid quantum circuits with unitary operations and projective measurements show interesting entanglement dynamics [5–7, 14, 119]. We previously alluded to this in Subsection 1.1.2. Unitaries usually create entanglement between qubits, while local measurements purify their state. This competition typically drives a transition between a volume-law and an area-law entangling phase. Transitions of this kind have already been realized

in experimental settings [18–20]. Similarly, it was shown that the competition of two types of non-commuting measurements in circuits without unitaries may drive a transition between two distinct area-law phases [21, 24]. For hybrid quantum circuits with free fermions — i.e., matchgate quantum circuits — the dynamics are different, as arbitrarily small finite monitoring rates are found to destroy any volume law [8, 21–23, 28]. Nonetheless, measurements do not necessarily reduce entanglement structures down to an area law. Instead, Alberton et al. found that an extended critical regime can exist at weak monitoring rates [30]. This *critical phase* is characterized by the logarithmic scaling of entanglement structures. Initially mixed states purify on a different (slower) time scale in the critical regime compared to an area-law phase. While an extended critical phase was first found in a time-continuous setting (see also Refs. [42, 120–124]), recent investigations demonstrate the existence of critical regimes in more accessible, trotterized quantum circuits [23, 26–29, 125–128]. In these realizations, criticality typically arises under the competition of at least three different types of operations. In this chapter, we study some specific hybrid quantum circuits (in the qubit picture), where the competition of just one unitary and one measurement is enough to realize a critical phase. Beyond that, we focus on the universality of the critical entanglement scaling on the boundaries of critical phases.

Typical hybrid quantum circuits are restricted to Clifford unitaries and Pauli measurements, such that they can be simulated exactly via the stabilizer formalism with polynomial overhead [46–49], as stated by the Gottesmann-Knill theorem [45]. Another class of quantum circuits that can be simulated efficiently is the class of matchgate quantum circuits [52, 54–57, 129], which can be mapped to circuits of quadratic fermions. We introduced both formalisms in Section 1.2. Critical entangling phases are typically subject to very strong finite-size effects and are often only distinguishable from area-law phases at large system sizes. Thus, it is important to utilize models that can be simulated very efficiently, in order to observe subtle scaling differences in entanglement structures. To this end, the computational overhead for Clifford and matchgate circuits is still too high. Instead, the most promising approach is to consider a special class of quantum circuits that can be mapped to classical randomized *loop models* [29, 126, 128], where loops typically represent world lines of Majorana fermions. This is possible in circuits with unitaries which are both — Clifford gates and matchgates — and under the application of appropriate measurements. The calculation of entanglement structures is then reduced to much simpler calculations on the Brauer algebra [130–132], allowing for the simulation of system sizes $L > 10^4$. Classical loop models have been investigated in different contexts for a long time [133–153]. This long-standing interest gives them a key advantage: In some special cases, there already exists a physical understanding of their dynamics. For example, the *completely packed loop model with crossings* (CPLC) is known to map to a σ model. This field theory provides a theoretical understanding of the properties of the critical entangling phase in quantum circuits represented by the CPLC [126, 128, 154]. However, the most generic loop models (where every loop represents a Majorana fermion) map to bosonic quantum circuits (via a Jordan–Wigner transformation) with twice as many types of unitaries and measurements

– distinguishing cases in which operations are applied on even or odd Majorana indices. Therefore, critical phases in such models are typically realized in circuits that feature multiple unitaries and/or multiple competing measurements. For example (as we will see later), models that map to the CPLC typically feature two unitaries and two measurements, and a critical phase can only be reached under application of all four of those operations [126, 128]. In a different model introduced by Klocke et al., three types of measurements are sufficient to realize a critical phase [29] (see also Refs. [27, 28]).¹ We note that quantum circuits, which are represented by loop models, are typically considered in $1 + 1$ dimensions. Higher-dimensional loop models have however also been investigated, for example on cube lattices [154–156] and on a hexagonal lattice with an additional temporal direction [157]. The additional spatial direction does however limit the system sizes that can be simulated.

In this chapter, we use the qubit language (which is likely the natural language for a possible future quantum simulator) to describe hybrid quantum circuits that feature a critical phase. These circuits can be mapped to less generic loop models, which allows us to investigate their critical properties in detail. We investigate multiple Clifford unitaries that lead to the realization of a variety of qualitatively different phase diagrams. In particular, we find circuits that reach the critical regime with only one type of Pauli measurement and one Clifford unitary. The study of phase diagrams with critical phases enables us to verify a previous observation that links the *orientability* of loop models to the existence of critical phases [29, 128, 154]. Our investigations are based on three common entanglement measures: The entanglement $S(A)$ of a subsystem of qubits A to all other qubits in a steady state, the mutual information $I(A, B)$ between two small subregions A and B of qubits, and the ancilla entropy S_{anc} of a system with an initially entangled system of ancilla qubits (these measures were introduced in detail in Subsection 1.1.1). Using these measures, we investigate the critical phases in our models and verify that they do not follow the scaling laws that would be expected from a conformal field theory description. We do however find evidence that the entanglement transition between the critical phases and area-law phases may be described by a conformal field theory.

3.2 Critical Scaling in Random Matchgate Circuits

Let us establish some intuition on extended critical phases in a generic example of a random monitored matchgate circuit. Consider an open chain of L qubits with T time steps initialized in the state $|0 \dots 0\rangle$. Every time step is divided into two substeps:

¹There also exist models that exhibit a critical phase and require only one type of measurement, but involve randomly sampled unitaries [26, 128]. These are however usually not represented by loop models.

1. Random matchgates $U_{i,i+1}$ are applied on every pair of neighboring qubits i and $i + 1$ with probability p . The matchgates are each constructed from two Haar random $SU(2)$ matrices [158–161] according to Equation (1.11). As they generally do not commute, the gates are applied in a brickstone pattern.
2. On every qubit i , a projective measurement of the observable Z_i is performed with probability $1 - p$ (monitoring rate).

We simulate the system as a matchgate quantum circuit (see Subsection 1.2.2) using a particularly efficient implementation, which is described in Section 3.A. First, we consider this circuit for the case $L = T$ and calculate the averaged ancilla entropy S_{anc} (see Subsection 1.1.1). In Figure 3.1 (a), we show the ancilla entropy S_{anc}/L , normalized by the system size L . At $p = 1$, we find $S_{\text{anc}}/L = 1$. As no measurements are performed, the entanglement between the system qubits and the ancilla qubits cannot be destroyed. This indicates a volume law. At finite monitoring rates $p < 1$, this volume law breaks down. With increasing system size L , the normalized ancilla entropy decreases. This rapid purification of the initially mixed state is consistent with the expectation for all monitored systems that can be mapped to free fermions [22].

As the volume law breaks down, the system does not necessarily follow an area law. Instead, there exists an intermediate critical regime with a transition at a value p_c . At sufficiently small monitoring rates $0 < (1 - p) < (1 - p_c)$ the entanglement follows a critical scaling law and only breaks fully down towards an area law at large monitoring rates $(1 - p) > (1 - p_c)$. The (not normalized) entanglement entropy S_{anc} makes this transition visible, as we show in Figure 3.1 (b). The point at which the system leaves the area-law phase is clearly indicated by a crossing. We estimate $p_c \approx 0.62$.

The entanglement with an ancilla system S_{anc} is very well-suited for finding such transitions, as it generally shows very clear crossings and does not require a simulation into the steady state ($L \propto T$ suffices). To see what differentiates the critical phase from the trivial area law, we now calculate the average entanglement entropy $S(L/2)$ of the half system in the steady state. Figure 3.1 (c) shows that at $p < p_c$, the entanglement in the system is approximately constant. At $1 > p > p_c$ however, we observe a logarithmic dependence $S(L/2) \sim \log(L)$ (note the logarithmic scaling on the axis). This behavior generally serves as an indicator of a critical point or regime.²

The model we described here serves us as a first example of an extended critical regime as first described in fermionic circuits by Alberton et al. in Ref. [30]. The logarithmic scaling of the critical phase is oftentimes very subtle and can easily be overlooked.³ In this thesis, we aim to gain more detailed insights into the scaling behavior of critical phases and their boundaries. This will require much more efficient simulations at much larger system sizes.

²We also observe a logarithmic scaling at some critical points, see for example Figure 1.4.

³The fact that volume laws break down in systems with free fermions at any finite monitoring rates [22] was known two years before the critical phase was discovered [30].

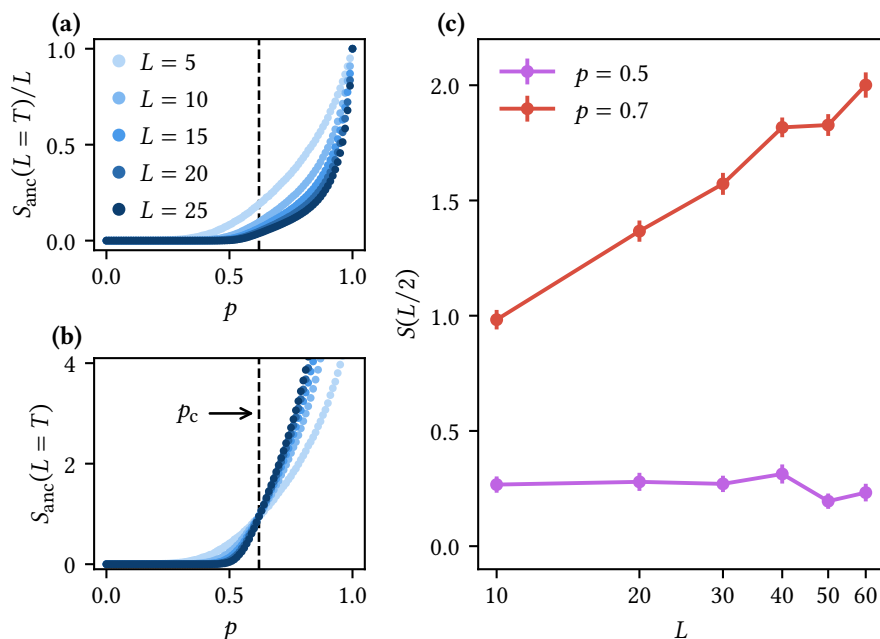


Figure 3.1 • Critical entanglement scaling in a random matchgate quantum circuit.

(a) Normalized entanglement S_{anc}/L with an ancilla system for different system sizes $L = T$ at $p \in [0, 1]$. At finite monitoring rates $p < 1$ the volume law breaks down. (b) S_{anc} shows a clear crossing indicating a transition from an area-law phase at $p < p_c$ to a critical regime at $p > p_c$. We estimate a transition at $p \approx 0.62$. (c) Scaling behavior of the entanglement $S(L/2)$ below and above the critical monitoring rate p_c in the steady state (given the initial state $|0 \dots 0\rangle$). At $p > p_c$, the entanglement grows logarithmically with the system size. All subfigures show averages over 10^4 samples and contain error bars [in (a) and (b), they are smaller than the data points].

3.3 Loop Models

In the remainder of this chapter, we consider a special class of stabilizer circuits that are connected to loop models. This will allow us to simulate them up to sizes of the order $L \sim 10^4$. Systems of this kind were already studied in physical and mathematical contexts before [21, 128, 154]. In the following, we will show that unitary gates that are part of the stabilizer formalism *and* the matchgate formalism, can always be simulated in loop models. Note however that this is not restrictive and in this chapter we will also present a stabilizer circuit which does *not* fall into the matchgate formalism but can still be represented by loops (cf. Figure 3.2).⁴

⁴While we specifically describe models from the orange region of the diagram in Figure 3.2, there may also exist loop models in the gray region. We make no statements about these here.

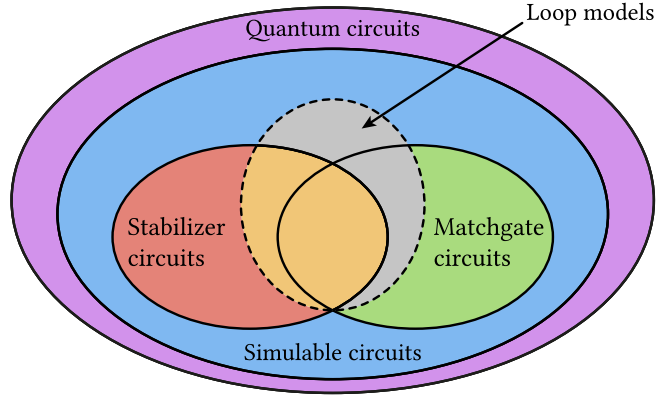


Figure 3.2 • Classes of quantum circuits. Incomplete Venn diagram of types of hybrid quantum circuits. Stabilizer circuits and matchgate circuits are known to be simulable in polynomial time (see Section 1.2). Some circuits are known to be represented by loop models. In this chapter, we consider models in the orange area of the diagram, i.e., loop models that contain Clifford gates that may also be matchgates. It is assumed, that loop model representations also exist in the gray areas of the diagram.

3.3.1 Unitaries that are Cliffords and Matchgates

Let the initial state $|\Psi_0\rangle \in \mathcal{H}$ of a circuit be a stabilizer state and U be a Clifford gate which maps the Pauli group onto itself: $U\mathcal{P}_L U^\dagger = \mathcal{P}_L$. The state is described by the stabilizer group $\mathfrak{S} \subset \mathcal{P}_L$. In Subsection 1.2.2 we introduced the Majorana operators γ_{2i-1} and γ_{2i} and the Jordan–Wigner transformation, which connects them to Pauli operators. It is easy to see that any element $\rho \in \mathcal{P}_L$ of the Pauli group can be written in terms of Majoranas

$$\rho = \chi \prod_{\mu=1}^{2L} \gamma_{\mu}^{\alpha_{\mu}} \quad (3.1)$$

with a prefactor $\chi \in \{\pm 1, \pm i\}$ and a set of exponents $\alpha_{\mu} \in \{0, 1\}$. This allows us to write all generators \mathfrak{s} of the stabilizer group \mathfrak{S} in terms of Majorana operators. Applying U to the state $|\Psi\rangle \mapsto U|\Psi\rangle$ amounts to mapping all generators

$$\mathfrak{s} \mapsto U\mathfrak{s}U^\dagger = U \left[\chi \prod_{\mu=1}^{2L} \gamma_{\mu}^{\alpha_{\mu}} \right] U^\dagger = \chi \prod_{\mu=1}^{2L} \left[U\gamma_{\mu}^{\alpha_{\mu}}U^\dagger \right]. \quad (3.2)$$

The new stabilizer generators are therefore found by mapping all Majorana operators $\gamma_{\mu} \mapsto U\gamma_{\mu}U^\dagger$. As these are again representations of Pauli operators via the Jordan–Wigner transformation, it is

$$U\gamma_{\mu}U^\dagger = \chi_{\mu} \prod_{v=1}^{2L} \gamma_v^{\alpha_{\mu,v}}. \quad (3.3)$$

Now consider the case in which U is *also* a matchgate, i.e., it fulfills

$$UY_\mu U^\dagger = \sum_{\nu=1}^{2L} R_{\mu\nu} \gamma_\nu \quad (3.4)$$

with some rotation $R \in SO(2L)$. For Equations (3.3) and (3.4) to be true, U must map Majorana operators to products of Majoranas and also act as a rotation on the space of all Majoranas. It must be

$$UY_\mu U^\dagger = \chi_\mu \gamma_\xi, \quad (3.5)$$

requiring R to be a signed permutation matrix that maps the Majorana mode γ_μ to another mode γ_ξ , up to some prefactor $\chi_\mu \in \{\pm 1\}$.⁵ In this chapter, we aim to calculate entanglement measures, which are not affected by phases. Therefore, we will omit them from now on. This allows us to reduce the stabilizer formalism to a procedure of tracking permutations of Majorana modes. In this process, unitaries U are mapped to elements of the symmetric group S_{2L} .

Simulations are performed by assigning two Majorana modes to every qubit and tracking them as *Majorana world lines* through time. We call this a *loop model*. Unitaries that are local in the fermionic picture, only permute a finite number of world lines and can thus be applied in constant time $\mathcal{O}(1)$. This makes simulations of circuits with unitaries that are Cliffords and matchgates very efficient. In Figure 3.3 we show how a circuit can be translated into a loop model. As we omitted prefactors, multiple quantum trajectories are represented by the same loop configuration, if they share the same entanglement dynamics. Note that we use the term “loop” very loosely here to represent connected lines — even if they are not closed. We use this terminology to match existing literature in mathematics [154].⁶

3.3.2 Encoding Initial States

When allowing hybrid quantum circuits to evolve into their steady state ($T \gg L$), they typically lose most of the information about their initial state.⁷ The scaling behavior of entanglement measures in the steady state is therefore unaffected by our choice of the initial state. Without loss of generality, we assume initial states of the form $|\Psi_0\rangle = |00 \dots 0\rangle$ with the stabilizer group $\mathfrak{S} = \langle Z_1, Z_2, \dots, Z_L \rangle$. A quick Jordan–Wigner transformation allows us to rewrite the generators in Majorana modes:

$$\mathfrak{S} = \langle i\gamma_1\gamma_2, i\gamma_3\gamma_4, \dots, i\gamma_{2L-1}\gamma_{2L} \rangle \quad (3.6)$$

The state is stabilized by pairs of Majorana operators. We implement this in the loop model by coupling Majorana world lines in pairs before the first time step (see Figure 3.3).⁸ Unitaries

⁵It is $\chi_\mu \in \{\pm 1\}$ because Equation (3.3) requires $|\chi_\mu| = 1$ and $R \in SO(2L)$ is a real matrix.

⁶Loop models in two dimensions are often considered on a torus. In our physical context, this corresponds to periodic boundaries in space and time. On such a geometry, all loops would be closed.

⁷Some information may be retained for long times; for example, the PTIM can protect a logical qubit (see Chapter 2).

⁸As we ignore the prefactors of generators, we would use the same loop representation for any initial product state $|m_1 m_2 \dots m_L\rangle$ with $m_i \in \{0, 1\}$.

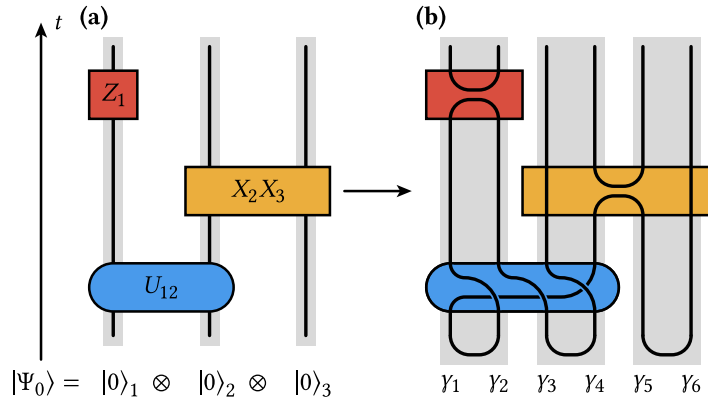


Figure 3.3 • Translation to the loop model. (a) Common representation of a quantum circuit where qubits are represented by vertical lines. Here we show a unitary gate U_{12} and measurements of the observables Z_1 and X_2X_3 . (b) Translation of the circuit into a loop model with two Majorana world lines per qubit. Unitaries are represented by permutations of world lines and measurements create a new pair of world lines. The loop model shown is initialized in a product state polarized in the z -direction (for example $|\Psi_0\rangle = |000\rangle$).

only permute the Majorana indices (ignoring prefactors), such that any future stabilizer group can still be generated by pairs of Majoranas. After applying the unitary shown in Figure 3.3 (b) the state is stabilized by $\mathfrak{S} = \langle i\gamma_1\gamma_4, i\gamma_2\gamma_3, i\gamma_5\gamma_6 \rangle$ (before the measurements are applied).

3.3.3 Projective Measurements

The loop model also allows for the projective measurement of observables of the form $O = i\gamma_\mu\gamma_\nu$. We understand this by following the rules of the stabilizer formalism (remember Subsection 1.2.1). If $\pm O \in \mathfrak{S}$, the measurement process is deterministic and nothing needs to be done. In this case, we will find the Majorana world lines γ_μ and γ_ν to be already paired. Otherwise, the stabilizer group has the form

$$\mathfrak{S} = \langle i\gamma_\mu\gamma_\xi, i\gamma_\nu\gamma_o, \dots \rangle = \langle i\gamma_\mu\gamma_\xi, -\gamma_\mu\gamma_\xi\gamma_\nu\gamma_o, \dots \rangle, \quad (3.7)$$

where only the first generator in the second expression anticommutes with O . Applying the measurement amounts to replacing this generator:

$$\mathfrak{S} \mapsto \langle O, -\gamma_\mu\gamma_\xi\gamma_\nu\gamma_o, \dots \rangle = \langle i\gamma_\mu\gamma_\nu, i\gamma_o\gamma_\xi, \dots \rangle \quad (3.8)$$

Thus, the measurement of $O = i\gamma_\mu\gamma_\nu$ pairs up the world lines γ_μ and γ_ν and then pairs up any “loose ends” if they exist.

As we only consider local operations, we restrict ourselves to on-site measurements $Z_i = i\gamma_{2i-1}\gamma_{2i}$ and off-site measurements $X_iX_{i+1} = i\gamma_{2i}\gamma_{2i+1}$ that couple neighboring qubits.

Figure 3.3 shows how such measurements are translated into the loop picture. It is straightforward to verify that this construction obeys the rules we described. Using hash tables, a single measurement can be applied in the loop model in $\mathcal{O}(1)$ time. The final state shown in Figure 3.3 (b) is stabilized by $\mathfrak{S} = \langle i\gamma_1\gamma_2, i\gamma_3\gamma_6, i\gamma_4\gamma_5 \rangle$.

Note that measurements do not correspond to permutations of Majorana world lines but instead model the Temperley-Lieb algebra TL_{2L} [162, 163]. A hybrid circuit includes unitaries and measurements and is a representation of the Brauer algebra \mathfrak{B}_{2L} [130–132].⁹

3.3.4 Entanglement Measures

In Subsection 1.2.1, we introduced a procedure which allows for the efficient calculation of entanglement entropies in stabilizer circuits, following a protocol described by Fattal et al. [50]. In loop models of Majorana world lines, there exists an even more efficient method. The following arguments are based on Ref. [6].

Take any stabilizer group \mathfrak{S} on L qubits and a subregion A which includes $|A| \leq L$ of those qubits. Let $\mathfrak{S}_A \subseteq \mathfrak{S}$ be the subset of operators which only act on A , i.e., which act trivially on the complement \bar{A} . Then, the entanglement entropy of A to its environment is [6, 50]

$$\mathcal{S}(A) = |A| - \log_2 |\mathfrak{S}_A|. \quad (3.9)$$

If \mathfrak{S}_A is generated by $\mathcal{G}_{\mathfrak{S}_A}$, then it is

$$\mathcal{S}(A) = |A| - |\mathcal{G}_{\mathfrak{S}_A}|. \quad (3.10)$$

Remember that the generating set for a stabilizer group is not unique — the choice of generators is a gauge. A loop configuration corresponds to one specific set of generators of the form $\mathcal{G} = \{i\gamma_\mu\gamma_\nu, i\gamma_\xi\gamma_\theta, \dots\}$ that generate the stabilizer group

$$\mathfrak{S} = \langle \mathcal{G} \rangle = \langle i\gamma_\mu\gamma_\nu, i\gamma_\xi\gamma_\theta, \dots \rangle. \quad (3.11)$$

Note that every Majorana mode appears exactly once in the generating set. When Jordan–Wigner transforming a generator, we find the form (assuming $\mu < \nu$)

$$i\gamma_\mu\gamma_\nu \propto \begin{Bmatrix} X_{\lceil \mu/2 \rceil} \\ Y_{\lfloor \mu/2 \rfloor} \end{Bmatrix} \cdot Z_{\lceil \mu/2 \rceil + 1} \cdots Z_{\lfloor \nu/2 \rfloor - 1} \cdot \begin{Bmatrix} X_{\lceil \nu/2 \rceil} \\ Y_{\lfloor \nu/2 \rfloor} \end{Bmatrix} \quad (3.12)$$

where the endpoints are either Pauli- x or Pauli- y matrices. For every stabilizer, we can thus define a leftmost (and rightmost) qubit, on which it acts nontrivially. Consider a single qubit site i and let l_i (r_i) be the number of generators with left (right) endpoints on i . The choice of generators \mathcal{G} in Equation (3.11) ensures that $l_i + r_i = 2$ at all sites i . If a generating set has this property, we say that \mathcal{G} is in the *clipped gauge* [6, 165].¹⁰ Note that the clipped gauge requires a fixed ordering of qubits. In our scenario, we use the ordering of the Jordan–Wigner string.

⁹The Temperley-Lieb algebra is a subalgebra of the Brauer algebra [164].

¹⁰Given any stabilizer group, it is always possible to find a generating set in the clipped gauge [165]. An algorithm for this was described in Ref. [6]. Here we get the clipped gauge immediately from the loop model.

Now let A be a contiguous subregion of qubits and $\mathcal{G}_A \subseteq \mathcal{G}$ be the subset of generators that only act on A . If \mathcal{G} is in the clipped gauge, then it is $\mathcal{G}_A = \mathcal{G}_{\mathcal{C}_A}$ and $\mathcal{C}_A = \langle \mathcal{G}_A \rangle$.¹¹ We may split the generating set \mathcal{G} into three groups.

1. If a generator is contained in A (i.e., its left and right endpoints are both in A), it is part of \mathcal{G}_A . There are $|\mathcal{G}_A| =: n_{A \leftrightarrow A}$ such generators.
2. A generator can have one endpoint in A and the other in \bar{A} . Assume that there are $n_{A \leftrightarrow \bar{A}}$ such generators. In the clipped gauge, every qubit site hosts two generator endpoints, i.e., the subregions A and \bar{A} host an even number of endpoints. It is easy to count that $n_{A \leftrightarrow \bar{A}}$ must be even.
3. A generator can have both endpoints in \bar{A} . Note that, since \bar{A} is not necessarily contiguous, such generators may still have support on A . Let there be $n_{\bar{A} \leftrightarrow \bar{A}}$ such generators.

Counting up all generators, it is $L = n_{A \leftrightarrow A} + n_{A \leftrightarrow \bar{A}} + n_{\bar{A} \leftrightarrow \bar{A}}$. In the clipped gauge, $2|A|$ endpoints of stabilizer generators are contained in the subregion A . They are split into two types

$$|A| = n_{A \leftrightarrow A} + \frac{1}{2}n_{A \leftrightarrow \bar{A}}. \quad (3.13)$$

We insert this in Equation (3.10) to find the result by Nahum et al. [165]

$$\mathcal{S}(A) = |A| - n_{A \leftrightarrow A} = \frac{1}{2}n_{A \leftrightarrow \bar{A}}. \quad (3.14)$$

In our loop models, this result is very intuitive: $n_{A \leftrightarrow \bar{A}}$ is the number of loops with one endpoint in A and one in \bar{A} . The entanglement entropy $\mathcal{S}(A)$ is calculated by counting these loops and dividing the result by 2.¹² A count of this kind is done in $\mathcal{O}[\min(|A|, |\bar{A}|)] \subseteq \mathcal{O}(L)$ time. Together with the application of unitaries and measurements, which occur in numbers proportional to L and T , loop model simulations have the complexity $\mathcal{O}(LT)$. This is a massive speedup compared to the $\mathcal{O}(L^4T)$ runtimes of the stabilizer formalism.

It is important to note that this method for the calculation of entanglement entropies fails for non-contiguous subsystems. This prohibits us from calculating non-local mutual informations in loop models [6, 29]. The reason for this lies in the existence of Jordan–Wigner strings contained in the stabilizer generators, which are hidden within the loop model (this may lead to $|\mathcal{G}_A| \neq n_{A \leftrightarrow A}$). We may however translate a given loop configuration into a set of stabilizer generators and use the (less efficient) standard method by Fattal et al. [50]. This allows us to also determine mutual informations in smaller systems.

¹¹This statement is not trivial. We refer to the proof in Ref. [6].

¹²As an example we can consider the final state shown in Figure 3.3 and assume that the subsystem A contains the first two qubits. There is one loop $i\gamma_1\gamma_2$ which is fully contained in A ($n_{A \leftrightarrow A} = 1$) and two loops $i\gamma_3\gamma_6$ and $i\gamma_4\gamma_5$ which span across both subsystems ($n_{A \leftrightarrow \bar{A}} = 2$). Therefore, it is $\mathcal{S}(A) = 1$.

3.3.5 Loop Models with Ancilla Systems

As we already demonstrated in Figure 3.1, it will be useful to investigate the entanglement \mathcal{S}_{anc} between the system and an initially entangled ancilla system.¹³ Tracking the decrease of \mathcal{S}_{anc} over time amounts to tracking how a circuit “forgets” its initial state; i.e., we measure the survival of information in a circuit [29]. Luckily, the loop model makes this very easy. Let the sites $\{1, \dots, L\}$ correspond to system qubits and $\{L + 1, \dots, 2L\}$ be the ancilla qubits. Without loss of generality, we assume the fully entangled initial state to be stabilized by

$$\mathfrak{C} = \langle i\gamma_1\gamma_{2L+1}, i\gamma_2\gamma_{2L+2}, \dots \rangle. \quad (3.15)$$

We do not need to track the world lines of Majorana modes, which correspond to ancilla qubits. Instead, we can initialize only the world lines of the system in an unpaired configuration and then perform a loop model simulation on the site $\{1, \dots, L\}$ as usual. \mathcal{S}_{anc} is calculated by counting the loops which connect the initial state with the final state (also called the *spanning number* [154]) and dividing the result by 2.

Loops that do not pair two Majorana modes, are not associated with stabilizer generators. In the approach we describe here, a fully mixed initial state ($\mathfrak{C} = \{\mathbb{1}\}$) is assumed and we track its purification. This allows us to simulate only L qubits (instead of $L + L$, including the ancilla qubits).

3.3.6 The PTIM as a Loop Model

As a first example we can translate the PTIM into the loop model. A simple local basis transformation allows us to rotate the measurements $E_i = Z_i$ and $S_e = S_{(i,i+1)} = X_i X_{i+1}$. This was previously done in Refs. [21, 126]. Simply following the rules from Figure 3.3, we can now translate the circuit illustrated in Figure 1.5. The resulting loop model is shown in Figure 3.4. Models of this kind are called *completely packed loop models without crossings* (the $1 + 1$ -dimensional plane is fully occupied by loops and they never cross due to the lack of unitaries in the PTIM). Here we show a configuration which assumes the initial state to be a product state, polarized in the z -direction.

Figure 3.4 allows us to understand the connection between the loop model and the bond percolation model (and by extension the colored cluster model). As the loops enclose areas, we can fill them with colors to find percolation clusters (we show the bonds as lines in Figure 3.4). If we successively add time steps — merging colors, whenever two areas are joined — we reproduce exactly the trajectory of the CCM. In Chapter 2, we commented on the survival of an initial cluster (or logical qubit), which is indicated by the initial color in the CCM surviving until the last time step. In other words, information survives in the system if there is a percolation cluster which connects the first and last time step. This occurs if and only if there are loops connecting the initial and final state. The survival of a logical qubit is therefore tightly connected with the spanning number (i.e., the entropy \mathcal{S}_{anc}).

¹³The concept of utilizing reference qubits to probe entanglement measures was pioneered by Gullans et al. in Refs. [71, 72, 102].

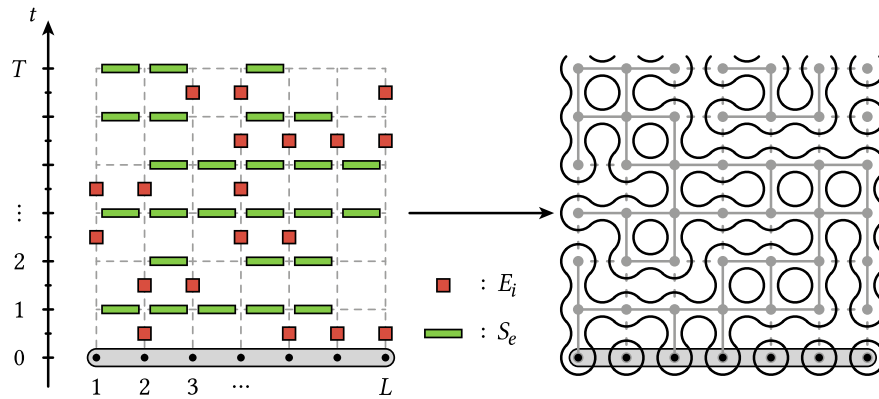


Figure 3.4 • Loop model representation of the PTIM. Translation of the PTIM into a loop model via Figure 3.3. We overlay the corresponding bond percolation pattern from Figure 1.5 to show how the two are related.

3.4 The Merritt–Fidkowski Model

In this section, we will cover a model which was first introduced by Merritt and Fidkowski in Ref. [128] (and very similarly by Sang et al. in Ref. [126]). We will call it the *Merritt–Fidkowski model* (MF model). It represents an expansion on the PTIM that also includes unitaries. These unitaries are both, Clifford gates and matchgates, and allow the MF model to be simulated in a loop representation. This makes it interesting for multiple reasons: As a circuit which can be mapped to a circuit of Gaussian fermions, the MF model exhibits nontrivial entanglement dynamics, including an extended critical phase. It therefore proves to be a great model system to investigate such critical regimes. Furthermore, the loop model, which represents the MF model, falls into the category of *completely packed loop models with crossings* (CPLCs) that have already been rigorously investigated by Nahum et al. in Ref. [154]. While this research was done from an abstract, theoretical perspective, it allows us to gain some great understanding of the phase diagram of the physical MF model. Some of these insights will also transfer to the critical phases of different systems. Here, we will give an introduction to the MF model and reproduce some of the results by Merritt and Fidkowski, and also add some findings of our own.

3.4.1 The Model

The MF model contains *on-site* operations that act on single qubits i , and *off-site* operations that act on neighboring qubits $e = (i, i + 1)$. We denote the unitaries as U_i^{on} and U_e^{off} , and the measurements as $M_i^{\text{on}} = Z_i$ and $M_e^{\text{off}} = X_i X_{i+1}$. Trajectories of the MF model are divided into even and odd time steps:

- In odd time steps, random on-site operations are performed on every qubit i . With probability p , the unitary gate U_i^{on} is applied, and with probability $(1 - p)q$, a projec-

tive measurement of M_i^{on} is performed. Otherwise [with probability $(1-p)(1-q)$], no gate (or the identity $\mathbb{1}_i$) is applied.

- In even time steps, off-site operations on pairs $e = (i, i+1)$ of neighboring qubits are performed. With probability p , the unitary gate U_e^{off} is applied, and with probability $(1-p)(1-q)$, a projective measurement of M_e^{off} is performed. Otherwise [with probability $(1-p)q$], no gate is applied.

In this setup, the probability p determines the ratio of unitaries and measurements and q controls the ratio of on- and off-site measurements. At $p = 0$, no unitaries are performed and the MF model maps to the PTIM.¹⁴ Further note that at $p = 1$ only unitaries are performed and the parameter q has no effect. Therefore, the parameter space of the MF model is best displayed in a triangular shape (barycentric coordinates) with the corner points $(p = 0, q = 0)$, $(p = 0, q = 1)$, and $p = 1$.

The unitaries of the MF model are Clifford gates and matchgates. We use

$$U_i^{\text{on}} = S_i \quad (3.16a)$$

$$U_{i,i+1}^{\text{off}} = H_i H_{i+1} S_i S_{i+1} CZ_{i,i+1} H_i H_{i+1} \quad (3.16b)$$

with the Hadamard gate H , the phase gate S and the symmetric controlled- Z gate $CZ = (\mathbb{1} \otimes H) \text{CNOT} (\mathbb{1} \otimes H)$. By writing these operators in matrix form, it is easy to verify that they are indeed matchgates [cf. Equation (1.11)].¹⁵ To find the representations of the unitaries in the loop model, we write them in fermionic language.¹⁶

$$U_i^{\text{on}} = \frac{1}{\sqrt{2}} (\mathbb{1} - \gamma_{2i-1} \gamma_{2i}) \quad (3.17a)$$

$$U_{i,i+1}^{\text{off}} = \frac{1}{\sqrt{2}} (\mathbb{1} - \gamma_{2i} \gamma_{2i+1}) \quad (3.17b)$$

Here we omitted some global phases. It is now easy to see that the unitary gates switch pairs of neighboring Majorana world lines

$$U_i^{\text{on}} \gamma_{2i-1} (U_i^{\text{on}})^\dagger = \gamma_{2i} \quad (3.18a)$$

$$U_i^{\text{on}} \gamma_{2i} (U_i^{\text{on}})^\dagger = -\gamma_{2i-1} \quad (3.18b)$$

$$U_{i,i+1}^{\text{off}} \gamma_{2i} (U_{i,i+1}^{\text{off}})^\dagger = \gamma_{2i+1} \quad (3.18c)$$

$$U_{i,i+1}^{\text{off}} \gamma_{2i+1} (U_{i,i+1}^{\text{off}})^\dagger = -\gamma_{2i} \quad (3.18d)$$

while commuting with all other modes. We illustrate this loop representation in Figure 3.5.¹⁷

¹⁴By convention, the probabilities of the MF model are called p and q and should not be confused with the probabilities of the PTIM (cf. Section 1.3).

¹⁵ U^{on} only acts on one qubit, but can easily be expanded as in $U^{\text{on}} \otimes \mathbb{1}$.

¹⁶The symmetric nature of the unitaries in the fermionic picture is by design, i.e., the gates were chosen to be represented by a “simple” loop model.

¹⁷Interestingly, the same loop model representation also emerges in a two-dimensional toric code model with three competing types of measurements [27].

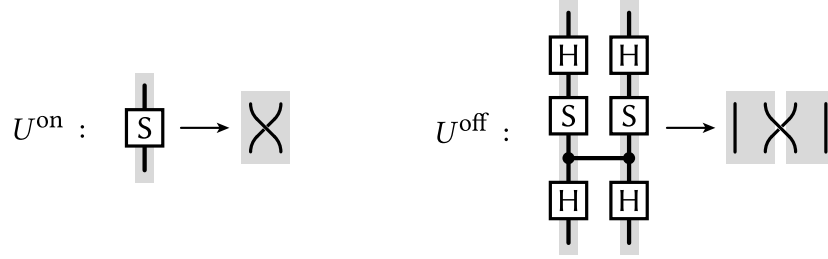


Figure 3.5 • Unitaries of the MF model. The on- and off-site unitaries of the MF model are part of the Clifford group and are represented by crossings in the loop model.

Together with the projective measurements, the MF model is represented by a *completely packed loop model with crossings* (CPLC) as shown in Figure 3.6. Most simulations in this chapter were performed in the loop representation. We verified this approach numerically by comparing it to an equivalent simulation in the stabilizer formalism.

In this thesis (differently from the previous literature [128]), we view the MF model from a bosonic perspective and define it via Pauli measurements and Clifford unitaries. The rationale is the following: The bosonic MF model is equivalent to the fermionic MF model under a Jordan–Wigner transformation, and the fermionic model can be represented as a loop model; i.e., our approach hinges on the Jordan–Wigner transformation of the unitaries in Equations (3.17a) and (3.17b) and the measurements $Z_i = iy_{2i-1}y_{2i}$, $X_iX_{i+1} = iy_{2i}y_{2i+1}$. However, the Jordan–Wigner transformation yields different fermionic operators if we assume periodic boundary conditions. In the bosonic MF model, periodic boundaries are implemented via the unitary $U_{L,1}^{\text{off}}$ [as defined in Equation (3.16b)] and the measurement $M_{L,1} = X_LX_1$. On the fermionic MF model, the boundaries are bridged by the unitary $(1 - \gamma_{2L}\gamma_1)/\sqrt{2}$ and the measurement of $iy_{2L}y_1$. These are distinctly different operators and make the loop model invalid as a means to simulate the bosonic MF model. Nonetheless, periodic boundaries will allow us to eliminate some unwanted boundary effects and thus obtain simulation data that makes the entanglement dynamics easier to interpret. In Subsection 3.B.1 we prove that the loop model can be used to calculate entanglement entropies $\mathcal{S}(l)$ in the MF model with periodic boundaries, if no ancilla qubits are included. When considering entanglement measures that include ancilla qubits however, the fermionic loop model with periodic boundaries does *not* match bosonic stabilizer simulations, and yields incorrect results. In Subsection 3.B.2 we show that the difference between the simulated entanglements $\mathcal{S}_{\text{anc}}^{\text{f}}$ (obtained in fermionic loop models) and the correct entanglements $\mathcal{S}_{\text{anc}}^{\text{b}}$ (in the bosonic MF model) can never be greater than 1. The sample-averaged difference approaches a constant

$$\lim_{L \rightarrow \infty} [\mathcal{S}_{\text{anc}}^{\text{f}} - \mathcal{S}_{\text{anc}}^{\text{b}}] = C \quad (3.19)$$

with $|C| \leq 1$. This offset will not be important in our analysis. For clarity, we will denote all entanglement measures that were obtained for the fermionic model and do not represent the true bosonic values with the superscript ^f.

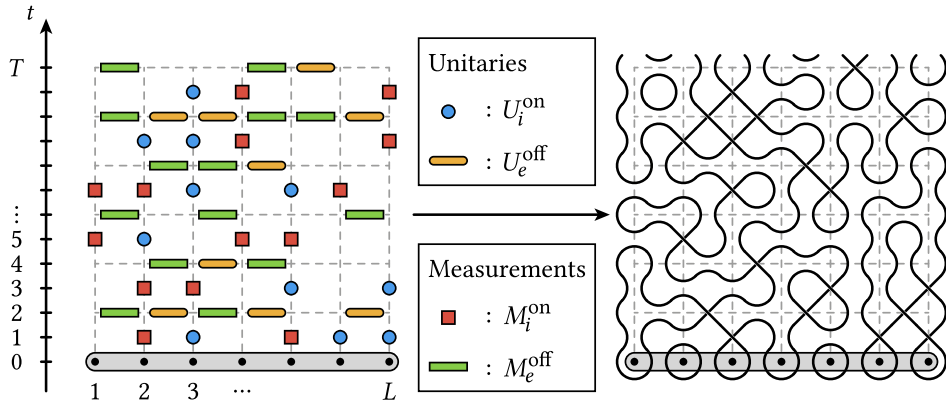


Figure 3.6 • Loop model representation of the MF model. Translation of the MF model (with open boundaries) into a loop model. Unitaries correspond to crossings of neighboring Majorana world lines; if no unitaries are performed, the model reduces to the PTIM (cf. Figure 3.4).

3.4.2 Phase Diagram

The MF model exhibits an extended critical phase [154]. To map out its phase diagram, we simulate the average entanglement entropy $S_{\text{anc}}^{\text{f}}$ for multiple system sizes $L = T$ with periodic boundaries. As we show in Figure 3.7 (a), the ancilla entropy exhibits a clear crossing at the entanglement transition from an area-law phase into the critical phase. We create the full phase diagram by considering pairs of sizes L and numerically locating the crossing points of $S_{\text{anc}}^{\text{f}}$ across the parameter space. To estimate the strength of finite-size effects, we do this for two pairs of system sizes. The resulting diagram shown in Figure 3.7 (b) is displayed in barycentric coordinates $q \leftarrow (1/2 - q)(1 - p) + 1/2$ (as q becomes superfluous at $p = 1$) and reproduces the results by Nahum et al. in Ref. [154].

The entanglement phase diagram features two distinct area-law phases and an extended critical phase. Only at the special point $p = 1$, the circuit exhibits a volume law. At the edges $q \in \{0, 1\}$, the area-law phases extend up to all values $p < 1$; i.e., the critical phase exists only at $0 < q < 1$, where both kinds of measurements are performed. This is due to symmetry reasons [128, 154], which we expand upon in Subsection 3.4.5. At the lower edge $p = 0$, the MF model reduces to the PTIM, and we find the two corresponding area-law phases with the critical point at $q = 0.5$ (cf. Subsection 1.3.2). The phase diagram is symmetric under $q \leftrightarrow 1 - q$ due to a symmetry of its loop model representation [128]. Note that only the average scaling behavior of entanglement measures exhibits this symmetry, while absolute values may differ.¹⁸

To better characterize the three phases, we analyze the entanglement entropy $S(L/2)$ in the steady state for increasing system sizes, given the initial state $|0 \dots 0\rangle$. We show this for points in each phase in Figure 3.7 (c). At large system sizes, the critical phase is

¹⁸See for example Figure 1.4, which shows that the entanglement itself is different in both phases, but the scaling behavior is consistent with an area law in both cases.

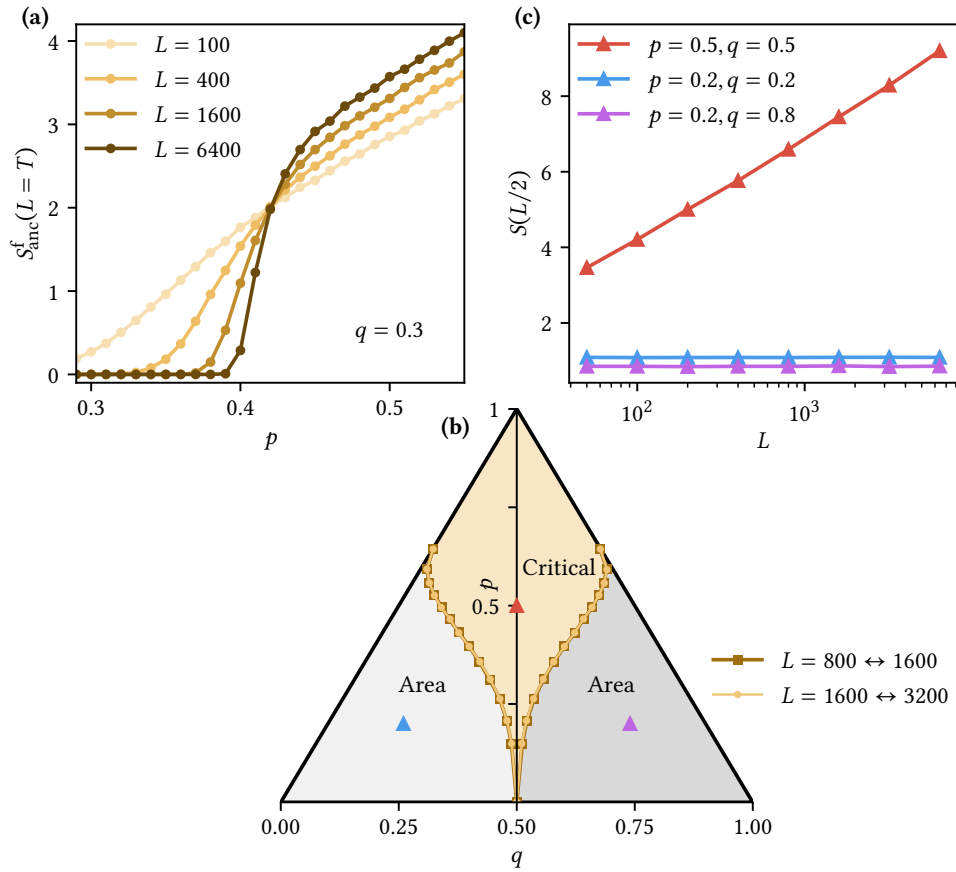


Figure 3.7 • Phase diagram of the MF model. (a) Entanglement transitions between an area-law phase and the critical phase manifest as a crossing in the entropy S^f_{anc} over multiple system sizes. Here we show data at $q = 0.3$ averaged over 10^4 samples (error bars are smaller than the data points). (b) The phase diagram was created by locating crossings of S^f_{anc} for pairs of system sizes. (c) Scaling behavior of the entanglement entropy $S(L/2)$ in the steady state for a point in every phase (given the initial state $|0 \dots 0\rangle$). The critical phase is characterized by a logarithmic growth of entanglement structures with L . Data points show averages over 10^4 sample trajectories; error bars are smaller than the points. All simulations were performed with periodic boundaries.

clearly dominated by a logarithmic growth of the entanglement entropy. [In fact, our data suggests a possible leading term of order $\sim \log^2(L)$ at *very* large sizes L .] The area-law phases exhibit the expected constant scaling of $S(L/2)$. These results are in agreement with Figure 3.1 (c), but the loop model allows us to reach much larger system sizes and reduce noise considerably.

From the PTIM we already know that the two area-law phases have different properties. In the bosonic picture, this is manifested by the existence of a global cluster in the entangling phase $q < 1/2$ – compared to only local clusters at $q > 1/2$. The fermionic loop model representation of the PTIM without periodic boundaries (see Figure 3.4) allows us to form a different intuition: In the entangling phase, a global *edge loop* that is located at the boundaries of the model emerges [154].¹⁹ This loop connects two Majorana modes on opposite sides of the system and is the fermionic equivalent of the global Bell cluster. It is stable in the left area-law phase (also at $p > 0$). In Figure 3.7 (a), we deliberately used periodic boundaries to remove the effects of the edge loop, because they tend to obscure the crossing point.

The true power of the MF model lies in the fact that its loop model representation – a completely packed loop model with crossings – allows for a field theory description. In Ref. [154], Nahum et al. demonstrated that the CPLC can be mapped to a σ model.²⁰ In this context, we can understand the critical phase of the MF model as a *Goldstone phase* in the field theory. This comes with some predictions for entanglement measures, which we will verify in the following.²¹

3.4.3 Goldstone Phase

In the Goldstone phase, the ancilla entanglement entropy S_{anc} depends approximately logarithmically on the system size L . This result was first found by Nahum et al. in Ref. [154] for spanning numbers on square-shaped loop models by using their connection to the σ model. We can directly transfer their prediction to the fermionic MF model with periodic boundaries:

$$S_{\text{anc}}^f(2L = T) \sim \frac{1}{4\pi} \log \left[\frac{L}{L_0(p, q)} \right] \quad (3.20)$$

Equation (3.20) is expected to approach equality in the thermodynamic limit $L \rightarrow \infty$. Here, $L_0(p, q)$ is a nonuniversal offset of the entanglement entropy. Crucially, the constant prefactor $1/4\pi \approx 0.080$ is universal across the full Goldstone phase. This specific value is only found for the fixed aspect ratio $2L = T$ – which is necessary to map the MF model to a square-shaped loop configuration (cf. Figure 3.6). More details on this map are provided in Section 3.C. We show simulation data of $S_{\text{anc}}^f(2L = T)$ for three sample points in the Goldstone phase in Figure 3.8 (a). Clearly, the data points do not follow a straight line, but exhibit a very strong finite-size effect (note the logarithmic scale). We use fit functions

¹⁹To see this, draw the loop model at $(p = 0, q = 0)$.

²⁰This is a type of field theory that is not necessarily a conformal field theory.

²¹The σ model itself will not be a topic of this chapter, but we will investigate how its predictions apply to different models that have not been mapped to a field theory.

$y = \alpha + \beta \log(x)$ to estimate the slope β of the data points. For more reliable results, we only perform the fits at large system sizes $L > 10^3$. The measured prefactors β range between 0.082 and 0.084. The deviation of these values from the prediction $1/4\pi$ is explained by residual finite-size effects, which extend to system sizes $> 10^4$. Comparing our results to the data shown in Ref. [154], we were able to estimate that the finite-size effects we observe here are similar in strength to those found in simulations by Nahum et al.

The work by Klocke et al. [29] allows us to make a more general prediction for the purification of an initially mixed state. For any large system dimensions L and T , the ancilla entropy approaches

$$S_{\text{anc}}^f \sim F\left(\frac{T}{L} \frac{4\pi}{\log\left[\frac{L}{L_0(p,q)}\right]}\right) \quad (3.21)$$

with some function F . At $2L = T$, this prediction aligns with Equation (3.20). Indeed, we can extend it to any fixed aspect ratio T/L to find

$$S_{\text{anc}}^f(L \propto T) \sim \beta \log\left[\frac{L}{L_0(p,q)}\right]. \quad (3.22)$$

The prefactor β is universal, i.e., within the Goldstone phase, it depends only on T/L and not on p and q . We verify this by performing simulations at the same points as before, but for $L = T$ [see Figure 3.8 (a)]. Using the same fit functions, we observe the prefactors $\beta_{p=0.5,q=0.5} \approx 0.169$, $\beta_{p=0.6,q=0.4} \approx 0.166$ and $\beta_{p=0.7,q=0.7} \approx 0.173$. Again, we attribute the differences to finite-size effects.

In general, Equation (3.21) estimates how quickly an initially mixed state purifies in the Goldstone phase for a given set of parameters p and q . To verify this, we arbitrarily choose the point $p = q = 0.5$ and simulate S_{anc}^f as a function of T for the system sizes $L \in \{500, 1000, 2000, 4000\}$. The data is shown in Figure 3.8 (b); we find a good collapse at $L_0 \approx \exp(-10)$. Note that we only obtain this result within the Goldstone phase. In fact, remember that Figure 3.7 (a) showed the entanglement transition of the MF model as a crossing of the entanglement S_{anc}^f . On the transition line, S_{anc}^f only depends on the ratio T/L (and the parameters p and q), which is clearly different from Equation (3.21). This indicates that the phase transitions of the MF model are described by a different field theory. We will explicitly analyze the scaling of entangling measures on the transition lines in Subsection 3.4.4.

Finally, we compare the Goldstone phase of the MF model to a prediction on the scaling behavior in steady states. Take a contiguous subsystem A of size $1 \ll |A| = l \ll L$ at parameters p and q within the Goldstone phase. Then the average entanglement entropy

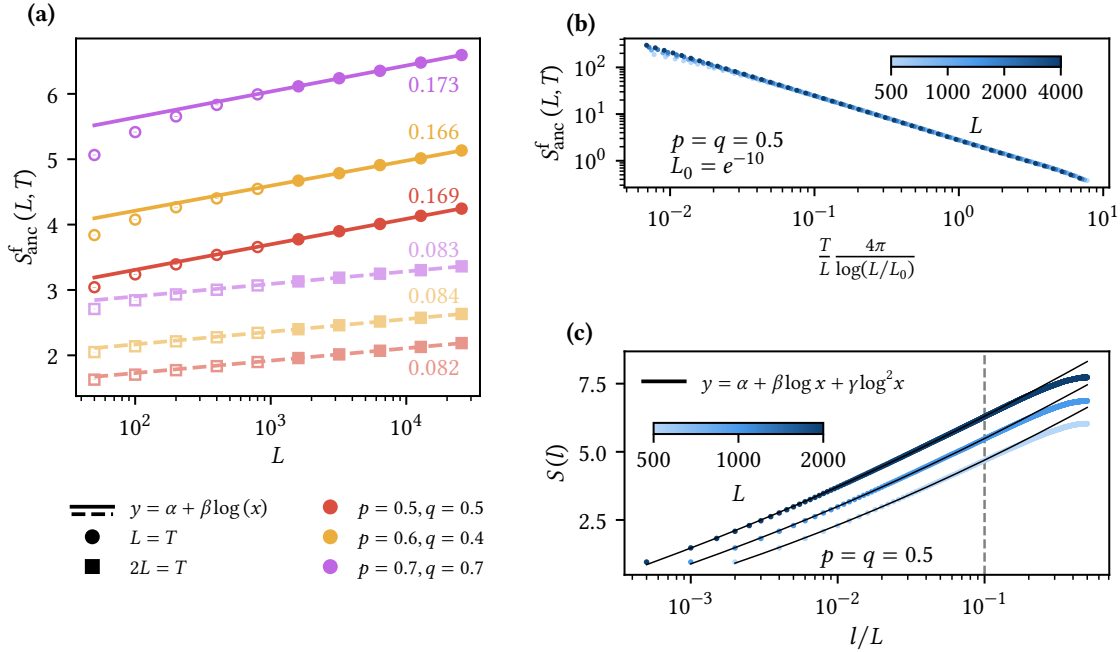


Figure 3.8 • Goldstone phase of the MF model. (a) In the Goldstone phase, the ancilla entropy $S_{\text{anc}}^f (L \propto T)$ scales logarithmically with L . We determine the prefactor β by fitting a function to the data points at $L > 10^3$ (solid points). The resulting values are shown next to the respective lines – indicating that β is universal. (b) Collapse of the entanglement data S_{anc}^f [cf. Equation (3.21)] for multiple values of L and T at $p = q = 0.5$. We estimate $L_0 \approx \exp(-10)$. (c) Entanglement entropy $S(l)$ in the steady state at the same point $p = q = 0.5$ (with initial state $|0 \dots 0\rangle$). At $l/L \leq 10^{-1}$ we fit the predicted function to the data. The quadratic contribution $\gamma \log^2 x$ is visible in the plot. Simulations in all subfigures show averages over 10^5 samples with periodic boundaries; error bars are smaller than the points.

$S(A)$ (assuming periodic boundaries) of the subregion in the steady state is predicted by the field theory description to scale as [126]

$$S(l) \sim \alpha + \beta \log l + \gamma \log^2 l. \quad (3.23)$$

Analogous predictions were recently made for other loop models [29] and similar time-continuous systems [38]. The quadratic term $\log^2 l$ would not be present if the Goldstone phase were described by a conformal field theory. [A similar quadratic contribution is barely visible in Figure 3.7 (c).] We verify Equation (3.23) by performing simulations of the entanglement entropy $S(l)$ at $p = q = 0.5$. In Figure 3.8 (c), we show our data and the corresponding fit functions $y = \alpha + \beta \log x + \gamma \log^2 x$. To comply with the requirement $l \ll L$, we perform the fits only at $l/L \leq 10^{-1}$. The fits match the data well and show a visible quadratic contribution ($\gamma > 0$). We note that Ref. [126] does give a prediction for the value of the prefactor $\gamma = (8\pi^2)^{-1}$. We were unable to verify this value in our own simulations — possibly due to strong finite-size effects.

We used this subsection to reproduce results that are already known for the MF model. In this context, our analysis serves as a check for our simulations. However, we will compare the conclusions made here with similar investigations on different systems later. Thus we may consider this subsection as a “benchmark” for scaling behaviors of extended critical phases. Note that Figure 3.8 illustrates very well, why it is necessary to reach very large system sizes (which we do by utilizing the loop model). Even at $L > 10^3$ we find finite-size effects. A similar scaling analysis on a generic matchgate circuit (cf. Figure 3.1) would be impossible.

3.4.4 Conformal Scaling of Entanglement Measures

The previous analyses in this section were predominantly reproductions of previously known results — preparing the investigations that will be presented in the remainder of this chapter. The following findings are new and were published in Ref. [118].

Without unitaries ($p = 0$), the MF model reduces to the PTIM, which maps to a bond percolation model on a square lattice (cf. Figure 1.5). The entanglement transition of the PTIM is well understood [24]. At the critical point $q = 1/2$, the PTIM can be described by a conformal field theory [59, 60]. This is a common property of second-order phase transitions. The field theory description of the PTIM allows for predictions for the scaling of the entanglement entropy and the mutual information at the phase transition, including some universal coefficients. The Goldstone phase of the MF model is described by a σ model which is *not* a conformal field theory [154] — we already made note of this when discussing Figure 3.8 (b). It is however reasonable to expect a conformal description of the boundaries between the Goldstone phase and the two area-law phases.²² In the following, we will investigate the scaling behaviors of entanglement measures on the phase boundaries of the MF model more thoroughly.

²²The phase boundaries are indicated by a crossing of the entanglement $S_{\text{anc}}^{\text{cf}}$, which is not described by Equation (3.21).

Entanglement Entropy

The conformal field theory of the PTIM predicts the entanglement entropy of a subsystem of length l

$$S(l) \sim \frac{c}{3} \log_2 \left[\frac{L}{\pi} \sin \left(\frac{\pi l}{L} \right) \right] \quad (3.24)$$

with the central charge c . As the field theory describes the continuum limit of a model, real systems approach this scaling law (up to a nonuniversal constant) at large sizes L with periodic boundaries in the steady state $T \gg L$. We will test if a similar scaling behavior can be found in the Goldstone phase of the MF model. If so, we will find the normalized entanglement entropy

$$\Delta S \left(\frac{l}{L} \right) \equiv S(l) - S \left(\frac{L}{2} \right) \sim \frac{\tilde{c}}{3} \log_2 \left[\sin \left(\frac{\pi l}{L} \right) \right] \quad (3.25)$$

with the prefactor \tilde{c} (which is not necessarily the central charge of the conformal field theory). At the critical point ($p = 0, q = 1/2$), the conformal field theory derived for the percolation transition predicts [24]

$$\tilde{c}(p = 0, q = 1/2) = \frac{3\sqrt{3} \log(2)}{2\pi} \approx 0.573. \quad (3.26)$$

We now consider different points in the phase diagram [Figure 3.7 (b)] and compare their scaling behavior with Equation (3.25). In Figure 3.9 (a1), we show simulation data of $\Delta S(l/L)$ for a point within the Goldstone phase and a point on its boundary. Simulations were performed for the system sizes $L \in \{100, 200, 300, 400, 500, 1000\}$ in the steady state. The insets clearly show that the collapse of the data points is better on the phase boundary. We further fit Equation (3.25) to the data for $L = 1000$. On the phase boundary, the fit matches the data points very well, while some minor deviations are visible within the Goldstone phase.

To systematically quantify how well the data points for different L collapse onto a single line, we evaluate $\Delta S(1/8)$ for different values L . The better the collapse is, the less these values differ from each other. We performed simulations for $L \in \{128, 526, 512\}$ in the vicinity of the phase boundary and evaluated the quality of the data collapse. An example is shown in the inset of Figure 3.9 (a2). Here, we indicate the quality of the collapse by the size of the data point; a smaller point indicates a better collapse. Clearly, the conformal description is most accurate at the phase transition. In regions close to the boundaries of the phase diagram, we find the point of best collapse to be slightly shifted away from the phase transition. We expect that this is due to finite-size effects [the phase boundaries were calculated using S_{anc}^f on system sizes up to $L = 3200$, cf. Figure 3.7 (b)]. In Figure 3.9 (a2), we show only the points of best collapse along the phase boundaries and indicate the fitted value of \tilde{c} by color. Clearly, \tilde{c} is not constant, but increases with p . This is not surprising; it indicates that the phase boundaries might be described by a conformal field theory which generally depends on p and q .

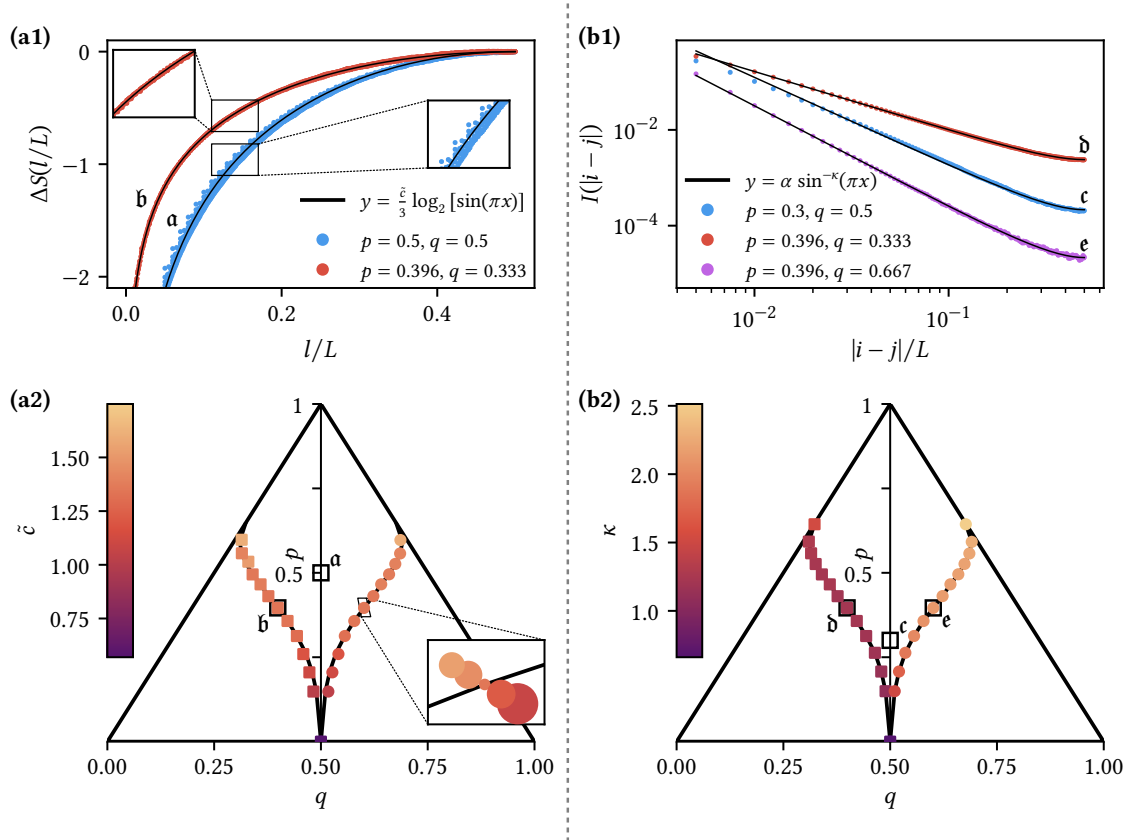
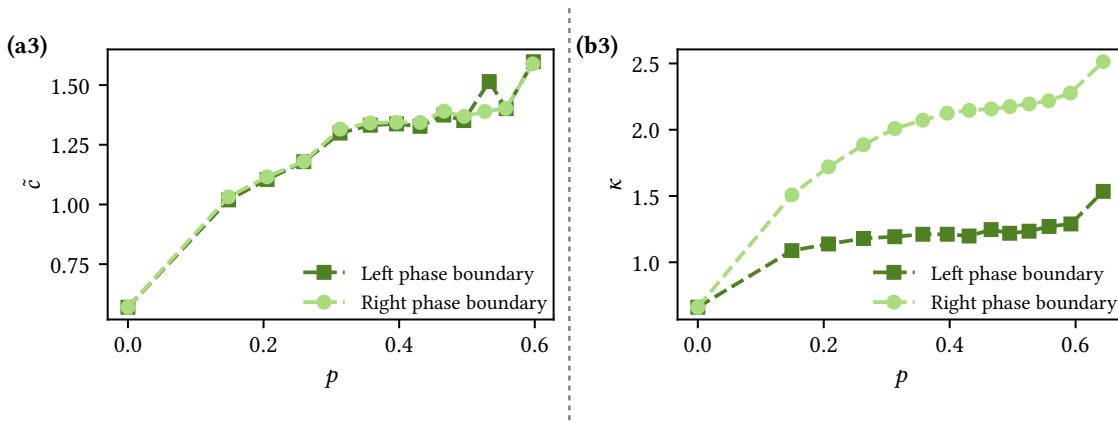


Figure 3.9 • Conformal scaling in the MF model. (a1) Collapse of the normalized entanglement entropy $\Delta S(l/L)$ for $L \in \{100, 200, 300, 400, 500, 1000\}$ averaged over 10^5 samples each (error bars are smaller than the data points). We fit the corresponding function to the data for the largest systems. The datasets **a** and **b** correspond to points within the Goldstone phase and on its boundary. (a2) The same analysis was performed in the vicinity of the phase transition. We only show the points with the best data collapse (simulated for $L \in \{128, 256, 512\}$). The inset shows multiple points in the vicinity of the phase boundary. The quality of the collapse is indicated by the size of the points (smaller points correspond to a better collapse). Colors represent the fitted value of \tilde{c} . (b1) Mutual information $I(|i-j|)$ on the phase boundaries and inside the Goldstone phase for systems of size $L = 400$ and 10^7 samples; error bars are mostly smaller than the data points. The corresponding fit was performed in logarithmic space. (b2) Similar simulations for $L = 128$ and 10^7 samples were performed along both phase boundaries, and the exponent κ was determined via fits. \curvearrowright



↷ **(a3)** Prefactors \tilde{c} for the data points in subfigure (a2) displayed in dependence of p . Our data clearly indicates a $q \leftrightarrow (1 - q)$ symmetry. **(b3)** The exponents κ from subfigure (b2) clearly break this symmetry. Both subfigures (a3) and (b3) match the prediction for the PTIM at $p = 0$.

We show this more clearly by plotting \tilde{c} as a function of p in Figure 3.9 (a3). The data shows some small step-like features – these are artifacts of our algorithm. As shown in the inset of Figure 3.9 (a2), around every point on the phase boundary, four more points were simulated. If the line of best collapse shifts to the next simulated point (due to finite-size effects), a small step appears in Figure 3.9 (a3). Clearly, \tilde{c} obeys a symmetry $q \leftrightarrow (1 - q)$. This is not surprising: We already found the same symmetry for the phase diagram and argued that the scaling behavior of all entangling measures derived from the loop model must obey it. Our findings indicate that the transition lines between the Goldstone phase and the area-law phases are well described by a conformal field theory, characterized by a prefactor $\tilde{c}(p, q)$ depending on p and q . This possibly extends the known theory for the PTIM transition to also include unitaries ($p > 0$).

Mutual Information

The conformal field theory for the PTIM transition also provides a prediction for the scaling behavior of the mutual information. Consider two qubit sites i and j in a system with periodic boundaries. Then, for large systems L in the steady state ($T \gg L$), it is [24]

$$I(i, j) = I(|i - j|) \sim \frac{\alpha}{\sin^\kappa\left(\pi\frac{|i-j|}{L}\right)}. \quad (3.27)$$

Here, α is a nonuniversal parameter and κ is a critical exponent. For the transition of the bond percolation model at $(p = 0, q = 1/2)$, it is $\kappa = 2/3$. To test the validity of Equation (3.27) at other points on the phase boundary and within the Goldstone phase, we choose representative parameter sets and perform simulations of the mutual information (in the steady state) at $L = 400$. The data is displayed in Figure 3.9 (b1). Here, we only show $|i - j| \geq 2$ to

avoid some local effects in the circuit model. We fit Equation (3.27) to the data to test the validity of a conformal description.²³ On the phase boundary, the fits match the data well. Within the Goldstone phase, the data points show a very slight right curve at small $|i - j|/L$, which cannot be perfectly matched by Equation (3.27). While the difference is subtle, we found that the conformal description consistently matches the data only in the vicinity of the phase boundary.

We simulate the mutual information along the phase boundaries and show the results in Figure 3.9 (b2). Similar to \tilde{c} , the exponent κ clearly depends on p and q . However, κ does break the symmetry $q \leftrightarrow (1 - q)$; see Figure 3.9 (b3). This is not surprising: At its core, the symmetry $q \leftrightarrow (1 - q)$ is based on the loop model description of the MF model. It subsequently applies to all quantities derived from this model, for example $\Delta S(l/L)$. However – as we discussed in Subsection 3.3.4 – the mutual information cannot be calculated directly from the loop model. Instead, we translated a loop configuration into a generating set of a stabilizer group and determined the mutual information using the standard approach [50]. Therefore, $I(|i - j|)$ may break the symmetry.

Our simulations of entanglement entropies and mutual information both suggest that there exists a conformal field description for the transition lines between the Goldstone phase of the MF model and the two area-law phases. At $(p = 0, q = 1/2)$, the coefficients $\tilde{c}(p, q)$ and $\kappa(p, q)$ coincide with those of the PTIM.

3.4.5 Transitions at $q \in \{0, 1\}$

At the phase diagram boundaries $q = 0$ and $q = 1$, the MF model does not show a transition into the Goldstone phase. To actually enter the critical regime, both Clifford unitaries (U_i^{on} and U_e^{off}) and both Pauli measurements (M_i^{on} and M_e^{off}) are needed. Here we show how a slight modification to the MF model allows for transitions at $q \in \{0, 1\}$, eliminating one of the measurements.

Take a square grid (rotated by 45°) which is aligned with the loop model in Figure 3.6. To every link of the lattice, assign a direction. We say that the grid orients the loop configuration, if it is possible to follow every loop without ever going against the directions on the lattice. We call a loop model *orientable* if there exists a single grid that orients all possible loop configurations. At $q \in \{0, 1\}$, the MF model is orientable; the orienting grid is the Manhattan lattice [139, 166].²⁴ This additional constraint on the loops translates to a stronger symmetry constraint on the σ model describing its continuum limit – promoting a microscopic \mathbb{Z}_2 symmetry to a continuous $U(1)$ symmetry [128, 154]. Now, the Mermin–Wagner theorem [167–169] applies: In the 1+1-dimensional model, the continuous symmetry $U(1)$ cannot be broken spontaneously. This is why the MF model does not feature a Goldstone

²³The function was fitted to the data in a logarithmic scale to yield the best results.

²⁴Similarly, the CPLC is also orientable at $p = 0$, via the so-called L-lattice [139].

phase at $q \in \{0, 1\}$.²⁵ Instead, the area-law phases extend up to $p \rightarrow 1$ (at large p , the loop lengths diverge exponentially and yield a volume law at $p = 1$).

We recognize that the MF model (as introduced in Subsection 3.4.1) may be considered to be unphysical. The probabilities p and q are finely tuned in a way to exactly match the CPLC, but result in trotterized trajectories that are densely packed with operations. A more realistic model might be a time-continuous version of the MF model as described by Fava et al. [38]. We generally assume that a sparsely populated trotterized circuit yields similar results to such a time-continuous approach.

We may make the MF model more realistic by rescaling it. To this end, we introduce a scaling factor s (in this chapter we generally choose $s = 10$), and assume that the probabilities for nontrivial operations in the circuit are divided by s . This results in diluted trajectories with fewer unitaries and measurements. To compensate for this, we also rescale the total number of time steps $T_s = T \cdot s$.

Consider the standard MF model at $q = 1$. In every odd time step, every qubit either undergoes a unitary evolution or a projective measurement (similarly for even time steps at $q = 0$). With the introduction of a rescaling $s > 1$, the circuit may act trivially on qubits in odd time steps. This breaks the orientability of the loop model and subsequently the field theory exhibits no $U(1)$ symmetry, which was necessary to protect the area-law phases on the boundaries of the phase diagram. The phase diagram for the rescaled MF model is shown in Figure 3.10. It features transitions into the Goldstone phase at $q = 0$ and $q = 1$, requiring only one type of measurement to realize a critical regime. Note that the $q \leftrightarrow (1 - q)$ symmetry of the phase diagram is not broken in the rescaling step.

3.4.6 Re-Interpretation of the MF Model

The MF model was specifically designed to be represented by the CPLC. However, it is not the only circuit with this property. Here, we present a stabilizer model with entanglement dynamics that are also described by the CPLC. We call it the SWAP model. Crucially, this circuit model is not described by the matchgate formalism and thus does not map to quadratic fermions (cf. Figure 3.2). Nonetheless, by construction, it shares the phase diagram of the MF model [see Figure 3.7 (b)].

Previously, we regarded the loops of the CPLC to represent Majorana world lines. Now we interpret them as qubit world lines instead, i.e., Majorana world lines are always combined in pairs and are collectively described by a single loop. This amounts to us “zooming out” of the original model by a factor of 2. A loop connecting two qubit sites then represents a Bell pair with the stabilizers $\langle X_i X_j, Z_i Z_j \rangle$. We choose SWAP_e gates on neighboring sites $e = (i, i + 1)$ as unitaries. They permute the sites on which the stabilizer generators act,

²⁵We are omitting some nuances here, in particular, why there was a Goldstone phase to begin with. It gets its name from the increased stiffness of the field theory, giving rise to Goldstone-like excitations. The nonlinear σ model describing the CPLC in the continuum limit is not Hermitian, and thus the Mermin-Wagner theorem does not apply. Only at $q = 0$ and $q = 1$ (and also at $p = 0$), a Hermitian representation exists. We refer the reader to the literature [146, 148, 154].

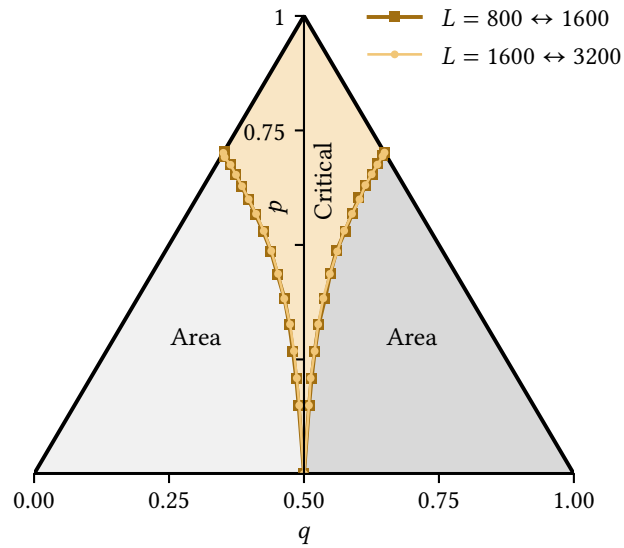


Figure 3.10 • Phase diagram of the rescaled MF model. The probabilities for operations to be applied in the MF model are rescaled by a constant factor s (here $s = 10$). This qualitatively changes its phase diagram, allowing for a phase transition into the critical phase at $q = 0$ and $q = 1$.

effectively swapping neighboring qubit world lines. Further, the SWAP model uses double measurements of $X_i X_{i+1}$ and $Z_i Z_{i+1}$, which are always performed consecutively. They are designed to correspond to the two stabilizer generators that are associated with a single loop (or on all four Majorana world lines corresponding to the two qubits). We show the loop representation of both operations in Figure 3.11. The time steps of a SWAP circuit are again split into even and odd steps. To this end, we divide neighboring pairs $e = (i, i + 1)$ into even and odd edges, depending on the parity of i .

1. In even time steps, gates are only applied on neighboring qubits across even edges. On every one of those edges, a SWAP gate is applied with probability p , and the two measurements are performed with probability $(1 - p)q$. With probability $(1 - p)(1 - q)$, no operation is performed.
2. In odd time steps, gates are only applied across odd edges. On every one of those pairs of qubits, the SWAP gate is applied with probability p , and the two measurements are performed with probability $(1 - p)(1 - q)$. With probability $(1 - p)q$, no operation is performed on the edge.

As the two consecutive Pauli measurements are performed, they project a pair of neighboring qubits onto a Bell state. Depending on the measurement outcomes, their state is either $|00\rangle \pm |11\rangle$ or $|01\rangle \pm |10\rangle$. The same action can alternatively be performed by a single

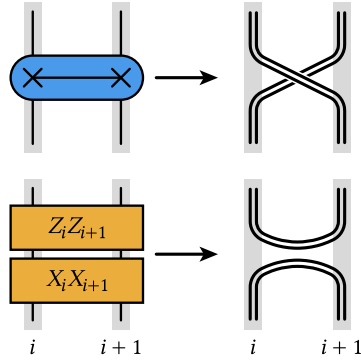


Figure 3.11 • Loop representation of the SWAP model. A SWAP circuit is represented by a loop configuration, where lines correspond to qubit world lines (or two Majorana world lines). Every loop represents two stabilizer generators. SWAP gates switch neighboring world lines. Measurements must adjust both stabilizer generators, which correspond to a single loop (to keep them bundled). They are always performed in pairs of $X_i X_{i+1}$ and $Z_i Z_{i+1}$.

measurement of the observable

$$O = \frac{1}{2} \begin{pmatrix} a+b & 0 & 0 & a-b \\ 0 & c+d & c-d & 0 \\ 0 & c-d & c+d & 0 \\ a-b & 0 & 0 & a+b \end{pmatrix} \quad (3.28)$$

with the four distinct (real) eigenvalues a , b , c , and d corresponding to the four possible Bell states. Our requirement to perform two measurements consecutively stems from the convention to perform only Pauli measurements if possible.

The SWAP model can be simulated in the stabilizer formalism. In Figure 3.12 (a) we show the entropy $S_{\text{anc}}(2L = T)$ of the system with an initially entangled ancilla system (with periodic boundaries). The initial state is realized by entangling every system qubit with one ancilla qubit in a Bell pair. Simulations were performed at $q = 0.3$ across multiple values of p . As the data points show a clear crossing, the model transitions into the Goldstone phase. The figure does also show the equivalent simulations performed in the loop model. Both approaches match perfectly, but the loop model allows us to reach much larger system sizes. Note that since the loops represent “bosonic” stabilizer generators (without hidden Jordan–Wigner strings), the data matches even though periodic boundaries are used. This is a key difference between the SWAP model and the MF model (cf. Section 3.B).

We further simulate the entanglement of the half system $S(L/2)$ in the steady state (with periodic boundaries). The results are shown in Figure 3.12 (b). Again — by construction — the loop model matches the stabilizer simulations, while allowing for much larger system sizes.

While these entanglement measures seem to perfectly mimic those of the MF model, the SWAP model’s entanglement *structure* is still different. This is due to the fact that the MF

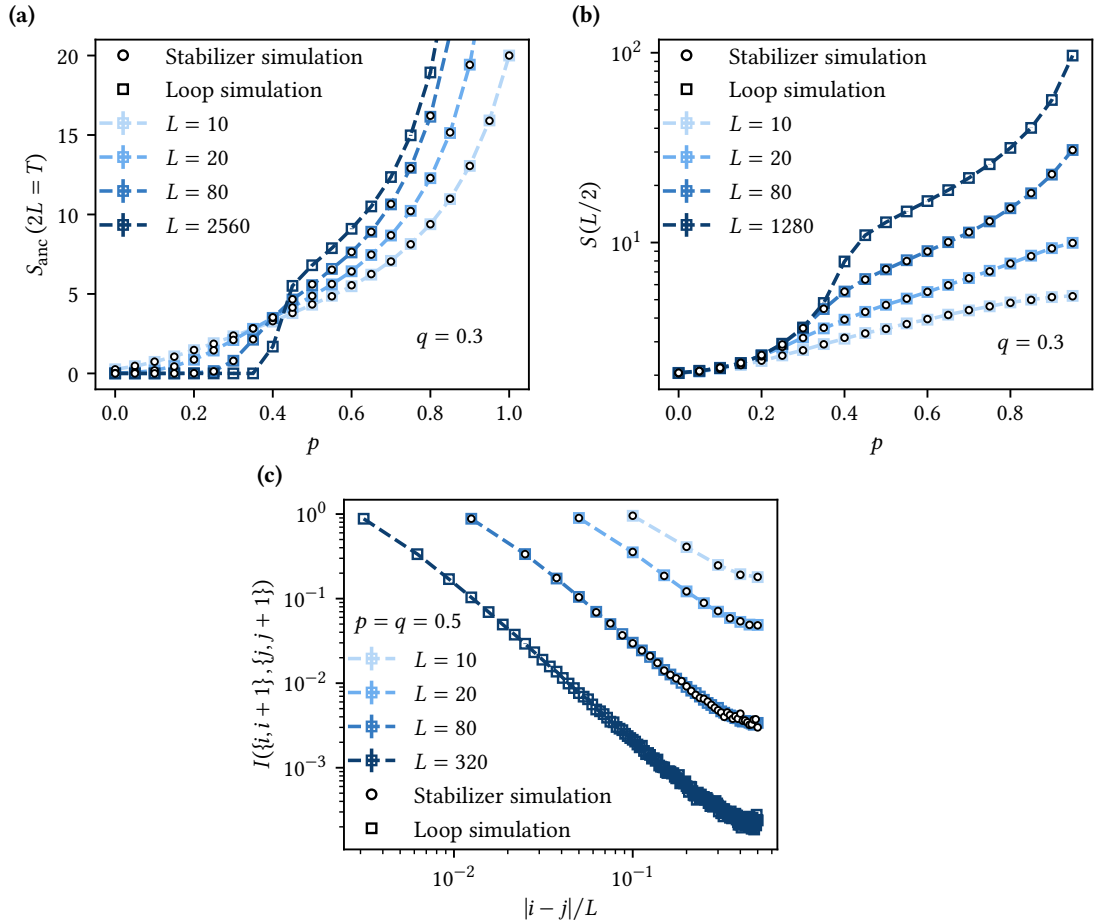


Figure 3.12 • SWAP model simulations in the stabilizer and loop formalism. (a) Entanglement entropy with an ancilla system S_{anc} at $q = 0.3$ for different values of p . Data points show averages over 10^4 samples. (b) Entanglement entropy $S(L/2)$ for the same parameters, again averaged over 10^4 samples. (c) Mutual information I between two pairs of qubits $\{i, i + 1\}$ and $\{j, j + 1\}$ within the Goldstone phase at $p = q = 0.5$. Stabilizer simulations were averaged over 10^5 samples and loop simulations average 10^6 samples. All subfigures compare stabilizer simulations and their equivalent loop model simulations – by construction, both methods yield the same results (up to noise). All simulations were performed with periodic boundaries. The plots show error bars, which are mostly smaller than the data points.

model has an inherent fermionic structure, while here we consider a purely bosonic system. With the lack of any Jordan–Wigner strings, we cannot only use periodic boundaries. The SWAP model also allows for the calculation of entanglement entropies of non-contiguous subsystems in the loop model. Therefore, the mutual information $\mathcal{I}(A, B)$ between any subsystems A and B may be calculated by counting the number of loops connecting them.

We simulate the mutual information in the SWAP model for pairs of qubits $\{i, i + 1\}$ and $\{j, j + 1\}$. This avoids some even-odd effects that would only reveal the local structure of the circuits.²⁶ The resulting data for a point within the Goldstone phase is shown in Figure 3.12 (c). At small distances $|i - j| \ll L$, we observe an algebraic decay. This is expected for a critical phase. Our simulations using the stabilizer formalism and the loop model match perfectly; the loop model again allows for much larger system sizes.²⁷ The MF model would not allow for this approach, and we would see different simulation results.

The lack of a Jordan–Wigner string leads to different entanglement structures, but this is not surprising. After all, the MF model and the SWAP model are not the same; they only share the same loop model representation, yielding identical phase diagrams in both cases. We reiterate that the SWAP model is not a matchgate circuit, because the SWAP gate is not a matchgate. This shows that extended critical phases do not only exist in fermionic hybrid quantum circuits. Similar results were found for non-Gaussian measurement-only circuits by Klocke and Buchhold in Ref. [29]. We further note that the SWAP model utilizes only one kind of unitary and one measurement [if the observable in Equation (3.28) is used].²⁸ This is a simplification over the MF model, which only allowed for a Goldstone phase under the application of at least three different operations (two unitaries and one measurement in rescaled circuits, see Subsection 3.4.5).

3.5 Generalized Loop Models

As the MF model was designed with the CPLC in mind, it takes a very simple form in the Majorana picture. However, in the more common qubit picture, the model requires two types of unitaries and measurements — distinguishing on- and off-site operations. In its original form, all four of those operations are needed to reach the Goldstone phase (cf. Figure 3.7). Here we will introduce more generalized loop models that build upon the MF model, but contain only one type of unitary gates. These models will allow for a variety of phase diagrams, and in particular for the realization of extended critical regimes utilizing the competition of only one type of unitary and measurement.²⁹

²⁶In the MF model, we would consider the mutual information between single qubits, which correspond to two Majorana world lines each. Here, we take pairs of qubits, which are also represented by two world lines in the loop model.

²⁷The system sizes shown in Figure 3.12 (c) are not the limit, but were chosen for aesthetic reasons.

²⁸The parameter q does not determine *which* measurements are performed, but *where* they are performed.

²⁹In the following, we will not refer to critical regimes as “Goldstone phases”, because this term was motivated by a continuous field theory description which does not necessarily describe the generalized loop models.

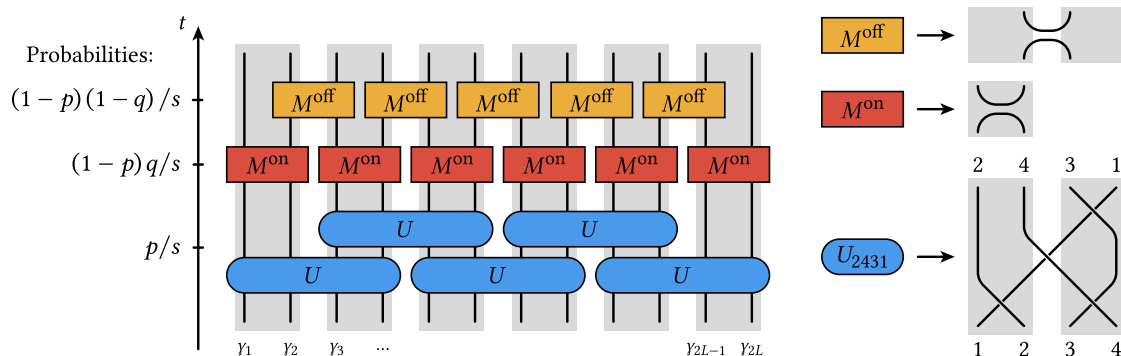


Figure 3.13 • Time step in the macro model. A single step contains three substeps, each of which is associated with one type of operation, and a probability for this operation to be applied. This illustration shows all potential operations; in a real circuit, a subset is chosen via the corresponding probabilities. Unitaries are applied in a brickstone pattern to account for their possibly nontrivial commutation relations. The model uses the same measurements M^{on} and M^{off} as the MF model (see Figure 3.6). All operations can be represented in the loop model on Majorana world lines. Unitaries correspond to permutations of four Majorana modes – we show the representation of U_{2431} as an example.

Consider an (open or closed) chain of L qubits with discrete time steps. Our model utilizes the same measurements ($M_i^{\text{on}} = Z_i$ and $M_e^{\text{off}} = X_i X_{i+1}$), which are also part of the MF model. As unitaries, we choose a gate U_e that acts on neighboring qubits $e = (i, i + 1)$ and has a loop representation. A single time step consists of three substeps, which we illustrate in Figure 3.13:

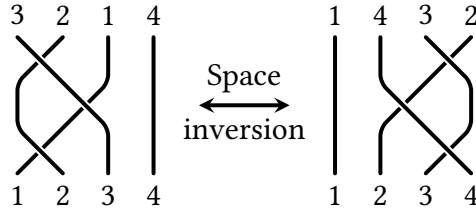
1. First, the unitaries U_e are applied to pairs of neighboring qubits with probability p/s each. As they do not necessarily commute, we need to specify the order of their application – here, we arrange them in a brickstone pattern.
2. Next, the on-site measurements M_i^{on} are performed on every qubit i , with probability $(1 - p)q/s$.
3. Lastly, the off-site measurements M_e^{off} are performed on every pair of neighboring qubits $e = (i, i + 1)$, with probability $(1 - p)(1 - q)/s$ each.

As in the MF model, the probabilities p and q determine the relative amount of unitaries and measurements (via p), and the relative amount of the two types of measurements (via q). By construction, at $p = 0$ our new models reduce to the PTIM with its transition between two area laws. We include a scaling factor $s \geq 1$. Here, it is not used to break a symmetry in the model (cf. Subsection 3.4.5). Instead, we “dilute” the circuit trajectories to hide the brickstone pattern and reduce even-odd effects. If not stated otherwise, in this section we arbitrarily choose $s = 10$ and consider periodic boundaries.

Unitaries that can be represented in the loop model generally act as permutations on the Majorana world lines. Unitaries U_e , which act on neighboring pairs of qubits, represent one of 24 possible permutations of 4 world lines. They are representations of the elements of the symmetric group S_4 . Any one of those 24 possible permutations may be chosen for our model with a corresponding unitary U_e . The symmetric group is generated by the local line-swaps that represent the unitaries U_i^{on} and U_e^{off} in the MF model. Thus, any unitary U_e can be written as a concatenation of the gates U_i^{on} , U_{i+1}^{on} and U_e^{off} . We call such unitaries *macro blocks* and denote them by their corresponding permutation. As an example, we show the macro block U_{2431} in Figure 3.13. We will refer to the generalized loop models described here as *macro models* (also labeled by the permutation associated with the unitary gates). In this section, we analyze different macro models and show how they can generate a multitude of distinct phase diagrams. This allows us to gain a general understanding of the qualitative features of those phase diagrams. We also repeat our scaling analysis from the previous section on the transition lines between phases.

3.5.1 Initial Considerations

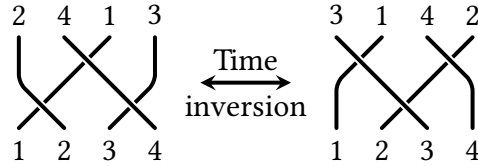
To make the set of 24 different possible macro models more manageable, we start with some general observations. Some of the macro blocks may be considered to be equivalent to each other if they produce the same entanglement measures. Take, for example, the macro blocks U_{3214} and U_{1423} . Clearly, their loop representations are connected by a simple space inversion:



A circuit in the macro model 1423 can be sampled by mirroring a circuit (or its loop model) with the unitary U_{3214} . Consequently, the loop measures $\mathcal{S}_{\text{anc}}^f$ and $\mathcal{S}(L/2)$ must remain the same. Entanglement measures that are not themselves symmetric under space inversion [for example $\mathcal{S}(L/4)$] will change if the loop model is mirrored, but it is easy to see that their sample averages $S = \langle\langle \mathcal{S} \rangle\rangle$ must be invariant. We thus write $U_{3214} \hat{=} U_{1423}$. This inherent symmetry of the loop model under space inversion reduces the macro models to 16 classes of equivalent macro blocks. Macro models in the same equivalence class must, by construction, share the same phase diagram.

As the time steps in the circuits are comprised of three substeps in every time step, the loop models are generally not symmetric under time inversion. Consequently, by switching $U \leftrightarrow U^{-1}$, a different macro model is generated with a (usually) distinct phase diagram. Only at $q \in \{0, 1\}$, one of the measurement substeps becomes redundant, and a “weak” time-inversion symmetry emerges: Generally, every circuit begins with unitaries and ends

with measurements (cf. Figure 3.13). Inverting its temporal direction in the loop model maps the measurements onto themselves and the unitaries to their inverted counterpart. As an example, we show that the unitaries U_{2413} and U_{3142} correspond to each other in this context:



Note that the inverted circuits begin with measurements and end with unitaries – therefore, entanglement measures may change by local effects that are generated at the boundary of the loop model. Statistical non-local measures (as for example the scaling behavior of S_{anc}^f) will however not be affected by this. For this reason, the macro models corresponding to unitaries which are connected by time inversion share the same global entanglement dynamics at $q \in \{0, 1\}$ (and their phase diagrams are identical at the boundaries of parameter space). Thus, if only one of the measurements is applied, the number of equivalence classes of macro models reduces to 13.³⁰

3.5.2 Volume Law at $p = 1$

As previously stated by Cao et al. in Ref. [22], any volume-law entanglement in free-fermion chains is destroyed by the presence of arbitrarily weak local monitoring. We find the same result for the macro models, because the macro blocks are matchgates. First, we will however consider the case $p = 1$ with no monitoring. We use the scaling $s > 1$ (here $s = 10$) to make the trajectories non-deterministic (otherwise, every unitary is always applied). In this case, a volume law can exist. At $p = 1$, the macro models obey the space-inversion and time-inversion symmetries we discussed previously, and there are only 13 non-equivalent models to consider. As a first example, we perform simulations for the macro block U_{2314} , calculating the entanglement $S(L/2)$ of the subsystem $A = \{1, 2, \dots, L/2\}$ and its complement \bar{A} . The system is initialized in a disentangled product state with $S(L/2, T = 0) = 0$. Figure 3.14 shows how the average entanglement entropy $S(L/2)$ grows over time for different system sizes L . At small times T , the entanglement grows algebraically $S(L/2, T \ll Ls) \sim T^\gamma$. At large times, the model settles into a volume law with $S(L/2, T \rightarrow \infty) \sim L/4$. This is consistent with fully randomized loop configurations in the final state: Consider a loop with one end in A . At $L \rightarrow \infty$, it is equally likely for this loop to have its other end in A or \bar{A} . On average, half of the loops contribute to the entanglement entropy $S(L/2)$. These observations show that the unitaries U_{2314} mix the loop model and generate entanglement. This process is also referred to as a *thermalization* in the sense of the eigenstate thermalization hypothesis [15, 16, 170–174].

We observed similar results for 5 out of the 13 macro models (2314, 2413, 2341, 3214 and 4132). The other models are limited to area laws at $p = 1$. We identified two possible

³⁰The same obviously also holds for $p = 1$, as no measurements are applied.

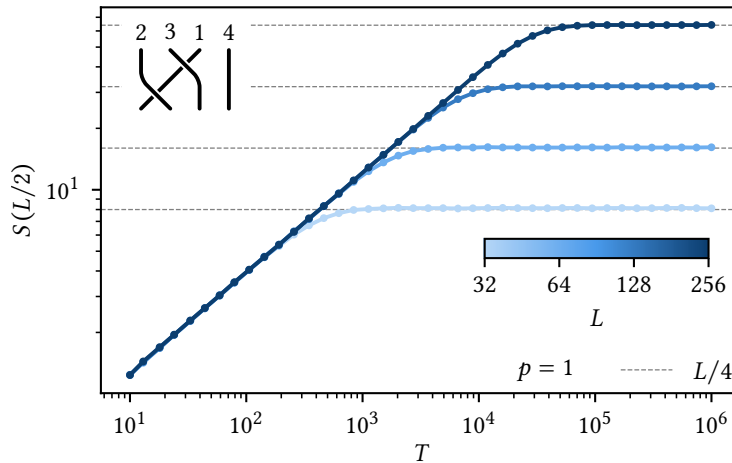
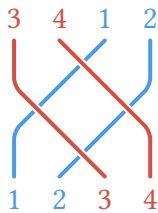


Figure 3.14 • Time evolution of the entanglement entropy at $p = 1$. The entanglement entropy initially grows algebraically and settles into a volume law at $S(L/2, T \rightarrow \infty) = L/4$. Here we simulated the macro model 2314. Data points show averages over 10^4 samples; error bars are smaller than the points.

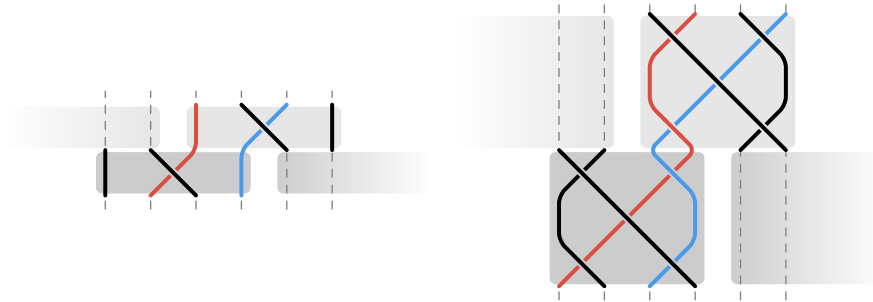
mechanisms to suppress the entanglement growth. They are best understood in the loop model representation of the macro model:

- The stabilizer group of the initial product state is generated by pairs of Majorana modes of the form $i\gamma_{2i-1}\gamma_{2i}$; they correspond to local loops connecting neighboring Majorana world lines. Entanglement between multiple subsystems can only be created if a trajectory separates the pairs of connected Majorana modes in space. Only then can an extensive number of loops span the distance between two subsystems. However, some macro blocks are not able to separate neighboring world lines. Consider for example the unitary U_{3412} :



The colors indicate world lines that — if they were previously paired — will not be separated. Instead, the loops travel arbitrary distances in pairs, but they can never contribute to the entanglement entropy. The same argument may be made for the macro blocks U_{1234} , U_{2134} , U_{2143} , U_{4312} and U_{4321} (and their inverted counterparts). Note that this mechanism very much depends on the initial state. The macro blocks described here may yield nontrivial entanglement dynamics if the initial state is described by a different loop configuration that does not pair Majorana world lines belonging to the same qubit.

- Some macro blocks inhibit the growth of entanglement via a different mechanism. Entanglement is created by Majorana world lines crossing the boundary between two subsystems A and \bar{A} . If a unitary gate limits the distance that a world line can travel in the system, the entanglement can never outgrow an area law. To be more precise: The entanglement entropy can never change by more than a constant amount (which does not scale with the subsystem size) from its initial value. An obvious example is the trivial unitary $U_{1234} = \mathbb{1}$. But we find the same mechanism for less trivial cases. Consider for example the macro blocks U_{1324} (left) and U_{4231} (right):³¹



Here we show a small cutout of the brickstone pattern in which those unitaries are (possibly) applied. The crucial insight is the following: Every world line is not affected by one substep of the pattern. In our examples, blue (red) lines cannot be affected by unitaries in the lower (upper) layer of the brickstone pattern. The layer that acts nontrivially on a world line can only switch its position between two possible sites. This effectively prohibits world lines from traveling through the system. While our image shows the case $s = 1$, it is easy to see that this holds true if only a fraction of the unitaries is applied in the circuit. Unitaries of this kind can never generate non-local entanglement structures.

3.5.3 Phase Diagrams

We now show the variety of phase diagrams created by different macro models. This will unveil some interesting phenomena that were not present in the MF model. All phase diagrams were obtained for the scaling factor $s = 10$.³²

As a first step, we show a trivial phase diagram in Figure 3.15 (a) for the macro block U_{3214} . In this case, no extended critical phase exists. The two area-law phases known from the PTIM extend to positive probabilities p . Similarly to Figure 1.4, we determined the phase diagram numerically by finding the maximum of the entropy $S(L/2)$ (here with periodic boundaries). The process was repeated for the system sizes $L = 200$ and $L = 400$ and our data shows some noise. We are however able to place the transition exactly at $q = 1/2$,

³¹The other macro blocks that follow this principle are U_{2134} and U_{2143} (and their inverted counterparts).

³²The scaling factor does have an effect on the phase diagrams, but generally does not change their qualitative features — differently from the MF model (cf. Figures 3.7 and 3.10).

because this MF model exhibits the same $q \leftrightarrow (1 - q)$ symmetry that was also observed in the MF model. This argument is further detailed at the end of Section 3.D.

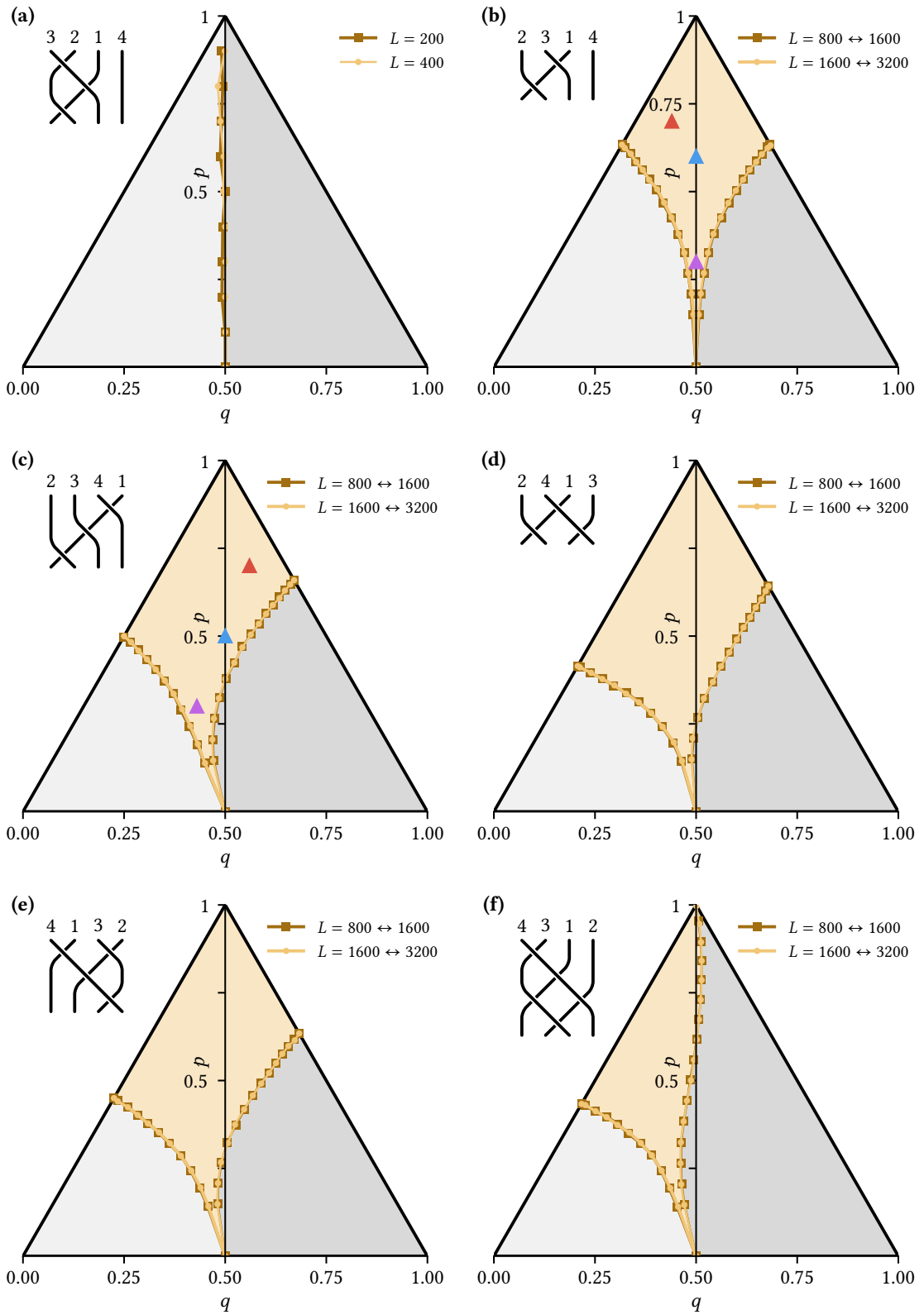
The phase diagram shown here is not unique to the macro block U_{3214} (and its mirror image U_{1423}). We find the same results for the blocks U_{2134} , U_{1243} and U_{1324} (which are very similar and connected by some symmetry arguments), the macro blocks U_{2143} and U_{3412} , as well as the trivial $U_{1234} = \mathbb{1}$. In the following, we will focus on the macro models, which do exhibit an extended critical phase.

Nontrivial phase diagrams were obtained as earlier for the MF model, by numerically finding crossing points in the ancilla entropy S_{anc}^f , given two system sizes $L = T/s$. The process was repeated once with different sizes to detect any possible noise or finite-size effects. In Figure 3.15 (b–h), we show seven such phase diagrams for a multitude of different macro models. All macro blocks that are not represented here, are connected to the ones that are shown by inversions in space and/or time (remember Subsection 3.5.1).

The convenience of macro models in the qubit picture is well illustrated by the phase diagrams of the models 2314, 2341, 2413 and 4132 shown in Figure 3.15 (b–e). These circuits allow for the realization of a critical phase with only one type of measurement M^{on} or M^{off} (i.e., $q \in \{0, 1\}$). Thus, an extended critical regime requires the competition of only one type of measurement and unitary. Note that the phase diagram shown in Figure 3.15 (b) for the unitary U_{2314} exhibits the same $q \leftrightarrow (1 - q)$ symmetry previously observed in the MF model. The same is true for the mirrored unitaries U_{3124} , U_{1342} and U_{1423} . We provide the proof for this in Section 3.D. All other extended critical phases in macro models assume asymmetric shapes in parameter space. Note that the asymmetric phase diagrams in Figure 3.15 have a peculiar feature: At the point $(p = 0, q = 1/2)$, all models feature the critical point of the PTIM, and their entanglement scales logarithmically. When introducing unitaries $(p > 0, q = 1/2)$, these models do however at first enter an area law, as the critical phases appear to veer to the left $(q < 1/2)$. Here, the addition of unitaries to measurement-only circuits (at $p = 0$) does decrease the entanglement in the systems. This behavior is unexpected, because random unitary gates usually increase entanglement. Focusing only on the line $q = 1/2$, unitaries only increase the entanglement entropy at a large enough rate p (when the phase diagrams enter criticality).

Figure 3.15 (f) and (g) show the phase diagrams of the models 4312 and 4321. Here we observe that a critical regime exists at $q = 0$ (with only M^{off}) but not at $q = 1$ (with only M^{on}).³³ Further, the diagram shown in Figure 3.15 (h) for the model 4231 does exhibit a critical phase that can only be realized if both measurements are applied (at $0 < q < 1$). Different from the MF model, this effect has remained robust under the rescaling of the circuits with a factor $s > 1$ (cf. Subsection 3.4.5). We were able to identify two possible mechanisms, which may prohibit a critical phase from existing with only one type of measurement: For some circuits, their loop representation bundles Majorana world lines in pairs such that any finite monitoring rate forces the systems into an area law. This occurs for the models 4312 and 4321 at $q = 1$. In contrast, the model 4231 does feature a loop model

³³We verified numerically that Figure 3.15 (g) does indeed show a transition at $q = 0$.



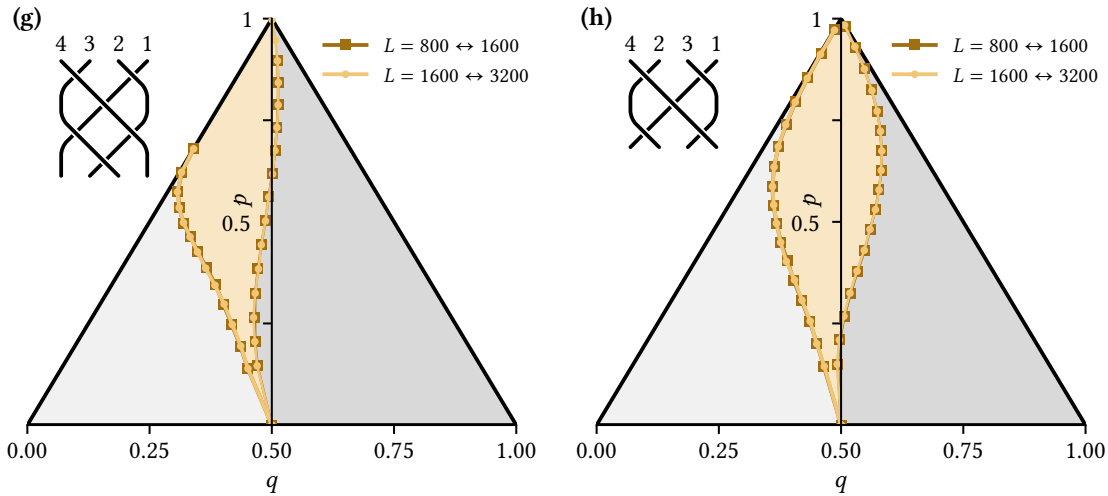


Figure 3.15 • Phase diagrams of macro models. (a) Trivial phase diagram for the macro block U_{3214} without a critical phase. All models that do not reach an extended critical phase share this phase diagram. (b–h) Phase diagrams of different macro models that exhibit extended critical phases. Macro blocks that are connected via space inversion share the same phase diagram. Macro blocks that are connected via time inversion may generate quantitatively different phase diagrams, but generally share the same key features and are thus omitted here. For all models, the scaling factor $s = 10$ was chosen. Triangles in subfigures (b) and (c) denote the points simulated in Figure 3.17.

that becomes orientable at $q \in \{0, 1\}$. This indicates that loop orientability still plays a major role, even in these macro models.

In a broader approach, we explain the qualitative features of all phase diagrams by examining the properties of their loop representations — including models that do not feature a critical phase. These considerations are rather lengthy and detailed in Section 3.E. Our key findings are the following:

- Phase diagrams without a critical phase do either correspond to orientable loop models, or are closely related to the PTIM and the bond percolation model (see Subsection 3.E.4).
- Models with a critical phase, are generally not orientable. If they do not show a transition into the critical phase at the boundaries $q \in \{0, 1\}$, this is either due to an emergent orientability of the loop model (see Subsection 3.E.1), or due to the unitary gates permuting world lines in pairs (see Subsection 3.E.3).
- Models that allow for a transition into the critical phase at $q \in \{0, 1\}$, are not orientable (see Subsection 3.E.2).

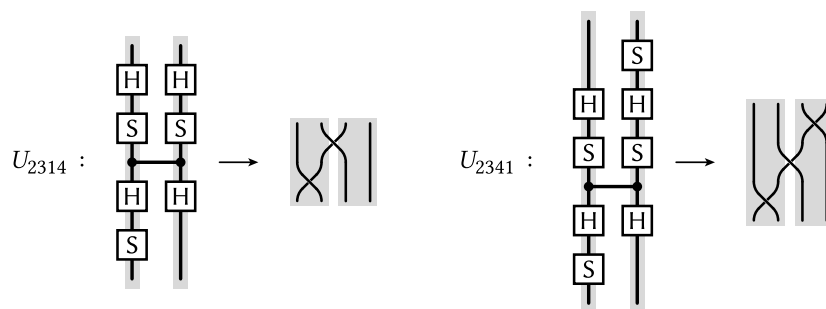


Figure 3.16 • Clifford and loop representations of the macro blocks U_{2314} and U_{2341} . Macro blocks are concatenations of multiple unitaries U^{on} and U^{off} (see Figure 3.5) which are applied concurrently.

In the following, we will analyze two phase diagrams in more detail. First, we study U_{2314} , a macro block that consists of only two swaps of neighboring Majorana world lines, but still allows for a critical phase to exist. We may consider it as the “simplest” nontrivial case. Secondly, we arbitrarily choose U_{2341} as a different nontrivial macro model. Both phase diagrams are depicted in Figure 3.15 (b) and (c). The representations of the unitaries in the stabilizer formalism and in the loop model are shown in Figure 3.16.

3.5.4 Extended Critical Phase

There is no known field theory description for the macro models we consider here. As a consequence, there are no predictions for the scaling behavior of entangling measures in the critical phases. We numerically investigate the scaling behavior of $S_{\text{anc}}^{\text{f}}$ in the critical regimes of the models 2314 and 2341 and compare our data with the MF model, as shown in Figure 3.8 (a).

First, consider the macro block U_{2314} . In Figure 3.15 (b), we arbitrarily denoted three points in the critical phase of this model. Figure 3.17 (a) shows the ancilla entropy $S_{\text{anc}}^{\text{f}}$ at these sets of parameters for scaled trajectories with $T = Ls$. Similar to the MF model, our data is dominated by a very strong finite-size effect, which makes a quantitative analysis difficult. Nonetheless, our numerical simulations suggest that the entropy in the critical phase follows Equation (3.22) with a universal prefactor β at very large system sizes. This is indicated by the similar slopes of the data points in the logarithmic plot.³⁴

We repeat the same analysis for the macro block U_{2341} , see Figure 3.17 (b) [points denoted in Figure 3.15 (c)]. Again, the data points appear to approach a constant slope, consistent with a universal prefactor β .

³⁴The finite-size effects tend to become larger with increasing probability p and extend well beyond our system sizes $L \sim 10^4$. Therefore, we do not show fit functions.

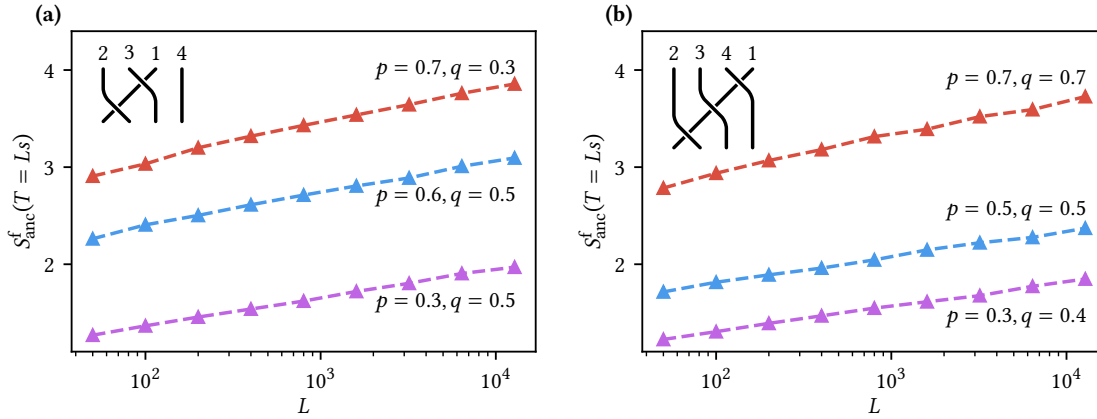


Figure 3.17 • Scaling analysis of the ancilla entropy in critical phases of macro models. Scaling of the entropy $S^f_{\text{anc}}(T=Ls)$ for the macro model 2314 in (a) and 2341 in (b). Simulations were performed for 3 arbitrary sets of parameters in the critical phase, cf. Figure 3.15 (b) and (c). Data points show averages over 10^4 samples and are larger than the error bars.

While a more quantitative analysis is not possible at our limited system sizes,³⁵ our data is at least consistent with the scaling law predicted for the MF model. We made the same observation for all other macro models, suggesting that there may exist field theory descriptions similar to the σ model that describes the MF model.

3.5.5 Conformal Scaling of Entanglement Measures

In Subsection 3.4.4, we found indications that entanglement measures on the boundaries of the critical phase of the MF model follow conformal scaling laws. Like the MF model, all macro models map to the PTIM at $p=0$. At $q=1/2$, they show the known phase transition (cf. Figure 1.4) described by a conformal field theory. Thus – just as for the MF model – it is reasonable to assume a conformal description along the boundaries of critical phases. Here, we repeat the conformal analysis previously performed on the MF model (see Figure 3.9) for the macro models 2314 and 2341, but this time with rescaled circuits ($s=10$).

Entanglement Entropy

First, we consider the normalized entanglement entropy $\Delta S(l/L) = S(l) - S(L/2)$ of the steady state. The subplots (a1–a3) in Figure 3.18 show our analysis for the macro block U_{2314} .

³⁵In Ref. [154], loop models with system sizes up to $\sim 10^6$ were simulated, which required some numerical tricks, including the sampling of large loop model sections and reapplying them at random positions. This may however affect the statistics of the loop model (although the effects are likely small). Therefore, we did not implement such techniques for this thesis.

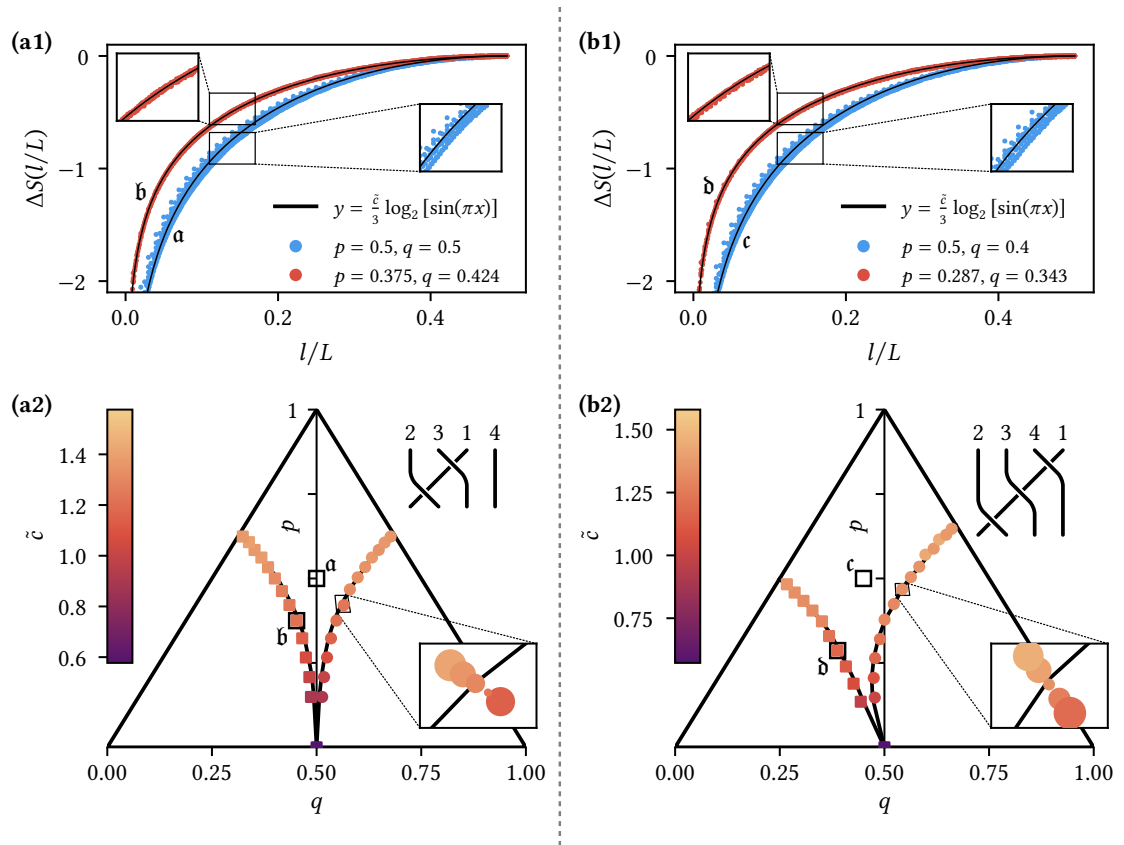
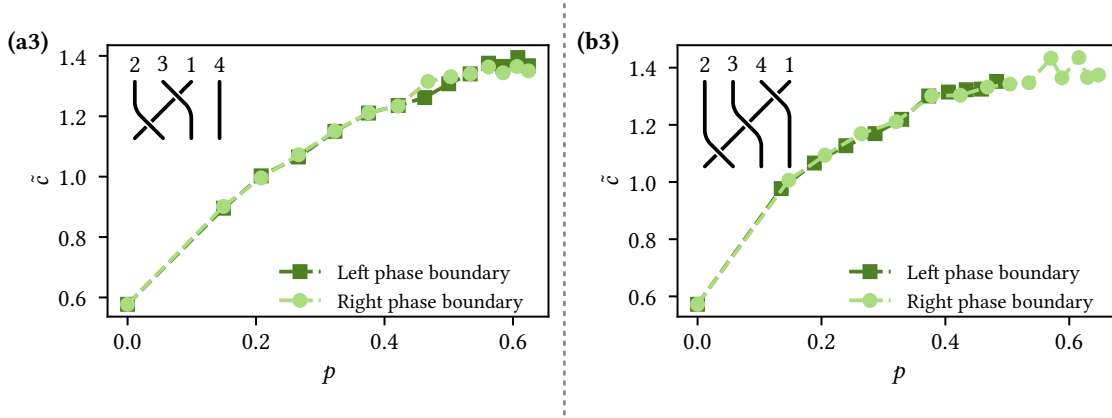


Figure 3.18 • Conformal scaling of the entanglement entropy in the macro models 2314 and 2341. (a1) Collapse of the normalized entanglement entropy $\Delta S(l/L)$ in the macro model 2314 for the steady state of systems of size $L \in \{100, 200, 300, 400, 500, 1000\}$, averaged over 10^5 samples (error bars are smaller than the data points). The datasets correspond to a point within the critical phase (a) and on its boundary (b). The scaling function for a conformal field theory was fitted to the data for $L = 1000$ [see Equation (3.25)]. (a2) The same analysis was performed in the vicinity of the phase transition for system sizes $L \in \{128, 256, 512\}$ with 10^5 samples. The inset shows the quality of the data collapse indicated by point sizes (smaller points correspond to a better collapse). The main plot only shows the points of best collapse. Colors represent the fitted value of \tilde{c} . We did the same analysis for the model 2341; shown on the right side in (b1) and (b2). \curvearrowright



↪ (a3) and (b3) The conformal prefactors \tilde{c} shown in (a2) and (b2) as functions of the probability p . For the macro model 2314, the symmetry $q \leftrightarrow (1 - q)$ is conserved.

Subfigure (a1) shows the normalized entropy for the system sizes $L \in \{100, 200, 300, 400, 500, 1000\}$ at parameters within the critical phase (blue points) and on its boundary (red points). As can be clearly seen in the insets, the data points collapse onto a single line on the phase boundary. The same is not true within the critical phase. If the normalized entanglement entropy follows a conformal description, at large system sizes it is expected to be described by Equation (3.25) with a prefactor \tilde{c} . We test this by fitting the equation to the data at $L = 1000$ in Figure 3.18 (a1). The data on the phase boundary fits this prediction much better than within the phase (the difference is not easy to see in the plot). This indicates that a conformal description exists for the boundary of the critical phase in the model 2314. Similar simulations were performed for the model 2341 and are shown in Figure 3.18 (b1) — with the same result.

To measure the behavior of the prefactor \tilde{c} , simulations with system sizes $L \in \{128, 256, 512\}$ were performed in the vicinity of the phase boundaries. For every point, the quality of the data collapse was determined by estimating the variations of $\Delta S(1/8)$. The inset in Figure 3.18 (a2) shows how the simulations were performed around a point on the transition line. The point sizes indicate the quality of the collapse; clearly, there is a minimum. Figure 3.18 (a2) shows the points of best collapse along the phase boundaries. The colors indicate the fitted prefactors \tilde{c} . Note that the points of best collapse are slightly shifted away from the transition; we previously found the same finite-size effect for the MF model. We repeat the analysis for the model 2341 in Figure 3.18 (b2) — with the same result.

We also show the prefactors \tilde{c} along both phase boundaries as a function of the probability p in Figure 3.18 (a3). As expected, the symmetry $q \leftrightarrow (1 - q)$ of the phase diagram for the model 2314 is also reflected here (cf. Section 3.D). Similar to our analysis for the MF model, our data for $\tilde{c}(p, q)$ exhibits some small steps, which are numerical artifacts. The prefactors \tilde{c} for the model 2341 are shown in Figure 3.18 (b3). Here, the phase diagram breaks the symmetry, and the right phase boundary extends to larger values p . Nonetheless, the numerical data suggests a symmetry in q . We checked for this by determining \tilde{c} as a

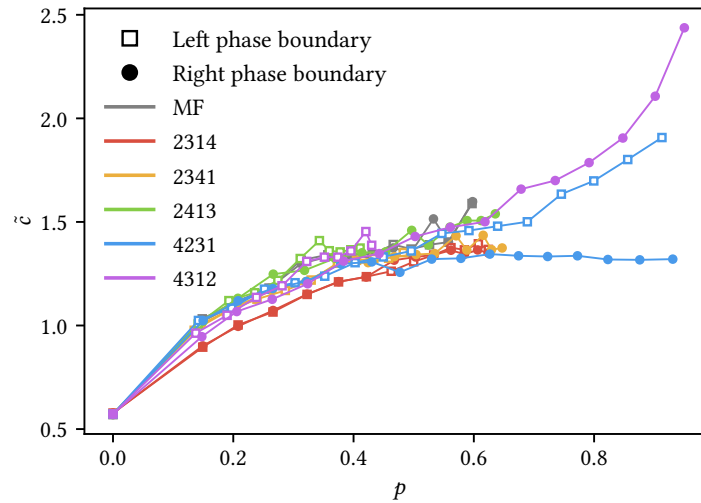


Figure 3.19 • Comparison of conformal prefactors for different models. Conformal prefactor \tilde{c} for the MF model and a collection of macro models along the boundaries of their critical phases as a function of p . Data points were collected at the points of best collapse [as in Figure 3.18 (a3) and (b3)], considering system sizes $L \in \{128, 256, 512\}$ with 10^5 samples. Prefactors were calculated by fitting the data at the largest system size.

function of p on the critical phase boundaries in a larger selection of models, see Figure 3.19. At $p = 0$, all models map to the PTIM and show a conformal scaling with the prefactor $\tilde{c} \approx 0.573$ [see Equation (3.26)]. At $p > 0$, the quality of our data is bound by the strong finite-size effects found at the phase boundaries. The prefactor generally increases with p , but differently for every macro model and the MF model. Apart from some special cases (in particular the MF model and the macro model 2314), the left and right boundaries of the critical phase show different values of \tilde{c} at the same value of p . This becomes especially apparent at $p > 0.5$ (consider for example the model 4231). We infer that $\tilde{c}(p, q)$ is generally a function of p and q . Note however that – especially at large p – the prefactor \tilde{c} is very sensitive to small changes in p and q , i.e., our data should be considered with some caution.³⁶

Similar to the MF model, our simulations of the normalized entanglement entropy $\Delta S(l/L)$ display some conformal behavior, especially in the vicinity of the boundaries of critical phases. We made the same observation for all macro models with nontrivial phase diagrams, not only the two examples shown here.

³⁶Note also that some models exhibit a volume law at $p = 1$. At $p < 1$ and in an infinitely large system $L, T \rightarrow \infty$ this volume law breaks down. At finite system sizes however, the transition into an area-law phase or a critical phase becomes continuous and may influence our numerical results at finite measurement rates. This may also corrupt our data for large p .

Mutual Information

We also performed simulations of the mutual information $I(|i - j|)$. Figure 3.20 (a1) shows numerical results for the model 2314 at $L = 400$ at a point within the critical phase (a) and on each phase boundary (b and c). Some local artifacts are avoided by only showing the data at $|i - j| \geq 2$. Equation (3.27) was fitted to all data points (fitting in the logarithmic scale yielded the best results). The data implies similarities between this macro model and the MF model (cf. Figure 3.9): Points on the phase boundaries are well described by a conformal scaling law, especially at larger distances $|i - j|/L \gtrsim 10^{-1}$. Within the critical phase, Equation (3.27) slightly deviates from the data points.³⁷ The critical exponent $\kappa(p, q)$ is a function of both probabilities p and q and is calculated as a fit parameter.

Figure 3.20 (a2) shows the critical exponents as colored points along the phase boundaries. They were determined by fitting Equation (3.27) to simulations of the model 2314 in the steady state with $L = 128$ and 10^7 samples. Clearly, the mutual information breaks the $q \leftrightarrow (1 - q)$ symmetry of the phase diagram, as previously explained for the MF model. The same data points are shown as a function of p in Figure 3.20 (a3). Note that — as expected — at $p = 0$ the critical exponents $\kappa(p = 0, q = 1/2) \approx 2/3$ coincide with the prediction for the PTIM.

The same analysis was repeated for the macro model 2341 and is shown in Figure 3.20 (b1–b3). We make similar observations, although this model exhibits no $q \leftrightarrow (1 - q)$ symmetry that could be broken by the mutual information.

The data shown in Figure 3.20 again serves merely as an example. We repeated the same procedure for all nontrivial macro models and consistently found the mutual information to be best described by a conformal scaling law on the phase boundaries. Together with our investigations of the entanglement entropy in Figure 3.18, we conclude that there is evidence for the existence of conformal descriptions for the macro models on the boundaries of their critical phases. While this result is consistent with our findings for the MF model, it is not necessarily obvious that the much more diverse collection of macro models should show such similar properties.

³⁷It is not easy to show in the plot that the data for points within the critical phase shows a slight right curve, which is not matched by the conformal prediction and is greatly reduced on the phase boundaries.

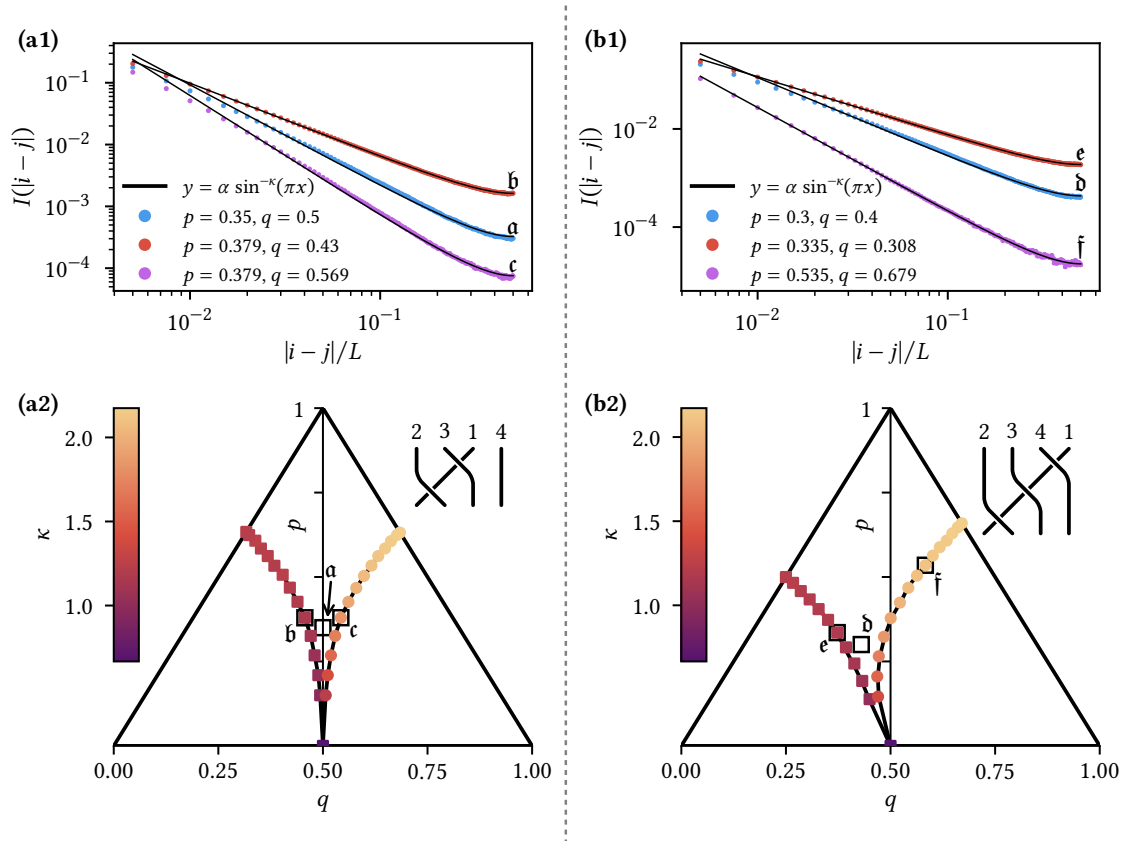
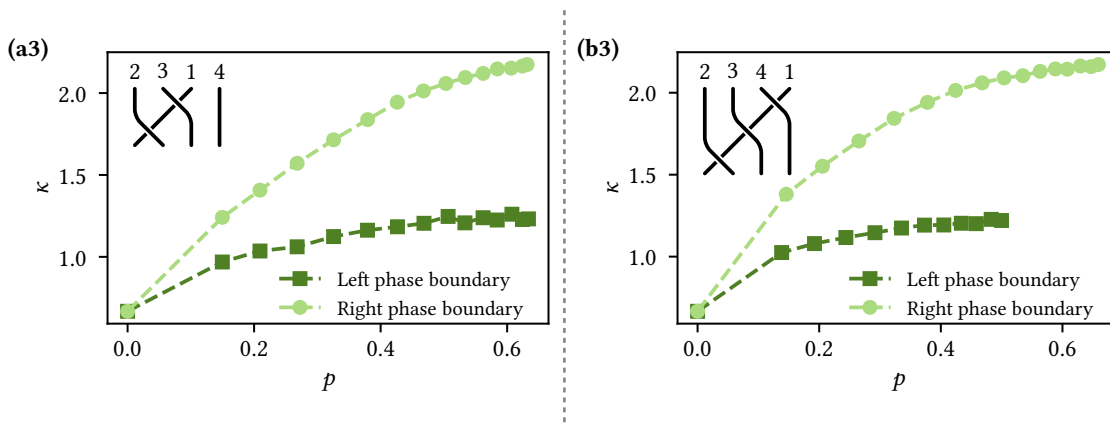


Figure 3.20 • Conformal scaling of the mutual information in the macro models 2314 and 2341. (a1) Mutual information $I(|i-j|)$ in the macro model 2314 for a point within the critical phase (a) and two points on its boundaries (b and c). Simulations were performed in the steady state at $L = 400$ with 10^7 samples; error bars are generally smaller than the data points. The prediction for the mutual information in systems described by conformal field theories is fitted to the data [see Equation (3.27)]. (a2) Similar simulations and fits were performed along the phase boundaries of the critical phase with $L = 128$ and 10^7 samples. The critical exponents κ were determined as fit parameters and are indicated by colors in the plot. The same analysis was performed for the macro model 2341 and is shown in subfigures (b1) and (b2). \curvearrowright



↷ (a3) and (b3) The critical exponents κ shown in (a2) and (b2) as functions of p for each boundary of the critical phases.

3.6 Conclusion

In this chapter, we studied the phase diagrams of a collection of quantum circuits that map to loop models, with a particular focus on the emergence of extended critical phases. To this end, we first considered the already well-known MF model, and provided some new detailed scaling analysis on its critical phase. In particular, we found evidence that the boundaries of this critical phase are well described by a conformal field theory. Furthermore, we showed that by rescaling the MF model, a symmetry (related to the loop model orientability) can be broken, allowing for the systems to enter criticality with only two unitaries and one measurement. The loop model representing the MF model can also be reinterpreted as a Clifford circuit with SWAP gates. Thus, critical phases are not only found in hybrid systems that map to fermionic circuits.

In the search for Clifford circuits that allow for the realization of critical phases with the least possible number of operations, we introduced *macro models*, which are generalizations of the loop models previously considered. These circuits with only one type of unitary gate and two types of measurements are able to generate a variety of qualitatively different phase diagrams, purely depending on which unitary is chosen. We were able to link the features of all of those phase diagrams to symmetries and other properties found in the loop models representing the circuits. In particular, we found that loop orientability plays a major role in the characteristics of a phase diagram — a result which matches previous findings for loop models that can be mapped to certain field theories. Notably, some of the macro models we described are capable of realizing a critical phase only under the application of one type of unitary gate and one measurement. This might simplify future endeavors in the experimental realization of critical phases. Finally, we performed a detailed scaling analysis on the critical phases of macro models and found remarkable similarities to the MF model. This concerns not only the scaling of entanglement measures in critical phases, but also the apparent conformal scaling behavior on the boundaries of critical phases.

Miscellaneous Projects for Chapter 3

3.7 On Popcorn and Stars over Babylon

When experimenting with matchgate quantum circuits, I came across a little mathematical curiosity that I would like to present here. Let me however preface this with the following warning: What follows now is very useless and bears no physical importance. With that being said, let me show you a special matchgate.

3.7.1 A Very Simple Quantum Circuit Model

Consider a circuit of L qubits and the matchgate

$$U_e(\phi) = \begin{pmatrix} \cos \phi & 0 & 0 & i \sin \phi \\ 0 & \cos \phi & -i \sin \phi & 0 \\ 0 & -i \sin \phi & \cos \phi & 0 \\ i \sin \phi & 0 & 0 & \cos \phi \end{pmatrix} \quad (3.29)$$

with the angle $\phi \in (0, \pi/2)$.³⁸ $U_e(\phi)$ is applied to neighboring sites $e = (i, i+1)$ with $i \in \{1, \dots, L-1\}$. For a circuit, we choose a single value ϕ and the initial state $|\Psi_0\rangle = |0 \dots 0\rangle$. Then, in discrete time steps, the unitary gate $U_e(\phi)$ is applied randomly (with probability $p = 0.5$) on neighboring pairs of qubits. We call this the *popcorn model*. In the limit $T \rightarrow \infty$ and with even system sizes L , we will then perform simulations to find the average entanglement entropy $S_\phi(L/2)$.

As it turns out, all gates $U_e(\phi)$ commute and the order in which they are applied does not affect the final state. Now consider two subsystems A and \bar{A} and first apply all instances of the Matchgate that couples them. All subsequent unitaries act either on A or on \bar{A} and cannot affect the entanglement entropy $S_\phi(A)$. Consequently, we may just ignore them and consider only systems of two qubits $\{1, 2\}$ (instead of L) with a single gate that is randomly applied.

³⁸At $\phi \in \{z\pi/2 \mid z \in \mathbb{Z}\}$, the gate $U_e(\phi)$ does not create entanglement. With $\phi \in (0, \pi/2)$ we focus on the interesting regime.

The von Neumann entanglement entropy of any subsystem A is then reduced to the entropy in a two-qubit system

$$\mathcal{S}_\phi(A) = \mathcal{S}_\phi(L/2) = \mathcal{S}_{1,\phi}(n) = -\text{Tr}_1 [\rho_1(n) \log_2 [\rho_1(n)]] \quad (3.30)$$

with the reduced density matrix (we omit the index e in U_e)

$$\rho_1(n) = \text{Tr}_2 \left[(U(\phi))^n |00\rangle \langle 00| (U^\dagger(\phi))^n \right] \quad (3.31)$$

and the traces $\text{Tr}_{1,2}$ over the corresponding single-qubit subspaces. n is the number of times the gate $U(\phi)$ was applied in the circuit; at large T , $n \leq T$ is some non-deterministic large number depending on the sample circuit. With

$$(U(\phi))^n = \begin{pmatrix} \cos(n\phi) & 0 & 0 & i \sin(n\phi) \\ 0 & \cos(n\phi) & -i \sin(n\phi) & 0 \\ 0 & -i \sin(n\phi) & \cos(n\phi) & 0 \\ i \sin(n\phi) & 0 & 0 & \cos(n\phi) \end{pmatrix} \quad (3.32)$$

it is easy to show that the reduced density matrix takes the form

$$\rho_1(n) = \begin{pmatrix} \cos^2(n\phi) & 0 \\ 0 & \sin^2(n\phi) \end{pmatrix} \quad (3.33)$$

in the single-qubit space with basis $\{|0\rangle_1, |1\rangle_1\}$. Correspondingly, the entanglement entropy of a single sample circuit (of any size L) is

$$\mathcal{S}_{1,\phi}(n) = \mathcal{S}_\phi(L/2; n) = - \underbrace{\left[\cos^2(n\phi) \cdot \log_2 [\cos^2(n\phi)] + \sin^2(n\phi) \cdot \log_2 [\sin^2(n\phi)] \right]}_{:=s(n\phi)}. \quad (3.34)$$

Note that the function $s(n\phi)$ is periodic in $n\phi$ with period $\pi/2$. We performed simulations of the average entanglement entropy³⁹ and show the corresponding data in Figure 3.21 (a) as a function of ϕ . The entanglement exhibits a striking, fractal-like structure that we will now explain.

3.7.2 Relation to the Popcorn Function

Thomae's function (named after Carl Johannes Thomae [175]) is defined as

$$f(x) = \begin{cases} \frac{1}{q}, & \text{if } x = \frac{p}{q} \in \mathbb{Q} \text{ with } p \in \mathbb{Z} \wedge q \in \mathbb{N} \text{ coprime,} \\ 0, & \text{if } x \notin \mathbb{Q}. \end{cases} \quad (3.35)$$

Nowadays, it is also commonly known as the *popcorn function*, or sometimes as *stars over Babylon*. As a function that distinguishes rational and irrational numbers, it has infinitely

³⁹For $\phi/\pi \in \mathbb{Q}$, some analytical considerations allow us to calculate the average entanglement in the limit of infinite samples at $T \rightarrow \infty$.

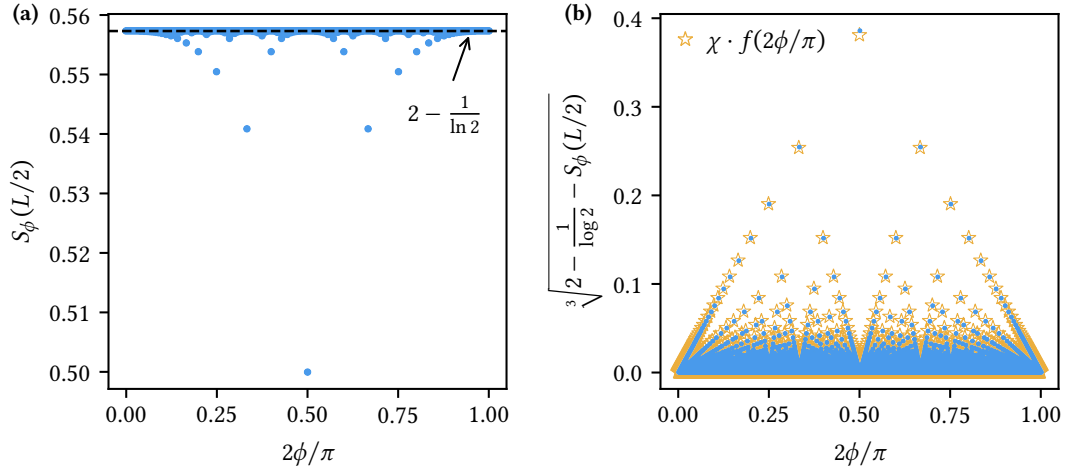


Figure 3.21 • Entanglement in the popcorn model. (a) Average entanglement entropy in the popcorn model at any size L with $T \rightarrow \infty$. (b) Rescaled version of the same entanglement values and the popcorn function f for comparison (scaled by a prefactor $\chi \approx 0.76$). Clearly, $f(p/q)$ is closely related to the entanglement of the popcorn model; the points align particularly well at large $q \in \mathbb{N}$.

many discontinuities on the interval $x \in (0, 1)$. It bears a hidden connection to our popcorn model. This becomes clear when nonlinearly rescaling the entanglement entropy by the cube root

$$S_\phi(L/2) \mapsto \sqrt[3]{2 - \frac{1}{\log 2} - S_\phi(L/2)}. \quad (3.36)$$

In Figure 3.21 (b) we show these rescaled entanglement values and overlay the popcorn function (rescaled by a prefactor χ). Surprisingly, the function closely matches the data. In the following, we aim to find the connection between our quantum circuit model and the stars over Babylon.

As a first step, consider the case of $\phi/\pi \notin \mathbb{Q}$ being irrational. Then, according to the equidistribution theorem [176–179], the infinite set $\mathcal{E}_\phi = \{n\phi \bmod \pi/2 \mid n \in \mathbb{N}\}$ is uniformly distributed on the interval $[0, \pi/2)$. In the limit $T \rightarrow \infty$, the values $n\phi$ sample elements out of this set sufficiently randomly, such that the average entanglement entropy

$$S_\phi(L/2) = \lim_{N \rightarrow \infty} \frac{1}{N} \sum_{j=1}^N S_\phi(L/2; n_j) \quad (3.37)$$

is just the Monte Carlo integral [180] over the $\pi/2$ -periodic function in Equation (3.34):

$$S_{\frac{\phi}{\pi} \notin \mathbb{Q}}(L/2) = -\frac{2}{\pi} \int_0^{\pi/2} d\theta \underbrace{\left[\cos^2\theta \cdot \log_2(\cos^2\theta) + \sin^2\theta \cdot \log_2(\sin^2\theta) \right]}_{=-s(\theta)} = 2 - \frac{1}{\ln 2} \quad (3.38)$$

We see this value as the maximum average entanglement in Figure 3.21 (a).

Now, consider rational values $\phi/\pi \in \mathbb{Q}$. In this case, the set $\mathcal{E}_\phi = \{n\phi \bmod \pi/2 \mid n \in \mathbb{N}\}$ is repeating and finite. To be precise, for $2\phi/\pi = p/q$ with $p \in \mathbb{Z}$ and $q \in \mathbb{N}$ coprime, the set \mathcal{E}_ϕ contains q distinct elements that are equidistant on the interval $[0, \pi/2)$. Thus, for many samples, the average entropy approaches the sum⁴⁰

$$S_{\frac{2\phi}{\pi} = \frac{p}{q} \in \mathbb{Q}}(L/2) = \frac{1}{q} \sum_{j=0}^{q-1} s\left(\frac{j\pi}{2q}\right) \quad (3.39a)$$

$$= -\frac{1}{q} \sum_{j=0}^{q-1} \left[\cos^2\left(\frac{j\pi}{2q}\right) \cdot \log_2\left(\cos^2\left(\frac{j\pi}{2q}\right)\right) + \sin^2\left(\frac{j\pi}{2q}\right) \cdot \log_2\left(\sin^2\left(\frac{j\pi}{2q}\right)\right) \right]. \quad (3.39b)$$

This is a Riemann summation for the integral in Equation (3.38), using the midpoint rule [181] with q subintervals of equal size.⁴¹ Consequently, the difference between the exact integral in Equation (3.38) and the sum in Equation (3.39) is

$$\Delta_q = \left| \int_0^{\frac{\pi}{2}} d\theta s(\theta) - \frac{1}{q} \sum_{j=0}^{q-1} s\left(\frac{j\pi}{2q}\right) \right| \leq \max_{\theta \in [0, \frac{\pi}{2}]} \left| \frac{d^2s(\theta)}{d\theta^2} \right| \cdot \frac{\pi^3}{192 \cdot q^2} \propto \frac{1}{q^2}. \quad (3.40)$$

This bounds, how much the data points in Figure 3.21 (a) may deviate from the value $2 - 1/\ln 2$. Note however that the integrand $s(\theta)$ is even in θ . Thus, Δ_q must only contain contributions odd in $1/q$; i.e., the difference between the sum and the integral is at most of order $\mathcal{O}(1/q^3)$. In Figure 3.21 (b), we show the cube root of Δ_q , which scales with $\mathcal{O}(1/q)$ in leading order. A quick comparison with Equation (3.35) explains, why the cube root of the average entanglement entropy of our matchgate circuits approaches the popcorn function at large q .⁴²

⁴⁰Figure 3.21 (a) was generated via Equation (3.39).

⁴¹Naively, this appears to be a left Riemann sum, but since $s(\theta)$ is periodic, the integration boxes can be shifted by half a step. This transforms the sum into a midpoint approximation of the integral, which gives us a stronger bound on its accuracy.

⁴²At small q , higher contributions result in a slight deviation between the entanglement entropy and the popcorn function; consider for example the data point at $2\phi/\pi = 1/2$ (i.e., $q = 2$).

3.8 Majorana Flavors

The macro models presented in Section 3.5 are not the only possible generalization of the MF model. Here I present a different approach that introduces Majorana flavors. Although this work is still unfinished, I will use this section to demonstrate that this model is at least interesting.

In Ref. [38], Fava et al. discussed a time-continuous fermionic model that closely resembles the MF model: A system with L sites evolves under the non-Hermitian Hamiltonian

$$H_{J,M} = \sum_{\mu=1}^L \sum_{a,b=1}^{n_{\text{fl}}} [J_{\mu}^{ab} + iM_{\mu}^{ab}] i\gamma_{\mu}^a \gamma_{\mu+1}^b. \quad (3.41)$$

Here, the Majorana modes γ_{μ}^a with $\mu \in \{1, \dots, 2L\}$ gain an additional “flavor” index $a \in \{1, \dots, n_{\text{fl}}\}$. They satisfy

$$\{\gamma_{\mu}^a, \gamma_{\nu}^b\} = 2\delta_{\mu,\nu} \delta_{a,b}. \quad (3.42)$$

When considering the case $n_{\text{fl}} = 1$, we can easily relate the terms in Equation (3.41) to the operations applied in the MF model:

- Contributions of the form $iJ_{\mu}\gamma_{\mu}\gamma_{\mu+1}$ are Hermitian and correspond to unitary evolutions of the form

$$U_J(t) = \exp[J_{\mu}\gamma_{\mu}\gamma_{\mu+1}t] = \cos(J_{\mu}t) \cdot \mathbb{1} + \sin(J_{\mu}t) \cdot \gamma_{\mu}\gamma_{\mu+1}. \quad (3.43)$$

In fermionic language, Equation (3.43) features hopping and superconducting contributions; the parameter J_{μ} describes the speed of the evolution. In the continuous model, all (non-commuting) unitary evolutions are applied simultaneously. In a discrete model, at $J_{\mu}t = -\pi/4 + 2\pi k$ with $k \in \mathbb{Z}$, we find the unitary gates applied in the MF model [cf. Equation (3.17)]:

$$U_J\left(t = \frac{-\pi/4 + 2\pi k}{J_{\mu}}\right) = \frac{1}{\sqrt{2}} (\mathbb{1} - \gamma_{\mu}\gamma_{\mu+1}) \quad (3.44)$$

- The terms $-M_{\mu}\gamma_{\mu}\gamma_{\mu+1}$ are non-Hermitian. We can intuitively understand them as continuous measurements of the operators $i\gamma_{\mu}\gamma_{\mu+1}$. The parameter M_{μ} sets the rate of these continuous measurements. The same operators are discretely measured in the MF model.

Thus, we may understand the model governed by the Hamiltonian in Equation (3.41) at $n_{\text{fl}} = 1$ as a time-continuous version of the MF model. Indeed, both models are described by nonlinear σ models and feature very similar phase diagrams with two area-law phases and an extended critical phase. However, when including Majorana flavors $n_{\text{fl}} > 1$, the continuous model realizes $n_{\text{fl}} + 1$ distinct area-law phases. This motivates the question: Can we naturally extend the MF model by including Majorana flavors, to realize variations of its phase diagram [cf. Figure 3.7 (b)]?

For convenience, we define the *flavored MF model* in the fermionic language.⁴³ $2n_{\text{fl}}L$ Majorana modes are set up on L sites in a circuit with T discrete time steps. The operations of the circuit are the unitary gates $U_{\mu,\mu+1}^{a,b} = (\mathbb{1} - \gamma_{\mu}^a \gamma_{\mu+1}^b) / \sqrt{2}$ and measurements of the observables $M_{\mu,\mu+1}^{a,b} = i\gamma_{\mu}^a \gamma_{\mu+1}^b$.⁴⁴ A trajectory is separated into even and odd steps:

- In odd time steps, “on-site” operations are performed on sites i ; i.e., on pairs $\gamma_{2i-1}^a \gamma_{2i}^b$. For each site, either a unitary gate $U_{2i-1,2i}^{a,b}$ is applied with probability p , or, with probability $(1-p)q$, a measurement $M_{2i-1,2i}^{a,b}$ is performed. For the respective operation, the Majorana flavors a and b are chosen at random. With probability $(1-p)(1-q)$, no operation is applied on site i .
- In even time steps, “off-site” operations are performed on neighboring sites $e = (i, i+1)$; i.e., on pairs $\gamma_{2i} \gamma_{2i+1}$. With probability p on every edge e , a unitary gate $U_{2i,2i+1}^{a,b}$ is applied, and measurements $M_{2i,2i+1}^{a,b}$ are performed with probability $(1-p)(1-q)$. The respective Majorana flavors a and b are chosen at random. With probability $(1-p)q$, no operation is applied on e .

We may consider the flavored MF model in the loop picture. For $n_{\text{fl}} = 1$, it reduces to the standard MF model described in Section 3.4 (cf. Figure 3.6). Otherwise, n_{fl} layers of MF models are stacked on top of each other. Operations that involve multiple flavors intertwine the layers by spanning loops between them.

To analyze how entanglement measures behave in the flavored MF model, let us first consider the case $p = 0$ (a “flavored PTIM”) with open boundaries. We performed simulations of the ancilla entropy S_{anc} at “square” aspect ratios $n_{\text{fl}}L = T$. The resulting data for the cases $n_{\text{fl}} = \{1, 2, 3\}$ is shown in Figure 3.22 (a–c). Clearly, the models exhibit $n_{\text{fl}} + 1$ distinct area-law phases. To understand what seems to happen here, first consider the case $q = 0$, where no operations are applied to the Majorana modes μ_1^a and μ_{2L}^a of any flavor $a \in \{1, \dots, n_{\text{fl}}\}$ and the corresponding world lines remain unaffected. Here, the loop model protects these *edge loops* localized at the system’s boundaries. For the PTIM, we already know this – the existence of an edge loop is connected to the survival of an initial cluster. At $n_{\text{fl}} > 1$, the number of edge loops is expected to increase, as $2n_{\text{fl}}$ Majorana world lines are unaffected by the circuit. Indeed, we observe $S_{\text{anc}} = n_{\text{fl}}$. At small $q > 0$, the edge loops remain stable. This is also consistent with the known behavior of the PTIM, which protects its initial cluster up to $q_c = 0.5$. In Figure 3.22 (b) and (c) we do however make a surprising observation: The edge loops do not all collapse at once when q reaches some critical value. Instead, the different area-law phases differ by the number of edge loops that are protected. This is reflected in a step-like behavior of the ancilla entropy S_{anc} with open boundaries. As q increases, the models cross multiple phase transitions that each remove one loop at every system boundary – until the final disentangled area-law phase is reached.

⁴³The model can be transferred into the qubit picture via a Jordan–Wigner transformation. In the case of open boundaries (and with an appropriate Jordan–Wigner string), the bosonic model is also local.

⁴⁴Transferring these operations into the loop model is straightforward.

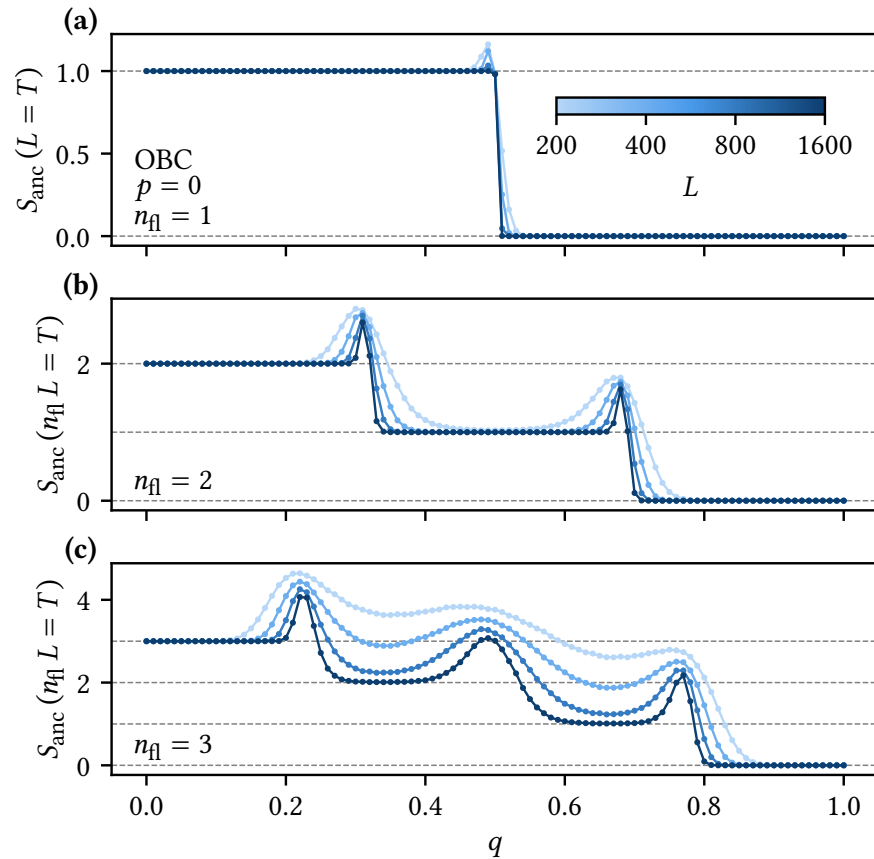


Figure 3.22 • Area-law phases in the flavored MF model at $p = 0$. Average ancilla entropy S_{anc} in flavored MF models with open boundary conditions (OBC) at $p = 0$ (without unitaries). **(a)** The case $n_{\text{fl}} = 1$ corresponds to the standard MF model that maps to the PTIM at $p = 0$. As seen in **(b)** and **(c)**, the number of distinct area-law phases increases with the number of Majorana flavors n_{fl} . They differ by the number of protected edge loops in the loop model. Data points show averages over 10^4 samples; error bars are smaller than the points.

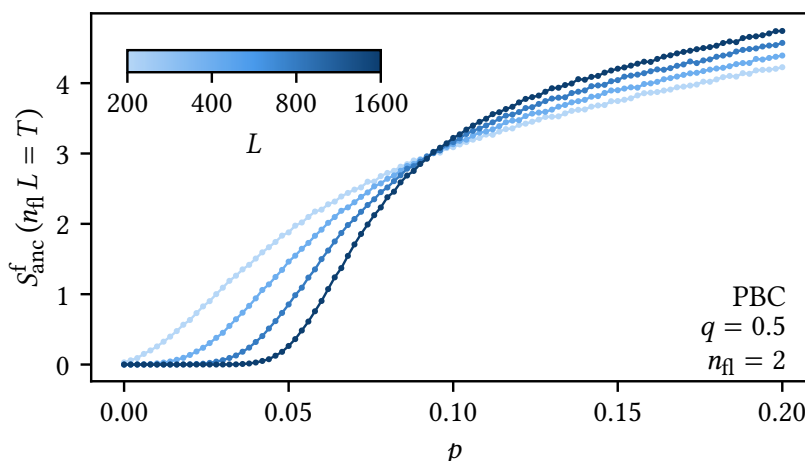


Figure 3.23 • Area-law phase of the flavored MF model at $p \neq 0$. The area-law phases in flavored MF models are stable under small unitary rates $p > 0$. Here we show the intermediate area-law phase of the $n_f = 2$ model. The ancilla entropy $S_{\text{anc}}^f(n_f L = T)$ at multiple L with periodic boundaries (PBC) shows a clear crossing into the critical regime. Data points show averages over 10^4 samples; error bars are smaller than the points.

This behavior is stable under the inclusion of unitaries. To illustrate this, we consider the case $n_f = 2$ as an example and demonstrate that its intermediate area-law phase (around $q = 0.5$) remains robust at small $p > 0$. Figure 3.23 shows the ancilla entropy of the model with periodic boundaries.⁴⁵ The emergence of a clear crossing at a finite value $p > 0$ proves that the area-law phase prevails under small rates of unitaries, before the model enters its critical phase. This allows us to qualitatively understand how Majorana flavors alter the lower part of the MF model’s phase diagram [cf. Figure 3.7 (b)]: With n_f , the critical phase gains more “peaks” that touch the line $p = 0$.

Note that these observations are consistent with the findings by Fava et al. [38], and it is reasonable to assume that their time-continuous model and our flavored MF model share some similar underlying physics. Indeed, the continuous model can be described by a nonlinear σ model (that is very reminiscent of the field theory for the MF model [154]). This field theory not only predicts the emergence of multiple area-law phases, but also the scaling behavior of entanglement measures in the critical phase. Here, the loop model offers a new perspective, revealing intriguing mechanisms that merit future investigation.

⁴⁵Periodic boundaries remove the edge loops, making a transition into the critical regime more visible.

3.9 Braiding Entanglement Dynamics and Simple Exclusion Processes

Before investigating loop models that model entanglement dynamics by tracking configurations of Majorana world lines (for example the MF model), I came across quantum circuit models with gates that generate representations of the braid group \mathcal{B}_L . Clearly, the two scenarios are connected. Here, I will shed some light on the relationship between a loop model and a braid representation and show how a classical simple exclusion process emerges in certain unitary circuits.

3.9.1 Unitary Bell Model

Consider L qubits with open boundaries and the Bell matrix [182–187]

$$B = \frac{1}{\sqrt{2}} \begin{pmatrix} 1 & 0 & 0 & 1 \\ 0 & 1 & -1 & 0 \\ 0 & 1 & 1 & 0 \\ -1 & 0 & 0 & 1 \end{pmatrix}, \quad (3.45)$$

which couples two neighboring qubits.⁴⁶ We can easily see that $B^{-1} = B^\top$, and we write B_e with $e = (i, i + 1)$ to indicate that the gate is applied on the qubits i and $i + 1$. Together, the matrices B_e and the inverse B_e^{-1} on all pairs e of adjacent qubits generate a finite-dimensional representation of the braid group \mathcal{B}_L , as they fulfill the Yang–Baxter equation

$$(B \otimes \mathbb{1})(\mathbb{1} \otimes B)(B \otimes \mathbb{1}) = (\mathbb{1} \otimes B)(B \otimes \mathbb{1})(\mathbb{1} \otimes B) \quad (3.46)$$

and it is $B^8 = \mathbb{1}$. It is also easy to verify that B is a matchgate [cf. Equation (1.11)]. In fact, we can write

$$B_{i,i+1} = \frac{1}{\sqrt{2}} (\mathbb{1} + iX_i Y_{i+1}) = \frac{1}{\sqrt{2}} (\mathbb{1} + Y_{2i} Y_{2i+2}) \propto U_{1432} \quad (3.47)$$

to relate the Bell matrix to the macro block U_{1432} with the corresponding phase diagram shown in Figure 3.15 (a) (U_{1432} and U_{3214} are connected via a space-inversion symmetry and are thus equivalent).

Using the Bell matrix, we define the *unitary Bell model* as follows: An open chain of L qubits is initialized in the disentangled state $|\Psi_0\rangle = |0 \dots 0\rangle$. The following evolution is separated into $T \cdot s$ discrete time steps. In every time step, Bell matrices B_e are applied to pairs e of neighboring qubits with probability $1/s$ in a brickstone pattern;⁴⁷ here we arbitrarily choose $s = 10$ to sufficiently randomize the evolution. We show a sample circuit in Figure 3.24 (a) (ignore the final measurement for now). Equation (3.47) allows

⁴⁶We call the Bell matrix “maximally entangling” because it maps product states in the z -basis onto fully entangled Bell states.

⁴⁷This is equivalent to the macro model 1432 at $p = 1$ with open boundaries.

us to understand the entanglement dynamics of the circuit in terms of a loop model, see Figure 3.24 (b). Note that the macro block $U_{1432} \propto B$ leaves every second Majorana world line unaffected. To track the entanglement entropy $\mathcal{S}(L/2)$ between the two system halves, we usually count the loops that go across the boundary between the subsystems (dashed line) and divide the result by two. Here, the properties of the Bell matrix B allow for a different approach that only tracks a single *braid* per qubit [184–186, 188–190] – effectively tracking only every second Majorana world line.⁴⁸ We show the braiding representation for our sample circuit in Figure 3.24 (c). The entanglement entropy is equal to the number of braids that start in the left subsystem and end on the right side (or vice versa).

Connection to the Symmetric Simple Exclusion Process

To better understand how entanglement grows over time, we make use of a different picture [see Figure 3.24 (d)]. Instead of braids, we consider colored balls in boxes, where a box can only hold a single ball. Unitaries translate to swaps of neighboring balls. If we are however only interested in the entanglement entropy $\mathcal{S}(L/2)$, we may simplify the picture by only tracking the balls of one subsystem without the need for colors (if no measurements are performed). We show the initial state of an infinite system $L \rightarrow \infty$ in Figure 3.24 (e). As time progresses, balls may randomly move to neighboring unoccupied boxes, and the entanglement entropy $\mathcal{S}(L/2)$ increases (decreases) whenever a ball crosses the subsystem boundary from left to right (right to left). This model is called a *symmetric simple exclusion process* (SSEP) [191–195] with a step initial condition, as previously investigated by Derrida et al. in Ref. [196]. The entanglement dynamics of the unitary Bell model are modeled by the total flux of balls in the SSEP, which is predicted as

$$S(L/2, T) \sim \sqrt{\alpha \frac{T}{s}} \quad (3.48)$$

for infinite systems $L \rightarrow \infty$ at large times $T/s \gg 1$. α is a constant prefactor. We performed simulations of the unitary Bell model at $L = 800$ and compared the entanglement growth with the corresponding fit function, as shown in Figure 3.25. Clearly, the simulation data is in agreement with the theoretical prediction.⁴⁹

3.9.2 Introducing Local Measurements

Finally, we may also include local measurements of the operator Z_i – this corresponds to the loop model 1432 at $p < 1$ and $q = 1$ [see Figure 3.15 (a)]. The circuit shown in Figure 3.24 (a–d) includes one such measurement. We already established its representation in the loop picture

⁴⁸We call them “braids”, to not confuse them with loops that correspond to Majorana world lines. Their braiding properties ($B^2 \neq \mathbb{1}$) are not important in this context.

⁴⁹For finite L , the average entanglement entropy $S(L/2)$ will eventually saturate at $L/4$. Thus, the prediction in [195] fails at very large T/s . For the standard SSEP, the total flux approaches $\sqrt{T/\pi}$ [196]; here we have slightly modified transition probabilities that rescale the dynamics (via the prefactor α).

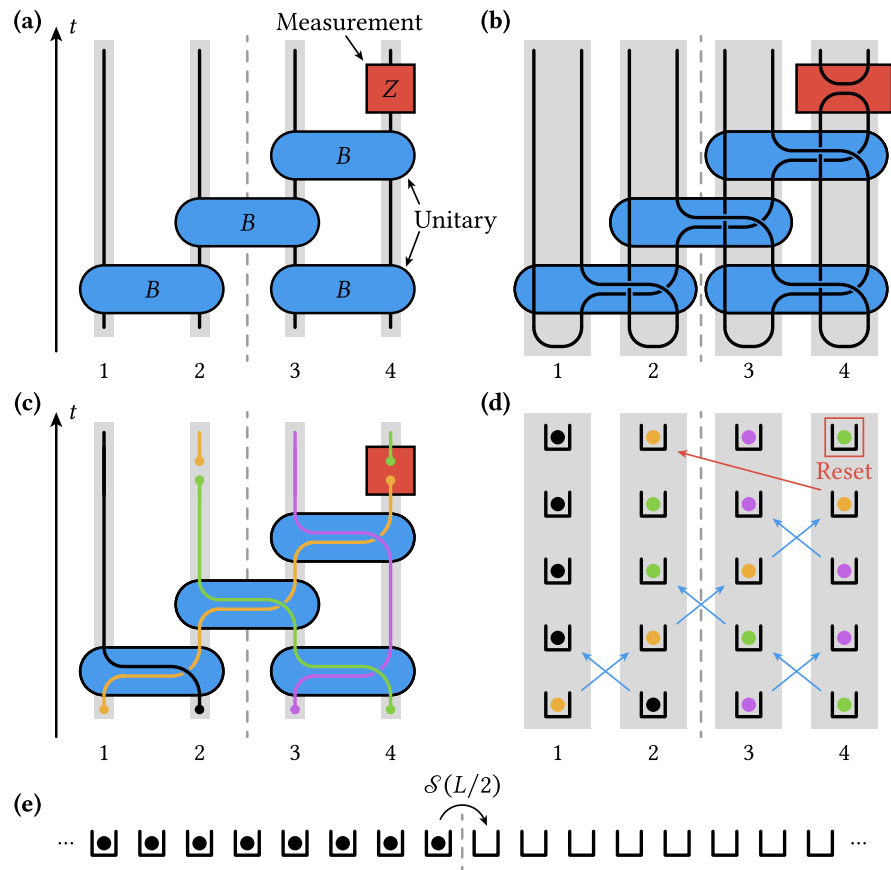


Figure 3.24 • Sample Bell circuit trajectory. (a) Sample Bell circuit including applications of the Bell matrix and a single Z_4 measurement. (b) Loop model representation of the same circuit with $B \propto U_{1432}$. (c) Unitaries only affect every second Majorana world line, allowing for a simplified braiding representation. Measurements correspond to non-local braid teleportations in this picture. (d) Instead of braids, one may also track the entanglement structure via colored balls in boxes. (e) The half-system entanglement entropy $\mathcal{S}(L/2)$ of a unitary Bell circuit can be modeled via a symmetric simple exclusion process with step initial condition.

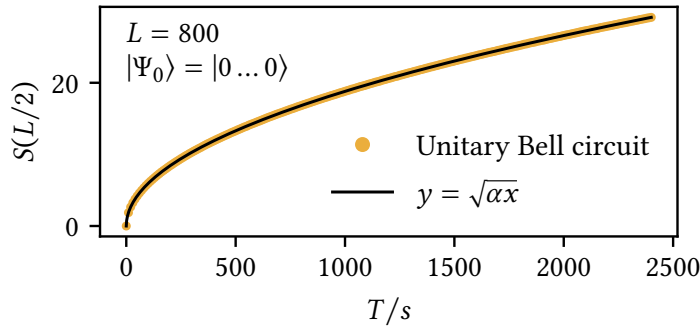


Figure 3.25 • Entanglement dynamics in the unitary Bell model. Average entanglement growth with a disentangled initial state and scaling factor $s = 10$ at $L = 800$. At $T \rightarrow \infty$, the entanglement entropy will settle to $S(L/2) = L/4$. Far away from this equilibrium, the model closely follows the predictions for a symmetric simple exclusion process on an infinite chain, as indicated by the fit. Data points show averages over 10^5 sample trajectories; error bars are negligible.

(cf. Figure 3.3). In the braid picture [Figure 3.24 (c)], projective measurements are modeled by non-local braid teleportations: Every braid is initially assigned to a qubit (shown as colors). If qubit i is measured, the corresponding braid is swapped with whichever braid is currently positioned at site i ; i.e., one braid is reset to its original position i and another braid is teleported away from i . It is not surprising to see this non-local nature of measurements emerge here. Entanglement is, at its heart, connected to the concept of locality.⁵⁰ A single measurement may destroy the entanglement of a qubit pair across any distance.

This gives us some intuition on the power of local measurements over local unitaries in this model and indicates why the volume-law phase breaks down under finite monitoring rates: For a volume law to exist, the braids must travel arbitrarily large distances. However, the monitored Bell model exhibits a characteristic time scale related to the monitoring rate, after which qubits are typically measured. Thus, all braids are reset regularly, seemingly reducing their average travel distance to some constant. This process breaks the volume law of the model down to an area law. However, this image comes with a major flaw. In the unitary Bell model, braids essentially perform random walks and travel the expected average distance $\propto \sqrt{T}$. If a measurement is performed, one braid is reset and another braid is teleported to the now vacant position, technically allowing for it to travel larger distances.

We may also consider a different scenario, where all measurements Z_i are performed at once with a small rate $r > 0$. This resets the entanglement entropy to the initial value $\mathcal{S}(L/2) = 0$. In this case, the entanglement entropy $\mathcal{S}(L/2)$ is modeled by a symmetric exclusion process under stochastic resetting, as investigated by Basu et al. in Ref. [197]. Even if the randomized resets are ignored, the model's dynamical properties are affected.

⁵⁰Any entangled state can, in principle, be disentangled by a non-local unitary transformation.

Consider the rate of change

$$\Delta S_T := \langle\langle \mathcal{S}(L/2, T) - \mathcal{S}(L/2, T - 1) \rangle\rangle \quad (3.49)$$

of the entanglement entropy. When calculating the sample average, we exclude circuits with a measurement step at T . At $r = 0$, the rate of change on average approaches $\Delta S_T \propto \sqrt{T}^{-1}$ (cf. Figure 3.25). At $r > 0$ however, it is predicted to be constant $\Delta S_T \sim c > 0$ [197].

Appendices for Chapter 3

3.A Efficient Implementation of Matchgate Quantum Circuits

All simulations of matchgate quantum circuits shown in this thesis were performed using an efficient algorithm outlined by Bravyi in Ref. [91]. As the implementation of this procedure is not quite obvious, we give some explicit instructions here. This is an extension of the introduction we gave in Subsection 1.2.2.

The general idea is to work in the fermionic picture, which is connected to our bosonic matchgate circuits via a Jordan–Wigner transformation [remember also Equation (1.20)]. Fermionic Gaussian states can be represented via a quadratic Hamiltonian H as⁵¹

$$\rho = \frac{e^{-H}}{\text{Tr}[e^{-H}]}. \quad (3.50)$$

Crucially, any fermionic Gaussian state is completely characterized by its $2L \times 2L$ *correlation matrix* [129]

$$M_{\mu\nu} = \frac{i}{2} \text{Tr}(\rho[c_\mu, c_\nu]) \quad (3.51)$$

with the Majorana operators c_μ .⁵² As the size of M only scales polynomially with L , this representation of a state can be calculated on a classical computer. For the initial state $\rho = |0 \dots 0\rangle\langle 0 \dots 0|$, it is

$$M = \bigoplus_{i=1}^L \begin{pmatrix} 0 & 1 \\ -1 & 0 \end{pmatrix}. \quad (3.52)$$

To apply a matchgate, we convert it to a fermionic Gaussian unitary U with the corresponding rotation matrix $R \in SO(2L)$ [using Equation (1.20)]. Under the unitary evolution, it is

$$M \mapsto R^\top M R. \quad (3.53)$$

⁵¹Applying Gaussian unitaries of the form $U = e^{i\tilde{H}}$ on both sides of the density matrix clearly produces another Gaussian state.

⁵²Any higher-order correlations can be reduced to this correlation matrix using Wick's theorem [58].

Note that when first defining a matchgate, we artificially restrict ourselves to nearest-neighbor fermionic operations. Equation (3.53) is true for *all* Gaussian unitaries U .

We may also measure $Z_i = (-1)^{a_i^\dagger a_i}$ with the possible results -1 ($+1$) if a fermion (no fermion) is found on the site i . Let K^i be an antisymmetric $2L \times 2L$ matrix

$$K_\pm^i = \bigoplus_{j=1}^L \delta_{ij} \begin{pmatrix} 0 & \pm 1 \\ \mp 1 & 0 \end{pmatrix}, \quad (3.54)$$

and P_- (P_+) be the probability of finding a fermion (no fermion) at the site i . Then it is

$$P_+ = 1 - P_- = \text{Tr} \left[\rho a_i a_i^\dagger \right] = \frac{1}{2} \text{Pf}(M) \text{Pf}(K_+^i - M^{-1}) = \frac{1}{2} \sqrt{\det(MK_+^i - \mathbb{1})} \quad (3.55)$$

with the Pfaffian $\text{Pf}(\bullet)$. The measurement result is selected based on this expectation value. According to the measurement result, we must also calculate the new state of the system. We define the matrix

$$L_\pm = [\mathbb{1} - MK_\pm^i]^{-1} M. \quad (3.56)$$

Given the measurement outcome ± 1 , the correlation matrix is updated as follows:

$$M_{\mu\nu} \mapsto \begin{cases} \pm 1, & \text{if } \mu = 2i \wedge \nu = \mu + 1, \\ \mp 1, & \text{if } \nu = 2i \wedge \mu = \nu + 1, \\ 0, & \text{if } \lfloor \frac{\mu}{2} \rfloor = i \vee \lfloor \frac{\nu}{2} \rfloor = i, \\ L_{\pm, \mu\nu}, & \text{otherwise} \end{cases} \quad (3.57)$$

Finally, it is also possible to calculate von Neumann entanglement entropies from a given correlation matrix [remember Equation (1.1)]. Our calculation follows Ref. [129]. Let A be a subsystem and M_A be the lines and columns of the correlation matrix that correspond to the sites in A . We define the modified correlation matrix

$$\Gamma_A = \frac{iM_A + \mathbb{1}}{2} \quad (3.58)$$

with the real-valued eigenvalues $\{\zeta_1, \dots, \zeta_{2|A|}\}$. Then the entanglement entropy is

$$\mathcal{S}(A) = - \sum_{j=1}^{2|A|} \zeta_j \log_2 \zeta_j. \quad (3.59)$$

Note that it is

$$\lim_{\zeta \rightarrow 0} [\zeta \log_2 \zeta] = 0. \quad (3.60)$$

To make Equation (3.59) numerically stable, we therefore exclude all vanishing eigenvalues (below a certain threshold) from the sum.

As this algorithm only uses $2L \times 2L$ matrices, its efficiency is only limited by the complexity of matrix multiplications, diagonalizations, inversions and determinants. These operations typically require $\mathcal{O}(L^3)$ steps. Thus, this implementation of matchgate quantum circuits is more efficient than the procedure described in Subsection 1.2.2. As the number of operations scales with the size $\mathcal{O}(LT)$, we find a total runtime of $\mathcal{O}(L^4 T)$.

3.B Periodic Boundaries in Fermionic Circuits

In the bosonic MF model, periodic boundaries are implemented via the unitary

$$U_{L,1}^{\text{off},b} = H_L H_1 S_L S_1 CZ_{L,1} H_L H_1 \propto \frac{1}{\sqrt{2}} (\mathbb{1} - iX_L X_1) \quad (3.61a)$$

and the measurement of

$$M_{L,1}^{\text{off},b} = X_L X_1. \quad (3.61b)$$

There is no representation for these operations in the loop model as $U_{L,1}^{\text{off},b}$ is *not* a matchgate and $M_{L,1}^{\text{off},b}$ is not a pair of Majorana modes in the stabilizer group. In the following, we will refer to the MF model, which includes these two operations as the *bosonic version*.

Implementing periodic boundaries in the loop model is straightforward. The additional loop operations represent the fermionic unitary

$$U_{L,1}^{\text{off},f} = \frac{1}{\sqrt{2}} (\mathbb{1} - \gamma_{2L} \gamma_1) = \frac{1}{\sqrt{2}} (\mathbb{1} - iX_1 X_L Z_1 Z_2 \cdots Z_L) \quad (3.62a)$$

and the measurement of

$$M_{L,1}^{\text{off},f} = i\gamma_{2L} \gamma_1 = -X_1 X_L Z_1 Z_2 \cdots Z_L. \quad (3.62b)$$

We call this the *fermionic version* of the MF model.

In this chapter we consider the bosonic version of the MF model, but we perform our simulations on the loop model with periodic boundaries. Thus, we actually simulate the fermionic version. Here, we show that our approach is still valid. In the following, we describe circuits with unitaries U^{on} and U^{off} and measurements M^{on} and M^{off} . We do not put any restrictions on which operation is applied when. Thus, the following proofs are not only true for the MF model but also for any model derived from the same components.⁵³

3.B.1 Without Ancilla Qubits

Consider the MF model with L qubits in an initial stabilizer state and assume that the global parity $\pm Z_1 Z_2 \cdots Z_L$ is a stabilizer of this state. This requirement is for example always fulfilled for states that are described by loop configurations, i.e., that are stabilized by L Majorana pairs of the form $i\gamma_\mu \gamma_\nu$.⁵⁴ However, the following considerations are true for *any* state with fixed parity, including mixed states.

Our proof takes the form of an induction. We will assume that both versions of the MF model start in the same stabilizer state and that the same operations are applied — once in the bosonic and once in the fermionic version. We will show that both versions of the MF

⁵³For example, circuit models with different probabilities or with macro blocks that group multiple operations together.

⁵⁴The stabilizer group \mathfrak{S} is generated by L pairs $i\gamma_\mu \gamma_\nu$. The product of all generators $\pm \gamma_1 \gamma_2 \cdots \gamma_{2L}$ is the parity.

model act identically on any stabilizer state with fixed parity. Thus, if both versions start out in the same initial state and follow the same circuit, their stabilizers must follow the same trajectory throughout all time steps.

The unitaries and measurements of both versions of the MF model commute with the parity $Z_1 Z_2 \cdots Z_L$, making it a conserved quantity. Assume that a state is stabilized by

$$\mathfrak{S} = \langle Z_1 Z_2 \cdots Z_L, g_2, g_3, \dots \rangle \quad (3.63)$$

with the generators g_i . All unitaries and measurements acting on the bulk of the bosonic and fermionic versions of the MF model act identically on the stabilizer group, as the respective operators are connected via the Jordan–Wigner transformation. Therefore both versions yield the same evolution of the stabilizer group. This is unsurprising and the reason why we can always use the loop model with open boundaries. If the boundary measurement $M_{L,1}^{\text{off,b}}$ or $M_{L,1}^{\text{off,f}}$ is performed, three cases must be distinguished as per the rules of the stabilizer formalism (cf. Subsection 1.2.1).

1. If the operator $\pm M_{L,1}^{\text{off,b}}$ is already an element of the stabilizer group \mathfrak{S} , the measurement result is deterministic and \mathfrak{S} remains unchanged in the bosonic version. In this case, the fermionic measurement operator $\pm M_{L,1}^{\text{off,f}} \propto M_{L,1}^{\text{off,b}} Z_1 \cdots Z_L$ must also be a stabilizer. Consequently, the stabilizer group also remains unchanged in the fermionic version of the MF model.
2. If the bosonic measurement operator $\pm M_{L,1}^{\text{off,b}}$ commutes with all stabilizers in \mathfrak{S} but is not one of them, the system is in a mixed state and will be purified by the measurement. The operator $\pm M_{L,1}^{\text{off,b}}$ will be added to the generating set of \mathfrak{S} (the sign depends on the measurement outcome). If $\pm M_{L,1}^{\text{off,b}}$ is not in \mathfrak{S} , then $\pm M_{L,1}^{\text{off,f}}$ can also not be in \mathfrak{S} , since they differ only by the parity, which is a stabilizer. Thus, in the fermionic version, $\pm M_{L,1}^{\text{off,f}}$ will be added to the stabilizer group. The new stabilizer groups are identical:

$$\tilde{\mathfrak{S}}^f = \langle Z_1 \cdots Z_L, \pm M_{L,1}^{\text{off,f}}, g_2, \dots \rangle = \langle Z_1 \cdots Z_L, \pm M_{L,1}^{\text{off,b}}, g_2, \dots \rangle = \tilde{\mathfrak{S}}^b \quad (3.64)$$

Here we again used the fact that $M_{L,1}^{\text{off,f}} \propto M_{L,1}^{\text{off,b}} Z_1 \cdots Z_L$.

3. If $M_{L,1}^{\text{off,b}}$ anticommutes with at least one generator of \mathfrak{S} , the measurement outcome is randomly ± 1 . As the parity always commutes with all measurements, we can bring the stabilizer generators in the form of Equation (3.63), such that only g_2 anticommutes with $M_{L,1}^{\text{off,b}}$. After the measurement was performed, the new stabilizer group is

$$\tilde{\mathfrak{S}}^b = \langle Z_1 \cdots Z_L, \pm M_{L,1}^{\text{off,b}}, g_3, \dots \rangle. \quad (3.65)$$

If g_2 anticommutes with $M_{L,1}^{\text{off,b}}$ it must also anticommute with $M_{L,1}^{\text{off,f}}$. Thus, the fermionic model follows the same procedure with

$$\tilde{\mathfrak{S}}^f = \langle Z_1 \cdots Z_L, \pm M_{L,1}^{\text{off,f}}, g_3, \dots \rangle = \tilde{\mathfrak{S}}^b. \quad (3.66)$$

The bosonic and fermionic versions follow the same evolution (up to signs) under any projective measurements.

Now we consider a unitary $U_{L,1}^{\text{off,b}}$ (or $U_{L,1}^{\text{off,f}}$) being applied to the stabilizer state. Let $g \in \mathfrak{S}$ be a stabilizer. First, we describe how g evolves in the bosonic version of the MF model. If g commutes with $X_1 X_L$, then it also commutes with $U_{L,1}^{\text{off,b}}$ [cf. Equation (3.61a)]. As $U_{L,1}^{\text{off,b}} g (U_{L,1}^{\text{off,b}})^\dagger = g$, the stabilizer remains unchanged after the unitary was applied. If g anticommutes with $X_1 X_L$, then it is

$$U_{L,1}^{\text{off,b}} g (U_{L,1}^{\text{off,b}})^\dagger = \frac{1}{2} (\mathbb{1} - iX_1 X_L) g (\mathbb{1} + iX_1 X_L) \quad (3.67a)$$

$$= \frac{1}{2} (g + igX_1 X_L - iX_1 X_L g + X_1 X_L g X_1 X_L) \quad (3.67b)$$

$$= igX_1 X_L. \quad (3.67c)$$

Now we consider the same stabilizer g in the fermionic version of the MF model, i.e., under the unitary action $U_{L,1}^{\text{off,f}}$. All stabilizers commute with the parity $Z_1 \cdots Z_L$. If g commutes with $X_1 X_L$, it also commutes with $X_1 X_L Z_1 \cdots Z_L$ and thus with $U_{L,1}^{\text{off,f}}$ [cf. Equation (3.62a)]. Again, g remains unchanged by the unitary action (as in the bosonic version). If g anticommutes with $X_1 X_L$ (and by extension anticommutes with $X_1 X_L Z_1 \cdots Z_L$), it will evolve under the fermionic unitary action as

$$U_{L,1}^{\text{off,f}} g (U_{L,1}^{\text{off,f}})^\dagger = \frac{1}{2} (\mathbb{1} - iX_1 X_L Z_1 \cdots Z_L) g (\mathbb{1} + iX_1 X_L Z_1 \cdots Z_L) \quad (3.68a)$$

$$= igX_1 X_L Z_1 \cdots Z_L. \quad (3.68b)$$

The stabilizers in Equations (3.67c) and (3.68b) only differ by the global parity $Z_1 \cdots Z_L$, which itself is also a stabilizer of the state. As the reasoning presented here applies to *all* stabilizers g , the stabilizer group \mathfrak{S} follows the same evolution under the action of $U_{L,1}^{\text{off,b}}$ and $U_{L,1}^{\text{off,f}}$.

This proves that, given the same initial stabilizer state with fixed global parity $\pm Z_1 \cdots Z_L$, both versions of the MF model will always yield the same stabilizers (omitting signs) and therefore all entanglement measures must also be identical. Therefore — without ancilla qubits — we may use the efficient loop model to calculate entanglement entropies of the bosonic MF model. \square

3.B.2 With Ancilla Qubits

Now we consider simulations of the bosonic MF model with L system qubits $\{1, \dots, L\}$ and another L ancilla qubits $\{L+1, \dots, 2L\}$. The initial state is chosen such that the system qubits are fully entangled with the ancilla qubits [for example, a state stabilized by the group described in Equation (3.15)]. Here, the system has a fixed global parity $Z_1 \cdots Z_{2L}$, but the system parity $Z_1 \cdots Z_L$ is not a stabilizer. Thus, our argument from Subsection 3.B.1 fails. Indeed, the two versions of the MF model generally yield different entanglement entropies,

i.e., the loop model does not accurately predict the entropy $S_{\text{anc}}^{\text{b}}$ of the bosonic MF model. Yet we argue that for our purposes, calculating the sample-averaged fermionic entropy $S_{\text{anc}}^{\text{f}}$ using the loop model with periodic boundaries is still a valid approach, because it follows the same scaling behavior as $S_{\text{anc}}^{\text{b}}$. Here, we will elaborate on this.

Phase Diagrams

Entanglement phases are most commonly defined by the scaling behavior of the average entropy $S(L/2)$ of a given model. The phase diagrams shown in this chapter were however not generated from $S^{\text{b}}(L/2)$ but instead from crossings emerging in the sample-averaged entropy $S_{\text{anc}}^{\text{f}}$. Simulations for this were performed on the loop model with periodic boundaries, as the crossings are generally clearer without unwanted boundary effects.

To justify why this is allowed, we follow the assumption that all entanglement measures on a given model yield the same phase diagram, i.e., the point at which the entanglement entropy $S(L/2)$ in the steady state of the system enters a critical phase is the same point at which the entropy $S_{\text{anc}}(L \propto T)$ shows a crossing. Now consider the phase diagram of the bosonic version of the MF model generated by the entropy $S^{\text{b}}(L/2)$. As we proved in Subsection 3.B.1, this entropy is equal to its fermionic counterpart $S^{\text{b}}(L/2) = S^{\text{f}}(L/2)$. Therefore, both versions of the MF model must share the same phase diagram. We create this diagram by performing simulations with ancilla qubits, because both entropies $S^{\text{f}}(L/2)$ and $S_{\text{anc}}^{\text{f}}(L = T)$ undergo the same transitions.

The final argument — claiming that both fermionic entanglement entropies yield the same phase diagram — is a rigorous one on the loop model. The scaling behaviors of S^{f} and $S_{\text{anc}}^{\text{f}}$ are both dictated by the scaling behavior of average loop lengths in the loop model [154]. Therefore, the fermionic entropy $S_{\text{anc}}^{\text{f}}(L = T)$ with periodic boundaries may be used to efficiently generate the phase diagram for $S^{\text{b}}(L/2)$.

Entanglement Entropy

Finally, we consider the value of the average entanglement entropy $S_{\text{anc}}^{\text{b}}$ of the system qubits and its fermionic counterpart $S_{\text{anc}}^{\text{f}}$. Under the assumption of periodic boundaries, these are not equal. Here we show that both entropies do however exhibit the same scaling behavior.

Consider any L -qubit stabilizer model with a given space-time pattern that includes Clifford gates and Pauli measurements. Given an initial state with stabilizers \mathfrak{S}_0 , the final state is (up to prefactors of the stabilizers) fully determined by this pattern. We will now consider two different initial states and apply the same circuit to both of them. First, we enter a fully mixed state with the trivial stabilizer group $\mathfrak{S}_0 = \{\mathbb{1}\} = \langle \rangle$, which evolves under the circuit $\mathfrak{S}_0 \mapsto \mathfrak{S}$. The entanglement entropy of the final state with the system's environment is determined by the number $n \leq L$ of generators for the stabilizer group $\mathfrak{S} = L - n$. Secondly, we consider a slightly less mixed initial state stabilized by $\tilde{\mathfrak{S}}_0 = \{\mathbb{1}, g\} = \langle g \rangle$ with some element of the Pauli group $g \in \mathcal{P}_L$. We let it evolve under the same circuit $\tilde{\mathfrak{S}}_0 \mapsto \tilde{\mathfrak{S}}$. Again, the number of generators $\tilde{n} \leq L$ of the final stabilizer group determines the entanglement

entropy $\tilde{\mathcal{S}} = L - \tilde{n}$ of the L qubits. The two entanglement entropies will either be equal or differ by one:

$$\mathcal{S} - \tilde{\mathcal{S}} = \begin{cases} 0, \\ 1 \end{cases} \quad (3.69)$$

To prove that Equation (3.69) is indeed true, we will show that both initial states follow very similar trajectories. We take an iterative approach and show how the two states evolve under single unitaries or measurements. From there, we can extrapolate how the two trajectories relate. As usual, when considering entanglement entropies, we will ignore all measurement results (signs of stabilizer generators).

Assume that \mathfrak{S} and $\tilde{\mathfrak{S}}$ are either equal or differ by just one additional generator in $\tilde{\mathfrak{S}}$. We take this as our induction hypothesis. If a unitary action is applied in our circuit, the number of stabilizer generators remains unchanged and the stabilizer groups \mathfrak{S} and $\tilde{\mathfrak{S}}$ are transformed identically, possibly with an additional generator in $\tilde{\mathfrak{S}}$. Now consider a projective measurement of an observable M :

1. If M is already in \mathfrak{S} , then it is also in $\tilde{\mathfrak{S}}$. The measurement leaves both stabilizer groups unchanged. After the measurement, the induction hypothesis is still intact.
2. If M anticommutes with a generator in \mathfrak{S} , it anticommutes with the same generator in $\tilde{\mathfrak{S}}$. Following the rules of the stabilizer formalism, this generator is replaced by M in both groups. Again, the induction hypothesis holds for the next time step.
3. If the measurement operator M commutes with all elements of \mathfrak{S} but is not a stabilizer, it is added to \mathfrak{S} , purifying the state. As $\tilde{\mathfrak{S}}$ has possibly an additional generator, we need to distinguish three possible cases for the second trajectory.
 - a) If M is an element of $\tilde{\mathfrak{S}}$, it must be due to the additional generator which is not in \mathfrak{S} . The measurement acts trivially on the second trajectory and from now on the states are the same $\mathfrak{S} = \tilde{\mathfrak{S}}$ and trivially share the same entanglement entropy $\mathcal{S} = \tilde{\mathcal{S}}$. Nonetheless, the induction hypothesis is still intact and must trivially hold for all subsequent time steps.
 - b) If M anticommutes with a generator of $\tilde{\mathfrak{S}}$, it must be the additional generator which is not part of \mathfrak{S} . This generator will be replaced by M and subsequently both trajectories assume the same state $\mathfrak{S} = \tilde{\mathfrak{S}}$ with identical entanglement entropies $\mathcal{S} = \tilde{\mathcal{S}}$. The induction hypothesis holds true for all following time steps.
 - c) If M commutes with all generators of $\tilde{\mathfrak{S}}$ but is not a stabilizer of the state, it is added to the stabilizer group and purifies the state — just as for the first trajectory \mathfrak{S} . The two stabilizer groups may still differ, but the induction hypothesis cannot be broken.

All circuits fall into two categories. Either both initial states yield the same final stabilizer groups $\mathfrak{S} = \tilde{\mathfrak{S}}$, or the second trajectory remains slightly more purified with exactly one

additional stabilizer generator g' (which is just g transformed by all unitaries that were performed). This proves Equation (3.69).

Finally, we use this result to understand how the entanglement entropies $S_{\text{anc}}^{\text{b}}$ and $S_{\text{anc}}^{\text{f}}$ of the two versions of the MF model (with periodic boundaries) relate. In the initial state ρ , the L system qubits are fully entangled with the L ancilla qubits, for example via L Bell pairs. Consequently, the initial state of the system qubits $\rho_{\text{sys}} = \text{Tr}_{\text{anc}}[\rho]$ is fully mixed. When combining all unitaries and projectors enacted upon by the circuit into a single matrix \mathcal{C} , we notice that $\mathcal{C} = \mathcal{C}_{\text{sys}} \otimes \mathbb{1}_{\text{anc}}$ (the circuit acts only on the system qubits). Consequently, we may simulate the system by only tracking the evolution of the qubits $\{1, \dots, L\}$ with the fully mixed initial state ρ_{sys} which is stabilized by $\mathfrak{S} = \{\mathbb{1}\} = \langle \cdot \rangle$. This is true for the bosonic and the fermionic versions of the circuit.

In Subsection 3.B.1, we showed that, if both versions of the circuit had started in the state $\tilde{\mathfrak{S}} = \langle Z_1 \dots Z_L \rangle$, they would follow the same trajectory and entanglement dynamics. We combine this with Equation (3.69) to find

$$\mathcal{S}_{\text{anc}}^{\text{b}} - \mathcal{S}_{\text{anc}}^{\text{f}} = \begin{cases} 1, \\ 0, \\ -1. \end{cases} \quad (3.70)$$

This relation bounds the sample-averaged difference $|\mathcal{S}_{\text{anc}}^{\text{f}} - \mathcal{S}_{\text{anc}}^{\text{b}}| \leq 1$. In the limit $L \rightarrow \infty$, the difference approaches a constant

$$\lim_{L \rightarrow \infty} [\mathcal{S}_{\text{anc}}^{\text{f}} - \mathcal{S}_{\text{anc}}^{\text{b}}] = C \quad (3.71)$$

with $|C| \leq 1$. As we are generally not concerned with the absolute value of the entropy $S_{\text{anc}}^{\text{b}}$ but its scaling behavior, our approach of using loop model simulations and instead calculating $S_{\text{anc}}^{\text{f}}$ is valid. \square

3.C On MF Model Aspect Ratios

In Figure 3.8 (a), we demonstrated that the average entropy $S_{\text{anc}}^{\text{f}}(2L = T)$ of the steady state of the MF model scales with $1/4\pi \cdot \log(L/L_0)$ in the thermodynamic limit. This prediction was originally made by Nahum et al. for a CPLC on a cylinder [154] with equal height and circumference. Here, we provide some insights into how the MF model must be scaled to match this shape, i.e., why we needed to choose the aspect ratio $2L = T$.

For an introduction to the CPLC we refer the reader to Ref. [154]. It is defined on a square grid with vertical and horizontal grid lines. Our Majorana world lines run diagonally through this grid, i.e., a section of an MF trajectory (cf. Figure 3.6) corresponds to a loop configuration which is rotated by 45° . The probabilities p and q were chosen to match the statistics of the CPLC [128].

The prediction made by Nahum et al. is the following: Consider a CPLC on a cylinder with length N and circumference N . That is, N lines enter the cylinder at the bottom and N

lines exit it at the top.⁵⁵ Then the average spanning number $\langle\langle n_s \rangle\rangle$ – the number of loops spanning the full length of the cylinder – approaches

$$\langle\langle n_s \rangle\rangle \sim \frac{1}{2\pi} \log \left[\frac{N}{N_0} \right]. \quad (3.72)$$

This is a result that directly arises from the representation of the CPLC as a σ model, i.e., it is obtained from a continuum description of the CPLC. Therefore, Equation (3.72) only applies at large N , where a continuous field theory becomes accurate. To recreate this result on the MF model, we must map the lengths L and T to the dimensions of the $N \times N$ cylinder. As a first step, we make sure that the loop representation of the MF trajectory does have a square aspect ratio. Since we distinguish between even and odd time steps, but two Majorana world lines correspond to a physical site, we must choose $2L = T$. This is also illustrated in Figure 3.6. Our loop representation does now resemble a square CPLC rotated by 45° . For large systems, we do not expect this rotation to have any effect, as the σ model exhibits a rotational symmetry. We enforce periodic boundary conditions on the MF model to recreate the shape of the cylinder.

Our system now has the correct shape, but we still need to map the system size L to N . Every physical site contributes two lines to the loop model, but with the 45° rotation, the side lengths of the grid are rescaled by an additional factor $\sqrt{2}$. Therefore, it is $\sqrt{2}L = N$. In Equation (3.20) we absorbed this prefactor in L_0 . It represents a shift in Figure 3.8 (a) and has no effect on the scaling behavior. Lastly, we remember that the entanglement entropy S_{anc}^f between a system and ancilla qubits is exactly the spanning number divided by 2. For this reason, we find the prefactor $1/4\pi$ in Equation (3.20).

3.D Symmetry of the 2314 Phase Diagram

We show that the macro block U_{2314} must yield a phase diagram that is invariant under the map $q \mapsto (1 - q)$. To this end, we make use of an argument for loop models with periodic boundaries, which was previously made by Merritt et al. in Ref. [128]: Non-local loop measures must be invariant under a shift of all Majorana indices $\mu \mapsto \mu + 1$. This specifically concerns the scaling behavior of the entropies S_{anc}^f and $S(L/2)$ which determine the phase diagram as shown in Figure 3.15 (b). Crucially, the shift maps the observables $M^{\text{on}} \mapsto M^{\text{off}}$ and $M^{\text{off}} \mapsto M^{\text{on}}$, effectively mapping $q \mapsto (1 - q)$.

For our proof, we consider a small section of the loop model (cf. Figure 3.13), showing only a single time step for two qubits. We show such a section in Figure 3.26 (top left), marking all potential positions of unitaries and measurements and denoting the respective probabilities. In the following, we perform a series of transformations on the loop model, which cannot change the scaling behavior of extensive entanglement measures. All steps are illustrated in Figure 3.26.

⁵⁵This is *not* equivalent to an MF model with periodic boundaries, because the CPLC lattice is oriented differently.

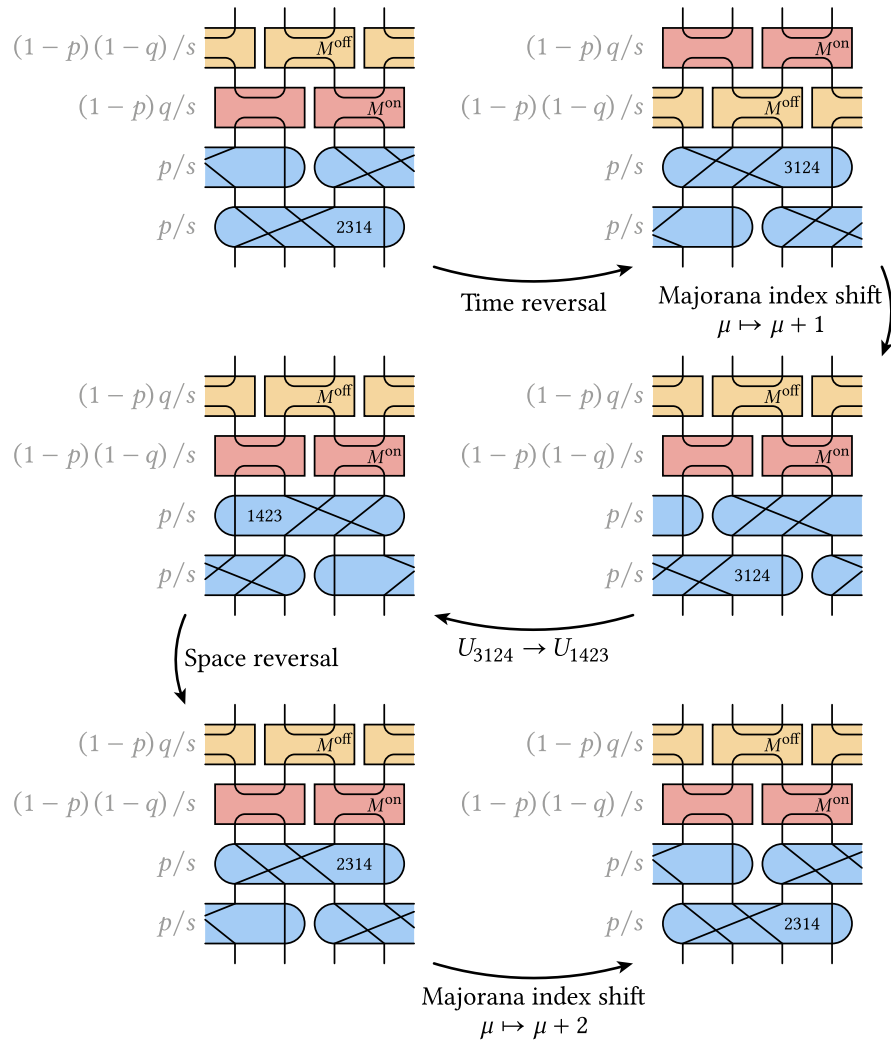


Figure 3.26 • Illustration of the proof for the $q \leftrightarrow (1 - q)$ symmetry of the model 2314. A section of the loop model is shown and transformed in steps, which leave extensive loop measures unchanged (apart from local effects). We are able to map $q \mapsto (1 - q)$, proving the symmetry of the phase diagram in Figure 3.15 (b). The same steps can be taken to verify the same symmetry in the model 3214 [see Figure 3.15 (a)].

1. As a first step, we invert the direction of time by flipping the loop model upside down. This maps the unitaries $U_{2314} \mapsto U_{3124}$ and changes the order in which operations are applied in a time step. For convenience, we always show a section of the trajectory with the unitaries at the bottom. The entropy $\mathcal{S}_{\text{anc}}^f$ remains unchanged by this transformation. Note that other measures as for example $\mathcal{S}(I)$ are generally not invariant due to local effects, but their averaged scaling behavior is.
2. Next, we shift the Majorana indices $\mu \mapsto \mu + 1$. This maps all on-site operations to off-site operations and vice versa. The measurements are switched, finalizing the map $q \mapsto (1 - q)$. The unitaries are shifted and now apply to Majorana world lines corresponding to three qubits.
3. Without changing the loop model, we redraw the macro blocks by exchanging $U_{3124} \rightarrow U_{1423}$. This is merely a redefinition of unitaries.
4. By applying a space inversion, we map the unitaries $U_{1423} \mapsto U_{2314}$ without changing the measurements. Again, this step can never affect the statistical scaling behavior of extensive loop measures.
5. Finally, we shift the Majorana indices $\mu \mapsto \mu + 2$, effectively showing a different part of the trajectory. This final picture is identical to the first one, but with swapped probabilities $q \leftrightarrow (1 - q)$. This completes the proof that the phase diagram of the macro model 2314 must be symmetric. \square

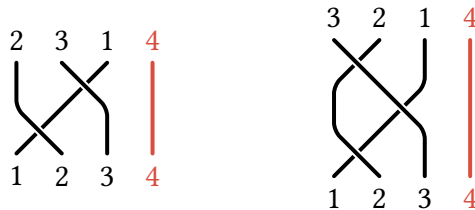
Note that the proof above only works with periodic boundaries. However, it is reasonable to assume that open boundaries would not affect the scaling behavior of entropies. The proof also indicates what makes the macro block U_{2314} special compared to different unitaries: The crux lies in the step $U_{3124} \rightarrow U_{1423}$. This redefinition is only possible because the unitary block leaves an outer Majorana world line untouched; i.e., it is either

$$U_{(i,i+1)}\gamma_{2i-1}U_{(i,i+1)}^\dagger \propto \gamma_{2i-1} \quad (3.73a)$$

or

$$U_{(i,i+1)}\gamma_{2i+2}U_{(i,i+1)}^\dagger \propto \gamma_{2i+2}. \quad (3.73b)$$

This is a property shared by U_{2314} (and the inverted U_{3124} , U_{1342} , and U_{1423}) and also the unitary U_{3214} (and the mirrored U_{1423}):⁵⁶



⁵⁶Some more trival macro blocks U_{1234} , U_{2134} , U_{1243} , and U_{1324} also fall into this group.

Here we marked the unaffected world lines in red. For the model 3214, we may again perform a very similar proof as above, and thus convince ourselves that the trivial phase diagram in Figure 3.15 (a) must indeed show a transition at exactly $q = 1/2$. Most other macro blocks do not fulfill either Equation (3.73a) or Equation (3.73b), and consequently break the $q \leftrightarrow (1 - q)$ symmetry.

3.E On Loop Models and their Phase Diagrams

The distinct macro models exhibit qualitatively different phase diagrams, as shown in Figure 3.15. Here, we connect their features to properties of the corresponding loop models. In Subsection 3.4.5, we already noted that the MF model does not enter a Goldstone phase at the three boundaries of its parameter space ($q = 0$, $q = 1$ and $p = 0$). The reason for this lies in the orientability of its loop model representation [128, 154]: If a loop model can be consistently oriented in any possible configuration, its field theory description features a continuous $U(1)$ symmetry and cannot feature an extended critical regime.⁵⁷ Similar results were found for other loop models [29] and also for models in higher dimensions [155–157, 198]. In the following, we will analyze to what extent the orientability of loop models informs their phase diagrams for the macro models.

3.E.1 Orientability in the Model 4231

Consider the phase diagram of the macro model 4231, as shown in Figure 3.15 (h). The numerical data indicates that there is no transition into the critical phase at $q = 0$ and $q = 1$. This is due to an emergent orientability of the loop model, as we will demonstrate in the following.

First, we consider the case $q = 0$ in which only the observables M^{off} are measured. We show a sample trajectory with 6 qubits and 2 time steps in Figure 3.27 (a). Note that the unitaries U_{4231} (indicated by gray boxes) are applied in a brickstone pattern; according to the probability p/s , sometimes no unitary is applied. Alternating with the unitaries, off-site measurements are performed (highlighted by purple boxes) with their respective probability $(1 - p)/s$. It is easy to see that the loop model separates into two sublattices, which are indicated by blue and red Majorana world lines. Note that this is true for *any* loop configuration with the macro block U_{4231} . Now consider only the blue (red) sublattice. It is easy to see that only the first (second) layer of the brickstone pattern affects the loops; the other layer acts as an identity on the sublattice. This allows us to show the sublattices separately in a reduced picture, as shown in Figure 3.27 (b) and (c). We show the square grid of the CPLC in the background of the sublattice loop representations. The arrows indicate how they can be oriented. Again, these orientations are consistent for *any* loop configuration that may arise in the model 4231 at $q = 0$. The orientability of the sublattice

⁵⁷The critical point at $p = 0$, $q = 1/2$ is not an extended regime.

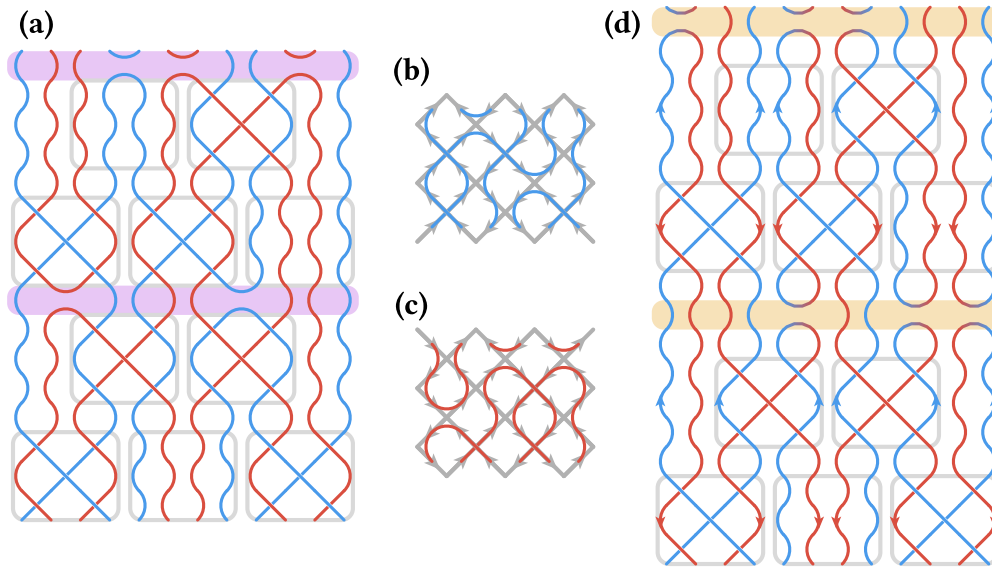


Figure 3.27 • Loop orientations for the model 4231 at $q \in \{0, 1\}$. (a) Sample trajectory of the macro model 4231 at $q = 0$. Unitaries (indicated by gray boxes) are applied in a brickstone pattern and alternate with measurement steps (highlighted in purple). Any loop configuration can be split into two sublattices (red and blue), which are shown in a reduced version in subfigures (b) and (c). The gray arrows indicate how the sublattices can be oriented. (d) Sample trajectory for the case $q = 1$ with on-site measurements connecting the sublattices. The model can be oriented by associating every sublattice with a temporal direction.

implies that the full loop model is also orientable. This finding is consistent with the lack of a transition into the critical phase at $q = 0$.

We also consider the case $q = 1$, in which only the observables M^{on} are measured. We show the loop representation of a sample trajectory in Figure 3.27 (d); the measurement steps are highlighted in orange. Note that now, the two sublattices are connected by measurements. Every measurement inverts the temporal direction of a Majorana world line and transfers it over to a different sublattice (color). It is easy to see that the loops can be consistently oriented by assigning a temporal direction to each sublattice; here, we arbitrarily consider blue (red) lines to go forward (backward) in time. Again, this result is consistent with our numerical observations in Figure 3.15 (h) and confirms that loop orientability governs the qualitative features of this phase diagram.

3.E.2 Non-Orientable Loop Models

If loop orientability is indeed always an indicator for the existence or absence of an extended critical phase, then we may also consider phase diagrams that *do* show a transition at $q \in \{0, 1\}$ and prove that their loop models cannot be oriented. To show that a loop model

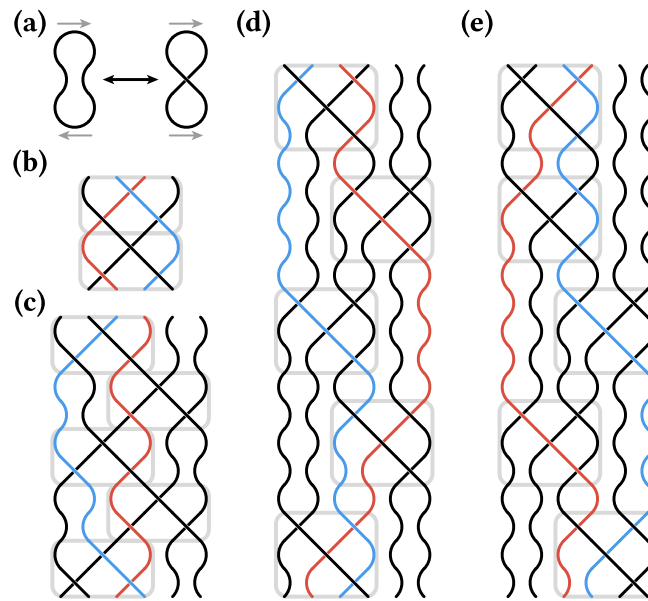


Figure 3.28 • Non-orientable loop models. (a) If it is possible to switch two neighboring Majorana world lines via unitaries, two loop configurations can be constructed that cannot be oriented at the same time. (b) Configuration of macro blocks U_{2413} to swap two neighboring world lines. In combination with off-site measurements M^{off} , the model cannot be oriented. (c) A similar configuration, which swaps world lines belonging to the same qubit; showing that the model cannot be oriented if M^{on} measurements are included. The same proof can be performed for the macro block U_{4132} as indicated in subfigures (d) and (e).

cannot be oriented in a consistent way, it is sufficient to find only two configurations that can never be oriented at the same time. We follow the approach illustrated in Figure 3.28 (a): First, we consider a configuration in which two Majorana world lines are connected by two measurements at the top and bottom, forming a closed loop. Then, we insert unitaries between the two measurements such that the world lines cross each other. This second configuration can clearly never be oriented at the same time as the first one.

As an example, we consider the macro model 2413. At $q = 0$, measurements connect neighboring Majorana world lines that belong to different qubits (off-site). In Figure 3.28 (b), we show a configuration of macro blocks that swaps such a pair of lines (here colored in red and blue). This proves that the model cannot be oriented. We repeat the same proof for the case $q = 1$. In Figure 3.28 (c), we show a configuration of macro blocks that swaps two world lines that belong to the same qubit. These findings are consistent with the phase diagram shown in Figure 3.15 (d), which clearly shows transitions to the critical phase at $q = 0$ and $q = 1$.

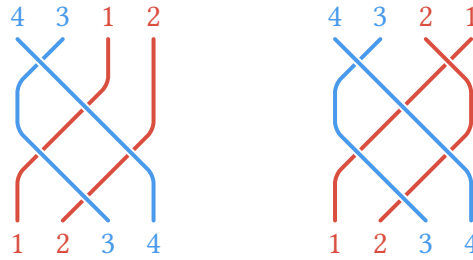
As a second example, we consider the macro model 4132 with the phase diagram shown in Figure 3.15 (e). In Figure 3.28 (d), we present a configuration of macro blocks to swap neighboring Majorana world lines that belong to different qubits. Similarly, the pattern in

Figure 3.28 (e) shows, how world lines corresponding to the same qubit can be exchanged. This implies that the loop model representing this macro model can neither be oriented at $q = 0$, nor at $q = 1$. This is again consistent with the phase diagram, which clearly exhibits a transition into the critical phase at the boundaries of parameter space.

We repeated the same analysis for all other macro blocks (with nontrivial phase diagrams) with similar results. As the concept is always the same, we omit the explicit proofs here. We highlight the models 4312 and 4321 as two notable exceptions and discuss them in more detail in the following.

3.E.3 Phase Diagram Boundaries of the Models 4312 and 4321

At $q = 1$, the model 4312 shows no transition into a critical phase, as indicated by the phase diagram Figure 3.15 (f). However, its loop representation is *not* orientable. To understand why still no extended criticality can be reached, a different explanation is necessary. The crux is that the unitary U_{4312} never separates Majorana world lines that belong to the same qubit. The same is true for the macro block U_{4321} [see Figure 3.15 (g)]:



Here we indicated the line pairs by color. Note that at $q = 1$, measurements are performed on-site (M^{on}). In the loop picture, every measurement closes a loop of neighboring world lines, and starts a new pair. Clearly, the lines of the same color can never separate from each other, and thus, entanglement cannot be created. This is why the area-law phase extends up to $p = 1$ and no critical phase is reached at $q = 1$.⁵⁸

The same argument can also be made for some of the models that exhibit trivial phase diagrams. Here we are however able to present even stronger arguments which hold for all values of $q \in [0, 1]$.

3.E.4 Trivial Phase diagrams

Finally, we examine all loop models that exhibit trivial phase diagrams [all diagrams are identical, cf. Figure 3.15 (a)]. The model 1234 is of course just the PTIM and can only exhibit the usual two area-law phases.⁵⁹

⁵⁸Remember that these models also cannot create a volume-law phase at $p = 1$, see Subsection 3.5.2.

⁵⁹Also remember that the loop representation of the model 1234 is oriented by the L-lattice [139, 154].

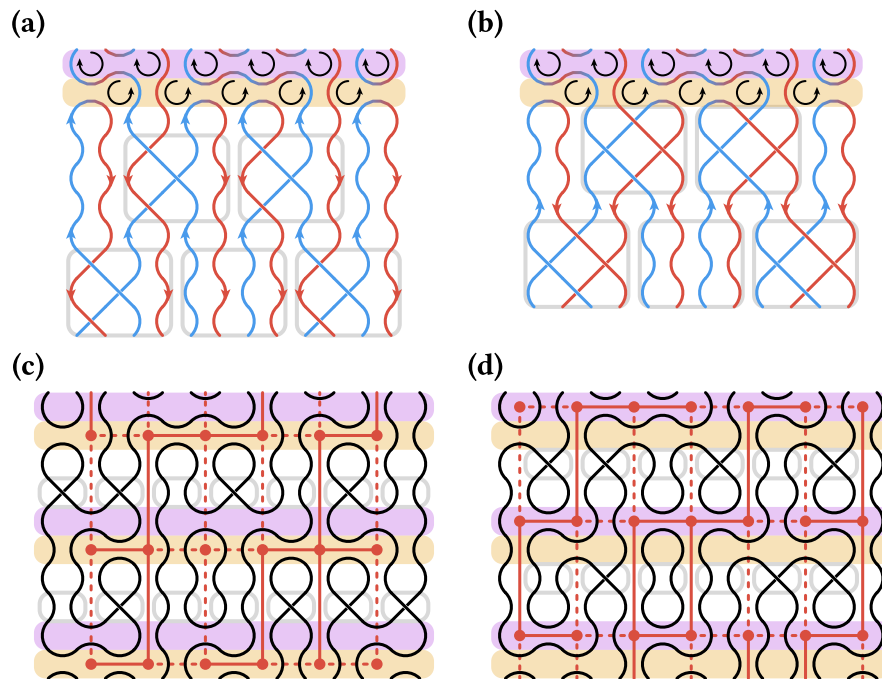


Figure 3.29 • Loop models with trivial phase diagrams. (a) The macro model 3214 can be oriented at any $q \in [0, 1]$. The same holds true for the model 3412, as shown in subfigure (b). This explains the lack of a critical phase in those models. (c) The models 2134, 1243 and 2143 share similar loop model representations, which are not orientable. However, these loop models obey the same percolation pattern, which is known from the PTIM. (d) The dual percolation pattern can be drawn into the loop representation of the model 1324. This indicates why those models do not exhibit critical phases.

Consider the model 3214. We show a sample trajectory in Figure 3.29 (a), including measurement steps for on-site and off-site measurements. Here we find loop configurations that are reminiscent of Figure 3.27 (d). The loops can be separated into even and odd Majorana indices (here shown in red and blue), which are interconnected by measurements. We can orient the loops by assigning temporal directions to the colors (indicated by arrows). The measurement steps are identical to the MF model at $p = 0$ and thus oriented by the L-lattice. This is characterized by assigning clockwise and counterclockwise directions to the plaquettes of the lattice. The model can thus be oriented for all values of q , which is consistent with its trivial phase diagram.

We make very similar observations for the macro model 3412. A sample trajectory is shown in Figure 3.29 (b). It is oriented in the same way, by assigning temporal directions to even and odd Majorana indices. Again, this is consistent with the lack of a critical phase in the model. The two macro blocks U_{3214} and U_{3412} are similar, as they both represent permutations that map even (odd) indices to even (odd) indices. This property allows for the orientation of these loop models.

The macro blocks U_{2134} , U_{1243} and U_{2143} allow for the swap of neighboring Majorana world lines (performed by the unitary U^{on}) and are represented by the same loop model.⁶⁰ We show a sample trajectory in Figure 3.29 (c) and note that this model cannot be oriented. To explain the lack of a critical phase, we follow a different approach. Remember the percolation pattern connected to the PTIM, as shown in Figure 1.5 and Figure 3.4. As the unitaries U^{on} are only applied to world lines that belong to the same qubit, a percolation pattern can be drawn into the pattern (shown in red). Here, the nodes of the pattern are placed between neighboring qubits. Note that the connected and disconnected bonds of the pattern are solely determined by the measurements. Vertical bonds are merely elongated to accommodate the unitary steps. No loop can cross a bond on the percolation pattern, thus their travel distance is bound by similar rules that also apply to the PTIM. This explains why no critical phase is possible here. Note that this result is not surprising, as the unitaries applied here are just on-site S gates, which affect the phases of Bell clusters, but do not create or destroy entanglement. The entanglement dynamics is therefore well described by the colored cluster model.

The same argument can be made for the macro model 1324 with the off-site unitary U^{off} , which shifts the previous loop model by a single Majorana index.⁶¹ We show a sample trajectory in Figure 3.29 (d). Again, the model cannot be oriented. Instead, it is obvious that the loop configurations are compatible with the dual percolation pattern, which has nodes at qubit sites. Again, this pattern is fully determined by just the measurements. No loops can ever cross connected bonds, and thus the entanglement dynamics follows the rules of the PTIM. This is consistent with the trivial phase diagram of the model 1324.

⁶⁰The loops of the model 2143 can be trivially simplified by removing consecutive crossings.

⁶¹Figure 3.29 (c) and (d) show the same loop model with inverted temporal direction (correctly ordering the measurement steps) and a shift by one Majorana index.

CHAPTER 4

Robust Detection of an Entanglement Transition

One of the biggest challenges in the field of measurement-induced entanglement transitions is to observe them in an experiment. This is due to the inherent randomness of projective measurements, which prohibits the repeated preparation of a state, and due to the unavoidable noise in large-scale experimental settings. In this chapter, we present a procedure that combines error correction techniques with classical shadow tomography. This allows for the experimentally accessible construction of upper and lower bounds on the entanglement transition of the projective transverse field Ising model, eliminating the need for postselection or full state tomography. These bounds remain robust under noise and their sharpness is only limited by the noise rate. This chapter is a more in-depth discussion of the work published in Ref. [199].

4.1 Related Works

So far, we have focused on the properties of entanglement phases (Chapter 3) and on their connection to quantum information (Chapter 2). A necessary next step in any *physics* thesis must be to examine the experimental observability of entanglement transitions, which turns out to present a number of challenges. In this chapter, we specifically consider the projective transverse field Ising model and how its entanglement transition can be made accessible in a realistic setup.

As explained in Subsection 1.1.2, measurement-induced entanglement transitions are generally characterized by a change in the scaling behavior of entanglement entropies in subsystems of pure states [2, 5–7, 14, 24, 119]. As the entanglement entropy \mathcal{S} is a *nonlinear* function of the (pure) state $|\Psi\rangle\langle\Psi|$,¹ the (mixed) density matrix of an ensemble of trajectories does not contain the information needed to compute the sample-averaged entanglement $S = \langle\langle\mathcal{S}\rangle\rangle$. This makes the observation of entanglement transitions difficult [18–20]: Assume that an experiment prepares an (unknown) state $|\Psi\rangle$ for which the entanglement entropy $\mathcal{S}(A)$ of a subsystem A is to be determined. This requires full knowledge of the state $\rho_A = \text{Tr}_{\bar{A}}[|\Psi\rangle\langle\Psi|]$, i.e., a *full state tomography*. To determine all $4^{|A|} - 1$ free parameters, an exponential (in $|A|$) amount of copies of the state $|\Psi\rangle$ is required [200–202]. But the problem lies not only in the large amount of copies, but also in the randomness of the quantum circuits, which makes the creation of even a *single* copy elusive.² Unitaries and measurements are generally applied randomly, but this classical randomness is (in principle) under the experimentalist’s control; we assume that a circuit pattern can be repeated. To make a copy of a state, it is however not enough to repeat a circuit, but also the outcomes of the projective measurements [there are $\mathcal{O}(LT)$ of them] must be the same. According to the Born rule [1], this quantum randomness is not under the experimentalist’s control, which makes the probability of a state being reproduced correctly exponentially small [18, 205]. This *postselection problem* is the major obstacle in the observation of measurement-induced entanglement transitions, as it makes the direct measurement of entanglement entropies in large systems inaccessible *in principle*.³ While these issues arise in every perfect experiment, we must also expect errors in realistic experimental scenarios with large numbers of qubits. Thus, a protocol to (directly or indirectly) observe transitions must also be robust under noise.

A number of approaches have been proposed to either alleviate or circumvent the postselection problem. Some quantum circuits exhibit a space-time duality [20, 206, 207], such that switching the temporal and spacial directions allows for their implementation using only unitaries.⁴ Setups like these are however not direct experiments on the system in question, but on a “stand-in” dual system. Another route may be to use weak measurements, which only extract very little information with every measurement, such that their outcomes are almost deterministic [208–210]. It was shown that such weak measurements can drive entanglement transitions [34, 211]. Weak measurements have however never been used to make entanglement transitions in random quantum circuits experimentally accessible; such an approach would face scaling issues in the thermodynamic limit. A quantum steering approach uses the measurement history of a single run and applies a tailored unitary to

¹Compare a linear observable O with $\langle O \rangle = \text{Tr}[\rho O]$.

²Remember also the no-cloning theorem [203, 204].

³In Ref. [18], Koh et al. detected an entanglement transition in a hybrid quantum circuit on superconducting qubits. To measure the entanglement, a brute-force state tomography with postselection was performed. Even with some optimizations, these experiments were limited to 14 qubits, requiring ~ 5200 hardware device-hours. This is not feasible for larger systems.

⁴For example, the measurement of Z_i in the loop model (see Figure 3.3) transforms into a trivial unitary action if space and time axes are switched.

“steer” a trajectory back to a desired state [19, 212, 213]. This does not only require the in-time creation and application of unitary feedback, but also assumes ideal measurements. Some approaches utilize special non-local models to reduce the impact of the postselection problem [214–216]. To observe an entanglement transition, it might not be necessary to measure the entanglement entropy itself. Instead, cross-entropies (which are linear observables and easier to measure) can be used to bound entanglement entropies [217–219]. Such bounds display a signature of entanglement transitions, but are usually not robust to noise. Furthermore, in Chapter 2, we already demonstrated the relation between the field of entanglement transitions and quantum error correction. The emergent quantum error correction capabilities of some entangling phases can serve as signatures that are reflected in the learnability of measurement statistics and purification transitions [64, 71, 72, 106–108]. Finally, *shadow tomography* [220–222] has been proposed as a tool to measure upper and lower bounds on entanglement entropies [223, 224]. This approach does avoid the postselection problem and can, in principle, be implemented efficiently to estimate the entanglement entropies of small subsystems, but it is not automatically robust to noise.⁵

In this chapter, we describe a platform-agnostic protocol, which makes the entanglement transition of the projective transverse field Ising model experimentally accessible. To do so, we combine efficient error correction (as discussed in Chapter 2 and Ref. [64]) with classical shadow tomography [223]. This combination makes our procedure robust to noise while also alleviating the postselection problem.

4.2 Setting

For simplicity, we consider the PTIM as introduced in Section 1.3 at $p = q$, such that only one free parameter remains which determines the fraction of E_i and S_e measurements. To make an experimental realization easier, we consider open boundaries. As we have already shown in Figure 1.4, the model exhibits a phase transition at $p_c = 1/2$, which presents itself as a signature in the sample-averaged half system entanglement entropy $S(L/2)$. In this chapter, we consider a different signature: the survival probability of an initial Bell cluster in trajectories with $L \propto T$. As both quantities are directly linked to the bond percolation model which underlies the PTIM, they feature the same transition. The cluster survival probability does however have some advantages. First, it approaches a perfect step function for $L \rightarrow \infty$, as shown in Figure 4.1. This is not only a clear signature to observe, but will also prove to be practical when working with upper and lower bounds to the entanglement entropy; i.e., if a bound crosses a threshold, the system must be in one of two phases. Furthermore, the survival probability can be probed on just one qubit if a suitable protocol is chosen. This is necessary because the shadow tomography approach fails for large subsystem sizes (since errors diverge [223]).⁶

⁵The upper and lower bounds remain valid bounds even under noise, but quickly become trivial and thus no longer convey information about the entanglement transitions.

⁶Figure 4.1 is equivalent to a diagonal cut through Figure 2.3 with different system sizes and a rescaled axis because the decoding probability approaches $P_{\mathcal{D}} = 0.5$ as the cluster survival probability goes to 0.

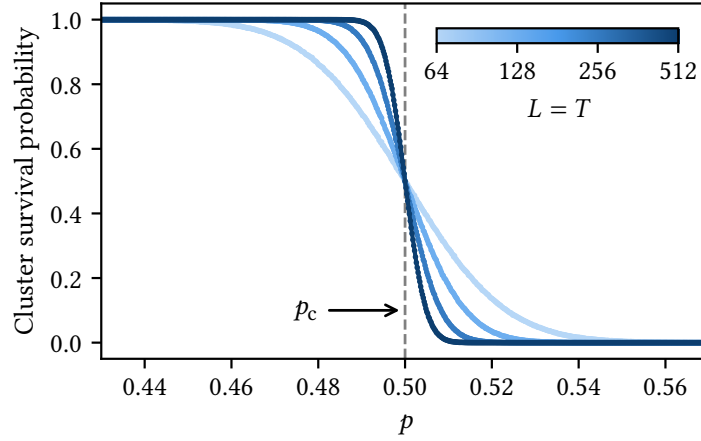


Figure 4.1 • Survival probability of an initial cluster in the PTIM. At $p = q$, the survival probability approaches a step function. Here we show the case $L = T$ for multiple system sizes. Simulations were performed using a loop model, and every data point shows averages over 10^5 sample trajectories. Error bars are smaller than the points.

A single circuit is characterized by its initial state $|\Psi_0\rangle$ and its measurement record $M^{P,r}$, which contains both the patterns $M^P = (E^P, S^P)$ and the corresponding results $M^r = (E^r, S^r)$. They determine the final state $|\Psi_f\rangle$. We call a single trajectory $s \equiv (|\Psi_f\rangle, M^{P,r})$ a *sample*. In a realistic setting, we expect that errors occur in the circuit. Here, we assume that these manifest as unrecorded measurements: With probability $\eta \in [0, 1]$ (*noise rate*), measurements that were applied in the circuit are not recorded in the history $M^{P,r}$. We choose this particular noise model because it does not affect the trajectories themselves but only the information accessible to an observer. Thus, the entanglement transition always remains at $p = 1/2$.

4.3 Lower Bound via Decoding

In Chapter 2, we already used the fact that entangling phases of random quantum circuits behave as emergent quantum codes [64, 71, 72]. Here we give a short summary of the key insights. In the PTIM, amplitudes that encode a single logical qubit in the initial state $|\Psi_0\rangle_s = \alpha_s |0 \dots 0\rangle + \beta_s |1 \dots 1\rangle$ (we use the index s to denote a single sample) can only survive in the entangling phase, i.e., for $p < 1/2$ in the thermodynamic limit (see Figure 4.1). In other words: The logical qubit can only be consistently recovered if the PTIM is in its entangling phase. To actually retrieve the amplitudes, we consider the PTIM with $L \propto T$ (here we choose $L = T$) and add a final time step where every S_e measurement is performed and recorded. If the logical qubit survives, the final state has the form $|\Psi_f\rangle_s = \alpha_s |\mathbf{m}_s\rangle + \beta_s |\bar{\mathbf{m}}_s\rangle$ with some configuration \mathbf{m}_s and its complement $\bar{\mathbf{m}}_s$. If however the environment gained access to the amplitudes via E_i measurements, the final state has the form $|\Psi_f\rangle_s = |\mathbf{m}_s\rangle \pm |\bar{\mathbf{m}}_s\rangle$.

We now describe a protocol that allows for the *certification* of the entangling phase of the PTIM via the retrieval of an encoded logical qubit, yielding a lower bound (in p) on its entanglement transition [see Figure 4.2 (a)]. Each sample circuit s is initialized in a state that encodes a random bit $m_s^* \in \{0, 1\}$ with $|\Psi_0\rangle_s = |m_s^* \dots m_s^*\rangle$.⁷ Next, the state evolves under a (possibly noisy) PTIM circuit with $T = L$ steps, followed by an additional (noise-free) step in which all S_e measurements are performed. This ensures that the final state has the form $|\Psi_f\rangle_s = |m_s\rangle$ if the information survived, and $|\Psi_f\rangle_s = |m_s\rangle \pm |\bar{m}_s\rangle$ otherwise. Finally, one qubit is measured in the z -basis, here we arbitrarily choose the first qubit. We call the outcome of this Z_1 measurement $z_{s,1} \in \{\pm 1\}$. For each sample s , we obtain the initial encoded bit m_s^* , the (possibly incomplete) measurement record $M_s^{\text{p,r}}$ and the final measurement outcome $z_{s,1}$.

The task is now to recover m_s^* from $M_s^{\text{p,r}}$ and $z_{s,1}$. For this, we use a decoder $\mathcal{D}(M_s^{\text{p,r}}) = C_s$, which maps a measurement history to a correction operator $C_s = \prod_i X_i^{c_{s,i}}$ with $c_{s,i} \in \{0, 1\}$, such that $C_s |\Psi_f\rangle_s = |m_s^* \dots m_s^*\rangle \equiv |\Psi_0\rangle_s$. We quantify the success of the decoding by evaluating the correlation

$$\mathcal{R}_s := (-1)^{m_s^*} \cdot (-1)^{c_{s,1}} \cdot z_{s,1}. \quad (4.1)$$

The sample average $R(p, \eta; L, T) \equiv \langle\langle \mathcal{R}_s \rangle\rangle_s$ approaches one if the PTIM is consistently decoded. R approaches zero if either the encoded information does not survive in the PTIM circuit, or the information does survive, but the decoder is unable to find the matching correction operator C_s .⁸

Consider a noise-free ($\eta = 0$) realization of the PTIM with a perfect measurement record. Here, the task of the decoder \mathcal{D} becomes trivial (see also Subsection 2.3.2). The circuit trajectory can be simulated efficiently via the stabilizer formalism. An even more efficient algorithm uses an *extended colored cluster simulation*, which we detail in Section 4.A. In Figure 4.2 (b) we show the average correlation $R(\eta = 0)$ for this case. As expected, this experimentally accessible measure perfectly matches the inaccessible entanglement transition of the PTIM.

If the PTIM trajectory is noisy ($\eta > 0$), the trajectory of the state cannot be simulated straightforwardly because the (incomplete) recorded results M_s^{r} may be inconsistent with the recorded pattern M_s^{p} . Thus, we extend the decoder \mathcal{D} by an error correction step \mathcal{E} , which augments the measurement history to a hypothetical history $M_s^{\text{p,r}} \mapsto \tilde{M}_s^{\text{p,r}}$. This augmented history contains additional measurements without predicting their outcomes and is constructed to be *consistent*. Then, the decoder finds the correction operator C by performing the extended colored cluster simulation on this augmented history. As the colored cluster model cannot benefit from additional S_e measurements without their results,

⁷As $X_1 X_2 \dots X_L$ (the logical X operator) is a symmetry of the PTIM, information encoded in the symmetry eigenstates $|0 \dots 0\rangle + (-1)^m |1 \dots 1\rangle$ cannot be used to detect the entanglement transition. Instead, we encode information in the logical z -basis (by either setting $\alpha = 0$ or $\beta = 0$).

⁸The average correlation R effectively rescales the decoding probability $P_{\mathcal{D}}$ which we used in Chapter 2. Note however that all quantities in Equation (4.1) are known to an experimentalist after realizing a single sample circuit s , whereas the evaluation function in Equation (2.17) requires knowledge of the actual final state $|\Psi_f\rangle$.

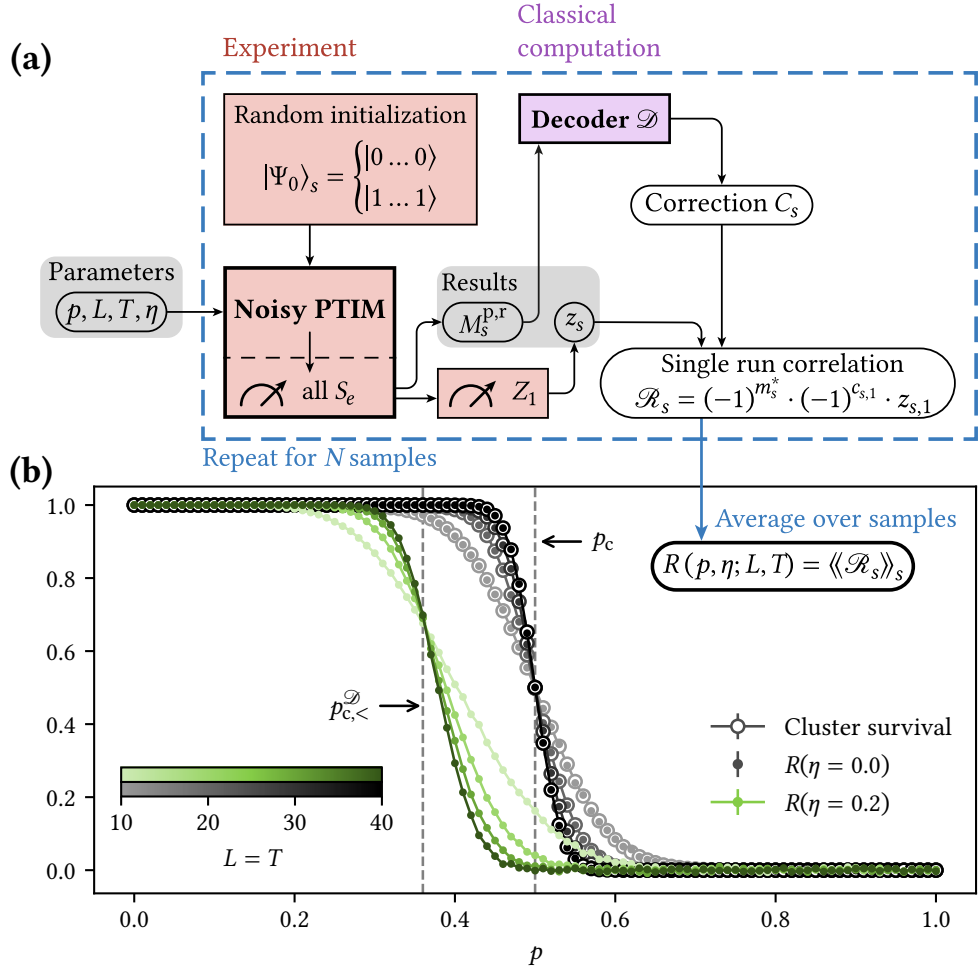


Figure 4.2 • Lower bound via decoding. (a) Protocol to experimentally measure the decoding transition of the PTIM, which provides a lower bound for the entanglement transition of this model. (b) Sample-averaged correlation function R with noise ($\eta = 0.2$, green) and without noise ($\eta = 0.0$, black), as a function of p . We show system sizes $L = 10, \dots, 40$. In the presence of noise, the decoding transition is shifted to the left $p_{c,<}^{\mathcal{D}} < p_c$. In the noise-free case, the correlation function matches the survival probability of an initial cluster. Data points show averages over 10^5 samples; error bars are smaller than the points.

it is enough to use an error correcting step \mathcal{E}_E which only augments $E_s^p \mapsto \tilde{E}_s^p$; we call this noise-resilient decoder \mathcal{D}_E .

The easiest way to find a consistent measurement record $\tilde{M}_s^{p,r}$ is to completely fill the pattern \tilde{M}_s^p under the assumption that every possible measurement was applied in every time step. While this pattern is always consistent with the recorded measurement outcomes, it is also very unlikely. Thus we employ an error correction algorithm \mathcal{E}_E that uses a minimum weight perfect matching to predict a *likely* pattern \tilde{E}_s^p . The algorithm itself is an extension of the algorithm described in Section 2.5, and capable of handling our generalized noise model.⁹ We describe it in detail in Subsection 4.C.1.

We use the decoder \mathcal{D}_E in the protocol in Figure 4.2 (a) and again measure the average correlation R . The data for the noise rate $\eta = 0.2$ and multiple system sizes $L = T$ is shown in Figure 4.2 (b). The decoding threshold $p_{c,<}^{\mathcal{D}}$ is clearly indicated by a crossing in $R(p)$, as it approaches a step function in the limit $L = T \rightarrow \infty$. As the survival of the initial cluster is a necessary condition for the successful decoding of the PTIM, the sample average $R(p)$ is a lower bound to the cluster survival probability. Consequently it is $p_{c,<}^{\mathcal{D}} \leq p_c$, where equality is only reached for $\eta = 0$. The protocol described here provides an experimentally accessible lower bound to the entanglement transition. The sharpness of this bound is limited by the noise rate η and the performance of the decoding algorithm. As \mathcal{D}_E is not a maximum likelihood decoder, the bound described here is not optimal. Our previous observations on such optimal decoders in Section 2.6 (and those made by Bravyi et al. in Ref. [91]) do however suggest that no significant improvements are to be expected.

4.4 Entanglement Bounds via Shadow Tomography

For an experimentally accessible upper bound on the entanglement transition of the PTIM, we employ a protocol proposed by Garratt and Altman [223] which uses shadow tomography to avoid the postselection problem. Here we briefly review the underlying idea behind this method; interested readers can find more details in Ref. [223].

Take a fixed quantum circuit with L qubits and a subsystem $A \subseteq \{1, \dots, L\}$. The (unknown) final state $\rho_A = \text{Tr}_{\bar{A}} |\Psi_f\rangle \langle \Psi_f|$ of this subsystem is derived from the (pure) state of all qubits $|\Psi_f\rangle$. As discussed previously, the entanglement entropy of ρ_A can only be computed if the state itself is known. To this end, let us first assume that the postselection problem does not exist and that we could perform multiple runs r (of the same circuit with the same measurement outcomes), preparing the same state ρ_A . At the end of every run, we can perform random measurements on the subsystem A . Then, the shadow $\rho_{r,A}^S$ is defined as the matrix that, in the limit of many runs (indicated by \xrightarrow{r}), satisfies

$$\langle\langle \rho_{r,A}^S \rangle\rangle_r \xrightarrow{r} \rho_A. \quad (4.2)$$

⁹The key difference to Chapter 2 is that here *some* E_i measurements are recorded.

Here, $\langle\langle \bullet \rangle\rangle_r$ denotes the average over multiple runs. Generally, the form of $\rho_{r,A}^S$ depends on the random set of measurements performed on the final state. Here we perform random Pauli measurements $O_{r,i} \in \{X_i, Y_i, Z_i\}$ on every qubit $i \in A$. Then the shadow of the qubit i is defined as

$$\rho_{r,\{i\}}^S := \frac{3}{2} (\mathbb{1} + o_r \cdot O_{r,i}) - \mathbb{1} \quad (4.3)$$

where $o_r \in \{\pm 1\}$ is the final measurement outcome.¹⁰ The shadow for the full subsystem A is defined as

$$\rho_{r,A}^S := \bigotimes_{i \in A} \rho_{r,\{i\}}^S. \quad (4.4)$$

Note that the shadow is *not* a density matrix as some of its eigenvalues are negative.

In an experiment, the postselection problem prohibits the repeated preparation of a state, but the shadow can still be of use – in particular to measure averages. Let now r denote a run of a specific circuit configuration with non-deterministic measurement outcomes m_r , creating the corresponding state $\rho_{r,A} = \rho_{m_r,A}$ (which may differ between runs). Let F_m be some function that depends only on the measurement history m (which does *not* include the randomized final measurements). Then, in the limit of many runs, it is

$$\langle\langle F_m \rho_{r,A}^S \rangle\rangle_r \xrightarrow{r} \langle\langle F_m \rho_{m,A} \rangle\rangle_m. \quad (4.5)$$

Here, $\langle\langle \bullet \rangle\rangle_m$ denotes the average over *all* possible measurement histories for a given circuit (weighted by their respective probabilities). Their number scales exponentially, and thus the right-hand side of Equation (4.5) is not experimentally accessible. The left-hand side however allows for a smaller number of runs and is therefore accessible (with some caveats, which we discuss later).

Now consider the von Neumann entanglement entropy $\mathcal{S}_{m,A} = -\text{Tr} [\rho_{m,A} \log_2 \rho_{m,A}]$ for a given measurement history m . The *cross-entropy* is defined as

$$\mathcal{S}_{m,A}^{\text{QC}} := -\text{Tr} [\rho_{m,A} \log_2 \rho_{m,A}^{\text{C}}] \quad (4.6)$$

where $\rho_{m,A}^{\text{C}}$ is an arbitrary density matrix. To make the ensemble average of $\mathcal{S}_{m,A}^{\text{QC}}$ experimentally accessible, we set $F_m = -\log_2 \rho_{m,A}^{\text{C}}$ and define the shadow of the cross-entropy as

$$\mathcal{S}_{r,A}^{\text{SC}} := -\text{Tr} [\rho_{r,A}^S \log_2 \rho_{m_r,A}^{\text{C}}]. \quad (4.7)$$

Then, as the trace is linear, Equation (4.5) reduces to

$$\langle\langle \mathcal{S}_{r,A}^{\text{SC}} \rangle\rangle_r \xrightarrow{r} \langle\langle \mathcal{S}_{m,A}^{\text{QC}} \rangle\rangle_m. \quad (4.8)$$

¹⁰Let the observables $O_{r,i}$ be constructed from a random unitary $U_{r,i}$ and a Z_i measurement. Equation (4.3) holds if $U_{r,i}$ is sampled from a set of unitaries which forms a two-design for the Haar ensemble of unitary operators on a single qubit [223]. The Clifford group is such a two-design [225] and maps Z_i to any of the Pauli matrices. This is why we choose random Pauli measurements here as they are also efficiently simulable within the stabilizer formalism.

Crucially, the cross-entropy is related to the entanglement entropy by Klein's inequality [45]:

$$\mathcal{S}_{m,A} \leq \mathcal{S}_{m,A}^{\text{QC}} \quad (4.9)$$

Both entropies are equal if $\rho_{m,A}^{\text{C}} = \rho_{m,A}$, otherwise the cross-entropy provides an upper bound on the entanglement entropy. The combination of Equations (4.8) and (4.9) allows for an experimentally accessible upper bound on the average entanglement entropy

$$\langle\langle \mathcal{S}_{m,A} \rangle\rangle_m \leq \langle\langle \mathcal{S}_{m,A}^{\text{QC}} \rangle\rangle_m \stackrel{r}{\leftarrow} \langle\langle \mathcal{S}_{r,A}^{\text{SC}} \rangle\rangle_r. \quad (4.10)$$

In this chapter, we describe entanglement transitions, which are only accessible if the average over multiple circuit configurations is also taken. Thus, we replace the runs r (which correspond to realizations of a single configuration with non-deterministic measurement outcomes) with samples s (which correspond to any possible circuit trajectory). Let n_s be the number of samples (not to be confused with the spanning number in Section 3.C). Then, in the limit of many samples, the inequality

$$S_A \equiv \lim_{n_s \rightarrow \infty} [\langle\langle \mathcal{S}_{s,A} \rangle\rangle_s] \leq \lim_{n_s \rightarrow \infty} [\langle\langle \mathcal{S}_{s,A}^{\text{SC}} \rangle\rangle_s] =: S_A^{\text{SC}} \quad (4.11)$$

holds, where we denote the sample average of the entanglement shadow as S_A^{SC} . Note that this upper bound comes with multiple caveats. First, the sharpness of the upper bound depends on the function $\rho_{m,s,A}^{\text{C}}$. In Subsections 4.4.2 and 4.4.3, we use a classical algorithm that aims to predict the actual state $\rho_{m,s,A}$. This is crucial to find a nontrivial upper bound. While Equation (4.11) holds in the limit of many samples, the variance of the shadows $\mathcal{S}_{s,A}^{\text{SC}}$ increases exponentially with the subsystem size $|A|$ [221, 223]. Thus, assuming a finite number of samples, only small subsystems can be evaluated. Lastly, the protocol described here is by itself not robust under noise. In the presence of errors, the success rate of the classical state prediction decreases rapidly – quickly making the upper bound on the entanglement entropy trivial.¹¹ In Subsections 4.4.2 and 4.4.3, we solve this problem by employing an error correction algorithm, which allows for a more robust state prediction.

Shadow tomography can also be used to create an accessible lower bound on the entanglement entropy S_A . To this end, consider a second subsystem B . The quantum relative entropy is defined as $\mathcal{H}_{s,A} := \mathcal{S}_{s,A}^{\text{SC}} - \mathcal{S}_{s,A}$; Klein's inequality makes it non-negative. Due to the monotonicity of this relative entropy [226], it is always $\mathcal{H}_{s,A} \leq \mathcal{H}_{s,A \cup B}$. This inequality implies the lower bound [223]

$$\lim_{n_s \rightarrow \infty} [\langle\langle \mathcal{S}_{s,A}^{\text{SC}} \rangle\rangle_s - \langle\langle \mathcal{S}_{s,A \cup B}^{\text{SC}} \rangle\rangle_s] \equiv S_A^{\text{SC}} - S_{A \cup B}^{\text{SC}} \leq S_A \quad (4.12)$$

on the entanglement entropy S_A , which holds in the limit of many samples.¹²

¹¹In large systems with many time steps, the probability for an error to occur is finite, even if the noise rate is arbitrarily small.

¹²The sharpness of this lower bound is restricted by the value of $\langle\langle \mathcal{S}_{s,A \cup B}^{\text{SC}} \rangle\rangle_s$, which itself is always larger than $S_{A \cup B}$. Thus, a useful lower bound can only be achieved if $S_{A \cup B}$ is small.

Lastly, we note that for pure state predictions $\rho_{m_s, A}^C$, the shadow $\mathcal{S}_{s, A}^{\text{SC}}$ diverges.¹³ We avoid this by regularizing the prediction

$$\rho_{m_s, A}^C(\varepsilon) := (1 - \varepsilon)\rho_{m_s, A}^C + \frac{\varepsilon}{2^{|A|}}\mathbb{1} \quad (4.13)$$

via a depolarizing channel of strength ε . Equations (4.11) and (4.12) hold for any value of ε .

4.4.1 Detection of the Entanglement Transition on a Single Qubit

We now describe a tailored protocol that allows for the measurement of experimentally accessible bounds on the entanglement transition of the projective transverse field Ising model. As the shadow tomography approach only allows for the observation of the entanglement of small subsystems, we must first find a setup that enables us to detect the entanglement transition by only measuring few qubits. One possibility would be to trace out all qubits $\{2, \dots, L - 1\}$ (i.e., purifying their states via local measurements) and only consider the entanglement between the two qubits 1 and L . The resulting measure is very similar to the mutual information, which undergoes a continuous transition at $p = p_c$ [24]. Here, we suggest a slightly different setup that makes use of an *ancilla qubit* and a post-processing step to create a discontinuous transition with a much clearer signature. The use of such ancilla qubits to probe entanglement transitions was proposed by Gullans and Huse in Refs. [71, 72].

Consider the circuit shown in Figure 4.3 with $L + 1$ qubits $\{a, 1, 2, \dots, L\}$, where the index $i = a$ denotes a single ancilla qubit. The system is initially prepared in a global Bell cluster $|\Psi_0\rangle = |0\rangle_a |0 \dots 0\rangle + |1\rangle_a |1 \dots 1\rangle$. We assume that this initial entangling step is perfect. The system qubits are subjected to a (possibly noisy) PTIM evolution with $T \propto L$ time steps (here we choose $L = T$). The ancilla qubit is unaffected by this evolution and is also not subjected to any noise. Note that if the initial cluster (which is still present on the ancilla qubit) was destroyed on all system qubits by the PTIM circuit, then the ancilla qubit is in a pure state $|\Psi_T\rangle_a$ and consequently its entanglement entropy \mathcal{S}_a vanishes. If the initial cluster does survive, we find $\mathcal{S}_a = 1$. The sample average $S_a = \langle\langle \mathcal{S}_a \rangle\rangle$ is thus identical to the cluster survival probability shown in Figure 4.1, which approaches a step function in the limit $L = T \rightarrow \infty$.

To make our approach robust to noise, it is useful to extract as much information on the final state as possible. Therefore, the trajectory is finalized by a (noise-free) *entanglement transfer*, where first all S_e measurements on system qubits are applied (merging the qubits into a single Bell cluster), followed by E_i measurements on the qubits $i \notin \{a, L\}$.¹⁴ This “post-processing” step does not affect \mathcal{S}_a and transfers any remaining entanglement between the system and the ancilla qubit to the rightmost qubit L , such that the two qubits $\{a, L\}$ are

¹³A pure state prediction $\rho_{m_s, A}^C$ has vanishing eigenvalues and thus some entries of $\log_2 \rho_{m_s, A}^C$ diverge. All eigenvalues of the shadow $\rho_{r, A}^S$ are non-zero [cf. Equation (4.3)] and thus $\mathcal{S}_{s, A}^{\text{SC}}$ diverges [see Equation (4.7)].

¹⁴The choice of the qubit L is arbitrary.

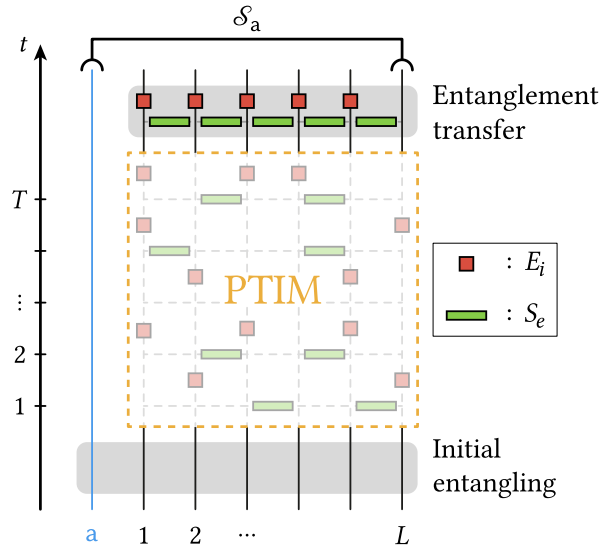


Figure 4.3 • PTIM trajectory with an ancilla qubit and an entanglement transfer step. The setup initially entangles all qubits (including one ancilla qubit) in a global Bell cluster. A PTIM circuit is applied only to the system qubits $\{1, \dots, L\}$. A final “post-processing” step is used to transfer any entanglement between the ancilla and system qubits to the rightmost qubit L ; i.e., if the ancilla qubit was previously entangled with any qubit, it is now entangled only with qubit L . The PTIM circuit may be subjected to noise.

in a pure state $|\Psi_f\rangle_{\{a,L\}}$. This allows us to perform shadow tomography on only two qubits while using the measurement results from the entanglement transfer for error correction.

To apply shadow tomography on this setup, we propose the protocol illustrated in Figure 4.4 (a). The sample state $|\Psi_0\rangle_s$ is prepared and undergoes the (noisy) PTIM evolution and the entanglement transfer. As usual, the measurements are recorded in the history $M_s^{\text{p,r}}$ (PTIM measurements subjected to noise are not recorded). To estimate the entanglement entropy of a subsystem A (here we choose either $A = \{a\}$ or $A = \{a, L\}$), random Pauli measurements are performed, and the shadow $\rho_{s,A}^S$ is calculated according to Equations (4.3) and (4.4). On the other hand, the classical prediction of the state $\rho_{M_s^{\text{p,r}},A}^C(\epsilon)$ is a function of the measurement record. We use an algorithm based on an error correction algorithm to make the prediction robust to noise.¹⁵ The shadow $\rho_{s,A}^S$ and the (artificially depolarized) prediction $\rho_{M_s^{\text{p,r}},A}^C(\epsilon)$ are then used to calculate the shadow of the cross-entropy $\mathcal{S}_{s,A}^{\text{SC}}(\epsilon)$. The process is repeated with randomized circuit configurations, and the average over many samples is evaluated.

¹⁵Importantly, the classical prediction aims to reproduce the state $\rho_{s,A}$ of the qubits in A before the final measurements $O_{i,s}$ and does *not* depend on the results of those measurements.

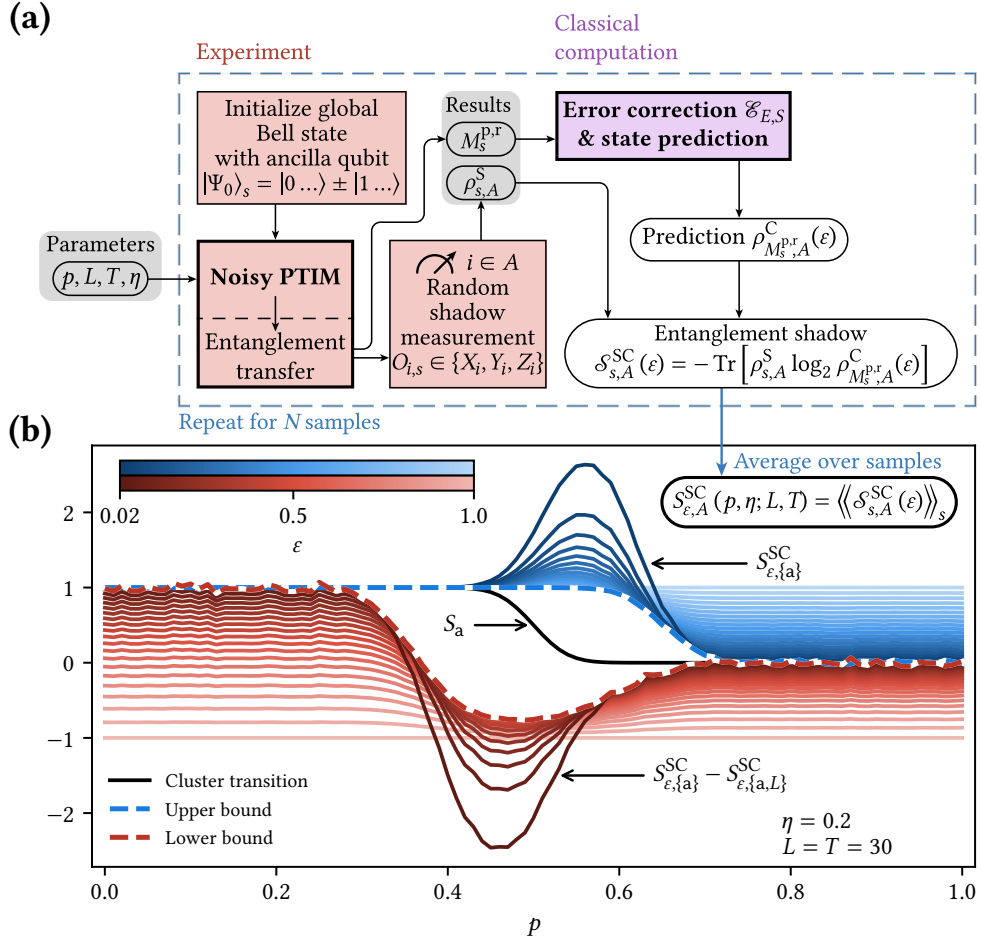


Figure 4.4 • Bounds on the PTIM entanglement transition via shadow tomography.

(a) Protocol to experimentally measure the shadow of the entanglement entropy of a subsystem A on a noisy PTIM in the setup shown in Figure 4.3. The procedure is made robust to noise by employing an error correction algorithm in the classical state prediction. (b) Different regularizations $0 < \epsilon \leq 1$ yield families of curves, which represent upper and lower bounds for the entanglement entropy of the ancilla qubit S_a (solid black line). The strongest bounds on the entanglement are given by the lower and upper envelopes of the curves (dashed lines). Simulations were performed for $L = T = 30$ with noise rate $\eta = 0.2$ and averaged over 10^5 samples. Error bars are negligible and not shown here.

4.4.2 Upper Bound

To measure an upper bound on the PTIM’s entanglement transition, we choose the subsystem $A = \{a\}$ (only the ancilla qubit) and measure the average shadow of the cross-entropy $S_{\varepsilon, \{a\}}^{\text{SC}}$. To compute $\rho_{M_s^{\text{p.r.}}, \{a\}}^{\text{C}}$, we first make a prediction for the state $|\Psi_f\rangle_{s, \{a, L\}}$ of both qubits a and L . The full algorithm for this prediction is described in Section 4.D; here we give a brief summary. Given any PTIM configuration, only 8 final stabilizer states are possible: If the qubits are entangled, their stabilizer group has the form $\langle \pm Z_a Z_L, \pm X_a X_L \rangle$, if they are disentangled, they are stabilized by $\langle \pm X_a, \pm X_a X_L \rangle$. To decide on the correct stabilizer group and signs, we employ the error correction algorithm \mathcal{E}_E , which was already used in Section 4.3, and combine it with the “complementary” algorithm \mathcal{E}_S that uses the results of recorded E_i measurements to augment the measurement pattern M_s^{p} by additional (unobserved) S_e measurements. Both error correction algorithms are based on an MWPM algorithm and are described in detail in Section 4.C. The combined output of \mathcal{E}_E and \mathcal{E}_S is an augmented pattern \tilde{M}_s^{p} , which makes all recorded measurement outcomes M_s^{r} consistent. The augmented history is then used to decide on the most likely state $|\Psi_f\rangle_{s, \{a, L\}}$: A colored cluster simulation first determines if the two qubits are likely to be in an entangled state or not. For each case, the measurement results are then used to predict the most likely signs of the stabilizer generators. Importantly, in some cases, such a sign is determined by a measurement outcome that was not observed (because the measurement was added by the error correction step). In this case we do not randomly choose a sign as this would result in incorrect state predictions in half of the cases. Instead, the algorithm returns a partially mixed state by removing the stabilizer generator. The predicted stabilizer generators are now translated into a density matrix¹⁶ $\rho_{M_s^{\text{p.r.}}, \{a, L\}}^{\text{C}}$ and the partial trace $\rho_{M_s^{\text{p.r.}}, \{a\}}^{\text{C}} = \text{Tr}_L \left[\rho_{M_s^{\text{p.r.}}, \{a, L\}}^{\text{C}} \right]$ is used as the prediction for just the ancilla qubit.

We plot $S_{\varepsilon, \{a\}}^{\text{SC}}$ for the noise rate $\eta = 0.2$ in Figure 4.4 (b). The family of curves shown represents different regularizations $0 < \varepsilon \leq 1$. A large value of ε can be understood as a “weaker” state prediction; this coincides with suppressed statistical fluctuations, but also a weaker upper bound on the actual entanglement entropy S_a . Small values of ε make the shadow of the entropy more susceptible to false state predictions. This leads to diverging values of $S_{\varepsilon, \{a\}}^{\text{SC}}$ in parameter regimes where the error correction often fails to produce correct predictions. Note that the statistical fluctuations also increase with smaller values ε . Since Equation (4.11) is true for *all* values of ε (as long as statistical fluctuations are sufficiently suppressed via a large number of samples n_s), the sharpest upper bound on the entanglement entropy S_a is the *lower envelope* on the family of curves for $0 < \varepsilon \leq 1$; i.e., we find the optimal value ε for each probability p that minimizes $S_{\varepsilon, \{a\}}^{\text{SC}}$.¹⁷ Clearly, Figure 4.4 (b) shows an upper bound on the entanglement entropy which is experimentally accessible and nontrivial. The real entanglement transition of the PTIM must occur left of the region where $S_{\varepsilon, \{a\}}^{\text{SC}}$ decays to zero.

¹⁶To do this, compute a projector $P_i = (\mathbb{1} + g_i) / 2$ from every stabilizer generator g_i . Then it is $\rho \propto \prod_i P_i$.

¹⁷The values of ε can be chosen after the experiment was performed. However, it is important to choose ε large enough to avoid diverging fluctuations. This must be taken into account when calculating the lower envelope.

We note that the error correction algorithm used for classical state prediction is indeed crucial. In Section 4.B we show that a naive approach, which ignores noise, only produces a trivial upper bound.

4.4.3 Lower Bound

We can also apply the protocol in Figure 4.4 (a) to the subsystem $A = \{a, L\}$ in order to measure the entanglement shadow $S_{\varepsilon, \{a, L\}}^{\text{SC}}$. To this end, the algorithm described in Subsection 4.4.2 already provides a prediction $\rho_{M_s^{p,r}, \{a, L\}}^{\text{C}}$ for the state of both qubits. Following Equation (4.12), the difference $S_{\varepsilon, \{a\}}^{\text{SC}} - S_{\varepsilon, \{a, L\}}^{\text{SC}}$ provides a lower bound on the average entanglement entropy S_a . We show the corresponding family of curves for different values of ε (for $\eta = 0.2$) in Figure 4.4 (b). As before, large values of ε yield a trivial bound on the entanglement entropy, while small values ε are more susceptible to noise. In this case, the sharpest bound is given by the *upper envelope*. Notably, this bound drops below zero for some values of p . This happens if the classical algorithm fails to correctly predict the state $\rho_{\{a, L\}}$. Nonetheless, the lower bound shown in Figure 4.4 is clearly nontrivial.

4.5 Summary

We performed shadow tomography simulations as shown in Figure 4.4 (b) for the system sizes $L \in \{10, 20, 30, 40\}$. For each dataset, the lower and upper envelopes were calculated. The resulting bounds are shown in Figure 4.5. Clear crossings emerge and indicate the exact position of the bounds that can be placed on the entanglement transition at $p_c = 1/2$. We denote the upper bound as $p_{c, >}^{\text{S}}$. Its position depends on the noise rate η (here $\eta = 0.2$) and the performance of the error correction algorithm \mathcal{E}_S . In addition, the shadow tomography protocol yields the lower bound $p_{c, <}^{\text{S}}$. A comparison with the decoding protocol from Section 4.3 (green lines) indicates that both critical points coincide: $p_{c, <}^{\text{S}} \approx p_{c, <}^{\mathcal{D}}$. This is not surprising as both protocols rely on the same error correction algorithm \mathcal{E}_E .¹⁸

Figure 4.5 shows two lower bounds and one upper bound on the entanglement transition of the projective transverse field Ising model. All are accessible via experimental protocols that avoid the (otherwise prohibitive) postselection problem. This was achieved by combining information retrieval and shadow tomography with advanced error correction algorithms to cope with faulty measurement records. We find the thresholds

$$p_{c, <}^{\mathcal{D}} \approx p_{c, <}^{\text{S}} \leq p_c \leq p_{c, >}^{\text{S}}. \quad (4.14)$$

All thresholds only coincide with p_c in the noise-free case. The interval $\delta = p_{c, >}^{\text{S}} - p_{c, <}^{\text{S}}$ increases with the noise η (and also depends on the performance of the error correction algorithms). We observe an approximately linear dependence (see inset of Figure 4.5). δ thus provides an independent probe of the noise rate η .

¹⁸Technically, the shadow tomography protocol uses \mathcal{E}_E and \mathcal{E}_S . The latter however has a critical point at $p_{c, >}^{\text{S}}$ and therefore does not influence the position of $p_{c, <}^{\text{S}}$.

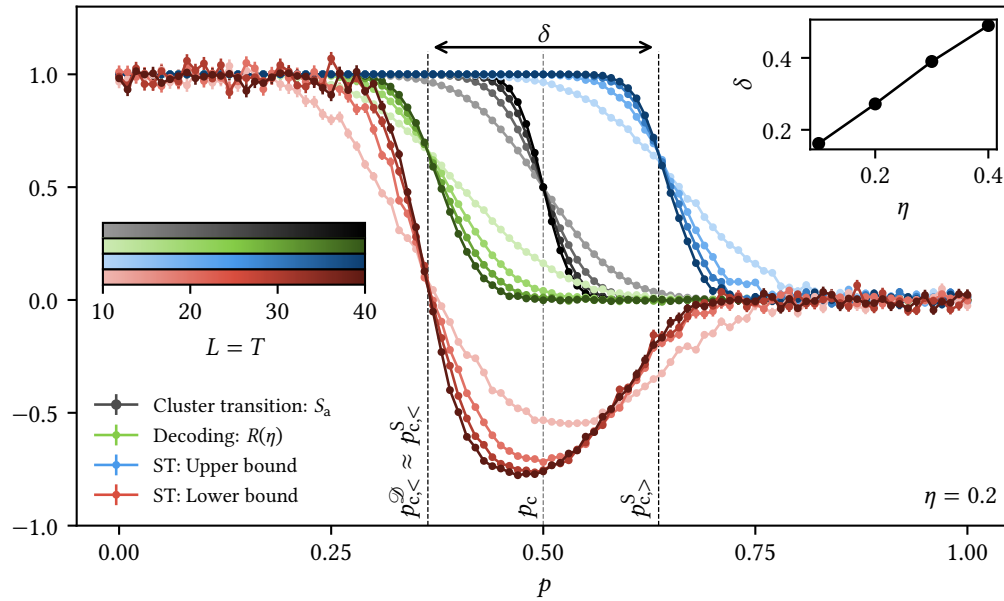


Figure 4.5 • Accessible bounds on the PTIM entanglement transition. Comparison of the two lower bounds from decoding (green) and shadow tomography (“ST”, red), and the upper bound from shadow tomography (blue). All methods show clear crossings for the system sizes $L = T \in \{10, 20, 30, 40\}$, indicating the existence of critical points $p_{c,<}^{\mathcal{D}}$, $p_{c,<}^S$ and $p_{c,>}^S$. These values serve as accessible bounds on the inaccessible entanglement transition at p_c . Our numerical data suggests that the two lower bounds coincide. The interval δ between the upper and lower bounds can be used as a measure of the noise rate η . All simulations were performed for 10^5 samples; most error bars are negligible. Crossing points (and subsequently δ) were estimated by hand.

Appendices for Chapter 4

4.A Extended Colored Cluster Model

In Subsection 1.3.1, we reviewed the colored cluster model (introduced in Ref. [24]) as a means to simulate the entanglement dynamics of the PTIM by tracking Bell clusters instead of the actual state of the system. The CCM assigns colors to every qubit, such that qubits that belong to the same cluster share a color. The model follows two rules:

1. If an E_i measurement is performed on the qubit i , it is assigned a unique new color.
2. If an S_e measurement is performed on two adjacent qubits $e = (i, i + 1)$ that have different colors, one of the corresponding clusters inherits the color of the other cluster.

To track the survival of information encoded in an initial global cluster in the PTIM, it is useful to assign a “dominant color” to all qubits initially. If qubits of this color are involved in S_e measurements, the dominant color is always inherited by the other cluster. The information survived in a circuit if and only if the final state features the initial color.

If the system is prepared in a product state $|m\rangle$ and this logical bit survives, the final state has the form $|\tilde{m}\rangle$ with a different configuration. Here, we present an extended version of the colored cluster model, which can be used to calculate the configuration \tilde{m} . To this end, the simulation not only utilizes the measurement pattern M^P but also the results S^f of the off-site measurements S_e . Next to a color, every qubit is also assigned a (classical) orientation 0 or 1. The initial orientations are determined by the state $|m\rangle$. The extended colored cluster model follows one additional rule:

3. If an S_e measurement is performed on two qubits, their classical orientations must match the measurement outcome. If the configuration is consistent with the opposite measurement result, all qubits that subsequently inherit a new color are also assigned their opposite orientation.

The extended CCM tracks one of the two possible configurations in every Bell cluster $|m\rangle \pm |\bar{m}\rangle$. For the initial cluster, only one of those configurations is possible, and with the dominant color, this configuration is always tracked correctly. Consequently, the model allows for an efficient state prediction if the logical qubit survives the PTIM trajectory.

4.B Shadow Tomography Without Error Correction

As a sanity check, we demonstrate that the shadow tomography protocol (see Figure 4.4) does require an error correction step in order to yield nontrivial bounds on the entanglement transition of the PTIM. To this end, we repeat the same procedure but replace the classical state prediction $\rho_{M_s^{p,r},\{a\}}^C$ with a different algorithm that does *not* use an error correction step.

First, a colored cluster model simulation is performed on the recorded pattern of measurements M^P . If this simulation suggests that the initial Bell cluster did survive the PTIM trajectory, then the ancilla qubit must be entangled with the qubit L . Consequently, its state is assumed to be fully mixed $\rho_{M_s^{p,r},\{a\}}^C = \mathbb{1}/2$. If the CCM simulation suggests that the Bell cluster was destroyed on the system qubits, the ancilla qubit is expected to be in a pure state $|\pm\rangle_a$ polarized in the x -direction. In this case, the recorded measurement results E^r can be used to choose which of those states should be predicted. As the initial cluster is destroyed on the system qubits, there exists a path of E_i measurements and omitted S_e measurements, which traverses spacetime from qubit 1 to L on the lattice \mathcal{L} [we describe this “horizontal percolation” in more detail in Section 4.C, see also Figure 2.2 (b)]. The product of all measurement outcomes E^r on this path corresponds to a measured parity $X_1 X_2 \cdots X_L$ on the systems. The parity of the ancilla qubit is determined by multiplying the parity of the initial state by the parity of the horizontal path that destroys the initial cluster on the system. The corresponding pure state $|\pm\rangle_a$ is predicted.

Note that this state prediction algorithm only operates on the *observed* pattern M^P , instead of the augmented pattern \tilde{M}^P . In particular, additional predicted S_e measurements in the pattern \tilde{S}^P might make a percolation path invalid and thus prevent some incorrect predictions. We show simulated data for this approach in Figure 4.6 for the same noise rate ($\eta = 0.2$) as in Figure 4.4 (b). The subfigures show the upper bounds on the entanglement entropy for $L = T = 50$ and $L = T = 400$.¹⁹ Clearly, the lower envelopes of the curve families do not cross (cf. Figure 4.5), but shift with increasing system size. This leads to a trivial upper bound on the entanglement transition $p_{c,>}^S \rightarrow 1$ for $L = T \rightarrow \infty$. We thus argue that the shadow tomography protocol can only produce meaningful bounds on the entanglement transition of the PTIM if a performant error correction algorithm is used to counter artifacts due to noise.

¹⁹We are able to reach these large system sizes, because our simulations are usually bottlenecked by the error correction algorithms, which are not applied here.

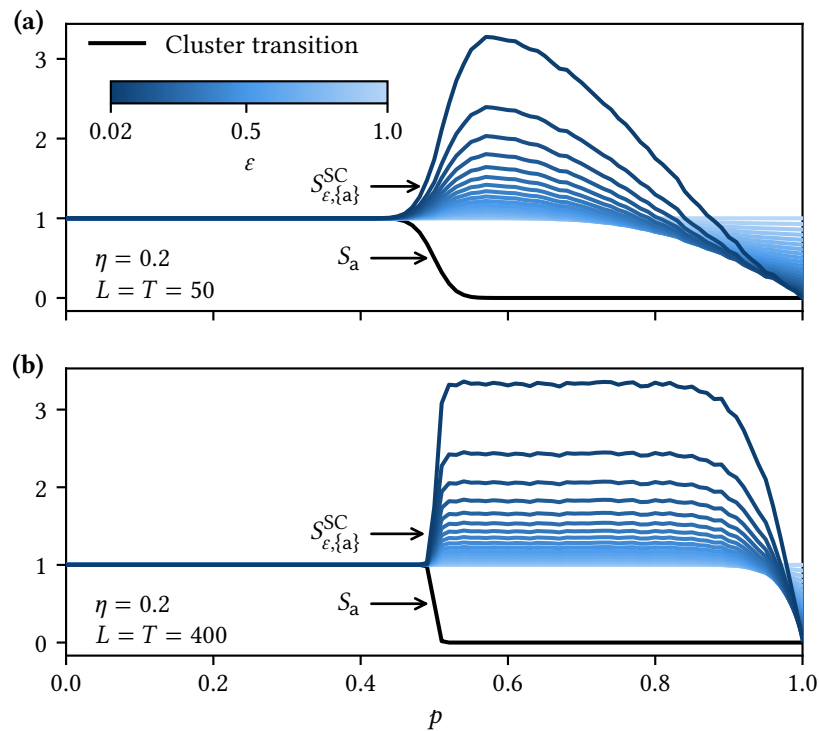


Figure 4.6 • Shadow tomography of a noisy PTIM without error correction. Upper bounds for the cluster transition obtained via shadow tomography based on a naive state prediction without an error correction step. **(a)** and **(b)** show simulations for system sizes $L = T = 50$ and $L = T = 400$. Clearly, the upper bound on the entanglement transition shifts towards $p = 1$ at large system sizes. Data points show averages over 10^5 samples.

4.C Error Correction Algorithms for the PTIM

In Chapter 2, we described a decoder for the PTIM, which uses a minimum weight perfect matching approach. There, we considered a noise model in which no E_i measurements are recorded while the S_e measurements are noise-free. Here, we introduce two error correction algorithms inspired by this approach. Together, these error corrections are tailored to handle our more generalized noise model, where some of the E_i measurements are recorded but S_e measurements are subjected to noise.

Given a noisy PTIM, the observer records an *incomplete* measurement pattern $M^{\text{P}} = (E^{\text{P}}, S^{\text{P}})$ and the corresponding measurement outcomes $M^{\text{r}} = (E^{\text{r}}, S^{\text{r}})$. Due to its incompleteness, this recorded history generally corresponds to an impossible PTIM trajectory. Consider, for example, two consecutive measurements of E_i on the same qubit with the opposite result. This is only possible if the qubit i was involved in an S_e measurement after the first E_i measurement was performed — allowing the second E_i measurement to project it onto the opposite eigenstate. This suggests that inconsistent results E^{r} can be used to

detect missing S_e measurements. Conversely, the results S^r contain information about E_i measurements that occurred in the circuit but were not recorded.²⁰

The goal is to find an error correction algorithm $\mathcal{E}_{E,S}(M^{\text{P},r})$ that takes an inconsistent measurement record and constructs an augmented (partially hypothetical) pattern $M^{\text{P}} \mapsto \tilde{M}^{\text{P}}$ that is consistent with all observed measurement outcomes. The simplest error correction assumes that *every* possible measurement was always performed. This makes any set of measurement results trivially consistent, but is also very unlikely. For successful decoding algorithms and state predictions (for shadow tomography), we need a more sophisticated approach, which aims to find a consistent augmented pattern that is also *likely*. To this end, we employ a minimum weight perfect matching algorithm.

We construct the algorithm $\mathcal{E}_{E,S}$ in two subroutines. First, a correction algorithm $\mathcal{E}_E(M^{\text{P}}, S^r)$ uses the recorded measurement pattern and the results of the S_e measurements to predict where additional E_i measurements may have occurred. An augmented pattern \tilde{E}^{P} is constructed without predicting the results of the hypothetical measurements. \mathcal{E}_E performs a similar task, as the MWPM decoder $\mathcal{D}_{\text{MWPM}}$ described in Section 2.5. Subsequently, the algorithm $\mathcal{E}_S(M^{\text{P}}, E^r)$ uses the full pattern and the results of the E_i measurements in order to generate an augmented pattern \tilde{S}^{P} with additional predicted S_e measurements. Since both algorithms \mathcal{E}_E and \mathcal{E}_S do not predict the outcomes of any unrecorded measurements, the combined augmented pattern $\tilde{M}^{\text{P}} = (\tilde{E}^{\text{P}}, \tilde{S}^{\text{P}})$ does make all observed results M^{P} self-consistent.

4.C.1 Error Correction Algorithm \mathcal{E}_E

The error correction algorithm $\mathcal{E}_E(M^{\text{P}}, S^r)$ is a modified version of the MWPM decoder used in Ref. [64] and Chapter 2. The idea is to reinterpret a PTIM trajectory in $1 + 1$ -dimensional spacetime as a two-dimensional error correcting code. This allows for an approach that is similar to MWPM decoding algorithms on the surface code [92, 114].

As in Subsection 2.5.1, our algorithm is split into three substeps: First, the recorded measurement history is used to construct an abstract weighted graph. Then, an MWPM algorithm is used to find an optimized node pairing on this graph. Lastly, these matchings are used to predict the positions of additional E_i measurements in spacetime — yielding the augmented pattern \tilde{E}^{P} . We illustrate these steps on a sample trajectory shown in Figure 4.7 (a).

1. First, in Figure 4.7 (b), the PTIM trajectory is visualized on a lattice \mathcal{L} , which also includes the recorded results of S_e measurements. This is a representation of the input for the correction algorithm $\mathcal{E}_E(M^{\text{P}}, S^r)$. Qubits live between the vertical lines of the lattice. The observed results S^r are shown as colors of vertical lines. Blue nodes are placed at the endpoints of vertical lines that correspond to S_e measurements with outcome -1 (no nodes are added on the boundary of the lattice).

²⁰In Chapter 2 we referred to the measurements as “errors” (E_i) and “syndromes” (S_e). Here, this designation does not make sense anymore, as our noise model applies to both types of measurements equally.

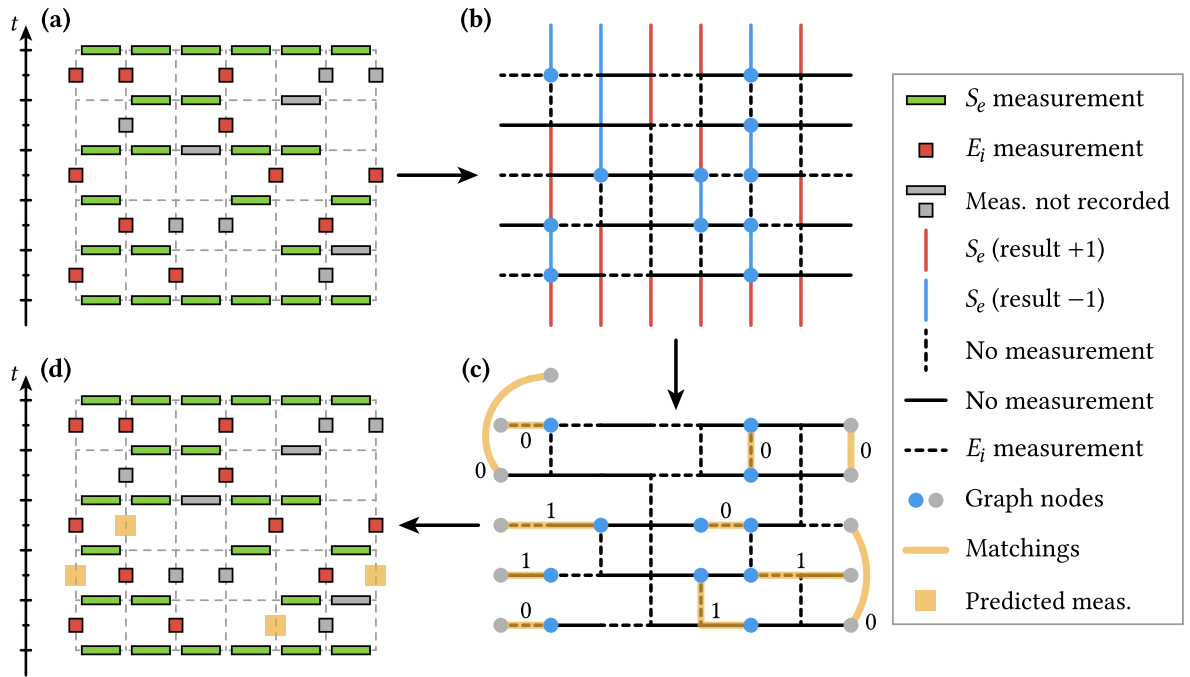


Figure 4.7 • Error correction algorithm \mathcal{E}_E . (a) Sample PTIM trajectory pattern M^P with unrecorded measurements indicated by gray boxes. (b) The same pattern is converted into a lattice \mathcal{L} that also shows the results S^r of S_e measurements as colors of vertical lines. \mathcal{L} is the input of the algorithm \mathcal{E}_E . Nodes (blue disks) are added at the endpoints of vertical blue lines (not at the lattice boundaries). (c) The lattice is reduced by deleting all solid vertical lines. Additional (gray) nodes are added at the system boundaries. If and only if the total number of nodes is odd, an additional boundary node is placed outside \mathcal{L} . This reduced representation corresponds to a weighted graph \mathcal{G} ; edge weights correspond to the minimum number of solid edges traversed when connecting two nodes. An MWPM is computed on \mathcal{G} and shown on \mathcal{L} with the corresponding weights. (d) Matched edges with non-zero weights correspond to additional E_i measurements in the augmented pattern \tilde{E}^P . They are placed wherever a matching traverses a solid edge.

In Figure 4.7 (c), we reduce the lattice by removing all S_e measurements (solid vertical edges). Additional (gray) nodes are placed on the left and right boundaries of the system for every time step.²¹ If the total number of nodes (blue and gray) is odd, another boundary node is placed outside the lattice. At this stage, we can construct an edge-weighted graph \mathcal{G} (which we do not show here), as illustrated in Figure 2.13: All nodes on the lattice correspond to nodes on the graph. Edges are created between all nodes that can be connected along a path on the reduced lattice (going along dashed vertical lines and any horizontal lines). Each edge is assigned a weight, which corresponds to the minimal number of horizontal solid edges on the lattice that are traversed when connecting two nodes. Additionally, all gray boundary nodes are interconnected by zero-weight edges.²²

Note that here, the algorithm \mathcal{E}_E deviates from the decoder $\mathcal{D}_{\text{MWPM}}$ described in Section 2.5. We know about *some* of the E_i measurements that were performed – and thus they do not contribute to the weight of an edge in \mathcal{G} . The following steps are mostly identical to those performed in $\mathcal{D}_{\text{MWPM}}$.

2. A minimum weight perfect matching is performed on the graph \mathcal{G} , pairing all nodes along edges such that the total weight of the matched edges is minimized. As before, we use the Blossom algorithm [116] in its implementation by Kolmogorov [117]. For our example, we highlighted the matched edges (here as connecting paths in \mathcal{L}) in Figure 4.7 (c) and indicated them by their corresponding weights. In noise-free trajectories, it is always possible to find a matching of weight zero; here, we find the total weight 4.
3. Finally, the matched graph is converted into a prediction \tilde{E}^{P} . The matched edges are drawn on the lattice \mathcal{L} as in Figure 4.7 (c). Every matched solid horizontal edge corresponds to a missing E_i measurement. We show the augmented pattern $E^{\text{P}} \mapsto \tilde{E}^{\text{P}}$ in Figure 4.7 (d). Note that the predicted measurements typically do not coincide with the real, unrecorded measurements [which are also shown in Figure 4.7 (d) for comparison]. The error correction algorithm \mathcal{E}_E only predicts *one* possible measurement pattern that is consistent with all results S^{f} .

By construction, the algorithm \mathcal{E}_E aims to find an augmented pattern \tilde{E}^{P} , which contains a small number of additional measurements. Under the assumption that noise is “unlikely”, this is a good approach. We refer to our interpretation in Subsection 2.5.2. Note that on average, at most half of the unrecorded E_i measurements will show as inconsistencies in S_e and can be detected here. Thus, this error correction algorithm should be viewed as a means to *correct* the recorded measurement history (make it consistent), and not as a reconstruction of the real PTIM trajectory.

²¹These boundary nodes create “virtual periodic boundaries” in the spacial direction. In principle, \mathcal{E}_E could also be applied to a PTIM with periodic boundaries – then no boundary nodes would be added.

²²To increase performance, our implementation uses the graph construction described in Subsection 2.C.2.

When applying the error correction \mathcal{E}_E in the context of the shadow tomography protocol, the circuit is augmented by an additional ancilla qubit [see Figure 4.3]. This one qubit is not subjected to noise. To account for this, it is not included in the lattice \mathcal{L} in Figure 4.7 (b). This guarantees that additional measurements are only predicted on the system qubits $\{1, \dots, L\}$.

Construction of Correction Operators

The protocol described in Section 4.3 employs the decoder \mathcal{D}_E , which uses the error correction step \mathcal{E}_E as a subroutine. In this context, the PTIM trajectory is finalized by a step of S_e measurements on every edge e . Here we explain how the decoder uses the augmented history $(\tilde{E}^p, S^{p,r})$ to predict a correction operator $C = \prod_i X_i^{c_i}$ with $c_i \in \{0, 1\}$, in order to retrieve encoded information from the final state. Note that the measurements in \tilde{E}^p *cannot* be interpreted as flips in a classical bit-flip model (this was possible in Subsection 2.5.1).²³ Thus, a different approach is needed.

First, consider the noise-free case ($\eta = 0$). With perfect knowledge of the circuit, a stabilizer simulation can be used to find the true correction operator, if the initial cluster survives. Even simpler, the extended colored cluster model described in Section 4.A can track the configurations of Bell clusters and find the correction operator more efficiently. This method uses the patterns $M^p = (E^p, S^p)$ but only relies on the results S^f of S_e measurements.

For the noisy PTIM ($\eta > 0$), we first use the algorithm \mathcal{E}_E to find the augmented pattern \tilde{E}^p . A colored cluster simulation is performed on the combined pattern (\tilde{E}^p, S^p) . If this simulation predicts that the initial cluster did not survive, one of the two possible correction operators (determined by the final step of S_e measurements) C or \bar{C} is chosen at random. If the CCM simulation predicts that the initial cluster survived, we may again use the results S^f to track its configuration and infer the true correction operator. An extended CCM simulation is used for this.

Note that the choice of a correction operator is only based on the outcomes S^f of S_e measurements, not on E^f . For this reason, it suffices to augment the pattern $E^p \mapsto \tilde{E}^p$. An error correction algorithm \mathcal{E}_S could find additional S_e measurements but not predict their outcomes, and would therefore be useless in finding a correction operator.²⁴

²³The recorded E_i measurements may or may not result in a flip in a classical model. In Chapter 2, no E_i measurements were recorded – allowing for a simpler interpretation.

²⁴If we were to perform \mathcal{E}_E and \mathcal{E}_S to find the fully augmented pattern $\tilde{M}^p = (\tilde{E}^p, \tilde{S}^p)$, we would predict the survival of the initial cluster in more cases. However, if the cluster is only propagated by a predicted measurement S_e without a known result, a correction string cannot be inferred.

4.C.2 Error Correction Algorithm \mathcal{E}_S

The error correction algorithm $\mathcal{E}_S(M^P, E^T)$ makes the results of recorded E_i measurements self-consistent by constructing an augmented pattern $S^P \mapsto \tilde{S}^P$. The algorithm is similar to \mathcal{E}_E (cf. Subsection 4.C.1) but operates on the dual lattice \mathcal{L}^* . We first describe the algorithm \mathcal{E}_S , followed by an explanation of the underlying physics.

A recorded PTIM trajectory [for example Figure 4.8 (a)] is transferred onto a lattice \mathcal{L}^* , as shown in Figure 4.8 (b). \mathcal{L}^* is dual to the lattice \mathcal{L} used in Figure 4.7 (b). Here, E_i measurements are represented by vertical lines, and their outcomes are indicated by color. Qubits live on the vertical lines, and the pattern S^P is represented by dashed and solid horizontal lines. Nodes (blue disks) are attached to the endpoints of error measurements with result -1 .

The following steps are very similar to the process described in Subsection 4.C.1. The lattice \mathcal{L}^* is reduced by removing all solid vertical lines [see Figure 4.8 (c)]. Note that this lattice has smooth edges at the left and right sides and no boundary nodes are needed there. In Figure 4.8 (c), we assume that the initial state was prepared with positive global parity $\prod_{i=1}^L X_i |\Psi_0\rangle = |\Psi_0\rangle$. If the parity is negative (or not determined), it is necessary to implement “virtual periodic boundaries” in the temporal direction by adding boundary nodes at every site before the first and after the final time step.

The reduced lattice in Figure 4.8 (c) is again interpreted as a weighted graph \mathcal{G} , where edge weights are determined by the minimum number of solid horizontal lines traversed on the path between two nodes. If boundary nodes were included at the top and bottom of the lattice, they are interconnected via edges of weight zero. A minimum weight perfect matching is performed on \mathcal{G} , for our example, we highlight the matched edges in their lattice representation in Figure 4.8 (c). Wherever a matched edge includes a solid horizontal line, an additional S_e measurement is predicted. This constructs the augmented pattern \tilde{S}^P , as shown in Figure 4.8 (d). Again, we note that the predicted patterns do generally not match the (unknown) actual pattern of measurements.

To understand *why* this error correction algorithm works, we must remember that the total parity $\prod_{i=1}^L X_i$ commutes with all measurements and therefore is a conserved quantity in the PTIM. First, consider a noise-free trajectory. Every E_i measurement creates a “single-site Bell cluster” $|0\rangle_i \pm |1\rangle_i$ with parity (relative sign) ± 1 fixed by the measurement outcome. Whenever two Bell clusters merge via an S_e measurement, the product of their individual parities determines the parity of the new combined cluster — independent of the result of the S_e measurement. Now consider the situation where E_i measurements are performed on a number of qubits which are subsequently merged into a Bell cluster (by S_e measurements). The product of the outcomes of these (“initializing”) E_i measurements determines the parity of the Bell cluster. If the cluster is later destroyed by other (“finalizing”) E_i measurements, its parity is measured; i.e., the product of the final E_i measurements must coincide with the combined parity of the initial E_i measurements in any noise-free trajectory.

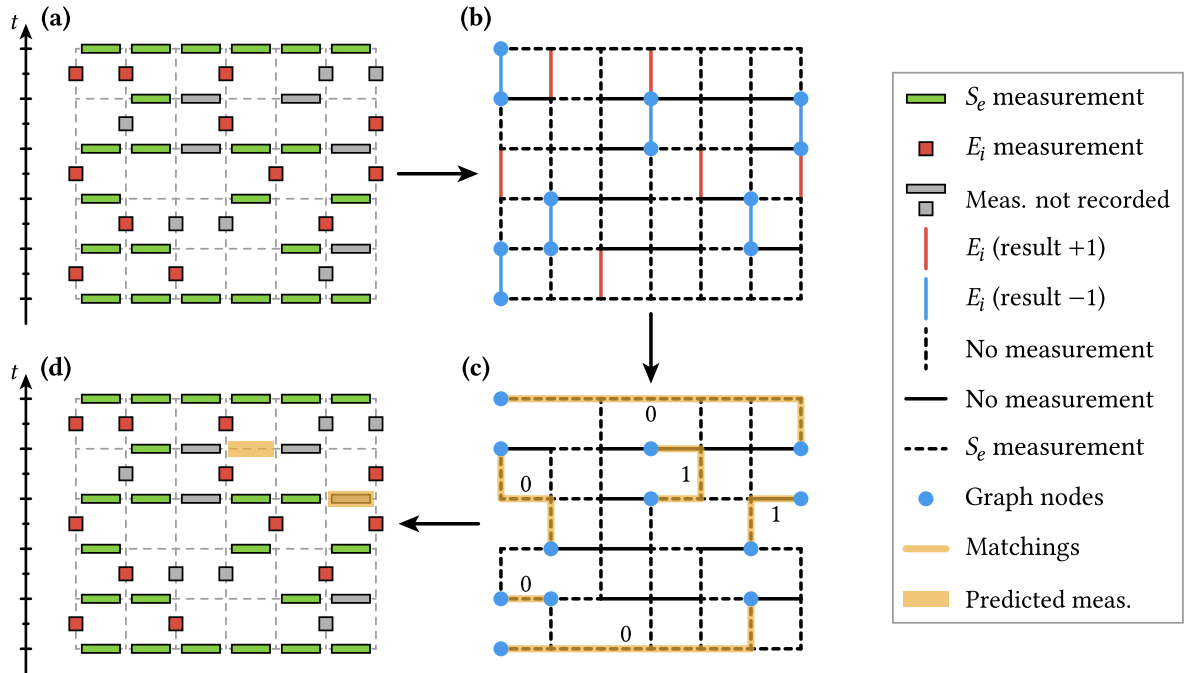


Figure 4.8 • Error correction algorithm \mathcal{E}_S . (a) Sample PTIM trajectory pattern M^P with unrecorded measurements indicated by gray boxes. (b) The same pattern is converted into a lattice \mathcal{L}^* [dual to the one shown in Figure 4.7 (b)] that also shows the results E^x of E_i measurements as colors of vertical lines. \mathcal{L}^* is the input of the algorithm \mathcal{E}_S . Nodes (blue disks) are added at the endpoints of vertical blue lines. (c) The lattice is reduced by deleting all solid vertical lines. This reduced representation corresponds to a weighted graph \mathcal{G} ; edge weights correspond to the minimum number of solid edges traversed when connecting two nodes. An MWPM is computed on \mathcal{G} and highlighted on \mathcal{L}^* next to the corresponding edge weights. (d) Matched edges with non-zero weights correspond to additional S_e measurements in the augmented pattern \tilde{S}^P . They are placed wherever a matching traverses a solid edge.

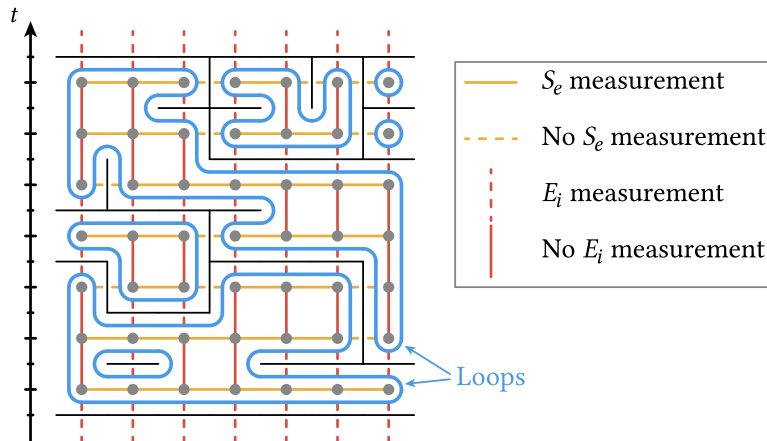


Figure 4.9 • Loop construction for parity checks on E_i measurements. When drawing a PTIM trajectory as a percolation pattern (cf. Figure 1.5), loops can be drawn around percolation clusters. The observed measurement results E^x are consistent with the recorded pattern M^p if and only if for all closed loops, the product of all corresponding E_i measurements is $+1$. If loops measure odd parities, the algorithm \mathcal{E}_S must find a MWPM with non-zero weight and augment the pattern \tilde{S}^p — effectively connecting loops to fix the respective parities.

More generally, we may now track clusters in spacetime as percolation clusters (cf. Figure 1.5). When drawing a loop on the lattice \mathcal{L} around a cluster, this path only traverses horizontally on E_i measurements and vertically on missing S_e measurements. We show this loop construction in Figure 4.9. As the parity must be conserved, we can convince ourselves that the product of the results of all E_i measurements along the loop must be $+1$. This holds true for all clusters and their surrounding loops.

In a noisy PTIM, missing S_e measurements may manifest as loops with odd parity. This occurs if two clusters were connected by an S_e measurement that was not recorded. The correction algorithm \mathcal{E}_S finds a minimal extension $S^p \mapsto \tilde{S}^p$ to join percolation clusters such that all remaining loops have parity $+1$. To understand how this works, consider only a single percolation cluster on the grid \mathcal{L} and draw a loop around it. Wherever this loop traverses an E_i measurement with result -1 , a node is added inside the loop on the dual lattice \mathcal{L}^* [cf. Figure 4.8 (b)]. Importantly, two nodes located in the same region enclosed by the loop are (by construction) connected by an edge of weight zero. If there is an even number of nodes within the enclosed region (this occurs if the loop parity is $+1$), they can be matched locally with total weight zero. If the loop parity is -1 , the number of nodes enclosed is odd. An MWPM must include an edge that connects to a node outside the loop, i.e., to a different percolation cluster. Whenever such a connection between clusters is drawn, the path must contain a missing S_e measurement. The augmented pattern \tilde{S}^p includes additional S_e measurements that merge loops to fix all loop parities.

Extensions for the Shadow Tomography Protocol

In Section 4.4, we used the error correction \mathcal{E}_S on the PTIM system with an ancilla qubit (see Figure 4.3). This requires some adjustments. As for the algorithm \mathcal{E}_E , the noise-free ancilla qubit is not included in the lattice \mathcal{L}^* . To accommodate the entanglement transfer step, an additional time step is added to the grid, which includes the E_i measurements on the qubits $\{1, \dots, L-1\}$. Note that the system is initialized in a global Bell cluster — with a fixed parity on all qubits $\{a, 1, \dots, L\}$. Consequently, the parity on the system qubits (excluding the ancilla) is not initially fixed. As mentioned previously, in this case boundary nodes are added before the first and after the last time step. This creates virtual periodic boundaries in the temporal direction.

To understand why this is necessary, note that here, the trajectory is not initialized at $t = 0$ by E_i measurements as in Figure 4.9. Consequently, loops cannot be closed at the bottom of the lattice \mathcal{L} . The same is true if the trajectory is not finalized by E_i measurements on all qubits at $t = T$. To account for the possibility that the parity of E_i measurements along open paths can multiply to ± 1 , we add the boundary nodes. This ensures that, in the noise-free case, a zero-weight perfect matching always exists.²⁵

4.D Classical State Prediction via Error Correction

The shadow tomography protocol described in Section 4.4 critically depends on a classical state prediction $\rho_{M^P, \{a, L\}}^C$ for the ancilla qubit and the rightmost qubit L . After the entanglement transfer step (see Figure 4.3), these two qubits must be in one of eight possible pure stabilizer states. If the initial cluster survived in the system, the ancilla qubit is fully entangled with the system qubit in a Bell state stabilized by $\langle \pm Z_a Z_L, \pm X_a X_L \rangle$. If the initial cluster is destroyed on the system qubits, the final state must be disentangled with both qubits polarized in the x -direction $\langle \pm X_a, \pm X_L \rangle = \langle \pm X_a, \pm X_a X_L \rangle$.

As a first step, our prediction algorithm determines the sign of the generator $\pm X_a X_L$. Since the total parity $X_a X_1 \cdots X_L$ of the (known) initial state $|\Psi_0\rangle = |0 \dots 0\rangle \pm |1 \dots 1\rangle$ is preserved, this is trivial: In the final entanglement transfer step, the partial parity $X_1 \cdots X_{L-1}$ is measured.²⁶ This parity is multiplied by the parity of the initial state to find the missing parity of the two remaining qubits $\{a, L\}$.

Next, the algorithm decides whether or not the qubits are likely to be entangled. To this end, an augmented measurement pattern $\tilde{M}^P = (\tilde{E}^P, \tilde{S}^P)$ is created, which is consistent with all recorded measurement results M^T . For this, we utilize the two error correction

²⁵These virtual periodic boundaries may even be required for the algorithm \mathcal{E}_S to find *any* valid solution. As a minimal example, consider a circuit with only one qubit ($L = 1$) initialized in the state $|\Psi_0\rangle = |0\rangle$. A single E_i measurement is performed with result -1 . The algorithm \mathcal{E}_S creates two nodes (one before and one after the measurement), which are not connected by an edge on the graph \mathcal{G} . Only by adding the boundary nodes, a perfect matching exists.

²⁶The entanglement transfer is assumed to be noise-free.

algorithms $\mathcal{E}_{E,S}$, described in Section 4.C. Subsequently, a CCM simulation is performed on the augmented pattern. If the initial Bell cluster survives on the qubits $\{1, \dots, L\}$, the algorithm predicts that the ancilla qubit must be entangled to the system. Otherwise, the qubits are assumed to be in a product state. In each case, the state prediction algorithm now aims to find the sign of the missing stabilizer generator:

- If an entangled state is expected, the algorithm must determine the sign of the generator $\pm Z_a Z_L$. In the noise-free case ($\eta = 0$), this can be achieved by tracking the initial cluster through spacetime via an extended colored cluster simulation (see Section 4.A). This allows us to track qubit configurations along a percolation path that connects the first and last time step in the circuit [cf. Figure 2.2 (a)]. If there is noise ($\eta > 0$), we follow the same approach. The extended CCM requires the measurement results S^f , but the algorithm \mathcal{E}_S does not predict any results for additional S_e measurements. Consequently, the augmented pattern \tilde{S}^p is useless here.

To check if a prediction can be made, the extended CCM simulation is performed on the pattern (\tilde{E}^p, S^p) . If the cluster survives, the sign of the generator $\pm Z_a Z_L$ can be inferred. By contrast, if the cluster is destroyed, it survived in the pattern $(\tilde{E}^p, \tilde{S}^p)$ only due to additional S_e measurements predicted by the error correction \mathcal{E}_S . In this case, the sign of the generator can only be guessed. Instead of risking an incorrect prediction $\rho_{M^p, \{a, L\}}^C$, the algorithm does not specify the sign and returns a partially mixed state $\langle \pm X_a X_L \rangle$.²⁷

- If the two qubits are expected to be in a product state, the algorithm must determine the sign of the generator $\pm X_a$. Again, it helps to first consider the noise-free case ($\eta = 0$). The initial Bell cluster was destroyed on the system qubits by a string of E_i measurements on all qubits [cf. Figure 2.2 (b)]. We can consider this as a percolation in spacetime, connecting the leftmost to the rightmost qubit. The percolation path on the lattice \mathcal{L} traverses across E_i measurements in the spacial direction and across missing S_e measurements in the temporal direction. The product of all E_i measurement results along the percolation path is the parity measured on the initial cluster on the system qubits. We multiply this result by the (known) parity of the initial state to infer the missing parity of the ancilla qubit; i.e., the sign of the generator $\pm X_a$. We find the percolation path via a simple breadth-first search on the lattice.

In the noisy PTIM ($\eta > 0$), we search for a similar horizontal percolation path on the augmented pattern \tilde{M}^p . Note however that a path is only useful to us if the outcomes of all included E_i measurements are known. Thus, the error correction \mathcal{E}_E is useless here. To check if a prediction can still be made — i.e., if a horizontal percolation path exists on the pattern (E^p, \tilde{S}^p) — we first perform another CCM simulation which ignores any predicted E_i measurements. If the initial cluster is destroyed, a percolation path exists and is subsequently found to infer the sign of the generator $\pm X_a$. If the cluster now survives, it was destroyed in the pattern $(\tilde{E}^p, \tilde{S}^p)$ by a predicted E_i measurement.

²⁷The shadow tomography protocol reacts sensitively to incorrect state predictions (cf. Section 4.B).

In this case, no prediction can be made, and the algorithm returns a partially mixed state $\langle \pm X_a X_L \rangle$.

The algorithm described here makes a classical prediction $\rho_{M^{p,r},\{a,L\}}^C$ in polynomial time. If the shadow of only the ancilla qubit is needed, the corresponding state prediction can be easily calculated via the partial trace

$$\rho_{M^{p,r},\{a\}}^C := \text{Tr}_L [\rho_{M^{p,r},\{a,L\}}^C]. \quad (4.15)$$

Ausführliche Zusammenfassung in deutscher Sprache

Diese Dissertation ist für Fachleute auf dem Gebiet der kondensierten Materie und der Quantenmechanik geschrieben. Für wissenschaftliche Arbeiten dieser Art ist die englische Sprache Standard – für viele Fachbegriffe gibt es gar keine anerkannten deutschen Übersetzungen. Aus diesem Grund richtet sich diese ausführliche Zusammenfassung explizit an diejenigen Leser:innen, die eine physikalische Grundausbildung genießen durften, aber nicht zwangsläufig mit Quantenschaltungen, Verschränkungsübergängen und dergleichen vertraut sind. Eine Warnung vorweg: Wir werden hier viele Details stark vereinfachen und insbesondere die Mathematik ganz auslassen. Das Ziel ist nur, eine Grundidee der wichtigsten Konzepte und Resultate zu vermitteln. Für Leser:innen, die auch die Details verstehen möchten, führt leider kein Weg am Rest dieser Dissertation vorbei...

Zunächst ordnen wir diese Arbeit ein: Sie gehört der theoretischen Physik an. Das bedeutet, dass wir ausschließlich mathematische Methoden und numerische Simulationen verwenden. Die Systeme, die wir hier betrachten, wurden so noch gar nicht experimentell realisiert.

Wir befassen uns mit Teilchen, die entlang einer langen Kette aufgereiht sind. Wir können diese Anordnung als eine sehr einfache eindimensionale Kristallstruktur verstehen. Damit gehört diese Dissertation in das Gebiet der *kondensierten Materie*. Wir gehen davon aus, dass sich die Teilchen wie Quanten-Bits (Qubits) verhalten und den Regeln der *Quantenmechanik* folgen. Wir stellen uns dafür eine sogenannte *Quantenschaltung* (auch bekannt als *quantum circuit*) vor, in der die Trajektorie eines Zustands in diskrete Zeitschritte aufgeteilt ist. In jedem Zeitschritt werden von einem externen Beobachter Operationen auf den Qubits ausgeführt, dazu zählen unitäre Gatter und quantenmechanische Messungen. Die Prozesse, die in Quantencomputern ablaufen, sind solche Quantenschaltungen:¹ Ein Quantenprozessor führt auf Qubits gezielte Operationen aus, sodass das gesuchte Ergebnis einer Berechnung im Endzustand codiert ist. Dieses Ergebnis wird dann mithilfe von Messungen ausgelesen.

In dieser Arbeit betrachten wir *zufällig generierte* Quantenschaltungen, also Schaltungen, in denen unitäre Gatter und projektive Messungen zufällig in diskreten Zeitschritten

¹In Quantencomputern werden die Qubits üblicherweise nicht entlang einer langen Kette aufgereiht.

angewendet werden. Solche Systeme erlauben es uns, statistische Phänomene von Quantensystemen zugänglich zu machen. Wir beschränken uns dabei auf *lokale* Operationen. Gatter und Messungen koppeln unter Umständen mehrere Qubits, aber ihre Reichweite wächst nicht mit der Gesamtzahl von Qubits an. In dieser Dissertation untersuchen wir, wie Qubits in Quantenschaltungen kollektiv verschränkt werden. Dafür betrachten wir folgendes Szenario: Eine Kette von Qubits wird in einem (reinen) Zustand präpariert und anschließend wird eine zufällig generierte Quantenschaltung auf diesen Zustand angewendet. Wir teilen nun die Qubits im Endzustand in zwei Subsysteme auf und messen/berechnen, wie stark diese miteinander verschränkt sind. Um die Stärke der Verschränkung zu quantifizieren, nutzen wir die *Verschränkungsentropie* [2]. Wir wiederholen denselben Prozess für viele zufällig generierte Schaltungen und bilden den Mittelwert über alle Verschränkungsentropien.

Da wir die Dynamik von Quantenschaltungen hier nicht als Zeitentwicklung unter einem Hamiltonian auffassen, stellt sich im System kein thermisches Gleichgewicht ein; wir gehen aber davon aus, dass gemittelte Größen nach vielen Zeitschritten einen *stationären Zustand* erreichen. So geschieht es auch mit der mittleren Verschränkung. Dabei machen wir die folgende Beobachtung [5–8, 14]: Unitäre Gatter, die mehrere Qubits koppeln, neigen dazu, ein System stärker zu verschränken. Lokale Messungen reduzieren dagegen die Verschränkung in Systemen. Wenn nun in einer Quantenschaltung die unitären Gatter dominieren, dann skaliert die mittlere Verschränkung der zwei Subsysteme mit der Zahl der Qubits, die sich im kleineren Subsystem befinden. Wir sprechen von einem *Volume Law*. Wenn dagegen projektive Messungen dominieren, dann wächst die Verschränkung auch in großen Systemen nur auf einen konstanten Wert an – wir nennen das ein *Area Law*. Nun führen wir einen Parameter ein, der das Verhältnis von unitären Gattern und projektiven Messungen in unseren Quantenschaltungen steuert. Dann finden wir im Parameterraum eine Volume-Law-Phase, eine Area-Law-Phase und dazwischen einen *Verschränkungsübergang*.² Solche Übergänge bilden die Grundlage für die vorliegende Arbeit.

Verschränkungsübergänge treten auch in anderen Szenarien auf. Ein Beispiel hierfür ist das *projektive Ising-Modell mit transversalem Feld* („projective transverse field Ising-Modell“, PTIM) [21, 24]. Es bezeichnet eine Klasse von Quantenschaltungen mit nur zwei verschiedenen Arten von Messungen, die nicht miteinander kommutieren. Je nachdem, welche der Messungen dominieren, befindet sich das PTIM in einer von zwei Area-Law-Phasen mit einem Verschränkungsübergang dazwischen. Die beiden Phasen unterscheiden sich in ihrer Verschränkungsstruktur voneinander: In einer Phase finden wir die meisten Qubits in einem Produktzustand vor, in der anderen entsteht ein globaler verschränkter Bell-Zustand von Qubits.³ Das PTIM stellt für uns eine Art Minimalbeispiel dar, welches

²Das hier beschriebene Szenario tritt so nur in Quantenschaltungen mit geeigneten Gattern und Messungen auf. Der Verschränkungsübergang trennt zwei Parameterbereiche voneinander – wir bezeichnen diese hier als „Phasen“. Dieser Begriff passt hier eigentlich nicht ganz, denn das gemittelte Skalierungsverhalten der Verschränkung ist keine Eigenschaft eines Zustands, sondern eines Ensembles von vielen verschiedenen Quantenschaltungen.

³Der globale Bell-Zustand wird größer, wenn wir ein größeres System betrachten. Damit wächst aber nicht die *Stärke* der Verschränkung an – deshalb handelt es sich auch hier um eine Area-Law-Phase.

sich besonders für Untersuchungen von Verschränkungen eignet. Das liegt nicht zuletzt daran, dass PTIM-Quantenschaltungen besonders effizient simuliert werden können.

Die wissenschaftliche Arbeit, auf der diese Dissertation basiert, umfasst drei Projekte, die alle mit dem PTIM und dessen Verschränkungsübergang zu tun haben. Im Folgenden beschreiben wir die zugehörigen Kapitel im Detail.

PTIM als Speicher für Quanteninformation

In Kapitel 2 betrachten wir das PTIM aus der Perspektive der Quanteninformation. Die Motivation dafür finden wir bei den Quantencomputern: Beim Bau eines Quantencomputers (egal welcher Art) ist es essentiell, Störsignale auf den Qubits so gut wie möglich zu unterdrücken. Wenn Gatter falsch angewendet werden oder gespeicherte Qubits ihren Zustand ändern, kann das Ergebnis eines Algorithmus ungültig werden.⁴ Je mehr Qubits ein Quantencomputer besitzt, desto größer wird die Wahrscheinlichkeit, dass Fehler passieren. Um dem entgegenzuwirken, nutzen wir die Methoden der *Quantenfehlerkorrektur* [45] – in dieser Arbeit beziehen wir uns speziell auf das Speichern eines einzelnen Qubits.

Naiv (ohne Fehlerkorrektur) könnten wir versuchen, ein einzelnes *logisches* Qubit (also Quanteninformation) in den Zustand eines einzigen *physikalischen* Qubits zu codieren. Aber als Beobachter kennen wir diesen Zustand nicht – ihn mit Messungen auszulesen, würde das Qubit zerstören. Wir können also nicht detektieren, ob sich ein gespeichertes Qubit ändert. Die Quantenfehlerkorrektur nutzt nun die Tatsache, dass sich Störungen üblicherweise lokal äußern: Wir speichern ein einziges logisches Qubit in einem verschränkten Zustand vieler physikalischer Qubits. Das heißt, wir *delokalisieren* die Quanteninformation um sie zu schützen. Das bedeutet nicht, dass die physikalischen Qubits keinen Fehlern unterliegen. Wir wenden deshalb periodisch Messungen an, die per Konstruktion etwaige Fehler detektieren, ohne das logische Qubit auszulesen (und damit zu zerstören). Die aufgenommenen Messergebnisse werden zuletzt einem *Decoder* übergeben. Dabei handelt es sich um einen klassischen Algorithmus, der versucht zu rekonstruieren, welche Fehler im System passiert sind, und diese anschließend korrigiert. Ein erfolgreicher Decoder stellt damit den Anfangszustand der physikalischen Qubits (und damit die gespeicherte Quanteninformation) wieder her.

Das PTIM mit seinen zwei Messungen lässt sich als fehlerkorrigierender Code nutzen, weil Quantenschaltungen in der verschränkenden Area-Law-Phase (mit globalem Bell-Zustand) in der Lage sind, ein logisches Qubit zu speichern und zu schützen. Wir teilen jeden Zeitschritt in zwei Unterschritte auf, in denen jeweils eine Art von Messungen ausgeführt wird. Hier interpretieren wir die Messungen, die Verschränkungen zerstören, als Fehler, welche zufällig von der Umgebung auf Qubits angewendet werden und uns unbekannt sind. Die verschränkenden Messungen werden dagegen vom Beobachter zufällig angewendet und aufgezeichnet, mit dem Ziel, möglichst viel über die Trajektorie der Qubits zu erfahren –

⁴Das gilt auch für klassische Computer. Allerdings ist es deutlich leichter, klassische Bits zu kontrollieren und etwaige Fehler zu erkennen.

die Messergebnisse nennen wir auch *Syndrome*.⁵ Wir betrachten in dieser Arbeit (Kapitel 2) drei verschiedene Ansätze für Decoder, die speziell auf das PTIM zugeschnitten sind:

1. Zunächst beschreiben wir einen Decoder, der auf *Mehrheitsentscheidungen* basiert. Dieser Algorithmus behandelt jeden Zeitschritt separat, indem er herausfindet, welche Kombinationen von Fehlern die beobachteten Syndrome erklären könnten. Der Decoder wählt in einem Zeitschritt das Fehlermuster mit der kleinstmöglichen Anzahl von Fehlern und merkt sich den neuen vermuteten Zustand für den nächsten Zeitschritt.

Jeder sinnvoll definierte Decoder funktioniert umso besser, je mehr Qubits verwendet werden. Um zu testen, wie gut der Decoder funktioniert, betrachten wir deshalb Quantenschaltungen mit gleicher Anzahl von Qubits und Zeitschritten – und simulieren jetzt möglichst große Systeme. Wenn in diesem Limes die Wahrscheinlichkeit, das logische Qubit korrekt zu rekonstruieren, gegen eins geht, dann nennen wir den Decoder *erfolgreich*.

Wir führen diesen Test nun für den oben beschriebenen Decoder aus und stellen fest, dass er bei allen endlichen Fehlerraten scheitert. Der Decoder minimiert nämlich nicht die Gesamtzahl von Fehlern, sondern versucht, die einzelnen Zeitschritte optimal zu verfolgen.⁶ Wichtig ist aber eigentlich nur der Endzustand des Systems.

2. Vom Misserfolg des vorangegangenen Ansatzes inspiriert, beschreiben wir als Nächstes einen Decoder, der alle Zeitschritte der PTIM-Quantenschaltung gleichzeitig betrachtet. Dieser Algorithmus nutzt die Syndrome, um eine Trajektorie mit der kleinstmöglichen Gesamtzahl von Fehlern zu finden. Dafür wird die Schaltung jetzt als ein zweidimensionales System interpretiert, bei dem eine Richtung die Zeitrichtung ist.

Es ist mitnichten offensichtlich, dass eine minimale Fehlerkonfiguration effizient gefunden werden kann. Unsere Methode bildet die beobachteten Syndrome auf einen abstrakten Graph mit gewichteten Kanten ab. Dann reduziert sich die Aufgabe des Decoders darauf, auf dem Graphen ein sogenanntes *minimum weight perfect matching* auszuführen – also alle Knoten des Graphen entlang Kanten zu paaren, sodass das Gesamtgewicht aller gepaarten Kanten minimiert wird. Diesem abstrakten Problem haben sich Mathematiker schon vor vielen Jahren angenommen; deshalb existieren hier bereits effiziente Algorithmen [116, 117].

Wir testen den hier beschriebenen Decoder mit der zuvor beschriebenen Methode und finden eine kritische Fehlerrate, unterhalb derer das PTIM erfolgreich decodiert

⁵In diesem Modell mit projektiven Fehlern sind die verschränkenden Messungen auch nötig, um die Quanteninformation zu schützen.

⁶Das gelingt nicht über viele Zeitschritte hinweg, weil das PTIM eindimensional ist. Der Decoder scheitert aus demselben Grund, aus dem es in einer Dimension keine spontane Magnetisierung gibt, siehe auch das Ising-Modell [109, 110].

wird. Hier existiert also ein Parameterbereich, in dem das PTIM prinzipiell als Quantenspeicher genutzt werden kann.⁷

3. Wie gut können Decoder sein? Um das herauszufinden, implementieren wir zuletzt einen *Maximum-Likelihood-Decoder* (also den per Definition bestmöglichen Decoder) für das PTIM. Dieser Algorithmus betrachtet *alle* möglichen Trajektorien und vergleicht deren Wahrscheinlichkeiten miteinander. So findet er die statistisch wahrscheinlichste Korrektur, die den Endzustand des Systems in den Anfangszustand überführt.

Erneut ist nicht zu erwarten, dass für einen solchen Decoder eine effiziente Implementierung existiert – schließlich ist die Zahl möglicher Trajektorien exponentiell groß (in der Zahl von Qubits und Zeitschritten). Es gelingt uns jedoch zu beweisen, dass diese Problemstellung mit einem bereits bekannten Maximum-Likelihood-Decoder für den surface code [91] vergleichbar ist,⁸ der erstaunlicherweise sowohl exakt als auch effizient ist. Wir passen diesen Ansatz auf unser Modell an und finden eine kritische Fehlerrate, die der des zuvor diskutierten Decoders (minimum weight perfect matching) nur wenig überlegen ist.

Praktisch betrachtet lohnt es sich also kaum, den optimalen Decoder zu implementieren, der zwar effizient, aber dennoch langsamer als die anderen Decoder ist. Wir machen hier aber dennoch eine interessante Erkenntnis: Die bestmögliche kritische Fehlerrate ist kleiner als die Fehlerrate, bei der das PTIM in die andere Area-Law-Phase übergeht und die Quanteninformation im System durch Fehler zerstört wird. Das bedeutet, dass ein Parameterregime existiert, in dem Quanteninformation im PTIM codiert und geschützt, aber nicht rekonstruiert werden kann. Die Amplituden des logischen Qubits befinden sich im Endzustand der Quantenschaltungen, können aber nicht weiter genutzt werden.

Modelle mit kritischen Phasen

Zuvor haben wir Quantenschaltungen beschrieben, die entweder einem Area Law oder einem Volume Law entsprechend verschränkt sind. In welcher Phase sich ein Modell befindet, hängt dabei von den gewählten Parametern ab – üblicherweise sind das die Wahrscheinlichkeiten, mit denen verschiedene Gatter oder Messungen angewendet werden. Um ein Modell im Parameterraum kontinuierlich von einer Phase in eine andere zu verschieben, muss ein Verschränkungsübergang durchlaufen werden (so sind Phasen definiert). An diesem Übergang befindet sich das Modell aber in keiner der beiden Phasen; es verhält sich *kritisch*.

⁷Das PTIM kann nur eine Sorte von Fehlern korrigieren. Reale Implementierungen von fehlerkorrigierten Quantenspeichern dieser Art setzen deshalb üblicherweise auf zweidimensionale Systeme, wie zum Beispiel den *surface code* [84–87, 95, 96], da diese nicht nur gegen eine Art von Fehlern robust sind.

⁸Obwohl wir im PTIM ein anderes Fehlermodell annehmen!

Wir können einen solchen kritischen Punkt beispielsweise im projektiven Ising-Modell mit transversalem Feld finden – wenn die Parameter genau so gewählt werden, dass keine der beiden Messungen dominiert. Dann skaliert die gemittelte Verschränkungsentropie von Subsystemen *logarithmisch* mit der Zahl der Qubits. Wir können dieses Skalierungsverhalten sogar verstehen [24]: Der Verschränkungsübergang des PTIM wird von einer *konformen Feldtheorie* beschrieben, die genau dieses Verhalten vorhersagt.⁹

Betrachten wir nun eine andere Klasse von Quantenschaltungen, die nicht auf gewöhnlichen Qubits basieren, sondern auf *freien Fermionen* (in diesem Kontext auch *gaußsche Fermionen* genannt). Wir betrachten jetzt also eine Kette von Gitterplätzen, an denen sich entweder ein Fermion befindet oder keines. Mit „freien“ Fermionen beschränken wir uns hier auf bestimmte unitäre Gatter und Messungen.¹⁰ Auch in solchen fermionischen Quantenschaltungen können wir Verschränkungsstrukturen untersuchen. Dabei machen wir aber eine andere Beobachtung als bei bosonischen Systemen: Die Volume-Law-Phase, die von unitären Gattern erzeugt wird, ist in fermionischen Systemen unter lokalen Messungen instabil. Das heißt, dass die weitreichenden Verschränkungen zusammenbrechen, sobald die Messrate über null steigt [21–23, 28].

In manchen Quantenschaltungen von freien Fermionen machen wir nun aber eine überraschende Entdeckung: Dass schon bei beliebig kleinen Messraten kein Volume Law existiert, bedeutet nicht, dass sich ein Modell zwingend in einer Area-Law-Phase befindet. Manche Modelle verhalten sich bei kleinen (aber endlichen) Messraten kritisch – mit logarithmisch skalierenden Verschränkungen [30]. Es ist wichtig, dieses Verhalten von den zuvor beschriebenen kritischen Punkten zwischen zwei Phasen zu unterscheiden. Hier entstehen *kritische Phasen*, die wir nun in Kapitel 3 anhand von modifizierten Versionen des PTIMs genauer untersuchen.

Wir erweitern das PTIM, indem wir den zwei verschiedenen Messungen noch zwei unitäre Gatter hinzufügen. Das resultierende Modell wurde bereits von Merritt und Fidkowski beschrieben [128]; wir nennen es das *MF-Modell*. Dieses Modell ist für uns aus drei Gründen interessant:

1. Quantenschaltungen im MF-Modell lassen sich mithilfe einer Jordan–Wigner-Transformation [53] auf Trajektorien von gaußschen Fermionen abbilden. Das MF-Modell fällt dabei in die Klasse von Modellen, die eine kritische Phase besitzen.
2. Verschränkungen im MF-Modell lassen sich mithilfe eines Loop-Modells modellieren. Dieses erlaubt besonders effiziente Simulationen von großen Systemen. Das ist wichtig, um das Skalierungsverhalten in kritischen Phasen möglichst genau zu vermessen.¹¹

⁹Ein solches konformes Verhalten ist für Phasenübergänge zweiter Ordnung üblich.

¹⁰Diese unitären Gatter werden *Gaussian unitaries*, oder in bosonischer Sprache (im Qubit-Bild) *matchgates* genannt [51, 52]; sie erhalten die Parität von Zuständen (also ob die Gesamtzahl von Fermionen gerade oder ungerade ist).

¹¹Kritische Phasen zeigen oft sehr starke finite-size-Effekte, die unsere Beobachtungen in Simulationen von kleinen Systemen beeinflussen.

3. Loop-Modelle werden schon seit vielen Jahren untersucht und wir können uns hier bereits bekannter Erkenntnisse bedienen [154]. Insbesondere ist deshalb bekannt, dass die kritische Phase des MF-Modells von einer Feldtheorie beschrieben wird, die nicht konform ist. Daraus ergeben sich Vorhersagen für das Skalierungsverhalten der gemittelten Verschränkungsentropie.

Unsere numerischen Simulationen zeigen, dass die kritische Phase des MF-Modells tatsächlich nicht den Skalierungsgesetzen folgt, die wir von einer konformen Feldtheorie erwarten würden – das tatsächliche Skalierungsverhalten der Verschränkungsentropie folgt stattdessen den Vorhersagen, die zuvor für das Loop-Modell gemacht wurden. Die Ränder der kritischen Phase (an denen sie auf Area-Law-Phasen trifft) verhalten sich jedoch anders; hier legen unsere numerischen Analysen nahe, dass das MF-Modell von einer (unbekannten) konformen Feldtheorie beschrieben wird.¹²

In unseren Simulationen nutzen wir das Loop-Modell, um die Verschränkungen von Fermionen zu beschreiben. Das ist aber nicht die einzig mögliche Interpretation: In Kapitel 3 führen wir ein bosonisches Modell von Qubits ein (das „SWAP-Modell“), das konstruiert ist, um vom gleichen Loop-Modell wie das MF-Modell beschrieben zu werden. Das SWAP-Modell lässt sich nicht mittels Jordan–Wigner-Transformation auf gaußsche Fermionen abbilden und zeigt eine andere Verschränkungsstruktur als im MF-Modell, obwohl beide Modelle das Phasendiagramm desselben Loop-Modells teilen. Damit betrachten wir nun Quantenschaltungen mit kritischer Phase, ohne dass gaußsche Fermionen involviert sind.

Zuletzt führen wir verallgemeinerte Versionen des MF-Modells ein, die wir *Makro-Modelle* nennen. Diese realisieren eine Vielzahl von qualitativ unterschiedlichen Phasendiagrammen mit und ohne kritische Phasen. Auch hier können wir feststellen, dass die Ränder von kritischen Phasen ein konformes Skalierungsverhalten aufweisen. Ähnlich wie im MF-Modell können Verschränkungen in Makro-Modellen durch Loop-Modelle beschrieben werden, für die wir aber keine bereits existierenden Feldtheorien kennen. So stellt sich die Frage: Können wir für ein vorgegebenes Loop-Modell die qualitativen Charakteristika des zugehörigen Phasendiagramms vorhersagen? Für die Makro-Modelle können wir zeigen, dass das (zumindest hier) möglich ist. Wir benennen für jedes Phasendiagramm die jeweiligen Eigenschaften des zugehörigen Loop-Modells, die eine kritische Phase erlauben oder verbieten.¹³ Dabei sind einige Makro-Modelle besonders interessant, weil sie eine kritische Phase mit nur einem unitären Gatter und einer Messung erlauben. Das steht im Kontrast zu bislang bekannten Quantenschaltungen, die üblicherweise mindestens drei verschiedene Operationen benötigen, um in eine kritische Phase einzutreten [26, 28, 29, 126, 128]. Für etwaige zukünftige Realisierungen solcher Modelle in Experimenten könnte diese Vereinfachung nützlich sein.

¹²Die Verschränkungsentropie skaliert im Inneren und auf dem Rand der kritischen Phase „vorrangig“ logarithmisch. Korrekturen, die die beiden Fälle voneinander unterscheiden, werden erst in großen Systemen mit vielen Qubits sichtbar.

¹³Ein wichtiger Aspekt ist die *Orientierbarkeit* von Loop-Modellen. Die Details hierzu sind für diese Zusammenfassung zu umfangreich (siehe Kapitel 3).

Experimentelle Messung von Verschränkungsübergängen

Verschränkungen in Quantenschaltungen zu messen ist allgemein schwierig. Das liegt in der Natur der Verschränkungsentropie: Sie kann nur berechnet werden, wenn der Zustand eines Systems bekannt ist. Um diesen Zustand in einem Experiment herauszufinden (wir sprechen von einer *vollständigen Zustandstomographie*), benötigen wir exponentiell viele (in der Zahl der Qubits) exakte Kopien desselben.¹⁴ Stellen wir uns dafür einmal vor, dass unsere zufällig generierten Quantenschaltungen nicht wirklich zufällig, sondern von uns generiert sind – sodass wir eine Schaltung wiederholt ausführen können. Das genügt aber nicht, um einen Zustand mehrfach zu präparieren. Schließlich haben wir es hier auch mit quantenmechanischen Messungen zu tun, deren Ergebnisse zufällig sind. Um einen Zustand erneut herzustellen, müssen auch die Messergebnisse in der Quantenschaltung übereinstimmen – was bei einer großen Zahl von Messungen exponentiell unwahrscheinlich wird [18, 205]. Wir sprechen hier von einem *Postselektionsproblem*, das es *prinzipiell* unmöglich macht, Verschränkungen in großen Systemen experimentell direkt zu messen.¹⁵ All diese Schwierigkeiten treten auf, bevor wir uns bewusst machen, dass Experimente nicht störungsfrei sind. Damit stellt sich nun die Frage: Können wir Verschränkungsübergänge jemals beobachten, oder machen wir hier nur numerische Simulationen von Phänomenen, die gar nicht nachweisbar sind? Mit anderen Worten – machen wir hier eigentlich noch Physik?

In Kapitel 4 nehmen wir uns speziell den Verschränkungsübergang im projektiven Ising-Modell mit transversalem Feld vor und suchen nach Messprotokollen, die diesen Übergang experimentell zugänglich machen. Da wir Verschränkungen nicht direkt messen können, betrachten wir stattdessen messbare Größen, die (nichttriviale) obere und untere Schranken für den Übergang bilden. Wir finden damit ein Parameterintervall, in dem sich der Verschränkungsübergang befinden muss.

Einen Teil der Arbeit haben wir bereits in Kapitel 2 erledigt: In einer der beiden Area-Law-Phasen des PTIM kann Quanteninformation codiert und gespeichert werden. Wenn wir das PTIM decodieren können, dann muss sich das System in dieser verschränkenden Phase befinden. Die kritische Fehlerrate des Decoders bildet damit eine nichttriviale Schranke für den Verschränkungsübergang. Um diese messbar zu machen, codieren wir ein bekanntes logisches Qubit in den Anfangszustand von PTIM-Quantenschaltungen. Dann ist es möglich zu überprüfen, ob dieser Zustand wiederhergestellt werden kann. Wir verallgemeinern den in Kapitel 2 beschriebenen Decoder (wir wählen hier den Algorithmus, der auf *minimum weight perfect matching* beruht) auf ein realistischeres Fehlermodell, in dem beliebige Messungen vom Beobachter nicht aufgenommen werden. Je geringer die Fehlerrate im System ist, desto enger liegt die Schranke am tatsächlichen Verschränkungsübergang.

Um die Existenz des Übergangs experimentell nachzuweisen, benötigen wir auch eine Methode, um diesen von der anderen Seite aus einzugrenzen. Dafür bedienen wir uns der sogenannten *shadow tomography* [220–222]. Das Ziel dieser Methode ist, Eigenschaften von

¹⁴Die Zahl der Einträge in der Dichtematrix skaliert exponentiell mit der Zahl von Qubits.

¹⁵Natürlich umgehen wir dieses Problem in unitären Schaltungen ohne Messungen. Wir sind hier aber auf der Suche nach Verschränkungsübergängen, die von projektiven Messungen induziert werden.

Quantensystemen vorherzusagen, obwohl nur wenige Messungen auf Zuständen durchgeführt werden können. So ist es möglich, die sogenannte *Kreuzentropie* eines Ensembles von Zuständen experimentell zu messen [223], die immer größer als die Verschränkungsentropie sein muss. Um das zu bewerkstelligen, werden auf dem Endzustand einer (leicht modifizierten) PTIM-Quantenschaltung lediglich zufällige Pauli-Messungen ausgeführt. Dann lässt sich eine obere Schranke für die Verschränkungsentropie und mit dem richtigen Setup auch eine Schranke für den Verschränkungsübergang des PTIM finden.

Für das shadow tomography Protokoll ist es nicht nötig, mehrere Kopien eines Zustands zu erzeugen. So umgehen wir hier das Postselektionsproblem. Um eine *nichttriviale* Schranke zu finden, benötigen wir aber für die Kreuzentropie eine (klassisch erzeugte) Vorhersage des Zustands. Um diese Vorhersage „aussagekräftig“ zu machen – auch dann, wenn das PTIM nicht störungsfrei ist – wenden wir auch hier wieder eine Quantenfehlerkorrektur an. Der Algorithmus, den wir hier vorschlagen, beruht auch auf minimum weight perfect matching und ist strukturell ähnlich (genauer: dual) zu dem Decoder, den wir zuvor verwendet haben.

Der Verschränkungsübergang des projektiven Ising-Modells mit transversalem Feld ist damit experimentell „eingrenzbar“; es ist also möglich, ein Intervall im Parameterraum zu bestimmen, in dem der Übergang stattfinden muss. Die Größe des Intervalls kann genutzt werden, um die Fehlerrate der imperfekten PTIM-Realisierungen abzuschätzen.

List of Figures

1.1	General setting of a one-dimensional hybrid quantum circuit	2
1.2	Example trajectory of the PTIM	13
1.3	Time step in the colored cluster model	15
1.4	Entanglement transition in the PTIM	16
1.5	Relation of the PTIM to bond percolation	17
2.1	Measures for decoder performances on the repetition code	24
2.2	Projective transverse field Ising model as a quantum error correction code	28
2.3	Decoding probability with full knowledge of the trajectory	33
2.4	Mapping PTIM trajectories to classical bits	37
2.5	Performance of the majority voting decoder on the PTIM	41
2.6	Propagating mistakes in the MVD	42
2.7	Minimum weight perfect matching on the PTIM	46
2.8	Classical bit-flip trajectory on the lattice \mathcal{L}	48
2.9	Performance of the MWPM decoder	50
2.10	Performance of the MWPM decoder at $p = q$	51
2.11	Performance of the maximum likelihood decoder	57
2.12	Analytical predictions for the MVD at $q = 0$	62
2.13	Graph construction for the MWPM decoder	63
2.14	Minimum weight perfect matching with a cutoff weight	65
2.15	Path construction with crossing nodes	66
2.16	Illustrations for the proof of the equivalence of MLDs	70
3.1	Critical entanglement scaling in a random matchgate quantum circuit . . .	85
3.2	Classes of quantum circuits	86
3.3	Translation to the loop model	88
3.4	Loop model representation of the PTIM	92
3.5	Unitaries of the MF model	94
3.6	Loop model representation of the MF model	95
3.7	Phase diagram of the MF model	96

LIST OF FIGURES

3.8	Goldstone phase of the MF model	99
3.9	Conformal scaling in the MF model	102
3.10	Phase diagram of the rescaled MF model	106
3.11	Loop representation of the SWAP model	107
3.12	SWAP model simulations in the stabilizer and loop formalism	108
3.13	Time step in the macro model	110
3.14	Time evolution of the entanglement entropy at $p = 1$	113
3.15	Phase diagrams of macro models	117
3.16	Clifford and loop representations of the macro blocks U_{2314} and U_{2341}	118
3.17	Scaling analysis of the ancilla entropy in critical phases of macro models	119
3.18	Conformal scaling of the entanglement entropy in the macro models 2314 and 2341	120
3.19	Comparison of conformal prefactors for different models	122
3.20	Conformal scaling of the mutual information in the macro models 2314 and 2341	124
3.21	Entanglement in the popcorn model	128
3.22	Area-law phases in the flavored MF model at $p = 0$	132
3.23	Area-law phase of the flavored MF model at $p \neq 0$	133
3.24	Sample Bell circuit trajectory	136
3.25	Entanglement dynamics in the unitary Bell model	137
3.26	Illustration of the proof for the $q \leftrightarrow (1 - q)$ symmetry of the model 2314	148
3.27	Loop orientations for the model 4231 at $q \in \{0, 1\}$	151
3.28	Non-orientable loop models	152
3.29	Loop models with trivial phase diagrams	154
4.1	Survival probability of an initial cluster in the PTIM	160
4.2	Lower bound via decoding	162
4.3	PTIM trajectory with an ancilla qubit and an entanglement transfer step	167
4.4	Bounds on the PTIM entanglement transition via shadow tomography	168
4.5	Accessible bounds on the PTIM entanglement transition	171
4.6	Shadow tomography of a noisy PTIM without error correction	174
4.7	Error correction algorithm \mathcal{E}_E	176
4.8	Error correction algorithm \mathcal{E}_S	180
4.9	Loop construction for parity checks on E_i measurements	181

Bibliography

- [1] M. Born. “Zur Quantenmechanik der Stoßvorgänge.” In: *Zeitschrift für Physik* **37** (Dec. 1, 1926), pp. 863–867. ISSN: 0044-3328. DOI: [10.1007/BF01397477](https://doi.org/10.1007/BF01397477) (cit. on pp. [1](#), [158](#)).
- [2] J. von Neumann. *Mathematische Grundlagen der Quantenmechanik*. Springer, (1932). DOI: [10.1007/978-3-642-61409-5](https://doi.org/10.1007/978-3-642-61409-5) (cit. on pp. [2](#), [158](#), [186](#)).
- [3] J. Bernoulli and E. Sylla. *The art of conjecturing, together with letter to a friend on sets in court tennis*. Johns Hopkins University Press, (2006). ISBN: 9780801882357 (cit. on p. [3](#)).
- [4] F. M. Dekking, C. Kraaikamp, H. P. Lopuhaä, and L. E. Meester. “The law of large numbers.” In: *A modern introduction to probability and statistics: understanding why and how*. Springer London, (2005), pp. 181–194. ISBN: 978-1-84628-168-6. DOI: [10.1007/1-84628-168-7_13](https://doi.org/10.1007/1-84628-168-7_13) (cit. on p. [3](#)).
- [5] Y. Li, X. Chen, and M. P. A. Fisher. “Quantum Zeno effect and the many-body entanglement transition.” In: *Phys. Rev. B* **98** (Nov. 2018), p. 205136. DOI: [10.1103/PhysRevB.98.205136](https://doi.org/10.1103/PhysRevB.98.205136) (cit. on pp. [4](#), [20](#), [81](#), [158](#), [186](#)).
- [6] Y. Li, X. Chen, and M. P. A. Fisher. “Measurement-driven entanglement transition in hybrid quantum circuits.” In: *Phys. Rev. B* **100** (Oct. 2019), p. 134306. DOI: [10.1103/PhysRevB.100.134306](https://doi.org/10.1103/PhysRevB.100.134306) (cit. on pp. [4](#), [20](#), [81](#), [89](#), [90](#), [158](#), [186](#)).
- [7] B. Skinner, J. Ruhman, and A. Nahum. “Measurement-induced phase transitions in the dynamics of entanglement.” In: *Phys. Rev. X* **9** (July 2019), p. 031009. DOI: [10.1103/PhysRevX.9.031009](https://doi.org/10.1103/PhysRevX.9.031009) (cit. on pp. [4](#), [20](#), [81](#), [158](#), [186](#)).
- [8] A. Chan, R. M. Nandkishore, M. Pretko, and G. Smith. “Unitary-projective entanglement dynamics.” In: *Phys. Rev. B* **99** (June 2019), p. 224307. DOI: [10.1103/PhysRevB.99.224307](https://doi.org/10.1103/PhysRevB.99.224307) (cit. on pp. [4](#), [20](#), [82](#), [186](#)).
- [9] A. Zabalo, M. J. Gullans, J. H. Wilson, S. Gopalakrishnan, D. A. Huse, and J. H. Pixley. “Critical properties of the measurement-induced transition in random quantum circuits.” In: *Phys. Rev. B* **101** (Feb. 2020), p. 060301. DOI: [10.1103/PhysRevB.101.060301](https://doi.org/10.1103/PhysRevB.101.060301) (cit. on p. [4](#)).

BIBLIOGRAPHY

- [10] C.-M. Jian, Y.-Z. You, R. Vasseur, and A. W. W. Ludwig. “Measurement-induced criticality in random quantum circuits.” In: *Phys. Rev. B* **101** (Mar. 2020), p. 104302. DOI: [10.1103/PhysRevB.101.104302](https://doi.org/10.1103/PhysRevB.101.104302) (cit. on p. 4).
- [11] X. Turkeshi, R. Fazio, and M. Dalmonte. “Measurement-induced criticality in $(2 + 1)$ -dimensional hybrid quantum circuits.” In: *Phys. Rev. B* **102** (July 2020), p. 014315. DOI: [10.1103/PhysRevB.102.014315](https://doi.org/10.1103/PhysRevB.102.014315) (cit. on p. 4).
- [12] Y. Li, S. Vijay, and M. P. Fisher. “Entanglement domain walls in monitored quantum circuits and the directed polymer in a random environment.” In: *PRX Quantum* **4** (Mar. 2023), p. 010331. DOI: [10.1103/PRXQuantum.4.010331](https://doi.org/10.1103/PRXQuantum.4.010331) (cit. on p. 4).
- [13] Y. Li, R. Vasseur, M. P. A. Fisher, and A. W. W. Ludwig. “Statistical mechanics model for Clifford random tensor networks and monitored quantum circuits.” In: *Phys. Rev. B* **109** (May 2024), p. 174307. DOI: [10.1103/PhysRevB.109.174307](https://doi.org/10.1103/PhysRevB.109.174307) (cit. on p. 4).
- [14] M. P. Fisher, V. Khemani, A. Nahum, and S. Vijay. “Random quantum circuits.” In: *Annual Review of Condensed Matter Physics* **14** (2023), pp. 335–379. ISSN: 1947-5462. DOI: [10.1146/annurev-conmatphys-031720-030658](https://doi.org/10.1146/annurev-conmatphys-031720-030658) (cit. on pp. 4, 81, 158, 186).
- [15] J. M. Deutsch. “Quantum statistical mechanics in a closed system.” In: *Phys. Rev. A* **43** (Feb. 1991), pp. 2046–2049. DOI: [10.1103/PhysRevA.43.2046](https://doi.org/10.1103/PhysRevA.43.2046) (cit. on pp. 4, 112).
- [16] M. Srednicki. “Chaos and quantum thermalization.” In: *Phys. Rev. E* **50** (Aug. 1994), pp. 888–901. DOI: [10.1103/PhysRevE.50.888](https://doi.org/10.1103/PhysRevE.50.888) (cit. on pp. 4, 112).
- [17] B. Misra and E. C. G. Sudarshan. “The Zeno’s paradox in quantum theory.” In: *Journal of Mathematical Physics* **18** (Apr. 1977), pp. 756–763. ISSN: 0022-2488. DOI: [10.1063/1.523304](https://doi.org/10.1063/1.523304) (cit. on p. 4).
- [18] J. M. Koh, S.-N. Sun, M. Motta, and A. J. Minnich. “Measurement-induced entanglement phase transition on a superconducting quantum processor with mid-circuit readout.” In: *Nature Physics* **19** (Sept. 1, 2023), pp. 1314–1319. ISSN: 1745-2481. DOI: [10.1038/s41567-023-02076-6](https://doi.org/10.1038/s41567-023-02076-6) (cit. on pp. 4, 82, 158, 192).
- [19] C. Noel, P. Niroula, D. Zhu, et al. “Measurement-induced quantum phases realized in a trapped-ion quantum computer.” In: *Nature Physics* **18** (July 1, 2022), pp. 760–764. ISSN: 1745-2481. DOI: [10.1038/s41567-022-01619-7](https://doi.org/10.1038/s41567-022-01619-7) (cit. on pp. 4, 82, 158, 159).
- [20] J. C. Hoke, M. Ippoliti, E. Rosenberg, et al. “Measurement-induced entanglement and teleportation on a noisy quantum processor.” In: *Nature* **622** (Oct. 1, 2023), pp. 481–486. ISSN: 1476-4687. DOI: [10.1038/s41586-023-06505-7](https://doi.org/10.1038/s41586-023-06505-7) (cit. on pp. 4, 82, 158).
- [21] A. Nahum and B. Skinner. “Entanglement and dynamics of diffusion-annihilation processes with Majorana defects.” In: *Phys. Rev. Res.* **2** (June 2020), p. 023288. DOI: [10.1103/physrevresearch.2.023288](https://doi.org/10.1103/physrevresearch.2.023288) (cit. on pp. 4, 12, 82, 85, 91, 186, 190).
- [22] X. Cao, A. Tilloy, and A. D. Luca. “Entanglement in a fermion chain under continuous monitoring.” In: *SciPost Phys.* **7** (2019), p. 024. DOI: [10.21468/SciPostPhys.7.2.024](https://doi.org/10.21468/SciPostPhys.7.2.024) (cit. on pp. 4, 81, 82, 84, 112, 190).

- [23] X. Chen, Y. Li, M. P. A. Fisher, and A. Lucas. “Emergent conformal symmetry in nonunitary random dynamics of free fermions.” In: *Phys. Rev. Res.* **2** (July 2020), p. 033017. DOI: [10.1103/PhysRevResearch.2.033017](https://doi.org/10.1103/PhysRevResearch.2.033017) (cit. on pp. 4, 82, 190).
- [24] N. Lang and H. P. Büchler. “Entanglement transition in the projective transverse field Ising model.” In: *Phys. Rev. B* **102** (Sept. 2020), p. 094204. DOI: [10.1103/PhysRevB.102.094204](https://doi.org/10.1103/PhysRevB.102.094204) (cit. on pp. 4, 12, 13, 15–17, 19, 21, 26, 27, 29, 82, 100, 101, 103, 158, 166, 172, 186, 190).
- [25] A. Lavasani, Y. Alavirad, and M. Barkeshli. “Measurement-induced topological entanglement transitions in symmetric random quantum circuits.” In: *Nature Physics* **17** (Jan. 2021), pp. 342–347. DOI: [10.1038/s41567-020-01112-z](https://doi.org/10.1038/s41567-020-01112-z) (cit. on p. 4).
- [26] S. Sang and T. H. Hsieh. “Measurement-protected quantum phases.” In: *Phys. Rev. Res.* **3** (June 2021), p. 023200. DOI: [10.1103/physrevresearch.3.023200](https://doi.org/10.1103/physrevresearch.3.023200) (cit. on pp. 4, 82, 83, 191).
- [27] A.-R. Negari, S. Sahu, and T. H. Hsieh. “Measurement-induced phase transitions in the toric code.” In: *Phys. Rev. B* **109** (Mar. 2024), p. 125148. DOI: [10.1103/PhysRevB.109.125148](https://doi.org/10.1103/PhysRevB.109.125148) (cit. on pp. 4, 82, 83, 93).
- [28] M. Ippoliti, M. J. Gullans, S. Gopalakrishnan, D. A. Huse, and V. Khemani. “Entanglement phase transitions in measurement-only dynamics.” In: *Phys. Rev. X* **11** (Feb. 2021), p. 011030. DOI: [10.1103/physrevx.11.011030](https://doi.org/10.1103/physrevx.11.011030) (cit. on pp. 4, 82, 83, 190, 191).
- [29] K. Klocke and M. Buchhold. “Majorana loop models for measurement-only quantum circuits.” In: *Phys. Rev. X* **13** (Nov. 2023), p. 041028. DOI: [10.1103/PhysRevX.13.041028](https://doi.org/10.1103/PhysRevX.13.041028) (cit. on pp. 4, 82, 83, 90, 91, 98, 100, 109, 150, 191).
- [30] O. Alberton, M. Buchhold, and S. Diehl. “Entanglement transition in a monitored free-fermion chain: from extended criticality to area law.” In: *Phys. Rev. Lett.* **126** (Apr. 2021), p. 170602. DOI: [10.1103/PhysRevLett.126.170602](https://doi.org/10.1103/PhysRevLett.126.170602) (cit. on pp. 4, 81, 82, 84, 190).
- [31] M. Buchhold, Y. Minoguchi, A. Altland, and S. Diehl. “Effective theory for the measurement-induced phase transition of Dirac fermions.” In: *Phys. Rev. X* **11** (Oct. 2021), p. 041004. DOI: [10.1103/PhysRevX.11.041004](https://doi.org/10.1103/PhysRevX.11.041004) (cit. on p. 4).
- [32] S. Goto and I. Danshita. “Measurement-induced transitions of the entanglement scaling law in ultracold gases with controllable dissipation.” In: *Phys. Rev. A* **102** (Sept. 2020), p. 033316. DOI: [10.1103/PhysRevA.102.033316](https://doi.org/10.1103/PhysRevA.102.033316) (cit. on p. 4).
- [33] Y. Fuji and Y. Ashida. “Measurement-induced quantum criticality under continuous monitoring.” In: *Phys. Rev. B* **102** (Aug. 2020), p. 054302. DOI: [10.1103/PhysRevB.102.054302](https://doi.org/10.1103/PhysRevB.102.054302) (cit. on p. 4).
- [34] M. Szytniszewski, A. Romito, and H. Schomerus. “Universality of entanglement transitions from stroboscopic to continuous measurements.” In: *Phys. Rev. Lett.* **125** (Nov. 2020), p. 210602. DOI: [10.1103/PhysRevLett.125.210602](https://doi.org/10.1103/PhysRevLett.125.210602) (cit. on pp. 4, 158).

BIBLIOGRAPHY

- [35] C. Liu, P. Zhang, and X. Chen. “Non-unitary dynamics of Sachdev–Ye–Kitaev chain.” In: *SciPost Phys.* **10** (2021), p. 048. DOI: [10.21468/SciPostPhys.10.2.048](https://doi.org/10.21468/SciPostPhys.10.2.048) (cit. on p. 4).
- [36] S.-K. Jian, Z.-C. Yang, Z. Bi, and X. Chen. “Yang–Lee edge singularity triggered entanglement transition.” In: *Phys. Rev. B* **104** (Oct. 2021), p. L161107. DOI: [10.1103/PhysRevB.104.L161107](https://doi.org/10.1103/PhysRevB.104.L161107) (cit. on p. 4).
- [37] M. Van Regemortel, Z.-P. Cian, A. Seif, H. Dehghani, and M. Hafezi. “Entanglement entropy scaling transition under competing monitoring protocols.” In: *Phys. Rev. Lett.* **126** (Mar. 2021), p. 123604. DOI: [10.1103/PhysRevLett.126.123604](https://doi.org/10.1103/PhysRevLett.126.123604) (cit. on p. 4).
- [38] M. Fava, L. Piroli, T. Swann, D. Bernard, and A. Nahum. “Nonlinear sigma models for monitored dynamics of free fermions.” In: *Phys. Rev. X* **13** (Dec. 2023), p. 041045. DOI: [10.1103/PhysRevX.13.041045](https://doi.org/10.1103/PhysRevX.13.041045) (cit. on pp. 4, 100, 105, 130, 133).
- [39] Q. Tang and W. Zhu. “Measurement-induced phase transition: a case study in the nonintegrable model by density-matrix renormalization group calculations.” In: *Phys. Rev. Res.* **2** (Jan. 2020), p. 013022. DOI: [10.1103/PhysRevResearch.2.013022](https://doi.org/10.1103/PhysRevResearch.2.013022) (cit. on p. 4).
- [40] O. Lunt and A. Pal. “Measurement-induced entanglement transitions in many-body localized systems.” In: *Phys. Rev. Res.* **2** (Oct. 2020), p. 043072. DOI: [10.1103/PhysRevResearch.2.043072](https://doi.org/10.1103/PhysRevResearch.2.043072) (cit. on p. 4).
- [41] S.-K. Jian, C. Liu, X. Chen, B. Swingle, and P. Zhang. “Measurement-induced phase transition in the monitored Sachdev–Ye–Kitaev model.” In: *Phys. Rev. Lett.* **127** (Sept. 2021), p. 140601. DOI: [10.1103/PhysRevLett.127.140601](https://doi.org/10.1103/PhysRevLett.127.140601) (cit. on p. 4).
- [42] T. Minato, K. Sugimoto, T. Kuwahara, and K. Saito. “Fate of measurement-induced phase transition in long-range interactions.” In: *Phys. Rev. Lett.* **128** (Jan. 2022), p. 010603. DOI: [10.1103/PhysRevLett.128.010603](https://doi.org/10.1103/PhysRevLett.128.010603) (cit. on pp. 4, 82).
- [43] M. Block, Y. Bao, S. Choi, E. Altman, and N. Y. Yao. “Measurement-induced transition in long-range interacting quantum circuits.” In: *Phys. Rev. Lett.* **128** (Jan. 2022), p. 010604. DOI: [10.1103/PhysRevLett.128.010604](https://doi.org/10.1103/PhysRevLett.128.010604) (cit. on p. 4).
- [44] T. Müller, S. Diehl, and M. Buchhold. “Measurement-induced dark state phase transitions in long-ranged fermion systems.” In: *Phys. Rev. Lett.* **128** (Jan. 2022), p. 010605. DOI: [10.1103/PhysRevLett.128.010605](https://doi.org/10.1103/PhysRevLett.128.010605) (cit. on p. 4).
- [45] M. A. Nielsen and I. L. Chuang. *Quantum computation and quantum information*. 10th ed. Cambridge University Press, (2010). DOI: [10.1017/CBO9780511976667](https://doi.org/10.1017/CBO9780511976667) (cit. on pp. 5, 19, 20, 22, 82, 165, 187).
- [46] D. Gottesman. *The Heisenberg representation of quantum computers*. (1998). ARXIV: [quant-ph/9807006](https://arxiv.org/abs/quant-ph/9807006) (cit. on pp. 6, 82).
- [47] D. Gottesman. “Class of quantum error-correcting codes saturating the quantum Hamming bound.” In: *Phys. Rev. A* **54** (Sept. 1996), pp. 1862–1868. ISSN: 1094-1622. DOI: [10.1103/physreva.54.1862](https://doi.org/10.1103/physreva.54.1862) (cit. on pp. 6, 82).

- [48] D. Gottesman. “Theory of fault-tolerant quantum computation.” In: *Phys. Rev. A* **57** (Jan. 1998), pp. 127–137. DOI: [10.1103/PhysRevA.57.127](https://doi.org/10.1103/PhysRevA.57.127) (cit. on pp. 6, 82).
- [49] S. Aaronson and D. Gottesman. “Improved simulation of stabilizer circuits.” In: *Phys. Rev. A* **70** (Nov. 2004), p. 052328. DOI: [10.1103/PhysRevA.70.052328](https://doi.org/10.1103/PhysRevA.70.052328) (cit. on pp. 6, 7, 82).
- [50] D. Fattal, T. S. Cubitt, Y. Yamamoto, S. Bravyi, and I. L. Chuang. *Entanglement in the stabilizer formalism*. (2004). ARXIV: [quant-ph/0406168](https://arxiv.org/abs/quant-ph/0406168) (cit. on pp. 8, 89, 90, 104).
- [51] L. G. Valiant. “Quantum computers that can be simulated classically in polynomial time.” In: *Proceedings of the thirty-third annual acm symposium on theory of computing*. STOC ’01. Association for Computing Machinery, (2001), pp. 114–123. ISBN: 1581133499. DOI: [10.1145/380752.380785](https://doi.org/10.1145/380752.380785) (cit. on pp. 8, 190).
- [52] R. Jozsa and A. Miyake. “Matchgates and classical simulation of quantum circuits.” In: *Proceedings of the Royal Society A: Mathematical, Physical and Engineering Sciences* **464** (2008), pp. 3089–3106. DOI: [10.1098/rspa.2008.0189](https://doi.org/10.1098/rspa.2008.0189) (cit. on pp. 8, 82, 190).
- [53] P. Jordan and E. Wigner. “Über das Paulische Äquivalenzverbot.” In: *Zeitschrift für Physik* **47** (Sept. 1928), pp. 631–651. DOI: [10.1007/BF01331938](https://doi.org/10.1007/BF01331938) (cit. on pp. 9, 190).
- [54] M. Hebenstreit, R. Jozsa, B. Kraus, and S. Strelchuk. “Computational power of matchgates with supplementary resources.” In: *Phys. Rev. A* **102** (Nov. 2020), p. 052604. DOI: [10.1103/PhysRevA.102.052604](https://doi.org/10.1103/PhysRevA.102.052604) (cit. on pp. 11, 12, 82).
- [55] B. M. Terhal and D. P. DiVincenzo. “Classical simulation of noninteracting-fermion quantum circuits.” In: *Phys. Rev. A* **65** (Mar. 2002), p. 032325. DOI: [10.1103/PhysRevA.65.032325](https://doi.org/10.1103/PhysRevA.65.032325) (cit. on pp. 11, 12, 82).
- [56] D. J. Brod. “Efficient classical simulation of matchgate circuits with generalized inputs and measurements.” In: *Phys. Rev. A* **93** (June 2016), p. 062332. DOI: [10.1103/PhysRevA.93.062332](https://doi.org/10.1103/PhysRevA.93.062332) (cit. on pp. 11, 12, 82).
- [57] S. Bravyi. “Lagrangian representation for fermionic linear optics.” In: *Quantum Info. Comput.* **5** (May 2005), pp. 216–238. ISSN: 1533-7146 (cit. on pp. 11, 12, 82).
- [58] G. C. Wick. “The evaluation of the collision matrix.” In: *Phys. Rev.* **80** (Oct. 1950), pp. 268–272. DOI: [10.1103/PhysRev.80.268](https://doi.org/10.1103/PhysRev.80.268) (cit. on pp. 11, 139).
- [59] P. Calabrese and J. Cardy. “Entanglement entropy and quantum field theory.” In: *Journal of Statistical Mechanics: Theory and Experiment* **2004** (June 2004), P06002. DOI: [10.1088/1742-5468/2004/06/P06002](https://doi.org/10.1088/1742-5468/2004/06/P06002) (cit. on pp. 16, 100).
- [60] P. Calabrese and J. Cardy. “Entanglement entropy and conformal field theory.” In: *Journal of Physics A: Mathematical and Theoretical* **42** (Dec. 2009), p. 504005. DOI: [10.1088/1751-8113/42/50/504005](https://doi.org/10.1088/1751-8113/42/50/504005) (cit. on pp. 16, 100).
- [61] Y. Li, X. Chen, A. W. W. Ludwig, and M. P. A. Fisher. “Conformal invariance and quantum nonlocality in critical hybrid circuits.” In: *Phys. Rev. B* **104** (Sept. 2021), p. 104305. DOI: [10.1103/PhysRevB.104.104305](https://doi.org/10.1103/PhysRevB.104.104305) (cit. on p. 16).

BIBLIOGRAPHY

- [62] S. C. van der Marck. “Percolation thresholds and universal formulas.” In: *Phys. Rev. E* **55** (Feb. 1997), pp. 1514–1517. DOI: [10.1103/PhysRevE.55.1514](https://doi.org/10.1103/PhysRevE.55.1514) (cit. on p. 17).
- [63] M. F. Sykes and J. W. Essam. “Some exact critical percolation probabilities for bond and site problems in two dimensions.” In: *Phys. Rev. Lett.* **10** (Jan. 1963), pp. 3–4. DOI: [10.1103/PhysRevLett.10.3](https://doi.org/10.1103/PhysRevLett.10.3) (cit. on p. 17).
- [64] F. Roser, H. P. Büchler, and N. Lang. “Decoding the projective transverse field Ising model.” In: *Phys. Rev. B* **107** (June 2023), p. 214201. DOI: [10.1103/PhysRevB.107.214201](https://doi.org/10.1103/PhysRevB.107.214201) (cit. on pp. 19, 44, 159, 160, 175).
- [65] E. Knill, R. Laflamme, and W. Zurek. *Threshold accuracy for quantum computation*. (1996). ARXIV: [quant-ph/9610011](https://arxiv.org/abs/quant-ph/9610011) (cit. on p. 19).
- [66] D. Aharonov and M. Ben-Or. “Fault-tolerant quantum computation with constant error.” In: *Proceedings of the Twenty-Ninth Annual ACM Symposium on Theory of Computing*. STOC ’97. Association for Computing Machinery, (1997), pp. 176–188. ISBN: 0897918886. DOI: [10.1145/258533.258579](https://doi.org/10.1145/258533.258579) (cit. on p. 19).
- [67] P. Shor. “Algorithms for quantum computation: discrete logarithms and factoring.” In: *Proceedings 35th Annual Symposium on Foundations of Computer Science*. (1994), pp. 124–134. DOI: [10.1109/SFCS.1994.365700](https://doi.org/10.1109/SFCS.1994.365700) (cit. on p. 19).
- [68] P. W. Shor. “Scheme for reducing decoherence in quantum computer memory.” In: *Phys. Rev. A* **52** (Oct. 1995), R2493–R2496. DOI: [10.1103/PhysRevA.52.R2493](https://doi.org/10.1103/PhysRevA.52.R2493) (cit. on pp. 19, 20, 22).
- [69] A. Steane. “Multiple-particle interference and quantum error correction.” In: *Proceedings of the Royal Society of London. Series A: Mathematical, Physical and Engineering Sciences* **452** (1996), pp. 2551–2577. DOI: [10.1098/rspa.1996.0136](https://doi.org/10.1098/rspa.1996.0136) (cit. on pp. 19, 20, 59).
- [70] B. M. Terhal. “Quantum error correction for quantum memories.” In: *Reviews of Modern Physics* **87** (Apr. 2015), pp. 307–346. DOI: [10.1103/revmodphys.87.307](https://doi.org/10.1103/revmodphys.87.307) (cit. on pp. 20, 59).
- [71] M. J. Gullans and D. A. Huse. “Dynamical purification phase transition induced by quantum measurements.” In: *Phys. Rev. X* **10** (Oct. 2020), p. 041020. DOI: [10.1103/PhysRevX.10.041020](https://doi.org/10.1103/PhysRevX.10.041020) (cit. on pp. 20, 21, 26, 30, 91, 159, 160, 166).
- [72] M. J. Gullans and D. A. Huse. “Scalable probes of measurement-induced criticality.” In: *Phys. Rev. Lett.* **125** (Aug. 2020), p. 070606. DOI: [10.1103/PhysRevLett.125.070606](https://doi.org/10.1103/PhysRevLett.125.070606) (cit. on pp. 20, 26, 30, 91, 159, 160, 166).
- [73] Y. Bao, S. Choi, and E. Altman. “Theory of the phase transition in random unitary circuits with measurements.” In: *Phys. Rev. B* **101** (Mar. 2020), p. 104301. DOI: [10.1103/PhysRevB.101.104301](https://doi.org/10.1103/PhysRevB.101.104301) (cit. on p. 20).
- [74] P. O. Boykin, T. Mor, V. Roychowdhury, and F. Vatan. “Algorithms on ensemble quantum computers.” In: *Natural Computing* **9** (June 1, 2010), pp. 329–345. ISSN: 1572-9796. DOI: [10.1007/s11047-009-9133-0](https://doi.org/10.1007/s11047-009-9133-0) (cit. on p. 20).

- [75] D. Crow, R. Joynt, and M. Saffman. “Improved error thresholds for measurement-free error correction.” In: *Phys. Rev. Lett.* **117** (Sept. 2016), p. 130503. DOI: [10.1103/PhysRevLett.117.130503](https://doi.org/10.1103/PhysRevLett.117.130503) (cit. on p. 20).
- [76] M. A. Perlin, V. N. Premakumar, J. Wang, M. Saffman, and R. Joynt. “Fault-tolerant measurement-free quantum error correction with multiqubit gates.” In: *Phys. Rev. A* **108** (Dec. 2023), p. 062426. DOI: [10.1103/PhysRevA.108.062426](https://doi.org/10.1103/PhysRevA.108.062426) (cit. on p. 20).
- [77] H. Goto, Y. Ho, and T. Kanao. “Measurement-free fault-tolerant logical-zero-state encoding of the distance-three nine-qubit surface code in a one-dimensional qubit array.” In: *Phys. Rev. Res.* **5** (Nov. 2023), p. 043137. DOI: [10.1103/PhysRevResearch.5.043137](https://doi.org/10.1103/PhysRevResearch.5.043137) (cit. on p. 20).
- [78] S. Heußen, D. F. Locher, and M. Müller. “Measurement-free fault-tolerant quantum error correction in near-term devices.” In: *PRX Quantum* **5** (Feb. 2024), p. 010333. DOI: [10.1103/PRXQuantum.5.010333](https://doi.org/10.1103/PRXQuantum.5.010333) (cit. on p. 20).
- [79] S. Veroni, M. Müller, and G. Giudice. “Optimized measurement-free and fault-tolerant quantum error correction for neutral atoms.” In: *Phys. Rev. Res.* **6** (Dec. 2024), p. 043253. DOI: [10.1103/PhysRevResearch.6.043253](https://doi.org/10.1103/PhysRevResearch.6.043253) (cit. on p. 20).
- [80] S. Veroni, A. Paler, and G. Giudice. “Universal quantum computation via scalable measurement-free error correction.” In: *PRX Quantum* **6** (Nov. 2025), p. 040337. DOI: [10.1103/lkk1-v6wp](https://doi.org/10.1103/lkk1-v6wp) (cit. on p. 20).
- [81] F. Butt, D. F. Locher, K. Brechtelsbauer, H. P. Büchler, and M. Müller. “Measurement-free, scalable, and fault-tolerant universal quantum computing.” In: *Science Advances* **11** (2025), eadv2590. DOI: [10.1126/sciadv.adv2590](https://doi.org/10.1126/sciadv.adv2590) (cit. on p. 20).
- [82] Y. Ouyang, Y. Jing, and G. K. Brennen. “Measurement-free code-switching protocol for low-overhead quantum computation using permutation-invariant codes.” In: *PRX Quantum* **6** (Nov. 2025), p. 040341. DOI: [10.1103/p28m-hb6x](https://doi.org/10.1103/p28m-hb6x) (cit. on p. 20).
- [83] K. Brechtelsbauer, F. Butt, D. F. Locher, S. H. Quintero, S. Weber, M. Müller, and H. P. Büchler. *Measurement-free quantum error correction optimized for biased noise.* (2025). ARXIV: [2505.15669](https://arxiv.org/abs/2505.15669) (cit. on p. 20).
- [84] S. B. Bravyi and A. Y. Kitaev. *Quantum codes on a lattice with boundary.* (1998). ARXIV: [quant-ph/9811052](https://arxiv.org/abs/quant-ph/9811052) (cit. on pp. 20, 49, 189).
- [85] A. Kitaev. “Fault-tolerant quantum computation by anyons.” In: *Annals of Physics* **303** (Jan. 2003), pp. 2–30. ISSN: 0003-4916. DOI: [10.1016/s0003-4916\(02\)00018-0](https://doi.org/10.1016/s0003-4916(02)00018-0) (cit. on pp. 20, 44, 49, 189).
- [86] M. H. Freedman and D. A. Meyer. “Projective plane and planar quantum codes.” In: *Foundations of Computational Mathematics* **1** (2001), pp. 325–332. ISSN: 1615-3375. DOI: [10.1007/s102080010013](https://doi.org/10.1007/s102080010013) (cit. on pp. 20, 189).
- [87] E. Dennis, A. Kitaev, A. Landahl, and J. Preskill. “Topological quantum memory.” In: *Journal of Mathematical Physics* **43** (Sept. 2002), pp. 4452–4505. ISSN: 1089-7658. DOI: [10.1063/1.1499754](https://doi.org/10.1063/1.1499754) (cit. on pp. 20, 49, 189).

BIBLIOGRAPHY

- [88] G. A. Paz-Silva, G. K. Brennen, and J. Twamley. “Fault tolerance with noisy and slow measurements and preparation.” In: *Phys. Rev. Lett.* **105** (Aug. 2010), p. 100501. DOI: [10.1103/PhysRevLett.105.100501](https://doi.org/10.1103/PhysRevLett.105.100501) (cit. on p. 20).
- [89] A. G. Fowler, A. M. Stephens, and P. Groszkowski. “High-threshold universal quantum computation on the surface code.” In: *Phys. Rev. A* **80** (Nov. 2009), p. 052312. DOI: [10.1103/PhysRevA.80.052312](https://doi.org/10.1103/PhysRevA.80.052312) (cit. on p. 20).
- [90] J. R. Wootton and D. Loss. “High threshold error correction for the surface code.” In: *Phys. Rev. Lett.* **109** (Oct. 2012), p. 160503. DOI: [10.1103/PhysRevLett.109.160503](https://doi.org/10.1103/PhysRevLett.109.160503) (cit. on p. 20).
- [91] S. Bravyi, M. Suchara, and A. Vargo. “Efficient algorithms for maximum likelihood decoding in the surface code.” In: *Phys. Rev. A* **90** (Sept. 2014), p. 032326. DOI: [10.1103/PhysRevA.90.032326](https://doi.org/10.1103/PhysRevA.90.032326) (cit. on pp. 20, 53, 54, 57, 58, 66, 68, 139, 163, 189).
- [92] A. G. Fowler, A. C. Whiteside, and L. C. L. Hollenberg. “Towards practical classical processing for the surface code.” In: *Phys. Rev. Lett.* **108** (May 2012), p. 180501. DOI: [10.1103/PhysRevLett.108.180501](https://doi.org/10.1103/PhysRevLett.108.180501) (cit. on pp. 20, 44, 49, 58, 59, 175).
- [93] D. S. Wang, A. G. Fowler, A. M. Stephens, and L. C. L. Hollenberg. *Threshold error rates for the toric and surface codes.* (2009). ARXIV: [0905.0531](https://arxiv.org/abs/0905.0531) (cit. on p. 20).
- [94] A. deMarti iOlius, P. Fuentes, R. Orús, P. M. Crespo, and J. Etxezarreta Martinez. “Decoding algorithms for surface codes.” In: *Quantum* **8** (Oct. 2024), p. 1498. ISSN: 2521-327X. DOI: [10.22331/q-2024-10-10-1498](https://doi.org/10.22331/q-2024-10-10-1498) (cit. on p. 20).
- [95] S. Krinner, N. Lacroix, A. Remm, et al. “Realizing repeated quantum error correction in a distance-three surface code.” In: *Nature* **605** (May 2022), pp. 669–674. ISSN: 1476-4687. DOI: [10.1038/s41586-022-04566-8](https://doi.org/10.1038/s41586-022-04566-8) (cit. on pp. 21, 189).
- [96] Y. Zhao, Y. Ye, H.-L. Huang, et al. “Realization of an error-correcting surface code with superconducting qubits.” In: *Phys. Rev. Lett.* **129** (July 2022), p. 030501. DOI: [10.1103/PhysRevLett.129.030501](https://doi.org/10.1103/PhysRevLett.129.030501) (cit. on pp. 21, 189).
- [97] D. Aharonov. “Quantum to classical phase transition in noisy quantum computers.” In: *Phys. Rev. A* **62** (Nov. 2000), p. 062311. DOI: [10.1103/PhysRevA.62.062311](https://doi.org/10.1103/PhysRevA.62.062311) (cit. on p. 21).
- [98] S. Choi, Y. Bao, X.-L. Qi, and E. Altman. “Quantum error correction in scrambling dynamics and measurement-induced phase transition.” In: *Phys. Rev. Lett.* **125** (July 2020), p. 030505. DOI: [10.1103/PhysRevLett.125.030505](https://doi.org/10.1103/PhysRevLett.125.030505) (cit. on pp. 21, 26).
- [99] Y. Li and M. P. A. Fisher. “Statistical mechanics of quantum error correcting codes.” In: *Phys. Rev. B* **103** (Mar. 2021), p. 104306. DOI: [10.1103/PhysRevB.103.104306](https://doi.org/10.1103/PhysRevB.103.104306) (cit. on p. 21).
- [100] R. Fan, S. Vijay, A. Vishwanath, and Y.-Z. You. “Self-organized error correction in random unitary circuits with measurement.” In: *Phys. Rev. B* **103** (May 2021), p. 174309. DOI: [10.1103/PhysRevB.103.174309](https://doi.org/10.1103/PhysRevB.103.174309) (cit. on p. 21).

- [101] Y. Nakata, E. Wakakuwa, and H. Yamasaki. “One-shot quantum error correction of classical and quantum information.” In: *Phys. Rev. A* **104** (July 2021), p. 012408. DOI: [10.1103/PhysRevA.104.012408](https://doi.org/10.1103/PhysRevA.104.012408) (cit. on p. 21).
- [102] M. J. Gullans, S. Krastanov, D. A. Huse, L. Jiang, and S. T. Flammia. “Quantum coding with low-depth random circuits.” In: *Phys. Rev. X* **11** (Sept. 2021), p. 031066. DOI: [10.1103/PhysRevX.11.031066](https://doi.org/10.1103/PhysRevX.11.031066) (cit. on pp. 21, 91).
- [103] L. Fidkowski, J. Haah, and M. B. Hastings. “How dynamical quantum memories forget.” In: *Quantum* **5** (Jan. 2021), p. 382. ISSN: 2521-327X. DOI: [10.22331/q-2021-01-17-382](https://doi.org/10.22331/q-2021-01-17-382) (cit. on p. 21).
- [104] Z. Chen, K. J. Satzinger, J. Atalaya, et al. “Exponential suppression of bit or phase errors with cyclic error correction.” In: *Nature* **595** (July 2021), pp. 383–387. ISSN: 1476-4687. DOI: [10.1038/s41586-021-03588-y](https://doi.org/10.1038/s41586-021-03588-y) (cit. on p. 25).
- [105] T. M. Cover and J. A. Thomas. *Elements of information theory*. Wiley-Interscience, (2006). ISBN: 0471241954 (cit. on p. 25).
- [106] H. Dehghani, A. Lavasani, M. Hafezi, and M. J. Gullans. “Neural-network decoders for measurement induced phase transitions.” In: *Nature Communications* **14** (May 2023), p. 2918. ISSN: 2041-1723. DOI: [10.1038/s41467-023-37902-1](https://doi.org/10.1038/s41467-023-37902-1) (cit. on pp. 30, 159).
- [107] M. Ippoliti and V. Khemani. “Learnability transitions in monitored quantum dynamics via eavesdropper’s classical shadows.” In: *PRX Quantum* **5** (Apr. 2024), p. 020304. DOI: [10.1103/PRXQuantum.5.020304](https://doi.org/10.1103/PRXQuantum.5.020304) (cit. on pp. 30, 159).
- [108] A. Khindanov, I. L. Aleiner, L. Faoro, and L. B. Ioffe. “Observable measurement-induced transitions.” In: *Annals of Physics* **479** (2025), p. 170047. ISSN: 0003-4916. DOI: [10.1016/j.aop.2025.170047](https://doi.org/10.1016/j.aop.2025.170047) (cit. on pp. 30, 159).
- [109] E. Ising. “Beitrag zur Theorie des Ferromagnetismus.” In: *Zeitschrift für Physik* **31** (Feb. 1925), pp. 253–258. ISSN: 0044-3328. DOI: [10.1007/BF02980577](https://doi.org/10.1007/BF02980577) (cit. on pp. 43, 188).
- [110] K. Huang. *Statistical mechanics*. 2nd ed. John Wiley & Sons, (1987) (cit. on pp. 43, 44, 188).
- [111] R. Peierls. “On Ising’s model of ferromagnetism.” In: *Mathematical Proceedings of the Cambridge Philosophical Society* **32** (1936), pp. 477–481. DOI: [10.1017/S0305004100019174](https://doi.org/10.1017/S0305004100019174) (cit. on p. 44).
- [112] R. B. Griffiths. “Peierls proof of spontaneous magnetization in a two-dimensional Ising ferromagnet.” In: *Phys. Rev.* **136** (Oct. 1964), A437–A439. DOI: [10.1103/PhysRev.136.A437](https://doi.org/10.1103/PhysRev.136.A437) (cit. on p. 44).
- [113] L. Onsager. “Crystal statistics. I. A two-dimensional model with an order-disorder transition.” In: *Phys. Rev.* **65** (Feb. 1944), pp. 117–149. DOI: [10.1103/PhysRev.65.117](https://doi.org/10.1103/PhysRev.65.117) (cit. on p. 44).

BIBLIOGRAPHY

- [114] G. Duclos-Cianci and D. Poulin. “Fast decoders for topological quantum codes.” In: *Phys. Rev. Lett.* **104** (Feb. 2010), p. 050504. DOI: [10.1103/PhysRevLett.104.050504](https://doi.org/10.1103/PhysRevLett.104.050504) (cit. on pp. 44, 49, 175).
- [115] Y. Li and M. P. A. Fisher. “Decodable hybrid dynamics of open quantum systems with Z_2 symmetry.” In: *Phys. Rev. B* **108** (Dec. 2023), p. 214302. DOI: [10.1103/PhysRevB.108.214302](https://doi.org/10.1103/PhysRevB.108.214302) (cit. on pp. 44, 51).
- [116] J. Edmonds. “Paths, trees, and flowers.” In: *Canadian Journal of Mathematics* **17** (1965), pp. 449–467. DOI: [10.4153/CJM-1965-045-4](https://doi.org/10.4153/CJM-1965-045-4) (cit. on pp. 47, 177, 188).
- [117] V. Kolmogorov. “Blossom V: a new implementation of a minimum cost perfect matching algorithm.” In: *Mathematical Programming Computation* **1** (2009), pp. 43–67. DOI: [10.1007/s12532-009-0002-8](https://doi.org/10.1007/s12532-009-0002-8) (cit. on pp. 47, 65, 177, 188).
- [118] F. Roser, H. Büchler, and N. Lang. “Scaling of entanglement measures in loop models with extended criticality.” In preparation (cit. on pp. 81, 100).
- [119] A. C. Potter and R. Vasseur. “Entanglement dynamics in hybrid quantum circuits.” In: *Entanglement in Spin Chains: From Theory to Quantum Technology Applications*. Ed. by A. Bayat, S. Bose, and H. Johannesson. Springer International Publishing, (2022), pp. 211–249. ISBN: 978-3-031-03998-0. DOI: [10.1007/978-3-031-03998-0_9](https://doi.org/10.1007/978-3-031-03998-0_9) (cit. on pp. 81, 158).
- [120] X. Turkeshi, A. Biella, R. Fazio, M. Dalmonte, and M. Schiró. “Measurement-induced entanglement transitions in the quantum Ising chain: from infinite to zero clicks.” In: *Phys. Rev. B* **103** (June 2021), p. 224210. DOI: [10.1103/PhysRevB.103.224210](https://doi.org/10.1103/PhysRevB.103.224210) (cit. on p. 82).
- [121] X. Turkeshi, M. Dalmonte, R. Fazio, and M. Schirò. “Entanglement transitions from stochastic resetting of non-Hermitian quasiparticles.” In: *Phys. Rev. B* **105** (June 2022), p. L241114. DOI: [10.1103/PhysRevB.105.L241114](https://doi.org/10.1103/PhysRevB.105.L241114) (cit. on p. 82).
- [122] M. Szytniszewski, O. Lunt, and A. Pal. “Disordered monitored free fermions.” In: *Phys. Rev. B* **108** (Oct. 2023), p. 165126. DOI: [10.1103/PhysRevB.108.165126](https://doi.org/10.1103/PhysRevB.108.165126) (cit. on p. 82).
- [123] G. Kells, D. Meidan, and A. Romito. “Topological transitions in weakly monitored free fermions.” In: *SciPost Phys.* **14** (2023), p. 031. DOI: [10.21468/SciPostPhys.14.3.031](https://doi.org/10.21468/SciPostPhys.14.3.031) (cit. on p. 82).
- [124] H.-Z. Li, J.-X. Zhong, and X.-J. Yu. “Measurement-induced entanglement phase transition in free fermion systems.” In: *Journal of Physics: Condensed Matter* **37** (July 2025), p. 273002. DOI: [10.1088/1361-648X/ade7e5](https://doi.org/10.1088/1361-648X/ade7e5) (cit. on p. 82).
- [125] Q. Tang, X. Chen, and W. Zhu. “Quantum criticality in the nonunitary dynamics of $(2 + 1)$ -dimensional free fermions.” In: *Phys. Rev. B* **103** (May 2021), p. 174303. DOI: [10.1103/PhysRevB.103.174303](https://doi.org/10.1103/PhysRevB.103.174303) (cit. on p. 82).

- [126] S. Sang, Y. Li, T. Zhou, X. Chen, T. H. Hsieh, and M. P. Fisher. “Entanglement negativity at measurement-induced criticality.” In: *PRX Quantum* **2** (July 2021), p. 030313. DOI: [10.1103/PRXQuantum.2.030313](https://doi.org/10.1103/PRXQuantum.2.030313) (cit. on pp. 82, 83, 91, 92, 100, 191).
- [127] C.-M. Jian, B. Bauer, A. Keselman, and A. W. W. Ludwig. “Criticality and entanglement in nonunitary quantum circuits and tensor networks of noninteracting fermions.” In: *Phys. Rev. B* **106** (Oct. 2022), p. 134206. DOI: [10.1103/PhysRevB.106.134206](https://doi.org/10.1103/PhysRevB.106.134206) (cit. on p. 82).
- [128] J. Merritt and L. Fidkowski. “Entanglement transitions with free fermions.” In: *Phys. Rev. B* **107** (Feb. 2023), p. 064303. DOI: [10.1103/PhysRevB.107.064303](https://doi.org/10.1103/PhysRevB.107.064303) (cit. on pp. 82, 83, 85, 92, 94, 95, 104, 146, 147, 150, 190, 191).
- [129] J. Surace and L. Tagliacozzo. “Fermionic Gaussian states: an introduction to numerical approaches.” In: *SciPost Phys. Lect. Notes* (2022), p. 54. DOI: [10.21468/SciPostPhysLectNotes.54](https://doi.org/10.21468/SciPostPhysLectNotes.54) (cit. on pp. 82, 139, 140).
- [130] R. Brauer. “On algebras which are connected with the semisimple continuous groups.” In: *Annals of Mathematics* **38** (1937), pp. 857–872. ISSN: 0003486X, 19398980. URL: <http://www.jstor.org/stable/1968843> (visited on 08/22/2025) (cit. on pp. 82, 89).
- [131] D. Bulgakova and O. Ogievetsky. “Fusion procedure for the walled Brauer algebra.” In: *Journal of Geometry and Physics* **149** (2020), p. 103580. ISSN: 0393-0440. DOI: [10.1016/j.geomphys.2019.103580](https://doi.org/10.1016/j.geomphys.2019.103580) (cit. on pp. 82, 89).
- [132] G. Benkart, M. Chakrabarti, T. Halverson, R. Leduc, C. Lee, and J. Stroomeer. “Tensor product representations of general linear groups and their connections with Brauer algebras.” In: *Journal of Algebra* **166** (1994), pp. 529–567. ISSN: 0021-8693. DOI: [10.1006/jabr.1994.1166](https://doi.org/10.1006/jabr.1994.1166) (cit. on pp. 82, 89).
- [133] A. R. Massih and M. A. Moore. “Phase transition in a polymer chain in dilute solution.” In: *Journal of Physics A: Mathematical and General* **8** (Feb. 1975), p. 237. DOI: [10.1088/0305-4470/8/2/014](https://doi.org/10.1088/0305-4470/8/2/014) (cit. on p. 82).
- [134] H. W. J. Blöte and B. Nienhuis. “Critical behaviour and conformal anomaly of the $O(n)$ model on the square lattice.” In: *Journal of Physics A: Mathematical and General* **22** (May 1989), p. 1415. DOI: [10.1088/0305-4470/22/9/028](https://doi.org/10.1088/0305-4470/22/9/028) (cit. on p. 82).
- [135] T. Vachaspati and A. Vilenkin. “Formation and evolution of cosmic strings.” In: *Phys. Rev. D* **30** (Nov. 1984), pp. 2036–2045. DOI: [10.1103/PhysRevD.30.2036](https://doi.org/10.1103/PhysRevD.30.2036) (cit. on p. 82).
- [136] J. Cardy. *Scaling and renormalization in statistical physics*. Cambridge Lecture Notes in Physics. Cambridge University Press, (1996). ISBN: 9781316036440. DOI: [10.1017/CBO9781316036440](https://doi.org/10.1017/CBO9781316036440) (cit. on p. 82).
- [137] J. Cardy. “SLE for theoretical physicists.” In: *Annals of Physics* **318** (2005). Special Issue, pp. 81–118. ISSN: 0003-4916. DOI: [10.1016/j.aop.2005.04.001](https://doi.org/10.1016/j.aop.2005.04.001) (cit. on p. 82).

BIBLIOGRAPHY

- [138] I. A. Gruzberg, A. W. W. Ludwig, and N. Read. “Exact exponents for the spin quantum Hall transition.” In: *Phys. Rev. Lett.* **82** (May 1999), pp. 4524–4527. DOI: [10.1103/PhysRevLett.82.4524](https://doi.org/10.1103/PhysRevLett.82.4524) (cit. on p. 82).
- [139] E. J. Beamd, J. Cardy, and J. T. Chalker. “Quantum and classical localization, the spin quantum Hall effect, and generalizations.” In: *Phys. Rev. B* **65** (May 2002), p. 214301. DOI: [10.1103/PhysRevB.65.214301](https://doi.org/10.1103/PhysRevB.65.214301) (cit. on pp. 82, 104, 153).
- [140] Y. Ikhlef, P. Fendley, and J. Cardy. “Integrable modification of the critical Chalker–Coddington network model.” In: *Phys. Rev. B* **84** (Oct. 2011), p. 144201. DOI: [10.1103/PhysRevB.84.144201](https://doi.org/10.1103/PhysRevB.84.144201) (cit. on p. 82).
- [141] K. O’Holleran, M. R. Dennis, F. Flossmann, and M. J. Padgett. “Fractality of light’s darkness.” In: *Phys. Rev. Lett.* **100** (Feb. 2008), p. 053902. DOI: [10.1103/PhysRevLett.100.053902](https://doi.org/10.1103/PhysRevLett.100.053902) (cit. on p. 82).
- [142] L. D. C. Jaubert, M. Haque, and R. Moessner. “Analysis of a fully packed loop model arising in a magnetic Coulomb phase.” In: *Phys. Rev. Lett.* **107** (Oct. 2011), p. 177202. DOI: [10.1103/PhysRevLett.107.177202](https://doi.org/10.1103/PhysRevLett.107.177202) (cit. on p. 82).
- [143] A. L. Owczarek and T. Prellberg. “The collapse point of interacting trails in two dimensions from kinetic growth simulations.” In: *Journal of Statistical Physics* **79** (June 1995), pp. 951–967. ISSN: 1572-9613. DOI: [10.1007/BF02181210](https://doi.org/10.1007/BF02181210) (cit. on p. 82).
- [144] R. M. Ziff, X. P. Kong, and E. G. D. Cohen. “Lorentz lattice-gas and kinetic-walk model.” In: *Phys. Rev. A* **44** (Aug. 1991), pp. 2410–2428. DOI: [10.1103/PhysRevA.44.2410](https://doi.org/10.1103/PhysRevA.44.2410) (cit. on p. 82).
- [145] C. Candu, J. L. Jacobsen, N. Read, and H. Saleur. “Universality classes of polymer melts and conformal sigma models.” In: *Journal of Physics A: Mathematical and Theoretical* **43** (Mar. 2010), p. 142001. DOI: [10.1088/1751-8113/43/14/142001](https://doi.org/10.1088/1751-8113/43/14/142001) (cit. on p. 82).
- [146] J. L. Jacobsen, N. Read, and H. Saleur. “Dense loops, supersymmetry, and Goldstone phases in two dimensions.” In: *Phys. Rev. Lett.* **90** (Mar. 2003), p. 090601. DOI: [10.1103/PhysRevLett.90.090601](https://doi.org/10.1103/PhysRevLett.90.090601) (cit. on pp. 82, 105).
- [147] M. J. Martins, B. Nienhuis, and R. Rietman. “Intersecting loop model as a solvable super spin chain.” In: *Phys. Rev. Lett.* **81** (July 1998), pp. 504–507. DOI: [10.1103/PhysRevLett.81.504](https://doi.org/10.1103/PhysRevLett.81.504) (cit. on p. 82).
- [148] N. Read and H. Saleur. “Exact spectra of conformal supersymmetric nonlinear sigma models in two dimensions.” In: *Nuclear Physics B* **613** (2001), pp. 409–444. ISSN: 0550-3213. DOI: [10.1016/S0550-3213\(01\)00395-9](https://doi.org/10.1016/S0550-3213(01)00395-9) (cit. on pp. 82, 105).
- [149] W. Kager and B. Nienhuis. “Monte Carlo study of the hull distribution for the $q = 1$ Brauer model.” In: *Journal of Statistical Mechanics: Theory and Experiment* **2006** (Aug. 2006), P08004. DOI: [10.1088/1742-5468/2006/08/P08004](https://doi.org/10.1088/1742-5468/2006/08/P08004) (cit. on p. 82).

- [150] Y. Ikhlef, J. Jacobsen, and H. Saleur. “Non-intersection exponents of fully packed trails on the square lattice.” In: *Journal of Statistical Mechanics: Theory and Experiment* **2007** (May 2007), P05005. DOI: [10.1088/1742-5468/2007/05/P05005](https://doi.org/10.1088/1742-5468/2007/05/P05005) (cit. on p. 82).
- [151] D. P. Foster. “Universality of collapsing two-dimensional self-avoiding trails.” In: *Journal of Physics A: Mathematical and Theoretical* **42** (Aug. 2009), p. 372002. DOI: [10.1088/1751-8113/42/37/372002](https://doi.org/10.1088/1751-8113/42/37/372002) (cit. on p. 82).
- [152] J. Cardy. “Quantum network models and classical localization problems.” In: *50 years of Anderson localization*. Ed. by E. Abrahams. World Scientific, (June 2010). Chap. 14, pp. 301–326. DOI: [10.1142/9789814299084_0014](https://doi.org/10.1142/9789814299084_0014) (cit. on p. 82).
- [153] E. Bettelheim, I. A. Gruzberg, and A. W. W. Ludwig. “Quantum Hall transitions: an exact theory based on conformal restriction.” In: *Phys. Rev. B* **86** (Oct. 2012), p. 165324. DOI: [10.1103/PhysRevB.86.165324](https://doi.org/10.1103/PhysRevB.86.165324) (cit. on p. 82).
- [154] A. Nahum, P. Serna, A. M. Somoza, and M. Ortuño. “Loop models with crossings.” In: *Phys. Rev. B* **87** (May 2013), p. 184204. DOI: [10.1103/PhysRevB.87.184204](https://doi.org/10.1103/PhysRevB.87.184204) (cit. on pp. 82, 83, 85, 87, 91, 92, 95, 97, 98, 100, 104, 105, 119, 133, 144, 146, 150, 153, 191).
- [155] A. Nahum, J. T. Chalker, P. Serna, M. Ortuño, and A. M. Somoza. “3d loop models and the CP^{n-1} sigma model.” In: *Phys. Rev. Lett.* **107** (Sept. 2011), p. 110601. DOI: [10.1103/PhysRevLett.107.110601](https://doi.org/10.1103/PhysRevLett.107.110601) (cit. on pp. 83, 150).
- [156] P. Serna. *3d unoriented loop models and the RP^{n-1} sigma model*. (2021). ARXIV: [2107.13366](https://arxiv.org/abs/2107.13366) (cit. on pp. 83, 150).
- [157] K. Klocke, D. Simm, G.-Y. Zhu, S. Trebst, and M. Buchhold. “Entanglement dynamics in monitored Kitaev circuits: loop models, symmetry classification, and quantum Lifshitz scaling.” In: *Phys. Rev. B* **111** (June 2025), p. 224301. DOI: [10.1103/PhysRevB.111.224301](https://doi.org/10.1103/PhysRevB.111.224301) (cit. on pp. 83, 150).
- [158] K. Zyczkowski and M. Kus. “Random unitary matrices.” In: *Journal of Physics A: Mathematical and General* **27** (June 1994), p. 4235. DOI: [10.1088/0305-4470/27/12/028](https://doi.org/10.1088/0305-4470/27/12/028) (cit. on p. 84).
- [159] P. Diaconis and P. J. Forrester. “Hurwitz and the origins of random matrix theory in mathematics.” In: *Random Matrices: Theory and Applications* **06** (2017), p. 1730001. DOI: [10.1142/S2010326317300017](https://doi.org/10.1142/S2010326317300017) (cit. on p. 84).
- [160] F. Mezzadri. “How to generate random matrices from the classical compact groups.” In: *Notices of the American Mathematical Society* **54** (May 2007), pp. 592–604. ISSN: 0002-9920 (cit. on p. 84).
- [161] P. Diaconis. “What is ... a random matrix?” In: *Notices Amer. Math. Soc.* **52** (2005), pp. 1348–1349. ISSN: 0002-9920,1088-9477 (cit. on p. 84).

BIBLIOGRAPHY

- [162] H. N. V. Temperley and E. H. Lieb. “Relations between the ‘percolation’ and ‘colouring’ problem and other graph-theoretical problems associated with regular planar lattices: some exact results for the ‘percolation’ problem.” In: *Proceedings of the Royal Society of London. A. Mathematical and Physical Sciences* **322** (1971), pp. 251–280. DOI: [10.1098/rspa.1971.0067](https://doi.org/10.1098/rspa.1971.0067) (cit. on p. 89).
- [163] D. Ridout and Y. Saint-Aubin. “Standard modules, induction and the structure of the Temperley–Lieb algebra.” In: *Advances in Theoretical and Mathematical Physics* **18** (2014), pp. 957–1041 (cit. on p. 89).
- [164] T. Halverson and T. N. Jacobson. “Set-partition tableaux and representations of diagram algebras.” In: *Algebraic Combinatorics* **3** (2020), pp. 509–538. DOI: [10.5802/alco.102](https://doi.org/10.5802/alco.102) (cit. on p. 89).
- [165] A. Nahum, J. Ruhman, S. Vijay, and J. Haah. “Quantum entanglement growth under random unitary dynamics.” In: *Phys. Rev. X* **7** (July 2017), p. 031016. DOI: [10.1103/PhysRevX.7.031016](https://doi.org/10.1103/PhysRevX.7.031016) (cit. on pp. 89, 90).
- [166] E. J. Beamd, A. L. Owczarek, and J. Cardy. “Quantum and classical localization and the Manhattan lattice.” In: *Journal of Physics A: Mathematical and General* **36** (Oct. 2003), p. 10251. DOI: [10.1088/0305-4470/36/41/001](https://doi.org/10.1088/0305-4470/36/41/001) (cit. on p. 104).
- [167] N. D. Mermin and H. Wagner. “Absence of ferromagnetism or antiferromagnetism in one- or two-dimensional isotropic Heisenberg models.” In: *Phys. Rev. Lett.* **17** (Nov. 1966), pp. 1133–1136. DOI: [10.1103/PhysRevLett.17.1133](https://doi.org/10.1103/PhysRevLett.17.1133) (cit. on p. 104).
- [168] P. C. Hohenberg. “Existence of long-range order in one and two dimensions.” In: *Phys. Rev.* **158** (June 1967), pp. 383–386. DOI: [10.1103/PhysRev.158.383](https://doi.org/10.1103/PhysRev.158.383) (cit. on p. 104).
- [169] N. D. Mermin. “Crystalline order in two dimensions.” In: *Phys. Rev.* **176** (Dec. 1968), pp. 250–254. DOI: [10.1103/PhysRev.176.250](https://doi.org/10.1103/PhysRev.176.250) (cit. on p. 104).
- [170] P. Calabrese and J. Cardy. “Evolution of entanglement entropy in one-dimensional systems.” In: *Journal of Statistical Mechanics: Theory and Experiment* **2005** (Apr. 2005), P04010. DOI: [10.1088/1742-5468/2005/04/P04010](https://doi.org/10.1088/1742-5468/2005/04/P04010) (cit. on p. 112).
- [171] P. Calabrese and J. Cardy. “Quantum quenches in extended systems.” In: *Journal of Statistical Mechanics: Theory and Experiment* **2007** (June 2007), P06008. DOI: [10.1088/1742-5468/2007/06/P06008](https://doi.org/10.1088/1742-5468/2007/06/P06008) (cit. on p. 112).
- [172] M. Rigol, V. Dunjko, and M. Olshanii. “Thermalization and its mechanism for generic isolated quantum systems.” In: *Nature* **452** (Apr. 2008), pp. 854–858. ISSN: 1476-4687. DOI: [10.1038/nature06838](https://doi.org/10.1038/nature06838) (cit. on p. 112).
- [173] H. Kim and D. A. Huse. “Ballistic spreading of entanglement in a diffusive non-integrable system.” In: *Phys. Rev. Lett.* **111** (Sept. 2013), p. 127205. DOI: [10.1103/PhysRevLett.111.127205](https://doi.org/10.1103/PhysRevLett.111.127205) (cit. on p. 112).

- [174] M. Mezei and D. Stanford. “On entanglement spreading in chaotic systems.” In: *Journal of High Energy Physics* **2017** (May 2017), p. 65. ISSN: 1029-8479. DOI: [10.1007/JHEP05\(2017\)065](https://doi.org/10.1007/JHEP05(2017)065) (cit. on p. 112).
- [175] C. J. Thomae. *Einleitung in die Theorie der bestimmten Integrale*. Louis Nebert, (1875), p. 48 (cit. on p. 127).
- [176] P. Bohl. “Über ein in der Theorie der säkularen Störungen vorkommendes Problem.” In: *Journal für die reine und angewandte Mathematik* **135** (1909), pp. 189–283. URL: <http://eudml.org/doc/149304> (cit. on p. 128).
- [177] W. Sierpinski. “Sur la valeur asymptotique d’une certaine somme.” In: *Bull Intl. Acad. Polonmaise des Sci. et des Lettres (Cracovie) series A* (1910), pp. 9–11 (cit. on p. 128).
- [178] H. Weyl. “Über die Gibbs’sche Erscheinung und verwandte Konvergenzphänomene.” In: *Rendiconti del Circolo Matematico di Palermo (1884-1940)* **30** (Dec. 1910), pp. 377–407. ISSN: 0009-725X. DOI: [10.1007/BF03014883](https://doi.org/10.1007/BF03014883) (cit. on p. 128).
- [179] H. Weyl. “Über die Gleichverteilung von Zahlen mod. Eins.” In: *Mathematische Annalen* **77** (1916), pp. 313–352. URL: <http://eudml.org/doc/158730> (cit. on p. 128).
- [180] S. Weinzierl. *Introduction to Monte Carlo methods*. (2000). ARXIV: [hep-ph/0006269](https://arxiv.org/abs/hep-ph/0006269) (cit. on p. 128).
- [181] G. M. Fichtenholz. *Differential- und Integralrechnung*. 10th ed. Vol. 2. VEB Deutscher Verlag der Wissenschaften, (1990). ISBN: 3-326-00399-4 (cit. on p. 129).
- [182] H. A. Dye. “Unitary solutions to the Yang–Baxter equation in dimension four.” In: *Quantum Information Processing* **2** (Apr. 1, 2003), pp. 117–152. ISSN: 1573-1332. DOI: [10.1023/A:1025843426102](https://doi.org/10.1023/A:1025843426102) (cit. on p. 134).
- [183] L. H. Kauffman and S. J. Lomonaco. “Braiding operators are universal quantum gates.” In: *New Journal of Physics* **6** (Oct. 2004), p. 134. DOI: [10.1088/1367-2630/6/1/134](https://doi.org/10.1088/1367-2630/6/1/134) (cit. on p. 134).
- [184] Y. Zhang, L. H. Kauffman, and M.-L. Ge. “Universal quantum gate, Yang–Baxterization and Hamiltonian.” In: *International Journal of Quantum Information* **03** (2005), pp. 669–678. DOI: [10.1142/S0219749905001547](https://doi.org/10.1142/S0219749905001547) (cit. on pp. 134, 135).
- [185] Y. Zhang. *Braid group, Temperley–Lieb algebra, and quantum information and computation*. (2008). ARXIV: [quant-ph/0601050](https://arxiv.org/abs/quant-ph/0601050) (cit. on pp. 134, 135).
- [186] Y. Zhang, N. Jing, and M.-L. Ge. “Quantum algebras associated with Bell states.” In: *Journal of Physics A: Mathematical and Theoretical* **41** (Jan. 2008), p. 055310. DOI: [10.1088/1751-8113/41/5/055310](https://doi.org/10.1088/1751-8113/41/5/055310) (cit. on pp. 134, 135).
- [187] B. Abdesselam, A. Chakrabarti, V. K. Dobrev, and S. G. Mihov. “Higher dimensional unitary braid matrices: construction, associated structures, and entanglements.” In: *Journal of Mathematical Physics* **48** (May 2007), p. 053508. ISSN: 0022-2488. DOI: [10.1063/1.2737266](https://doi.org/10.1063/1.2737266) (cit. on p. 134).

BIBLIOGRAPHY

- [188] J.-L. Chen, K. Xue, and M.-L. Ge. “Braiding transformation, entanglement swapping, and Berry phase in entanglement space.” In: *Phys. Rev. A* **76** (Oct. 2007), p. 042324. DOI: [10.1103/PhysRevA.76.042324](https://doi.org/10.1103/PhysRevA.76.042324) (cit. on p. 135).
- [189] C.-L. Ho, A. I. Solomon, and C.-H. Oh. “Quantum entanglement, unitary braid representation and Temperley–Lieb algebra.” In: *Europhysics Letters* **92** (Nov. 2010), p. 30002. DOI: [10.1209/0295-5075/92/30002](https://doi.org/10.1209/0295-5075/92/30002) (cit. on p. 135).
- [190] Y. Ben-Aryeh. *The use of braid operators for implementing entangled large n-qubits Bell states (n>2)*. (2014). ARXIV: [1403.2524](https://arxiv.org/abs/1403.2524) (cit. on p. 135).
- [191] T. M. Liggett. “Exclusion processes.” In: *Stochastic interacting systems: contact, voter and exclusion processes*. Springer Berlin Heidelberg, (1999), pp. 209–316. ISBN: 978-3-662-03990-8. DOI: [10.1007/978-3-662-03990-8_4](https://doi.org/10.1007/978-3-662-03990-8_4) (cit. on p. 135).
- [192] C. Kipnis, S. Olla, and S. R. S. Varadhan. “Hydrodynamics and large deviation for simple exclusion processes.” In: *Communications on Pure and Applied Mathematics* **42** (1989), pp. 115–137. DOI: [10.1002/cpa.3160420202](https://doi.org/10.1002/cpa.3160420202) (cit. on p. 135).
- [193] J. E. Santos and G. M. Schütz. “Exact time-dependent correlation functions for the symmetric exclusion process with open boundary.” In: *Phys. Rev. E* **64** (Aug. 2001), p. 036107. DOI: [10.1103/PhysRevE.64.036107](https://doi.org/10.1103/PhysRevE.64.036107) (cit. on p. 135).
- [194] B. Derrida, B. Douçot, and P.-E. Roche. “Current fluctuations in the one-dimensional symmetric exclusion process with open boundaries.” In: *Journal of Statistical Physics* **115** (May 2004), pp. 717–748. ISSN: 1572-9613. DOI: [10.1023/B:JOSS.0000022379.95508.b2](https://doi.org/10.1023/B:JOSS.0000022379.95508.b2) (cit. on p. 135).
- [195] A. Imparato, V. Lecomte, and F. van Wijland. “Equilibriumlike fluctuations in some boundary-driven open diffusive systems.” In: *Phys. Rev. E* **80** (July 2009), p. 011131. DOI: [10.1103/PhysRevE.80.011131](https://doi.org/10.1103/PhysRevE.80.011131) (cit. on p. 135).
- [196] B. Derrida and A. Gerschenfeld. “Current fluctuations of the one dimensional symmetric simple exclusion process with step initial condition.” In: *Journal of Statistical Physics* **136** (July 2009), pp. 1–15. ISSN: 1572-9613. DOI: [10.1007/s10955-009-9772-7](https://doi.org/10.1007/s10955-009-9772-7) (cit. on p. 135).
- [197] U. Basu, A. Kundu, and A. Pal. “Symmetric exclusion process under stochastic resetting.” In: *Phys. Rev. E* **100** (Sept. 2019), p. 032136. DOI: [10.1103/PhysRevE.100.032136](https://doi.org/10.1103/PhysRevE.100.032136) (cit. on pp. 137, 138).
- [198] A. Nahum, J. T. Chalker, P. Serna, M. Ortuño, and A. M. Somoza. “Phase transitions in three-dimensional loop models and the CP^{n-1} sigma model.” In: *Phys. Rev. B* **88** (Oct. 2013), p. 134411. DOI: [10.1103/PhysRevB.88.134411](https://doi.org/10.1103/PhysRevB.88.134411) (cit. on p. 150).
- [199] F. Roser, E. M. Springer, H. P. Büchler, and N. Lang. *Robust detection of an entanglement transition in the projective transverse field Ising model*. (2025). ARXIV: [2511.17370](https://arxiv.org/abs/2511.17370) (cit. on p. 157).

- [200] U. Fano. “Description of states in quantum mechanics by density matrix and operator techniques.” In: *Rev. Mod. Phys.* **29** (Jan. 1957), pp. 74–93. DOI: [10.1103/RevModPhys.29.74](https://doi.org/10.1103/RevModPhys.29.74) (cit. on p. 158).
- [201] R. O’Donnell and J. Wright. “Efficient quantum tomography.” In: *Proceedings of the Forty-Eighth Annual ACM Symposium on Theory of Computing*. STOC ’16. Association for Computing Machinery, (2016), pp. 899–912. ISBN: 9781450341325. DOI: [10.1145/2897518.2897544](https://doi.org/10.1145/2897518.2897544) (cit. on p. 158).
- [202] T. Scharnhorst, J. Spilecki, and J. Wright. *Optimal lower bounds for quantum state tomography*. (2025). ARXIV: [2510.07699](https://arxiv.org/abs/2510.07699) (cit. on p. 158).
- [203] W. K. Wootters and W. H. Zurek. “A single quantum cannot be cloned.” In: *Nature* **299** (Oct. 1982), pp. 802–803. ISSN: 1476-4687. DOI: [10.1038/299802a0](https://doi.org/10.1038/299802a0) (cit. on p. 158).
- [204] D. Dieks. “Communication by EPR devices.” In: *Physics Letters A* **92** (1982), pp. 271–272. ISSN: 0375-9601. DOI: [10.1016/0375-9601\(82\)90084-6](https://doi.org/10.1016/0375-9601(82)90084-6) (cit. on p. 158).
- [205] S. Czischek, G. Torlai, S. Ray, R. Islam, and R. G. Melko. “Simulating a measurement-induced phase transition for trapped-ion circuits.” In: *Phys. Rev. A* **104** (Dec. 2021), p. 062405. DOI: [10.1103/PhysRevA.104.062405](https://doi.org/10.1103/PhysRevA.104.062405) (cit. on pp. 158, 192).
- [206] M. Ippoliti and V. Khemani. “Postselection-free entanglement dynamics via spacetime duality.” In: *Phys. Rev. Lett.* **126** (Feb. 2021), p. 060501. DOI: [10.1103/PhysRevLett.126.060501](https://doi.org/10.1103/PhysRevLett.126.060501) (cit. on p. 158).
- [207] M. Ippoliti, T. Rakovszky, and V. Khemani. “Fractal, logarithmic, and volume-law entangled nonthermal steady states via spacetime duality.” In: *Phys. Rev. X* **12** (Mar. 2022), p. 011045. DOI: [10.1103/PhysRevX.12.011045](https://doi.org/10.1103/PhysRevX.12.011045) (cit. on p. 158).
- [208] H. F. Hofmann. “Complete characterization of post-selected quantum statistics using weak measurement tomography.” In: *Phys. Rev. A* **81** (Jan. 2010), p. 012103. DOI: [10.1103/PhysRevA.81.012103](https://doi.org/10.1103/PhysRevA.81.012103) (cit. on p. 158).
- [209] S. Wu. “State tomography via weak measurements.” In: *Scientific Reports* **3** (Feb. 2013), p. 1193. ISSN: 2045-2322. DOI: [10.1038/srep01193](https://doi.org/10.1038/srep01193) (cit. on p. 158).
- [210] A. Gaikwad, G. Singh, K. Dorai, and Arvind. “Direct tomography of quantum states and processes via weak measurements of Pauli spin operators on an NMR quantum processor.” In: *The European Physical Journal D* **77** (Dec. 2023), p. 209. ISSN: 1434-6079. DOI: [10.1140/epjd/s10053-023-00791-6](https://doi.org/10.1140/epjd/s10053-023-00791-6) (cit. on p. 158).
- [211] M. Szyniszewski, A. Romito, and H. Schomerus. “Entanglement transition from variable-strength weak measurements.” In: *Phys. Rev. B* **100** (Aug. 2019), p. 064204. DOI: [10.1103/PhysRevB.100.064204](https://doi.org/10.1103/PhysRevB.100.064204) (cit. on p. 158).
- [212] S. Roy, J. T. Chalker, I. V. Gornyi, and Y. Gefen. “Measurement-induced steering of quantum systems.” In: *Phys. Rev. Res.* **2** (Sept. 2020), p. 033347. DOI: [10.1103/PhysRevResearch.2.033347](https://doi.org/10.1103/PhysRevResearch.2.033347) (cit. on p. 159).

BIBLIOGRAPHY

- [213] K. Pöyhönen, A. G. Moghaddam, M. N. Ivaki, and T. Ojanen. *Postselection-free approach to monitored quantum dynamics and entanglement phase transitions*. (2025). ARXIV: [2406.19052](https://arxiv.org/abs/2406.19052) (cit. on p. 159).
- [214] G. Passarelli, X. Turkeshi, A. Russomanno, P. Lucignano, M. Schirò, and R. Fazio. “Many-body dynamics in monitored atomic gases without postselection barrier.” In: *Phys. Rev. Lett.* **132** (Apr. 2024), p. 163401. DOI: [10.1103/PhysRevLett.132.163401](https://doi.org/10.1103/PhysRevLett.132.163401) (cit. on p. 159).
- [215] X. Feng, B. Skinner, and A. Nahum. “Measurement-induced phase transitions on dynamical quantum trees.” In: *PRX Quantum* **4** (Sept. 2023), p. 030333. DOI: [10.1103/PRXQuantum.4.030333](https://doi.org/10.1103/PRXQuantum.4.030333) (cit. on p. 159).
- [216] X. Feng, J. Côté, S. Kourtis, and B. Skinner. *Postselection-free experimental observation of the measurement-induced phase transition in circuits with universal gates*. (2025). ARXIV: [2502.01735](https://arxiv.org/abs/2502.01735) (cit. on p. 159).
- [217] Y. Li, Y. Zou, P. Glorioso, E. Altman, and M. P. A. Fisher. “Cross entropy benchmark for measurement-induced phase transitions.” In: *Phys. Rev. Lett.* **130** (June 2023), p. 220404. DOI: [10.1103/PhysRevLett.130.220404](https://doi.org/10.1103/PhysRevLett.130.220404) (cit. on p. 159).
- [218] M. Tikhanovskaya, A. Lavasani, M. P. A. Fisher, and S. Vijay. “Universality of the cross-entropy in \mathbb{Z}_2 symmetric monitored quantum circuits.” In: *Phys. Rev. B* **109** (June 2024), p. 224313. DOI: [10.1103/PhysRevB.109.224313](https://doi.org/10.1103/PhysRevB.109.224313) (cit. on p. 159).
- [219] H. Kamakari, J. Sun, Y. Li, J. J. Thio, T. P. Gujarati, M. P. A. Fisher, M. Motta, and A. J. Minnich. “Experimental demonstration of scalable cross-entropy benchmarking to detect measurement-induced phase transitions on a superconducting quantum processor.” In: *Phys. Rev. Lett.* **134** (Mar. 2025), p. 120401. DOI: [10.1103/PhysRevLett.134.120401](https://doi.org/10.1103/PhysRevLett.134.120401) (cit. on p. 159).
- [220] S. Aaronson. “Shadow tomography of quantum states.” In: *SIAM Journal on Computing* **49** (2020), STOC18-368-STOC18-394. DOI: [10.1137/18M120275X](https://doi.org/10.1137/18M120275X) (cit. on pp. 159, 192).
- [221] H.-Y. Huang, R. Kueng, and J. Preskill. “Predicting many properties of a quantum system from very few measurements.” In: *Nature Physics* **16** (Oct. 2020), pp. 1050–1057. ISSN: 1745-2481. DOI: [10.1038/s41567-020-0932-7](https://doi.org/10.1038/s41567-020-0932-7) (cit. on pp. 159, 165, 192).
- [222] A. Elben, S. T. Flammia, H.-Y. Huang, R. Kueng, J. Preskill, B. Vermersch, and P. Zoller. “The randomized measurement toolbox.” In: *Nature Reviews Physics* **5** (Jan. 2023), pp. 9–24. ISSN: 2522-5820. DOI: [10.1038/s42254-022-00535-2](https://doi.org/10.1038/s42254-022-00535-2) (cit. on pp. 159, 192).
- [223] S. J. Garratt and E. Altman. “Probing postmeasurement entanglement without postselection.” In: *PRX Quantum* **5** (July 2024), p. 030311. DOI: [10.1103/PRXQuantum.5.030311](https://doi.org/10.1103/PRXQuantum.5.030311) (cit. on pp. 159, 163–165, 193).
- [224] M. McGinley. “Postselection-free learning of measurement-induced quantum dynamics.” In: *PRX Quantum* **5** (May 2024), p. 020347. DOI: [10.1103/PRXQuantum.5.020347](https://doi.org/10.1103/PRXQuantum.5.020347) (cit. on p. 159).

- [225] C. Dankert, R. Cleve, J. Emerson, and E. Livine. “Exact and approximate unitary 2-designs and their application to fidelity estimation.” In: *Phys. Rev. A* **80** (July 2009), p. 012304. DOI: [10.1103/PhysRevA.80.012304](https://doi.org/10.1103/PhysRevA.80.012304) (cit. on p. 164).
- [226] G. Lindblad. “Completely positive maps and entropy inequalities.” In: *Communications in Mathematical Physics* **40** (June 1975), pp. 147–151. ISSN: 1432-0916. DOI: [10.1007/BF01609396](https://doi.org/10.1007/BF01609396) (cit. on p. 165).

Acknowledgments

I worked on this dissertation for more than five years. During this time, I was incredibly lucky to work with and be supported by the kindest and most talented people anyone could have wished for. Without them, this thesis would not exist. So I want to take this opportunity to thank them individually.

First of all, I want to thank Hans Peter Büchler, whose guidance over the past seven years has been invaluable. Thank you for allowing me to stay at the institute after my master's thesis, for all our long discussions, for giving me the freedom to work on what I found interesting, and most importantly, for creating an amazing team to work with. Your support means a lot. Furthermore, I thank you for your enthusiasm in your lectures that creates a culture where teaching is more than a mere obligation.

My thanks also go to Eric Lutz, who not only took on the role of a secondary examiner for my master's thesis but also accepted to be an examiner for this thesis, and to Tilman Pfau for presiding over the examining board.

In a stroke of pure luck, more than seven years ago, I met Nicolai Lang, with whom I not only wrote my master's thesis, but who also became a true mentor to me to this today. Working with you for so many years was enjoyable beyond measure. Thank you for your guidance, for your incredible explanations, and for your endless patience when I would not stop knocking at your door. Talking to you was always very easy and I have never left your office without having learned something. Thank you also for keeping our institute running, specifically its IT infrastructure that made my research possible.

Speaking of people who keep our institute running — I want to thank Oliver Nagel. Research in physics seems very easy once one tries to navigate the bureaucracy of a German university. Your knowledge and *savoir-faire* is invaluable to all of us. Thank you also to Nadine Prellwitz for joining our institute and taking on these tasks with Oliver.

Thank you Katharina Brechtelsbauer for the countless hours of gossip during your “occasional” coffee breaks. Having you as an office neighbor was one of the great joys of my day-to-day life and no one could have organized the lectures and tutorials with as much patience as you did. Thank you also for being the antithesis to Nicolai — whenever we talked, I probably forgot something very important.

ACKNOWLEDGEMENTS

A special thanks to Denis Sedov, with whom I shared an office during the last few years. Thank you for making this so much fun — you might be the only person at the institute who can match my weird working hours. Thank you also to Yanek Verghis for looking only slightly disappointed when finding me instead of Denis at the office...

Thank you Rukmani Bai for making Kaffeklatsch like no one else, Sebastian Weber for bringing me to the institute, Chris Bühler for thinking deeply about *any* question I could ask you, Manya Willberg for being my fellow institute photographer, Johannes Mögerle for your readiness to help in any situation, and Nastasia Makki for the great talks and for sharing the stressful times while we both wrote our theses. Thank you also to the rest of the current and former Büchler group (in no particular order): Luka Jibuti, Tobias Ilg, Kevin Kleinbeck, Jan Kumlin, Simon Fell, Santiago Higuera Quintero, Alicia Biselli, Gina Warttmann, Hannah Richter, Jakob Hartmann, and Tobias Maier. Thank you for all the game nights, the dinners, for allowing me to skip the volleyball tournaments, and so much more.

I also want to highlight my bachelor students Melvin Ruffner, Maurizio Trigilia and Marius Gericke (I prefer to call you the M&M&Ms) and my master student Etienne Maurice Springer. Thank you for making me think with your questions, making me learn with your work and for making teaching such a great joy.

Further, I want to thank Mathias Scheurer and his group for joining our institute not only with your research but also by enriching the social life at ITP III.

Beyond my colleagues, I have been lucky to have some great physicist friends. In particular, I want to thank Annika Belz for giving me a chance to dump all my complaints about anything to you (this has been surprisingly therapeutic), for all the movie sessions, all the gossip, and for sharing the struggle that comes with doing research in physics. Thank you Tobias Reinsch for the spontaneous chess sessions, our late-night talks, and your general excitement for anything worth being excited about. The two of you made studying physics a lot more fun.

Thank you also to the Arbeitskreis Photographie that has been my greatest source of well-needed distraction over the last eight years. Thank you Katrin Bidmon for being so welcoming when I joined the group and for being a real force of support when the group (and especially I) needed you. Thank you Espen Xylander for being such a kind person, a great photographic inspiration, and for all the late-night sessions in the studio and darkroom. Thank you also Christiane Müller for completing our small team and for being such an inspiration to all of us. Working with the three of you to coordinate and reorganize our group was a great experience.

I also want to deeply thank my roommate Nina Walther, who — as I have been told — is also my girlfriend of 12 years. Thank you for putting up with me, for your patience and your unwavering support. Thank you also for all the great times I get to spend with you. Thank you for going on a hike without me so I could instead figure out a proof that had tormented me, thank you for doing every Kehrwoche for a whole year, and thank you for proofreading this whole thesis (I still have no idea how I tricked you into doing this)!

Thank you to my parents Anne & Michael Roser and my sister Tabea Roser-Hofmann for being a great family that has always had my back. Thank you also to my grandparents Ursula & Dieter Roser for your great support and for inspiring me to do a PhD.

Thank you to Nikon, Sony, Sigma, Godox, Shen Hao, Mamiya, Kodak, Fujifilm, and Ilford for helping me keep my sanity – although therapy might have been cheaper..

Thank you, to the English, language for being, so very elegant, much more elegant than the German language, but, for some reason I, will never figure out, where to put the, commas.

Finally, I want to thank the bosons for being so nice. Dear fermions, please be less difficult and confusing. Try to be more like the bosons. And to you, hard-core bosons: You guys rock!

Felix Roser
Leinfelden-Echterdingen, November 2025